NASA CR-175022

Rocket Thrust Chamber Thermal Barrier Coatings

Final Report
under contract NAS3-23262

SOLAR TURBINES INCORPORATED

NASA CR-175022

Rocket Thrust Chamber Thermal Barrier Coatings

Final Report
under contract NAS3-23262

by
A.P. Batakis
J.W. Vogan

for
National Aeronautics & Space Administration
Communications & Propulsion Center
21000 Brookpark Road
Cleveland, OH 44135

July 1985
SR84-R-5052-16

SOLAR TURBINES INCORPORATED
SUBSIDIARY OF CATERPILLAR TRACTOR CO.
P.O. Box 85376, San Diego, CA 92138-5376

1. Report No.	2. Government Accession No.	3. Recipient's Catalog No.
CR-175022		

4. Title and Subtitle	5. Report Date
Rocket Thrust Chamber Thermal Barrier Coatings	July 1985
	6. Performing Organization Code

7. Author(s)	8. Performing Organization Report No.
A. P. Batakis and J. W. Vogan	SR85-R-5052-16
	10. Work Unit No.

9. Performing Organization Name and Address	11. Contract or Grant No.
Solar Turbines Incorporated P.O. Box 85376 San Diego, CA 92138-5376	NAS 3-23262
	13. Type of Report and Period Covered
12. Sponsoring Agency Name and Address	Final Report Dec. 1981 - Oct. 1984
National Aeronautics & Space Administration Communications & Propulsion Center 21000 Brookpark Road Cleveland, OH 44135	14. Sponsoring Agency Code 5310

15. Supplementary Notes

16. Abstract

A research program was conducted to generate data and develop analytical techniques to predict the performance and reliability of ceramic thermal barrier coatings in high heat flux environments. A finite element model was used to analyze the thermomechanical behavior of coating systems in rocket thrust chambers. Candidate coating systems (using a copper substrate, NiCrAlY bond coat and $ZrO_2.8Y_2O_3$ ceramic overcoat) were selected for detailed study based on photomicrographic evaluations of experimental test specimens. The effects of plasma spray application parameters on the material properties of these coatings were measured and the effects on coating performance evaluated using the finite element model. Coating design curves which define acceptable operating envelopes for selected coating systems were constructed based on temperature and strain limitations.

Spray gun power level was found to have the most significant effect on coating structure. Three coating systems were selected for study using different power levels. Thermal conductivity, strain tolerance, density, and residual stress were measured for these coatings. Analyses indicated that extremely thin coatings (<0.02 mm) are required to accommodate the high heat flux of a rocket thrust chamber and ensure structural integrity. High heat flux coatings are extremely sensitive to material property and thickness variations; thus precise control of these variables is essential to successful coating utilization. Coating tests indicate that the bond-substrate interface may be the weak link in the coating system. Further development of the analytical model and the plasma spray techniques are recommended.

17. Key Words (Suggested by Author(s))	18. Distribution Statement

19. Security Classif. (of this report)	20. Security Classif. (of this page)	21. No. of pages	22. Price*
Unclassified	Unclassified	164	

*For sale by the National Technical Information Service, Springfield, Virginia 22161

TABLE OF CONTENTS

TABLE OF CONTENTS (Continued)

LIST OF FIGURES

LIST OF FIGURES (Continued)

LIST OF FIGURES (Continued)

LIST OF FIGURES (Continued)

LIST OF FIGURES (Continued)

LIST OF FIGURES (Continued)

LIST OF TABLES

LIST OF TABLES (Continued)

1

INTRODUCTION

The objective of this program is to develop a zirconia based thermal barrier coating (TBC) system for use in high heat flux rocket applications such as the Space Shuttle main engine (SSME) thrust chamber. The technology developed is also pertinent to other applications such as hot components in the gas turbine engine. Previous TBC development and test has concentrated on ceramic overlays ranging from 0.25 mm to 0.38 mm in thickness. The high heat fluxes encountered in high pressure rocket engines dictate that thinner, 0.012 mm to 0.10 mm, coatings be used to avoid surface melting and mechanical failure of the coating.

The plasma sprayed TBC required in this application is a complex structure. No currently accepted model is known that relates coating performance to thickness and to controllable process variables. The use of very thin coatings, such as those under consideration, is particularly complicated. Four examples of this complexity are given below. These illustrate some of the difficulties that were anticipated in the practical and the analytical development program.

1. Structures are frequently two phase (e.g., monoclinic plus transformable tetragonal in the case of zirconia) and may vary from point to point.

2. Each successively deposited grain impacts a surface whose temperature may increase as coating thickness increases.

3. Defects (e.g.,pores) are of significant size in relation to coating thickness so that bulk or average coating properties may not be appropriate.

4. Individual grain size of the plasma spray powder approaches total coating thickness as does the normal surface roughness of plasma sprayed coatings.

2

PROCEDURES

2.1 LABORATORY MATERIALS AND PROCEDURES

The coating system selected for evaluation in this study was a copper substrate, NiCrAlY bond coat and yttria stabilized zirconia ceramic thermal barrier. This bond coat/ceramic combination has been extensively investigated as a TBC for heat engines and shows great promise as a reliable coating.

The coating deposition performed in this study was accomplished using a Metco 7M plasma system. During the program, deposition parameters such as gas flow, power levels, standoff, etc. were varied. The methods used to define these variations, and tests used to establish the resulting effects on coating properties, are given in this section.

2.1.1 Powder Specification and Preparation

The powder materials used in this study were as follows:

Bond Coat = Amdry powder #961
18.3% Cr, 5.8% Al, 0.5% Y, bal. Ni
-170 + 325 mesh

Ceramic TBC = Cerac Zirconium Oxide-Yttria Stabilized powder
$ZrO_2.8Y_2O_3$
-325 mesh

The ceramic powder was determined to have the following size distributions:

+100 mesh - trace
-100 + 140 mesh - 4%
-140 + 200 mesh - 30%
-200 + 325 mesh - 61%
-325 mesh - 5%

Early tests indicated that narrowing the particle size range within that of the starting material had a negligible effect on coating structure. Thus, the as-received material was used in this study.

2.1.2 Plasma Variables

The following deposition parameters were varied during the test program. The effects of each variable on coating structure were evaluated by metallurgical examination.

Arc Current

During the program, current to the plasma gun was varied over a range of 300 to 1000 amperes. The current was measured at the control console using a 50 millivolt shunt and meter. Calibration tests indicated that, with manual correction for drift by the operator, an accuracy of ±25 amperes could be maintained during a test run.

Arc Voltage

Arc voltage was also monitored at the control console and these values are reported to an accuracy of ±2.5 volts. Voltage measurements at the gun input connections showed a voltage drop of 1 to 3 volts in the water cooled power cables. The voltage drop to the gun was dependent upon the current.

Plasma and Carrier Gas Flows

The flow of plasma on carrier Porter gas was controlled by Fisher purge meters. Pressure at the meters was maintained at 689 kPa. Flow was regulated by needle valves giving a reproducibility of ±5%.

Powder Feed Rate

Powder feed control utilized a Model 1250 Plasmadyne hopper. This unit incorporates a metering disc with a digital speed readout to introduce powder into the carrier gas stream. Delivery rates were periodically verified by collecting and weighing the powder from the delivery tube over a period of thirty minutes. In addition, the initial weight of powder introduced into the cannister was recorded and at the completion of the test, the weight of powder remaining was established. The difference in these two weights was recorded. The latter method was subject to errors resulting from material retained in the powder feed system after emptying the cannister.

Deposition Rates

The rate of coating deposition was established by direct measurement. The plasma gun was traversed at a constant rate for a specified number of cycles. Thickness measurements were made after every five cycles to determine if deposit rates were constant. At completion of the test, metallurgical sections were made to verify coating thickness.

Nozzle Effects

The effect of changing the plasma nozzle (anode) were determined using the various configurations supplied for the Metco 7M system. No modifications were made in the base or configuration. Data supplied by the manufacturer were used as a guide in establishing basic operational characteristics.

2.1.3 Property Measurement

Density/Porosity

Five methods were used to determine coating density. In initial trials, test specimens were weighed before and after coating. The increased weight was attributed to the coating deposit. Coating thickness and area measurements were then made, the apparent volume calculated, and the apparent density (weight divided by volume) reported.

Porosity of the coating was also determined by immersing pre-weighed coated specimens in boiling water. The heat was removed and the water cooled to room temperature. The specimens were then removed from the water, excess water removed and the specimen rapidly weighed. The gain in weight was attributed to water entrapped in pores, the pore volume was then calculated using the known density of water.

The third and fourth methods used for determining coating density required the preparation of metallurgical coating sections. Test specimens were sectioned and photomicrographs were made, usually at 100X magnification. From these photomicrographs, porosity was established by photometrically comparing average reflectance of the coating section with the nonporous substrate and by direct measurement of the average pore area in a unit area of coating.

The fifth method used to determine density was by direct measurement. The area of a rectangular coated specimen was measured. The substrate and bond coat (if used) were carefully removed by chemical etching and the coating was weighed after rinsing and drying. The specimen was then mounted and polished for metallographic examination and coating thickness measurement. The volume of the coating was then calculated from this data and the density calculated using the previously determined coating weight.

Coating Thickness

Because of the extremely thin coatings being evaluated, thickness measurement required a high degree of precision. During the coating process, measurement of coating thickness was approximated using a micrometer. These measurements were limited to ±0.013 mm by the roughness and irregularities in the coating. More precise measurements were made after coating the specimens using a metallurgical section and a microscope with a calibrated eyepiece.

Coating Strength

Coating strength was determined using a four point bend test (see Fig. 1). The analytical methods used to determine the coating stresses developed during this test are described in Appendix 1.

Copper specimens 0.81 mm thick x 13 mm wide x 76 mm long were coated on one side with a 0.03 mm NiCrAlY bond coat. A yttria stabilized TBC was then applied over this bond coat at selected thicknesses ranging from 0.02 mm to 0.15 mm. The specimen was then placed on two knife edge supports spaced a distance of 51 mm apart. For tensile loading of the coating the coated surface was placed on the supports and for compressive coating loads the coated surface was placed opposite from the supports. The specimen was then loaded symmetrically by knife edges spaced 25 mm apart at a rate of 0.08 mm/second until coating failure occurred as evidenced by an abrupt decrease in the load required to maintain a constant rate of strain. Deflection was initially measured using a dial gauge mounted directly below the mid-point of the specimen. Subsequent tests used crosshead travel during loading to monitor specimen deflection.

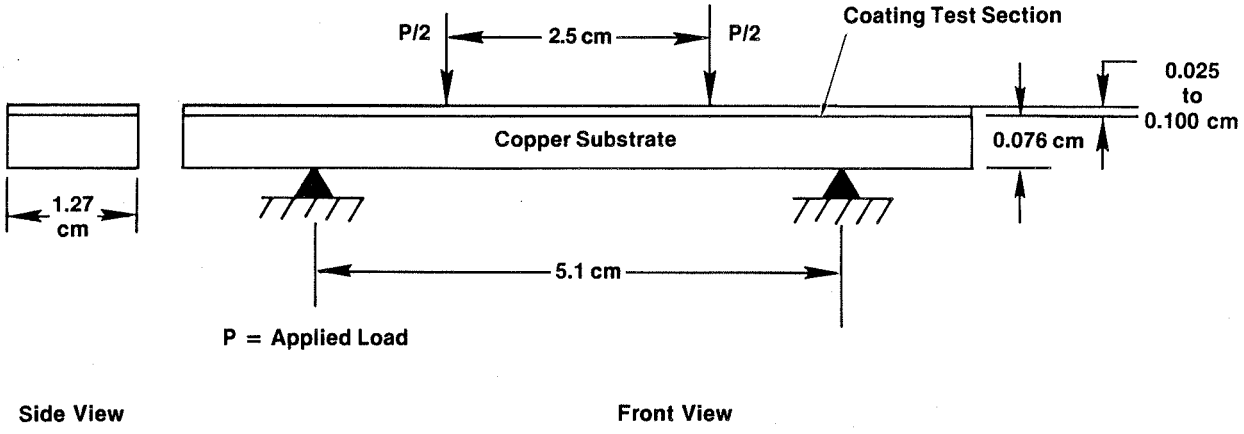

Figure 1. Schematic of Four Point Flexure Test

Thermal Diffusivity and Conductivity

Thermal conductivity of the coatings were measured at Purdue Laboratories using a laser heat pulse technique. A detailed discussion of this technique is given by Taylor (Ref. 1).

For this measurement, copper specimens 13 mm x 13 mm x 1.6 mm thick were coated on one side with the TBC to be tested. Coating thickness was a nominal 0.18 mm. A thermocouple was attached to the uncoated surface of the specimen, the assembly furnace heated to the desired test temperature and a laser heat pulse applied to the coating. Temperature rise of the back face as a function of time was measured. This, combined with coating and substrate thicknesses, densities and specific heats enabled the calculation of diffusivity and conductivity using the methods described by Taylor in the previously cited reference.

2.1.4 Calorimeter Testing

A water cooled calorimeter was used to measure average heat flux from the plasma torch, heat flux during coating deposition and the reaction of the coatings to high heat inputs. This calorimeter, shown in Figure 2, consists of two water cooled copper components. The first is the central test area and the second is the outer guard ring used to shield areas other than the test surface from external influences. In operation, a constant metered flow of water is supplied to the test area, and water inlet and outlet temperatures are monitored. The calorimeter is inserted into the plasma flame and the heat absorbed by the cooling water is presumed to be the total heat input over the test area.

The calorimeter data is then converted to heat flux in the following manner:

$$Q = \frac{(0.279)\ (W)\ (\Delta T)}{\pi d^2}$$

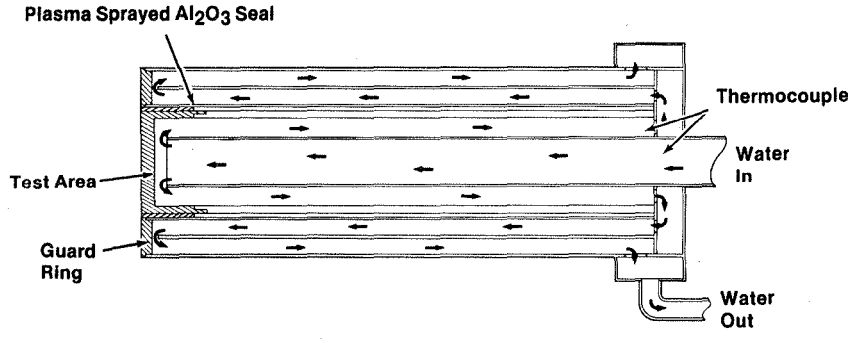

Figure 2. Calorimeter

where:

Q = heat flux (watts/mm^2)
ΔT = $T_{inlet} - T_{outlet}$ (°C)
W = water flow (grams/min.)
d = test diameter (mm)

2.1.5 Residual Stress and Stress Free Temperature

Residual stress in the coating was evaluated using the techniques described by Andrews (Ref. 2). The model is shown in Figure 3 and the symbol definitions are given below:

Subscript (1) ceramic
Subscript (2) copper
α = coefficient of thermal expansion
E = modulus of elasticity
I = moment of inertia
h = total composite thickness
a_1 = ceramic thickness
a_2 = copper thickness
L = active length
r = radius of curvature = $L^2/2$
δ = tangential deflection
S_1 = stress in ceramic

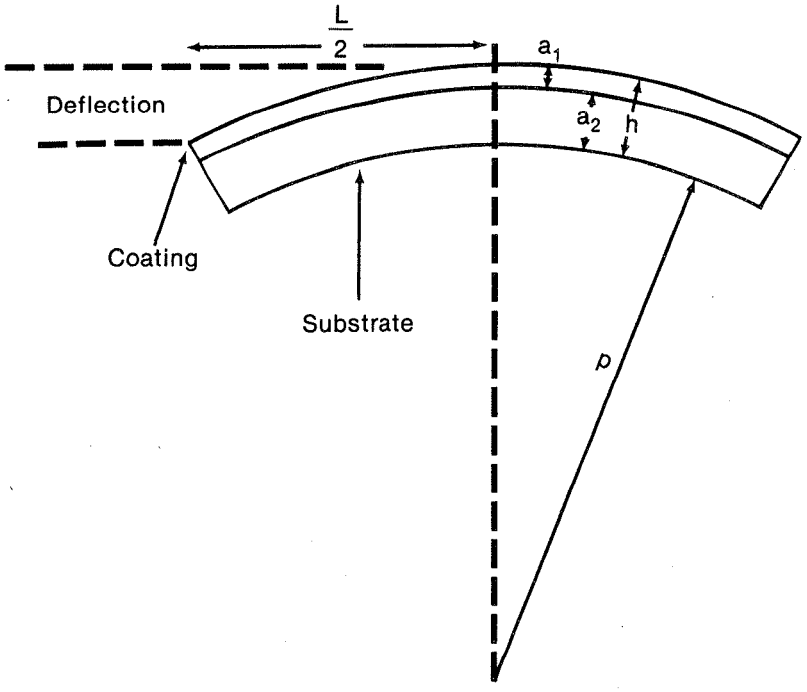

Figure 3. Residual Stress Model

b = specimen width
ΔT = $T_{SF} - T_{ambient}$
T_{SF} = stress-free temperature

This approach was initially developed for calculation of stresses in porcelain enamels and fits well with the requirements of thin TBC's. The methodology is described by the following equation:

$$S_1 = \frac{-2\delta}{L^2}\left[\frac{2}{ha_1}(E_1I_1 + E_2I_2) + \frac{a_1E_1}{2}\right] \quad (1)$$

Since deflection (δ) can be measured directly, equation (1) is easily applied.

For most calculations E_1I_1 and a_1E_1 are small and can be omitted from the calculation, reducing equation (1) to:

$$S_1 = \frac{-4\delta E_2I_2}{L^2ha_1} \quad (2)$$

where

$$I = \frac{b\,a^3}{12} \quad (3)$$

The stress-free temperature of the system is calculated from the bi-metallic relationship:

$$\delta = K\frac{(\alpha_2 - \alpha_1)(\Delta T)L^2}{h} \quad (4)$$

where

$$K = \frac{3(1+m)^2}{3(1+m)^2 + (1+m)\left(m^2 + \frac{1}{mn}\right)} \quad (5)$$

and

$$m = \alpha_1/\alpha_2 \quad (6)$$

$$n = E_1/E_2 \quad (7)$$

Hence:

$$\Delta T = \frac{h}{(\alpha_2 - \alpha_1)L^2K} \quad (8)$$

and

$$T_{SF} = \Delta T + 20°C \quad (9)$$

For the purposes of these calculations the following constants were used:

$E_1 = 45 \times 10^6$ kPa
$E_2 = 117 \times 10^6$ kPa
$\alpha_1 = 7.15 \times 10^{-6}/°C$
$\alpha_2 = 17.6 \times 10^{-6}/°C$

The following procedures were used to obtain the deflection values (δ) used in these calculations. Copper test strips, 0.8 mm x 13 mm x 76 mm, were bond coated with 0.03 mm of NiCrAlY on one side. The deflection, or chord height, if any, was determined over the 50 mm midspan (L). The specimen was then coated with the zirconia TBC and the measurement repeated. Any change in curvature was recorded and the resulting value used to calculate the residual stress in the coating.

Stress free temperatures were also calculated from this data. The results were then confirmed by furnace heating the specimen to the calculated temperature and determining if it returned to its original configuration.

Similar tests were performed using copper rings 68 mm in diameter rolled and butt welded from 13 mm wide, 0.8 mm strips. The rings were vacuum annealed at 760°C after bond coating to relieve initial forming and coating stresses. After coating and segmenting, the change in diameter of the ring, due to the coating process, was established and used in Equation (1) for an alternate means of calculating residual stress.

2.1.6 Substrate Temperature

During trial coating application, the substrate temperature was monitored using an Inconel sheathed chromel-alumel thermocouple, 0.76 mm in diameter. The thermocouple was installed in the copper substrate by first drilling a 0.77 mm hole through the specimen and then inserting the thermocouple. The edges of the hole were then staked to retain the thermocouple with its tip flush with the surface to be coated. Then a NiCrAlY bond coat was applied to bond the tip of the thermocouple to the substrate. Temperature recording was done with a conventional strip chart recorder.

2.2 ANALYTICAL PROCEDURES

2.2.1 Coating System Performance Analysis

Finite element analyses, using the ANSYS code, were used to evaluate coating system performance under simulated operating conditions. The coating system model used for these analyses (shown in Fig. 4) simulates the coated thrust

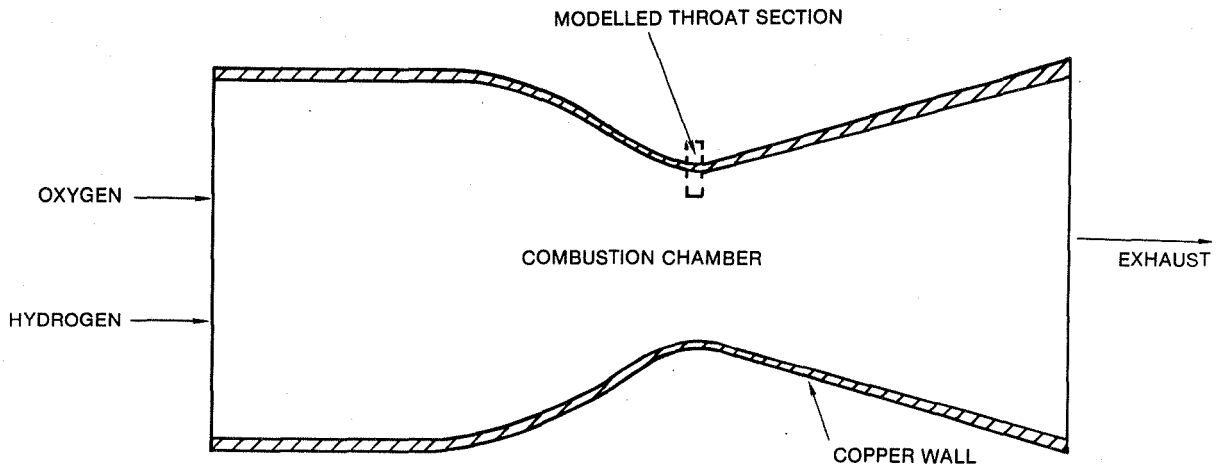

Figure 4a. Rocket Thrust Chamber

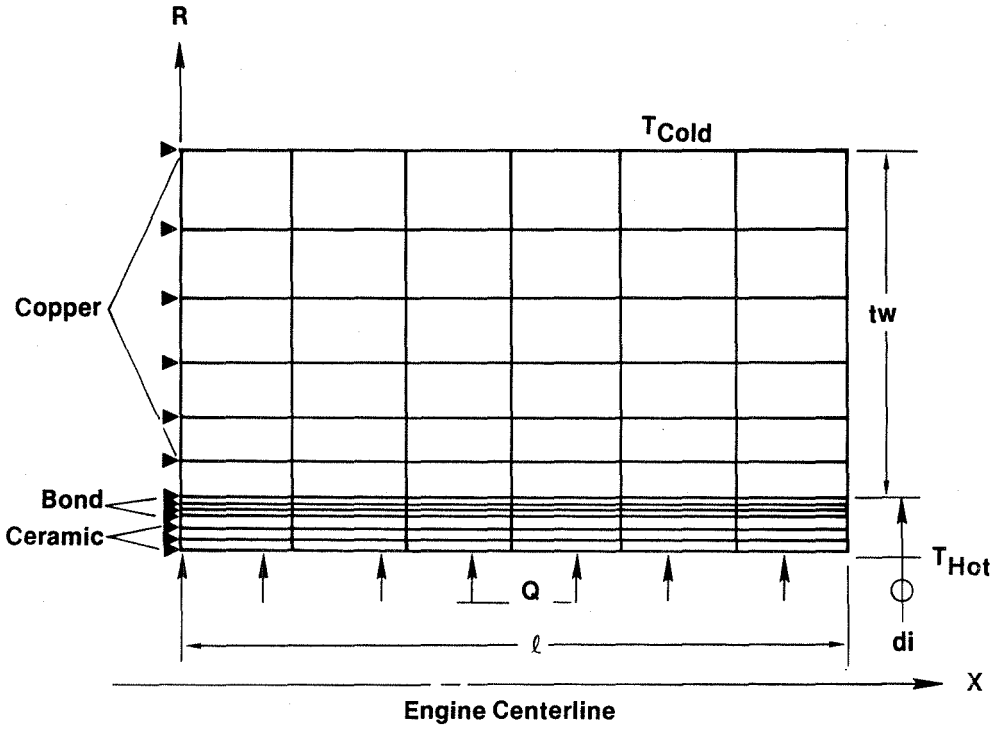

Figure 4b. Thrust Chamber Model

chamber wall of a rocket engine. This two-dimensional, axisymmetric model represents a cross-section of the wall at the throat of the thrust chamber.

The elements used in this finite element model were two-dimensional, isoparametric, axisymmetric ring elements. Each element was defined by four nodal

points and each node was defined by a radius and an axial location. For thermal analyses, each node had a single degree of freedom: temperature. For structural analyses, each node had two degrees of freedom: translations in the radial and axial directions.

The finite element geometry for the thermal analyses was identical to that for the structural analyses. This allowed the temperature distributions which were derived from the thermal analyses to be directly translated to the structural model.

The basic geometry of the thrust chamber model consists of a 66.04 mm internal diameter (di) copper cylinder with a 0.889 mm wall (tw). Attached to the inner surface of this cylinder is a 0.038 mm thick (tb) NiCrAlY bond coat, and a variable thickness (tc) $ZrO_28Y_2O_3$ ceramic coating. Ceramic coating thicknesses from 0.0127 mm to 0.203 mm were investigated. The axial length (ℓ) of the model was 0.229 mm, although a 50.8 mm length was used in some of the preliminary analyses.

The finite element model was divided into nine equal elements in the axial direction, to accommodate axial variations in boundary conditions. In the radial direction, the ceramic and bond coats were divided into three element layers each, and the copper substrate was divided into six. This element configuration resulted in element aspect ratios (axial length to radial thickness ratios) from 0.375 to 6 in the ceramic coating, 2 in the bond coat and 0.17 in the copper substrate. Use of the long (50 mm) preliminary model resulted in element aspect ratios from 83 to 667 in the ceramic and 444 in the bond coat. It is generally desirable to maintain an aspect ratio between 1 and 4, to ensure numerical accuracy. The effect of aspect ratio on the accuracy of these analyses was evaluated by comparing results using the long and short finite element models.

The three coating system materials were assumed to be homogeneous and isotropic. Properties of all three materials were initially obtained from the literature. These properties are listed in Table 1. In the final analyses, measured material properties were substituted for literature values where applicable. The temperature dependency of these material properties created a non-linear problem. This required iterative analyses, with the solutions defined using a specified measure of convergence.

A variety of thermal boundary conditions were selected for these coating systems analyses. These conditions were intended to simulate the range of anticipated operating conditions in a typical high pressure rocket engine thrust chamber and to define an operating envelope based on coating material limitations. Thermal boundary conditions were established in two ways: (1) a hot surface temperature and a cold surface temperature were defined or (2) a heat flux and a cold surface temperature were defined.

The outer surface of a typical rocket thrust chamber is cooled with liquid hydrogen, which has a boiling point of -240°C at ambient pressure. Test data indicate that the actual cold surface temperature of a rocket chamber during operation is between 0 and 200°C. For these analyses, three cold surface temperatures were evaluated: -240, 0, and 200°C. Heat fluxes in the range

Table 1

Material Properties From the Literature (Refs. 10-16)

Material	Thermal Conductivity (W/mK)	Elastic Modulus (GPa)	Specific Heat (J/kg.K)	Thermal Expansion Coefficient ($\times 10^{-6}$/C)	Density (g/cc)	Poisson's Ratio
$ZrO_2 8Y_2O_3$ Ceramic Coating	$2.2 \times 10^{-4}T + 1.09$ ($400<T<2200$°K)	$45.06 - 0.0248T$ (90°C$<T<1200$°C)	$317 + 0.813T - 9.55 \times 10^{-4}T^2 + 6.30 \times 10^{-7}T^3$ (200°K$<T<1500$°K)	$7.1844+0.003888T$ (90°C$<T<1200$°C)	--	0.23
Solid Zirconia (Stabilized ZrO_2)	$2.708 - 5 \times 10^{-4}T$ (70°C $< T <$ 1100°C)	205	400 to 640	8.6 to 15.2	5.63 to 6.27	0.23 to 0.35
NiCrAlY Bond Coat	$8.3 \times 10^{-3}T + 6.7$ (400°K$<T<1400$°K)	$125.6-0.0149T$ (90°C$<T<550$°C)	$0.476 + 0.00086T - 0.0000015T^2$ (90°C$<T<1100$°C)	$13.3182-0.0121T + 5.8729E-5T^2$ (90°C$<T<1100$°C)	6.98	0.23
Oxygen Free Copper Substrate	391	117	0.39	5.4	8.94	0.350

typically encountered in rocket thrust chambers, 50 to 165 W/mm^2, were also used for these analyses. Typically values of 49, 82 and 164 W/mm^2 were used. Ceramic surface temperatures were evaluated in the range of 1000 to 2600°C ($ZrO_28Y_2O_3$ melting point). A maximum desirable ceramic operating temperature of 1650°C was established based on past experience, and this value was used for most of the analyses in which a ceramic surface temperature was specified.

One structural boundary condition was imposed for these analyses: one radial edge of the coating system model was restrained from movement in the axial direction. This condition was held for all analyses. No external loads, pressures, or displacements were imposed.

The thermal and structural boundary conditions are indicated graphically in Figure 4. Examples of the ANSYS finite element input and output are included in Appendix 2. The output from the thermal analyses consisted of heat flow rates and temperature distributions. The output from the structural analyses consisted of displacements, stresses, and reaction forces.

2.2.2 Coating Structure Analysis

The effect of coating microstructure on the thermal conductivity of a coating was evaluated using the ANSYS finite element code. A two-dimensional, planar model of a coating system was used for these analyses. This model, shown in Figure 5, used a biaxial plane thermal element. Each element was defined by four nodes having a single degree of freedom, temperature, at each node.

The model shown in Figure 5 represents a simplified porous coating structure. This geometry was selected to facilitate the finite element modeling. The model was essentially composed of "blocks" of coating material. Pores were simulated by eliminating some of these blocks, in specified patterns.

The model used in these analyses simulates the basic coating system being considered by NASA for rocket thrust chambers: a 0.889 mm thick copper substrate with a 0.038 mm NiCrAlY bond coat and a variable thickness ZrO_28YO_3 ceramic coat. The material properties that were used are presented in Table 1. The value of thermal conductivity for the ceramic in Table 1 was used for the solid ceramic elements in the finite element model.

Boundary conditions for this model were established by specifying the hot ceramic surface temperature and the cold copper surface temperature. To maintain an accurate temperature gradient along the edges of the coating, the nodes along each edge were coupled to similar nodes within the coating.

The effect of radiation across the individual pores was investigated using this model. Radiation links were specified between the upper and lower surfaces of the pores. Radiative heat transfer was calculated from the standard radiation function defined as follows:

$$q = \sigma \Sigma F A (T_1^4 - T_2^4)$$

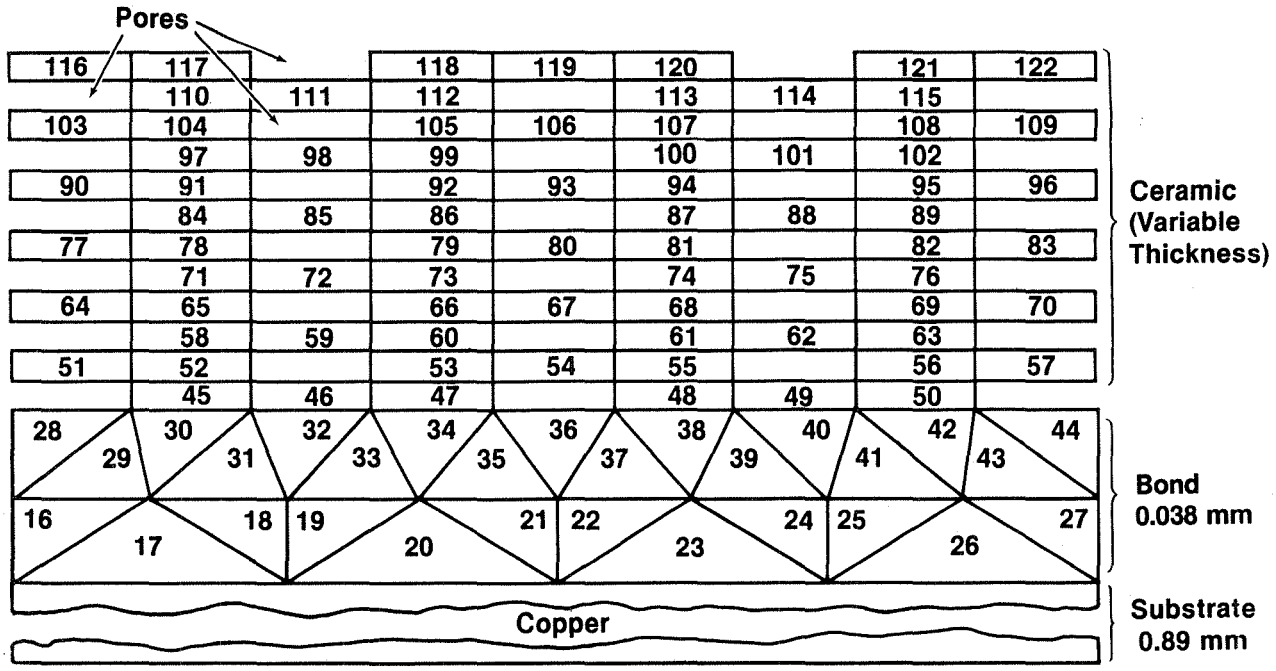

Figure 5. Finite Element Model of a Porous Coating

where:

σ = Stefan-Boltzmann constant
Σ = emissivity
F = geometric form factor
A = area
q = heat flow rate

T_1 = temperature of hot surface
T_2 = temperature of cold surface

The effect of coating microstructure on the thermal conductivity of ceramic coatings was investigated using this finite element model. Various coating structures were evaluated, having different pore sizes, pore shapes, pore densities, etc. Each coating structure was characterized by three geometric parameters:

1. P_t - total porosity; the volume of pores divided by the total coating volume (% of total volume)

2. D_r - dimension ratio; the pore length (axial) divided by the pore thickness (radial)

3. P_i - pore size; total porosity divided by the number of pores (% of total volume)

The goal of these analyses was to establish a relationship between the three coating variables (D_r, P_t, P_i) and effective thermal conductivity.

The approach was to subject each coating structure to a fixed temperature differential and calculate, using finite element analyses, the heat flow through the coating. The effective thermal conductivity of each coating structure was then calculated from

$$k = Q\, t/A\, \Delta T$$

where

k = effective thermal conductivity of the coating
Q = heat flow through the coating
A = overall area of coating model perpendicular to heat flow
ΔT = temperature drop across coating
t = coating thickness

The effective conductivity of each coating structure was normalized to the maximum possible thermal conductivity. This maximum value was established by analyzing a coating with no porosity. Thus, each conductivity is expressed as a percent of maximum.

This analytical model of the coating structure did not consider thermal contact resistance between layers of ceramic or between different materials. It was anticipated that the effect of thermal contact resistance, and any other unaccounted for phenomena, would be reflected in an empirical adjustment of the analytical model. Conflicting reports as to the significance of thermal contact resistance in TBC's have been observed in the literature (Ref. 3, 4).

2.2.3 Failure Strain Analyses

The four-point flexure test was initially evaluated using coating strength data from the literature (Ref. 5). This reference quoted a compressive failure strain of 0.78% in a $MgO\text{-}ZrO_2$ coating, using a similar four-point flexure test. It was calculated that hardened copper could accommodate this strain level without plastic deformation. An elastic stress-strain analysis was thus derived, for a composite beam, to evaluate the failure strains in the coated specimens.

Preliminary testing with the four point flexure test for measuring coating strengths revealed that plastic deformation of the copper substrate occurred before coating failure. The initial stress-strain analysis, derived for an elastic composite beam specimen, was then replaced by a more sophisticated analysis which accounted for plasticity in the copper substrate. This analysis is described in Appendix 1 with the computer program created to perform the numerical solution.

2.3 COATING OF SUBSCALE THRUST CHAMBER

Initial development work on this program was accomplished using flat specimens and a standard plasma spray gun configuration. The test chambers were 66 mm diameter cylinders and were not accessible to the standard gun configuration. A 61 cm small bore extension gun was therefore used to coat these chambers. The two gun configurations are shown in Figure 6.

In the conventional configuration, the electrode, plasma gas flow and coating deposition were along a single axis normal to the coated surface. Gun standoff was varied over a range of 50-100 mm to aid in process control. The small bore coating equipment deflects the plasma gas stream at an angle of 45° to the gun axis, and to the coated surface. Gun standoff was limited by the cylinder ID. Further coating development tests were required to produce equivalent coatings with changed equipment.

The evaluation procedure consisted of first establishing three coating structures using conventional test specimens as described in Section 2.1.2. Metallurgical and material property evaluations were used to characterize each coating. Test rings 66 mm in diameter, formed from 0.81 mm thick copper strips, were then coated using the angle extension. Using the previously determined power levels, the gas flows and powder feed rates were varied until equivalent structures were obtained with the internal diameter equipment. In addition, the ring was periodically reversed relative to the gun entry end to compensate for the 45° impingement angle and offset the shadowing effects of previously deposited coating particles.

To verify coating quality on the test cylinder, extensions of the same diameter were attached to each cylinder and coated simultaneously using the settings established by the previous ring tests. After the coating operation was completed, these extensions were removed, sectioned and evaluated metallurgically.

The use of thermocouples to measure substrate temperatures during deposit was not feasible due to the double wall construction of the test chamber. Temperature recorders* in the form of adhesive strips which indicated the maximum temperature by a permanent color change were located in selected locations on the thrust chambers. These provided information on the maximum temperature developed during the coating operation.

The fixture used to coat the chamber is shown in Figure 7. The thrust chamber was located on a variable speed, rotating head. For control of substrate temperature, a controlled cooling air flow was introduced through the fuel line fittings on one end. Exhaust air temperature was monitored to further insure part-to-part repeatability.

---

* Manufactured by Tedatemp Corporation, Fullerton, CA

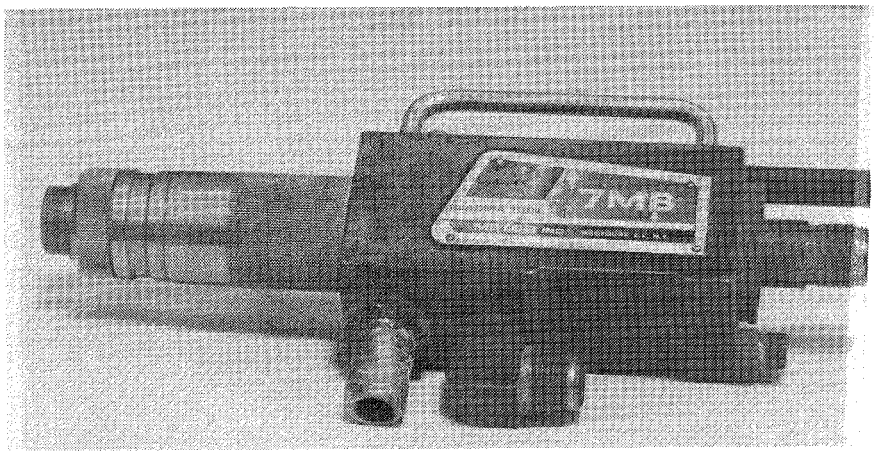

(A) Metco 7MB Direct Spray Gun

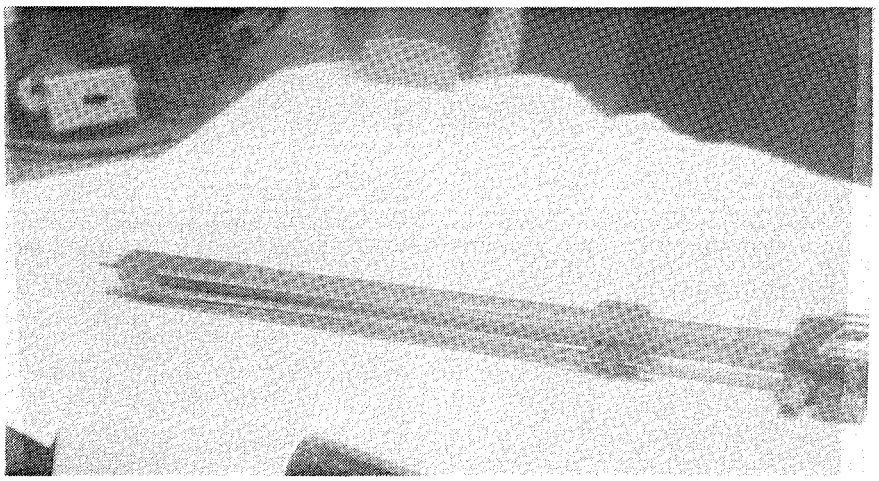

(B) Metco 7MBT-12 45 Degree Angle Spray Gun

Figure 6. Two-Gun Configurations

The procedure consisted of mounting the thrust chamber as shown and abrasive blasting the internal diameter while rotating the assembly. The bond coat and ceramic overlay were then plasma sprayed using the angle extension. The operation was interupted during application of both the bond and ceramic coats after a thickness of 0.01 mm had been applied. The chamber was removed from the fixture and remounted on the opposite end to compensate for the directionality of the spray and provide a more uniform coating structure. This reversal was repeated periodically throughout the coating cycle after each 0.01 mm, until full coating thickness was achieved.

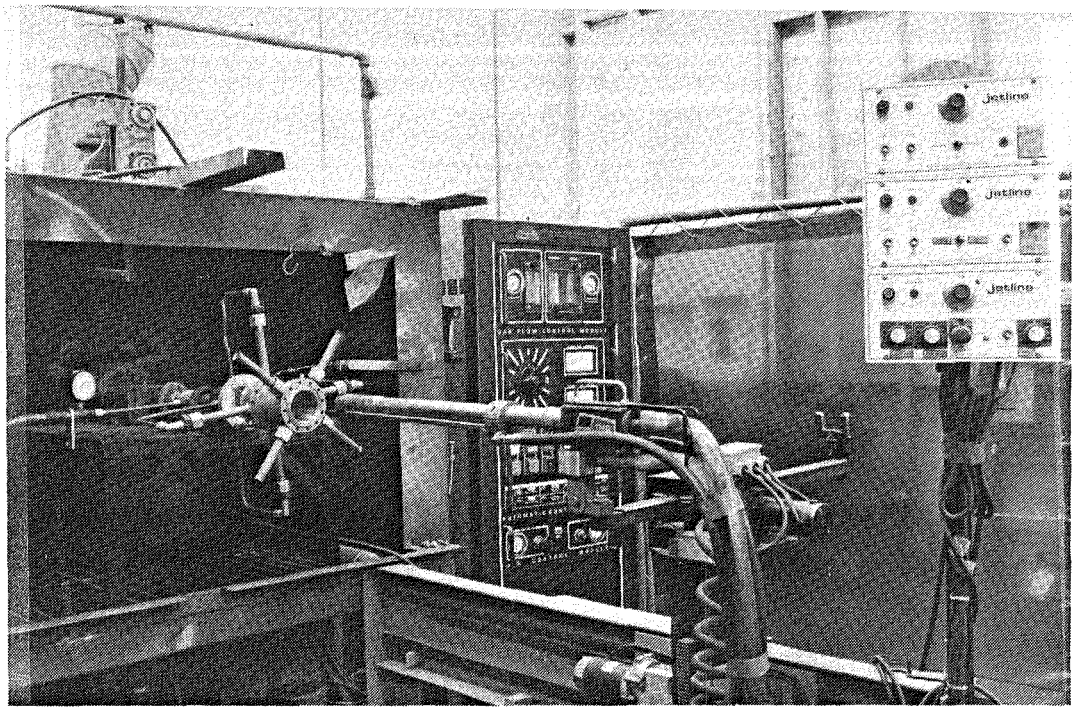

Figure 7. Coating Fixture

3

RESULTS

3.1 PLASMA DEPOSITION VARIABLES

Results of tests to determine the effects of plasma deposition parameters on TBC's are reported in Sections 3.1 and 3.2. Section 3.1 reports the general effects of varying process parameters on the resulting coating. These tests were used to select three sets of deposition parameters for material property evaluation. The results of the property measurements for the three coatings are given in Section 3.2.

3.1.1 Effect of Plasma Gas Flow on Coating Characteristics

For these tests the basic parameters presented in Table 2 were used with the Metco 7M system for deposition of the NiCrAlY bond coat.

The first variable selected was plasma gas flow. The results of these tests are presented in Table 3 and Figures 8 through 16. At this time no attempt was made to optimize the coating but only to determine the effect of an individual parameter (gas flow) on coating structure.

Based on thickness measurements alone, coating deposit rate was established as a function of plasma gas flow. The deposit rate decreased steadily with increasing gas flow. At a gas flow of 2.69 m^3/hr no measurable deposit could be obtained.

The photomicrographs shown in Figures 8 through 16, illustrate the effect of gas flow on coating structure. At the lowest gas flow (1.70 m^3/hr) coating buildup was irregular with large voids. The asperities visible in Figure 8 show the peaks that give rise to the apparent rapid coating buildup. As flow was increased, the coating tended towards a denser structure with some large voids. At a gas flow of 2.12 m^3/hr the spherical unmilled particles observed at lower gas flow tended to disappear although some porous regions existed in the coating as shown in Figure 11. The most uniform coating obtained with these parameters was developed at a gas flow of 2.26 m^3/hr. As the gas flow was further increased, the coating tended to deteriorate with only the larger particles having deposited. At the maximum flow of 2.69 m^3/hr only an occasional deposited particle was observed and the substrate was significantly oxidized.

Similar tests were performed to determine the effect of plasma gas flow on the ceramic coating structure. For these test the parameters in Table 4 were used as a starting point.

Table 2

Basic NiCrAlY Test Parameters

Current	500 amperes
Voltage	60 volts
Argon Flowrate	Variable
Hydrogen Flowrate	0.28 m^3/hr
Standoff Distance	3.1 cm
Powder Port No.	#2
Carrier Argon Flowrate	0.28 m^3/hr
Powder Feedrate	5.7 gm/min.
Cooling Air Jet Pressure	550 kPa
Nozzle Model No.	713
Traverse Rate	2.5 cm/sec
Substrate Material	0.81 mm copper

Table 3

Effect of Plasma Gas Flow on Deposit Rate of NiCrAlY

Gas/Flow (m^3/hr)	Deposit Rate (mm/traverse)
1.70	0.016
1.84	0.012
1.98	0.0074
2.12	0.0064
2.26	0.0031
2.40	0.0021
2.55	0.0010
2.69	*

*Too small to measure.

Monitoring of the substrate temperature during coating deposition was accomplished using a 1.6 mm Inconel sheathed thermocouple inserted into a hole drilled through the specimen. It was located so that its tip was flush with the substrate surface.

A photomicrograph of the baseline ceramic coating is shown in Figure 17. The average thickness of the ceramic is 0.09 mm. The individual coating particles can be distinguished at 1000X magnification. The majority of the particles have been flattened by impact to an average thickness of 0.005 mm.

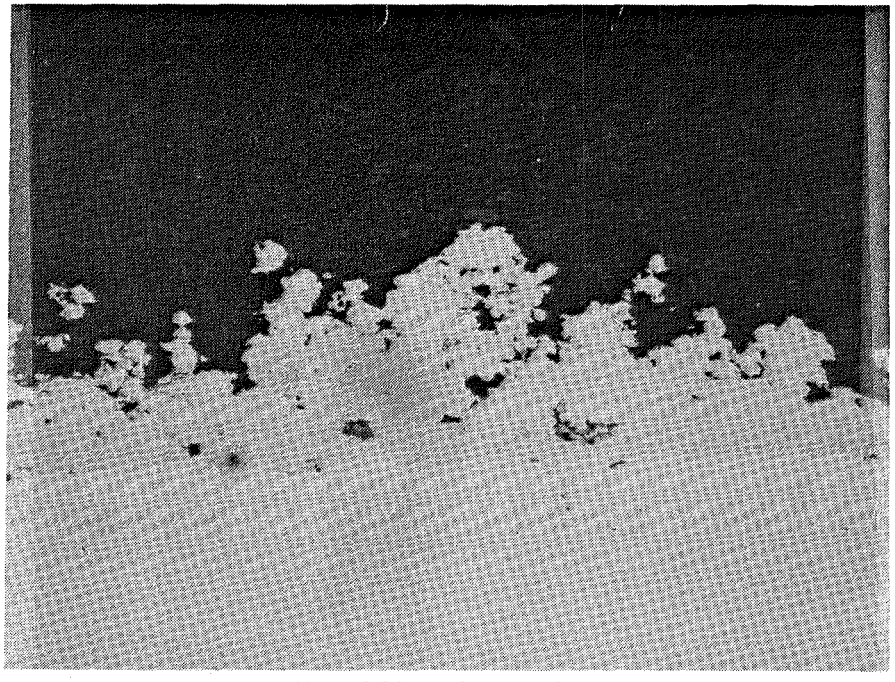

Magnification: 100X

Figure 8. NiCrAlY Bond Coat Applied for 12 Cycles at a Gas Flow of 1.70 m^3/Hour

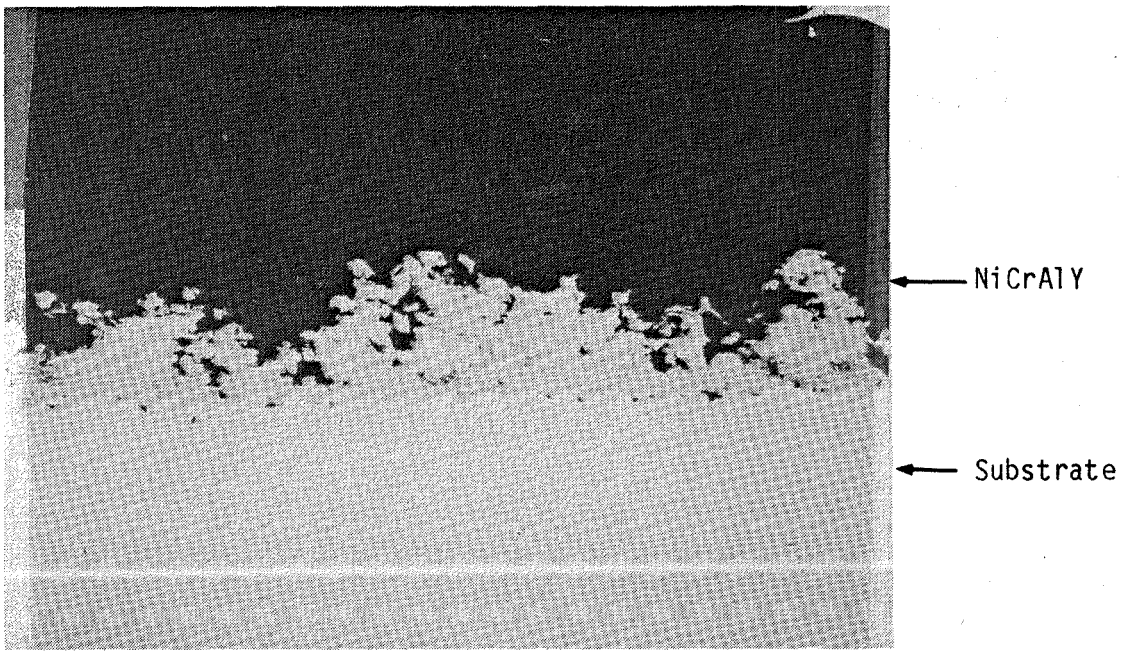

Magnification: 100X

Figure 9. NiCrAlY Bond Coat Applied for 12 Cycles at a Gas Flow of 1.84 m^3/Hour

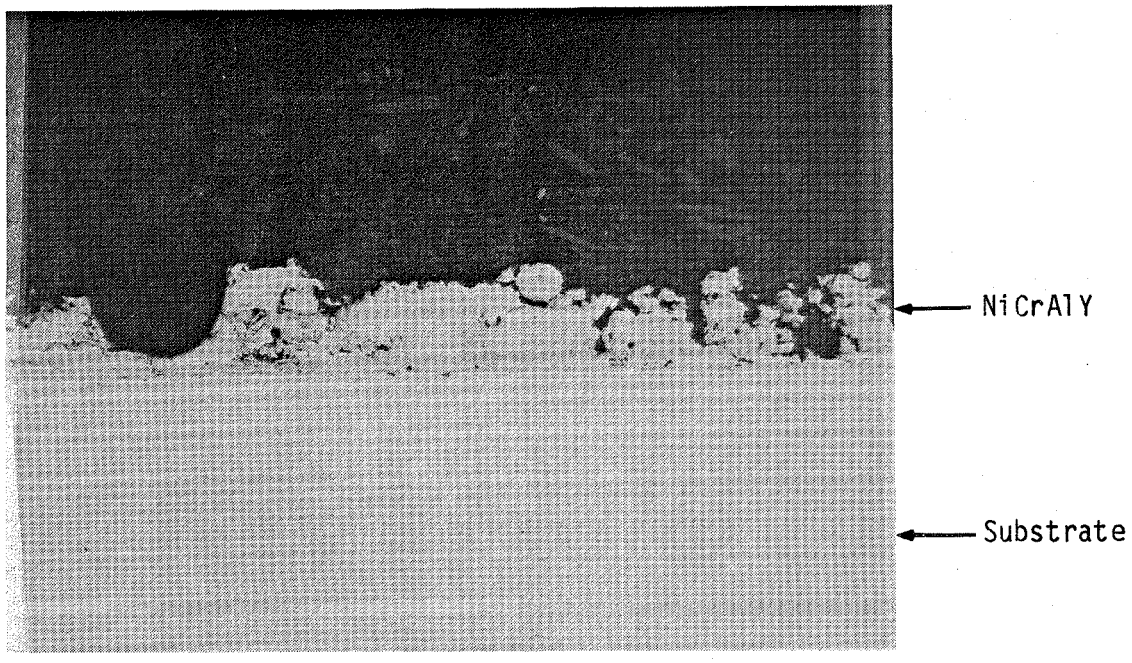

Magnification: 100X

Figure 10. NiCrAlY Bond Coat Applied for 12 Cycles at Gas Flow of 1.98 m^3/Hour

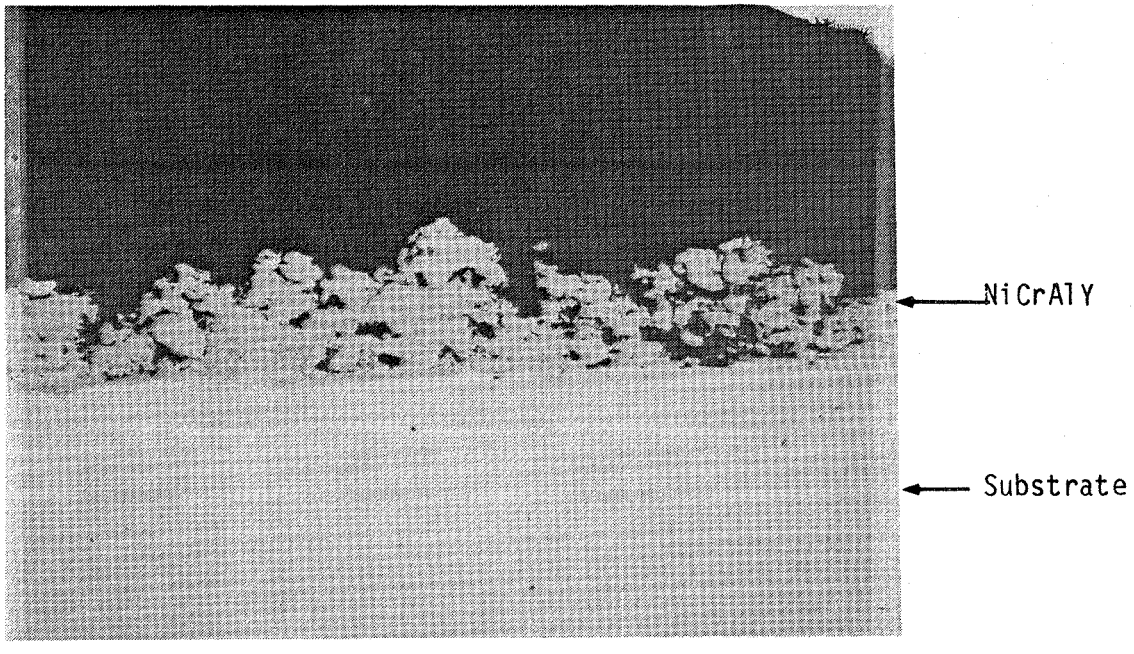

Magnification: 100X

Figure 11. NiCrAlY Bond Coat Applied for 12 Cycles at a Gas Flow of 2.12 m^3/Hour

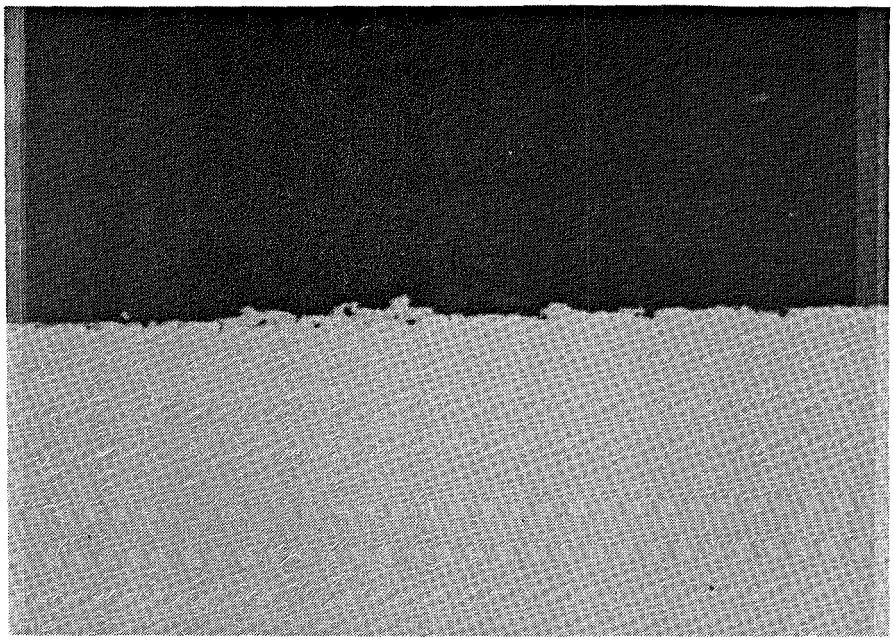

Magnification: 100X

Figure 12. NiCrAlY Bond Coat Applied for 12 Cycles at a Gas Flow of 2.15 m^3/Hour

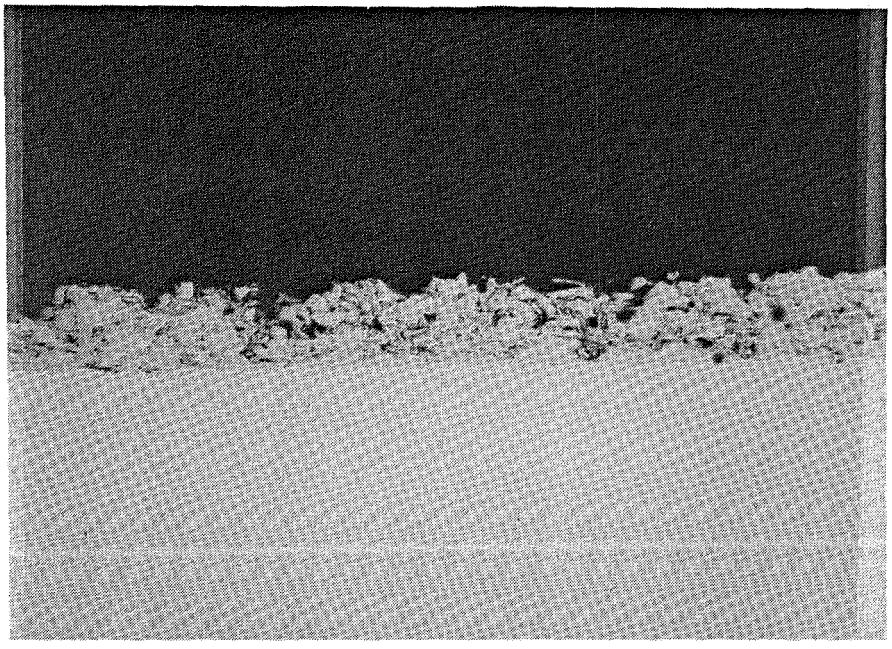

Magnification: 100X

Figure 13. NiCrAlY Bond Coat Applied for 12 Cycles at a Gas Flow of 2.26 m^3/Hour

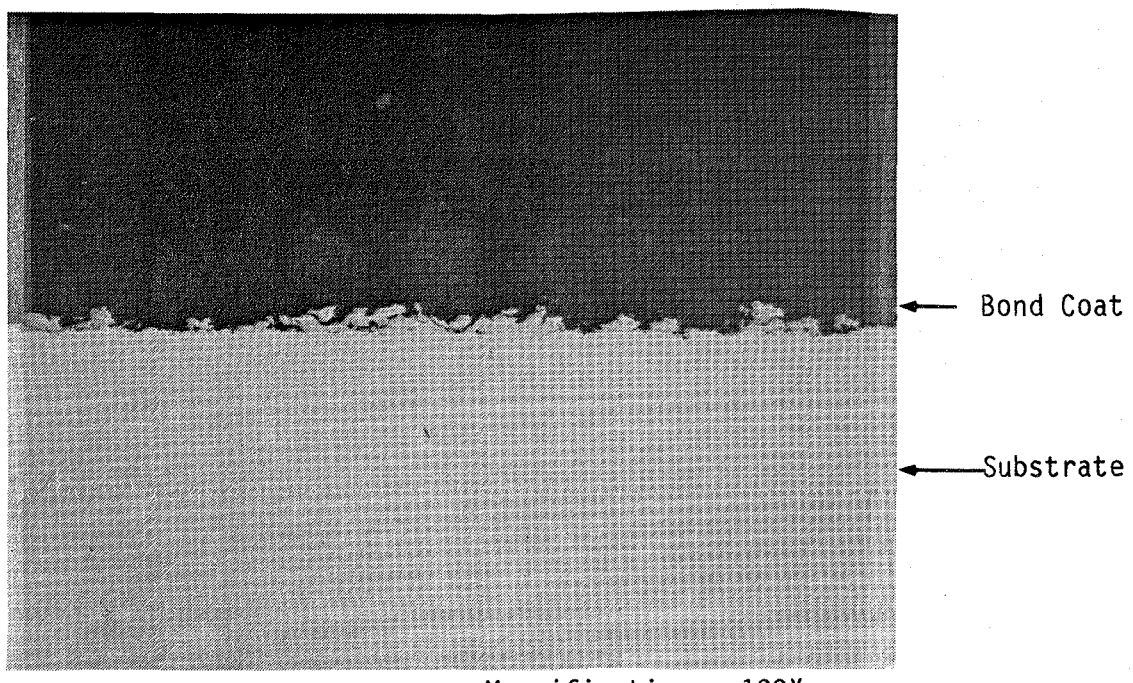

Magnification: 100X

Figure 14. NiCrAlY Bond Coat Applied for 12 Cycles at a Gas Flow of 2.40 m^3/Hour

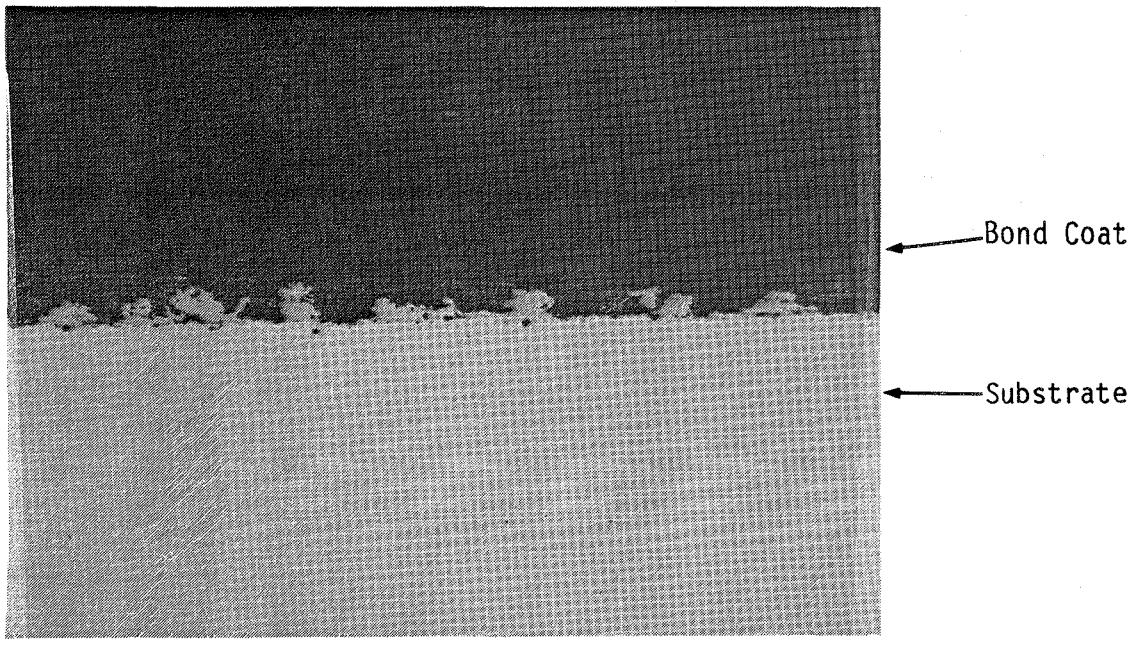

Magnification: 100X

Figure 15. NiCrAlY Bond Coat Applied for 12 Cycles at a Gas Flow of 2.40 m^3/Hour

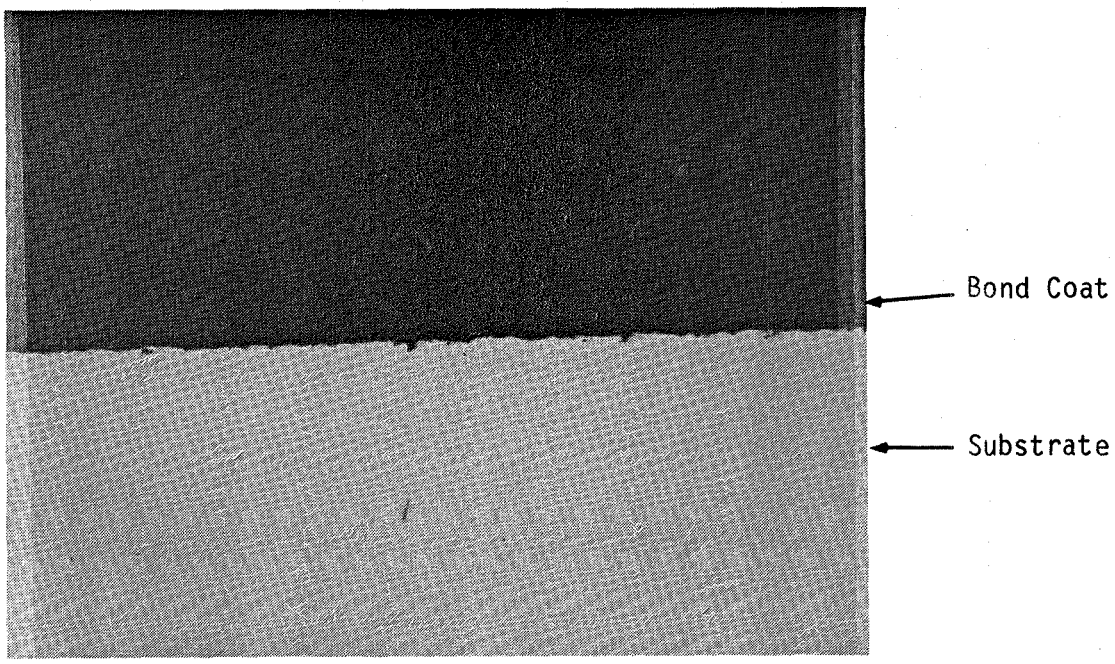

Magnification: 100X

Figure 16. NiCrAlY Bond Coat Applied for 12 Cycles at a Gas Flow of 2.69 m^3/Hour

Table 4

Baseline Ceramic Coating Spray Parameters

Current	400 amps
Voltage	50 volts
Argon Flowrate	1 m^3/hr
Hydrogen Flowrate	0.23 m^3/hr
Standoff Distance	10.2 cm
Cooling Air Pressure	551 kPa
Deposit Rate (avg)	0.008 mm
Traverse Rate	2.5 cm
Powder Feedrate	3.0 gms/min.
Substrate Temperature	97-119°C
Coating Thickness	0.10 mm

Some voids and numerous microcracks are also visible. Increasing the plasma gas flow to 1.15 m^3/hr and then to 1.43 m^3/hr did not produce a visible change in microstructure. However, it was observed that this gas flow rate increase decreased the rate of deposition by 42 percent. The substrate temperature also increased with increasing gas flow, by 80°C in the first case and by 13°C in the second.

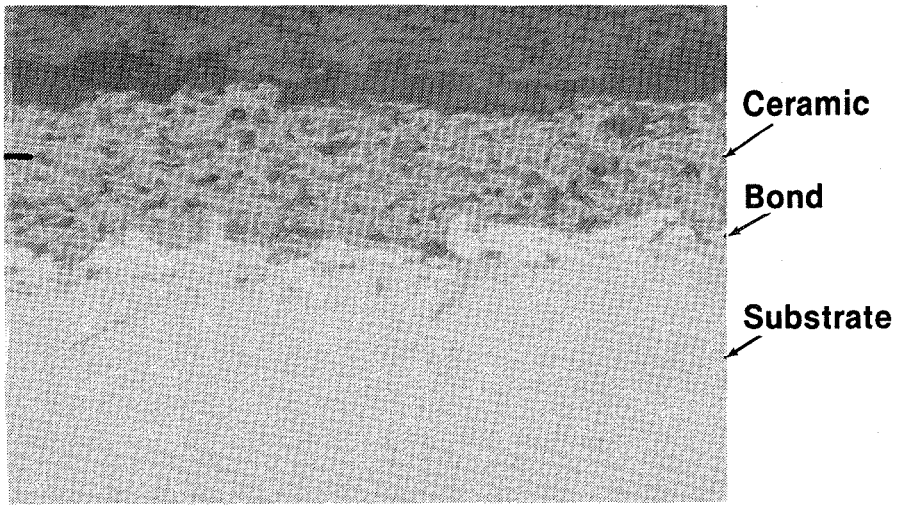

Magnification: 200X

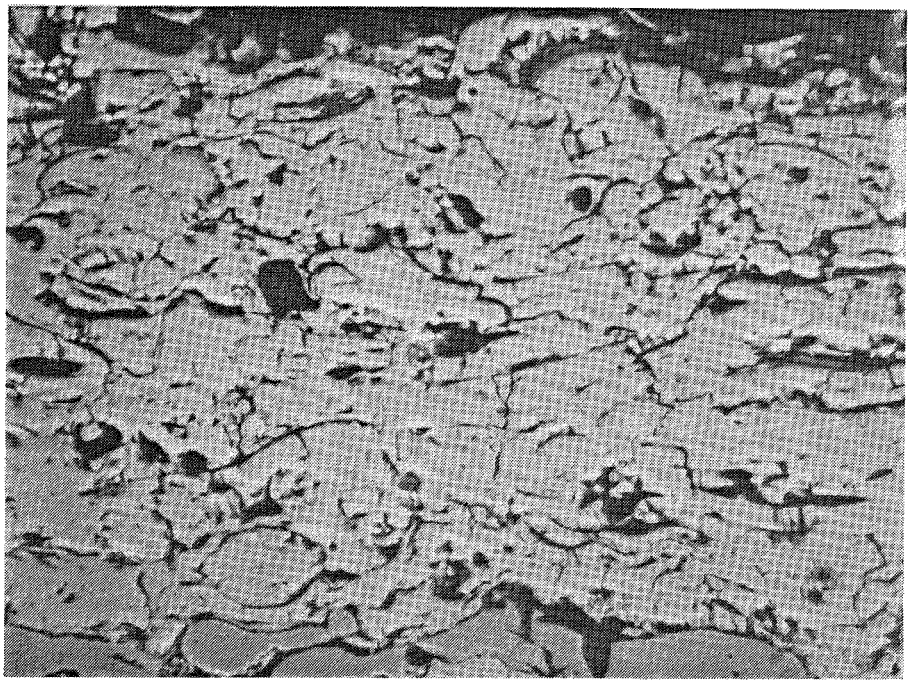

Magnification: 1000X

Figure 17. Baseline Thermal Barrier Coating (Mount No. 5263)

3.1.2 Standoff Distance Effects

The effects of standoff distance (distance between gun and substrate) are tabulated below. This data was generated using the baseline parameters given in Table 4.

Standoff	Substrate Temperature	Deposit Rate (per cycle)	Effect on Coating Structure
10.2 cm*	97-119°C	0.008 mm	Figure 17
9.0 cm	108-128°C	0.008 mm	Slight porosity decrease
7.6 cm	144-167°C	0.008 mm	Larger interlaminar structure
11.4 cm	129-153°C	0.003 mm	Large particles entrapped

*Baseline coating

Decreasing the standoff distance to 9.0 cm increased the coating density slightly as shown in Figure 18. The substrate temperature also increased to a maximum of 132°C. Further reducing the standoff to 7.6 cm increased the size of the agglomerated particles and caused wider laminar separations as shown in Figure 19. Substrate temperature also increased to a maximum of 167°C during coating.

Increasing gun standoff to 11.4 cm produced a coating with poor integrity as shown in Figure 20. During normal plasma spraying, with the selected spray parameters, the cooling jet was adjusted to impinge at the point where the plasma hit the substrate. The jet served to cool the substrate and to remove unmelted nonadherent particles.

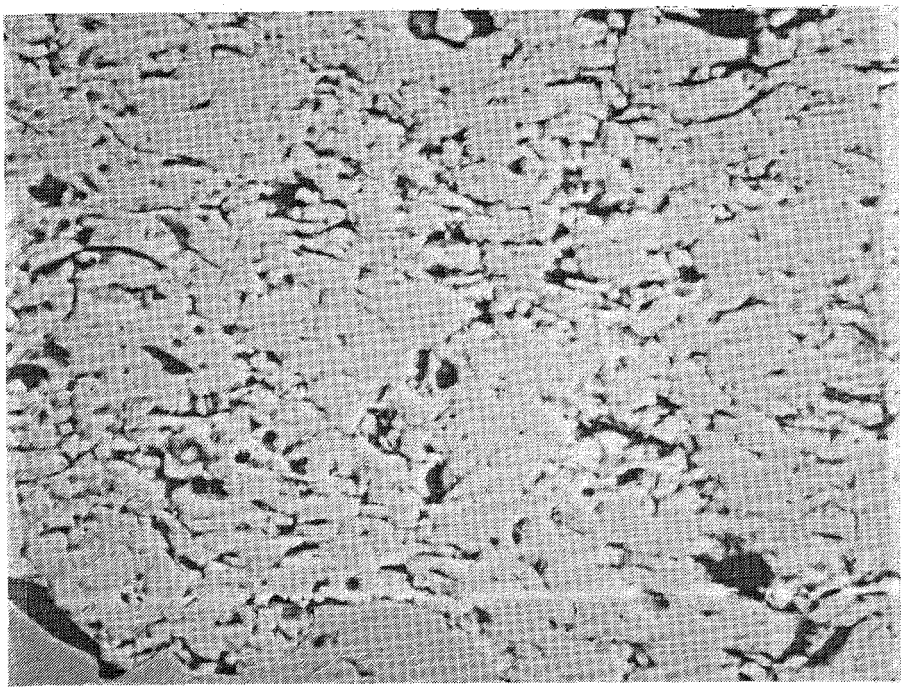

Magnification: 1000X

Figure 18. Thermal Barrier Coating With Gun Stand-off Distance of 9.0 cm

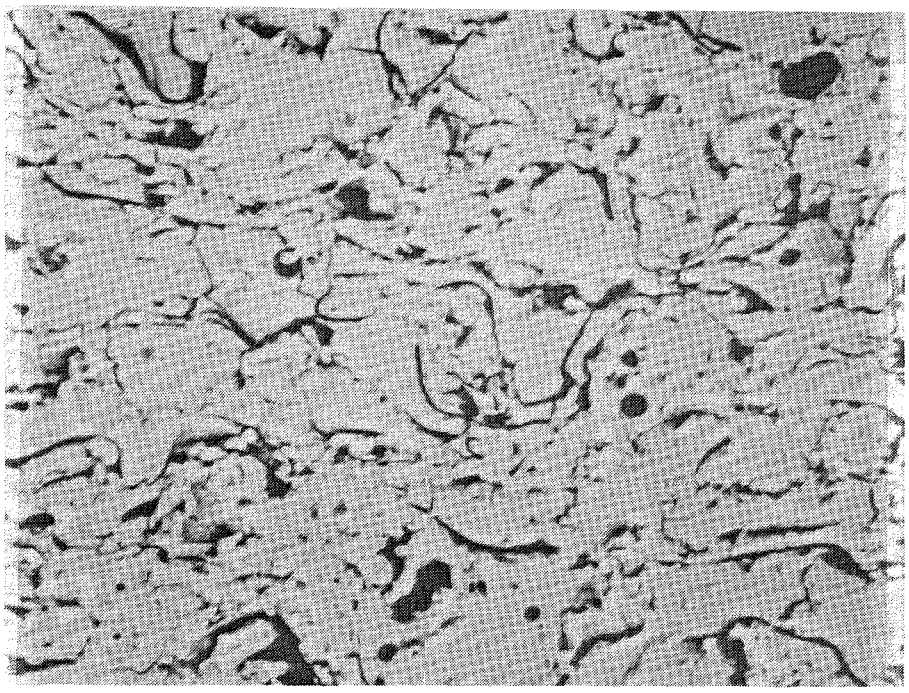

Magnification: 1000X

Figure 19. Thermal Barrier Coating With Gun Stand-off Distance of 7.6 cm

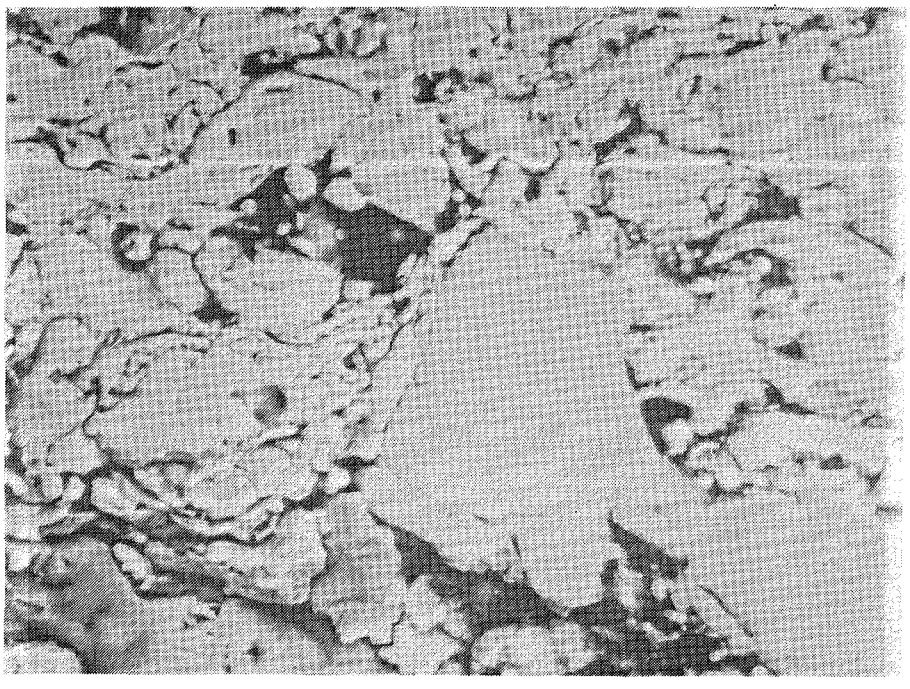

Magnification: 1000X

Figure 20. Thermal Barrier Coating With Gun Stand-off Distance of 11.4 cm

At 11.4 cm the effectiveness of the jet was greatly diminished. Large unmelted particles were entrapped in the coating and the substrate temperature increased to a maximum of 153°C, approximately midway between the temperature observed at 7.6 cm and 9.0 cm. Also, particle temperatures decreased to the point where interparticle bonding was decreased. Deposit efficiency also dropped to 40 percent of that recorded at the baseline standoff.

Attempts to spray at standoffs greater than 11.4 cm were unsuccessful. No measurable deposit was obtained.

3.1.3 Arc Voltage Effects on Coating Structures

In the plasma spray system, arc voltage (a dependent variable) is a function of the plasma gas composition. As the amount of hydrogen in the argon/hydrogen plasma gas mixture is raised, gas enthalpy, heat transfer and arc voltage all increase. For practical reasons, this effect is generally controlled by adding sufficient hydrogen to produce the desired voltage. Data is therefore reported on the basis of voltage.

The baseline parameters in this study are those reported in Table 2 except that hydrogen flow was adjusted to vary the voltage. Results are summarized below:

Voltage	Substrate Temperature (°C)	Deposit Rate (mm per Cycle)	Effect on Coating Structure
60*	97-119	0.008	Figure 17
66	108-130	0.008	None definable
72	149-171	0.007	Slight densification
78	143-152	0.006	Laminar separation

*Baseline coating

Increasing the voltage from the baseline of 60 volts to 66 volts had no visible effect on coating quality. A substrate temperature increase of 11°C was observed. The coating is shown in Figure 21. When the voltage was raised to 72 volts (Fig. 22) interlaminar bonding appeared to improve and the size of the large voids was reduced. Also, less evidence of ceramic bond coat voids was evidenced. The substrate temperature also increase by 52°C.

Further increasing the voltage to 78 volts tended to produce laminar separation in the coating. The deposit rate decreased by 29 percent and substrate temperatures were 5°C lower than at 72 volts, due to the lower density of the coating. Voltage could not be increased beyond this point due to equipment limitations.

The effect of voltage on the bond coat was established using a 61 cm angle extension gun. This unit was selected for these tests since it was capable of

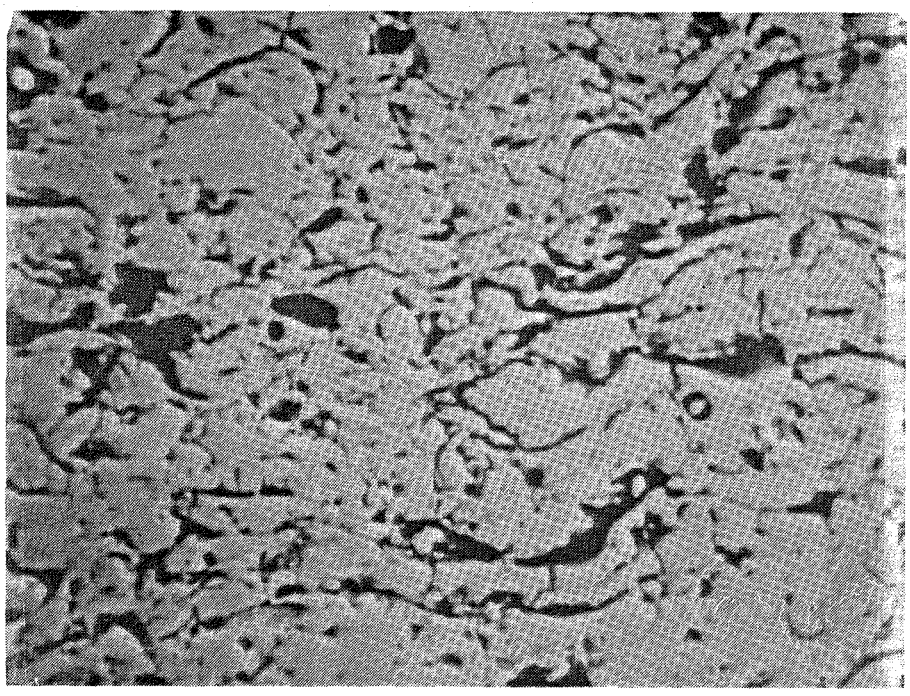

Magnification: 1000X

Figure 21. Thermal Barrier Coating With Plasma Arc Voltage of 66 Volts

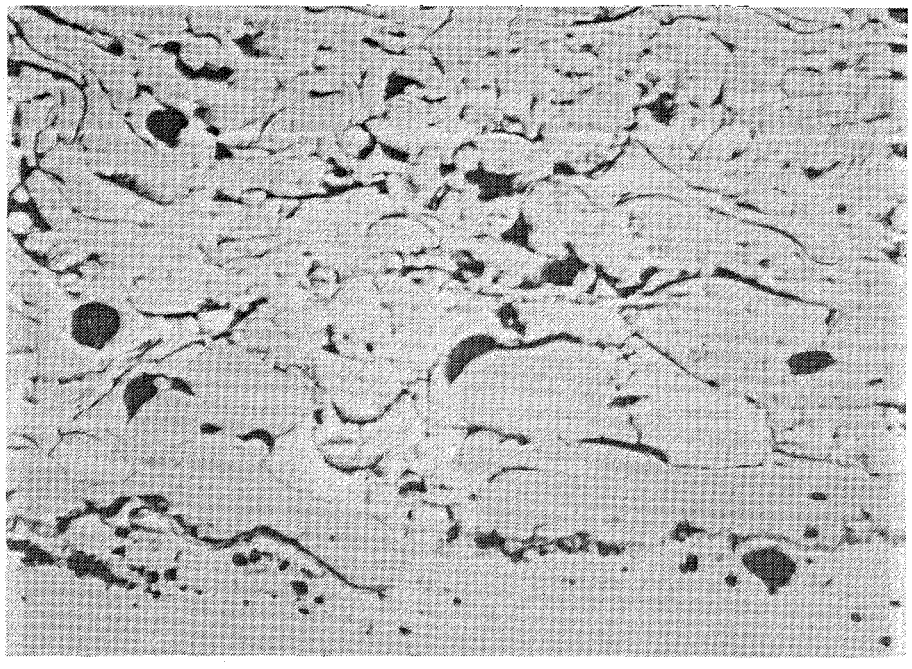

Magnification: 1000X

Figure 22. Thermal Barrier Coating With Plasma Arc Voltage of 72 Volts

coating the 6.6 cm base of a test thrust chamber. The parameters in Table 5 were used as a baseline for these tests.

Table 5

Baseline, Angle Extension Spray Parameters

Current	500 amperes
Voltage	45 volts
Argon Flowrate	1.7 m^3/hr
Hydrogen Flowrate	0.8 m^3/hr
Standoff Distance	3.2 cm
Powder Port Type	#2
Carrier Gas Flowrate	0.28 m^3/hr
Powder Feedrate	0.098 gm/sec
Anode Model	#713
Traverse Rate	2.5 cm/sec
Deposit Rate	0.0025 mm/traverse

Table 6

Effect of Voltage on Bond Coat Structure

Voltage	Hydrogen Flowrate (m^3/hr)	Deposit Rate (mm/cycle)	Deposit Width (mm)
45	0.085	0.0025	not definable
50	0.20	0.0051	3.2
55	0.33	0.010	4.8
60	0.51	0.020	6.4
65	0.65	0.028	6.4
70	0.76	0.033	7.9
75	0.82	0.038	7.9

Table 6 summarizes the measured results of these tests. The relationship between arc voltage and hydrogen flow proved to be linear. The width over which the deposit occurred also increased linearly with increasing hydrogen. The width measurement was made directly using a machinists scale. Thus, the accuracy of this measurement is limited. The increase over a 5 volt range was less than the measured accuracy (±0.5 mm) making this relationship less definitive. The deposit rate increased rapidly over the 55 to 65 volt range indicating that this range is especially sensitive to voltage variations.

The effect of voltage variations on bond coat deposition is shown in Figure 23 to Figure 29. In each case the plasma spray gun was traversed across the specimen twelve times.

In Figure 23 the arc voltage was 45 volts. There is no visual evidence of bond coat deposition. Oxidation of the substrate is apparent. At 50 volts, coating deposition has begun. In Figure 24 small local areas evidence individual particle deposition. The coating is sporadic and again the copper substrate is oxidized. The effect of increasing the voltage to 55 volts is evident in Figure 25, where significant bond coat deposition has occurred. The oxidation of the substrate observed in the two previous specimens is absent and the bond-substrate interface is relatively clean. (In viewing these photomicrographs the main deposit is in the central third. Material at each end is overspray.)

At 60 volts the coating thickness is nearly twice that of the coating deposited at 55 volts. The substrate is just beginning to evidence overheating at the edges. The effect of the 45 degree plasma jet impingement angle is also evident. The coating buildup slopes to the left with elongated voids that are created by the masking effects of previously deposited particles. With the voltage increased to 65 volts, the coating substrate bond shows evidence of significant oxidation. Wide variations in coating density were also observed, ranging from large porous areas to high density regions.

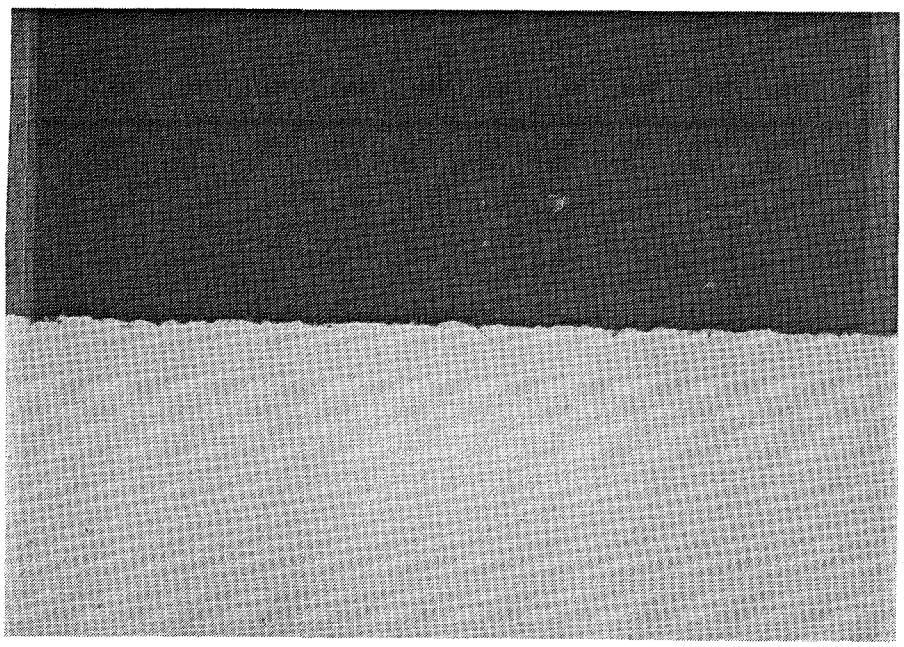

Magnification: 100X

Figure 23. Substrate After 12 Traverses at 45 Volts

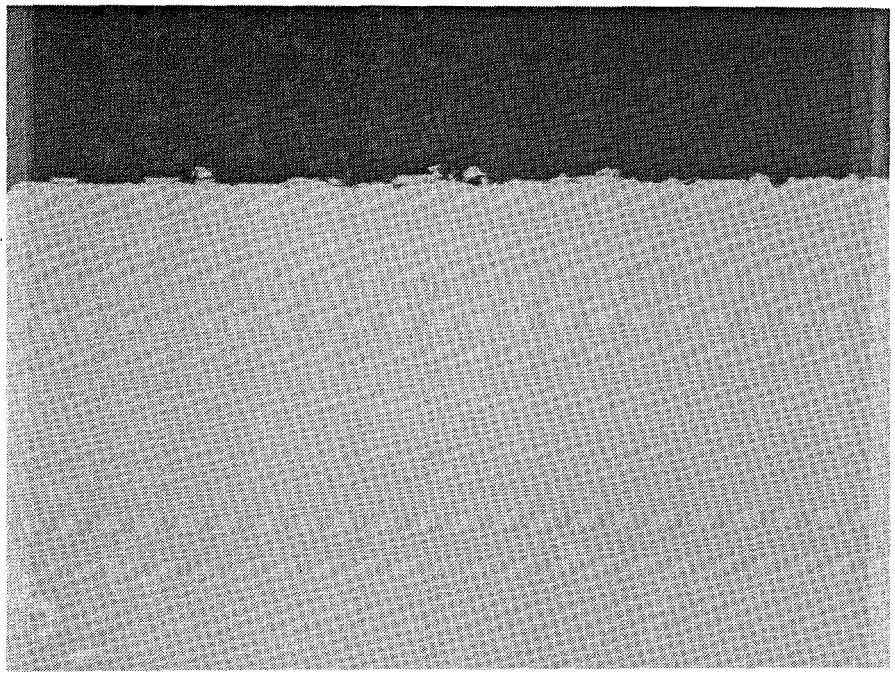

Magnification: 100X

Figure 24. Substrate After 12 Traverses at 50 Volts

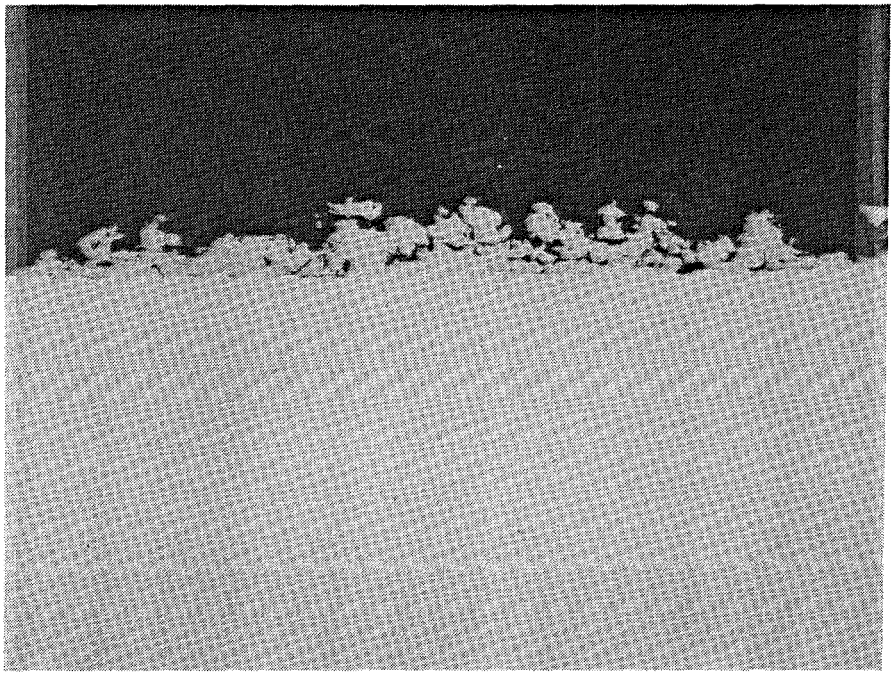

Magnification: 100X

Figure 25. NiCrAlY Deposit After 12 Traverses at 55 Volts

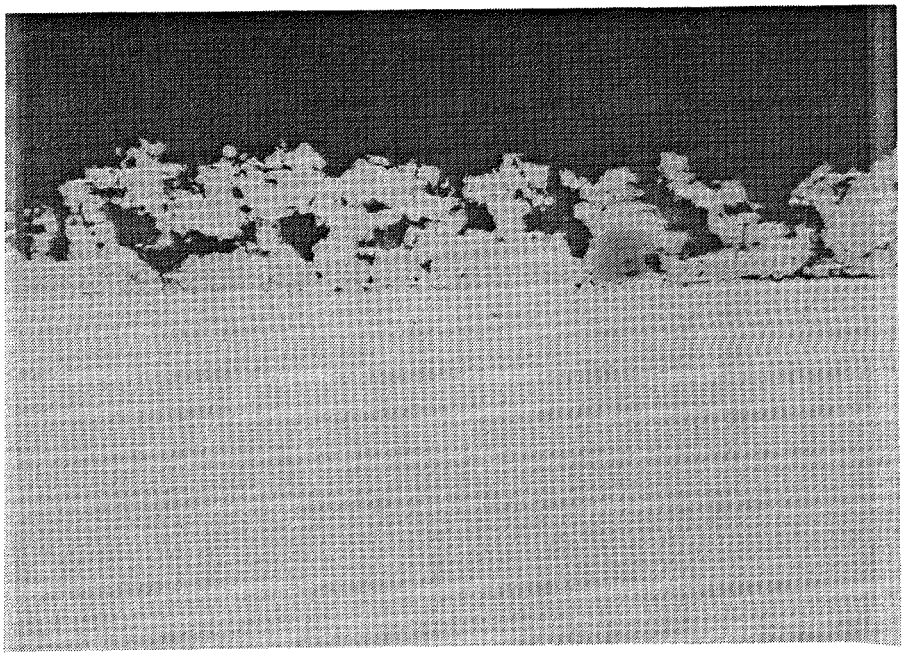

Magnification: 100X

Figure 26. NiCrAlY Deposit After 12 Traverses at 60 Volts

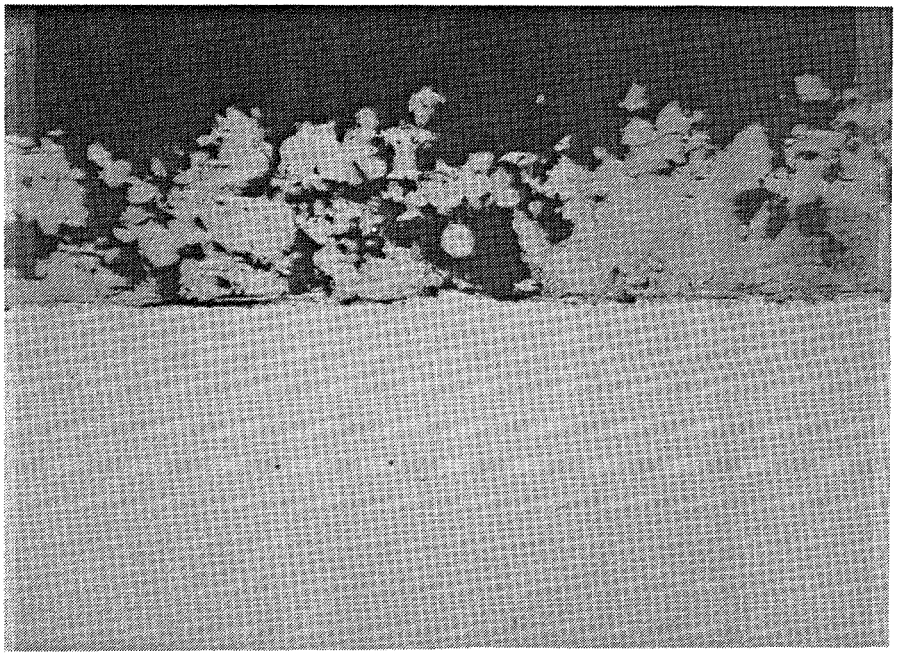

Magnification: 100X

Figure 27. NiCrAlY Deposit After 12 Traverses at 65 Volts

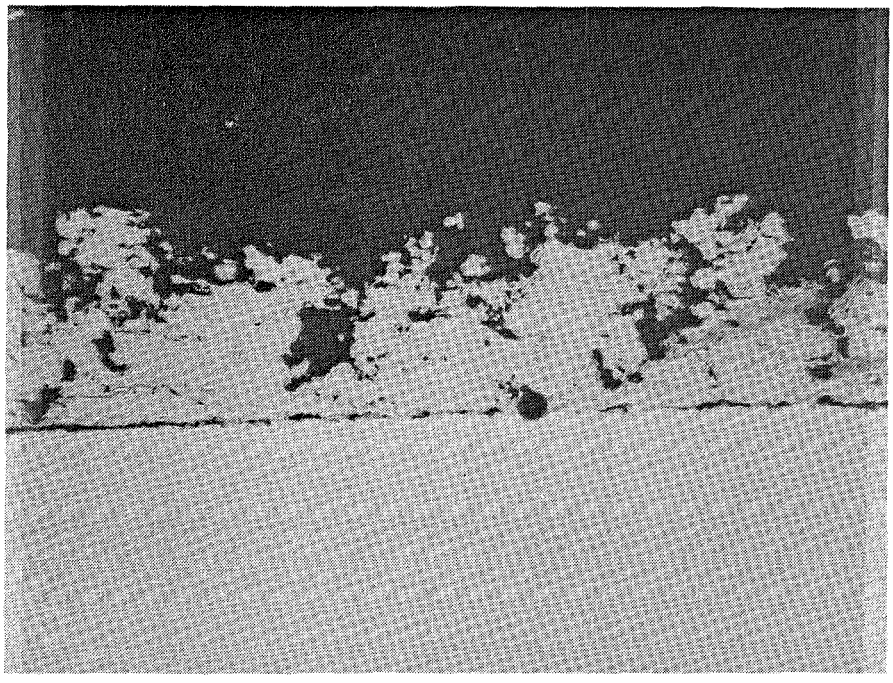

Magnification: 100X

Figure 28. NiCrAlY Deposit After 12 Traverses at 70 Volts

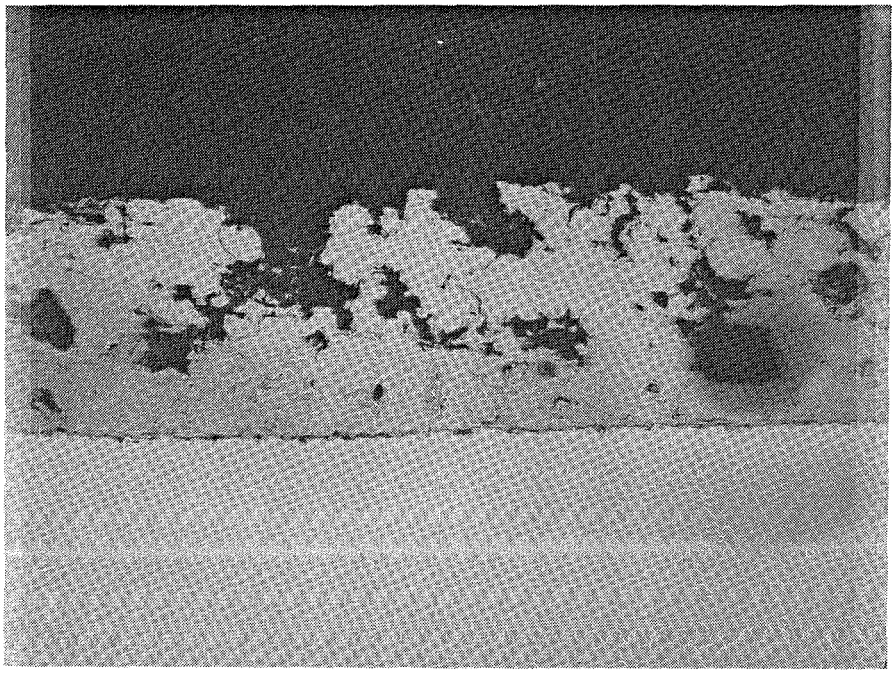

Magnification: 100X

Figure 29. NiCrAlY Deposit Ater 12 Traverses at 75 Volts

At 70 volts, Figure 28, the coating exhibited some densification with large voids. The substrate-coating interface is severely oxidized indicating poor adherence. The slope of the voids and deposit to the right is evidence of the 45 degree spray angle.

The deposit at 75 volts (Fig. 29) is similar to that at 70 volts. Void size has increased but the coating is more uniform, particularly at the bond line.

3.1.4 Effect of Arc Current on Structure

Varying the arc current independently within normal operating parameters had little effect on coating structure. With the equipment configuration used for this test, operating current is limited to the range of 350-500 amperes. The ceramic baseline coating sprayed at 400 amperes was shown in Section 3.1.1. The current was reduced to 350 amperes for the specimen shown in Figure 30. Little, if any, differentiation can be made between it and the baseline coating that is attributable to the lower current. A coating sprayed at 475 amperes (Fig. 31) showed little change in structure. A slight tendency of the voids towards a spherical shape was observed but this could not be established on a reproducible basis. Additional tests with higher currents

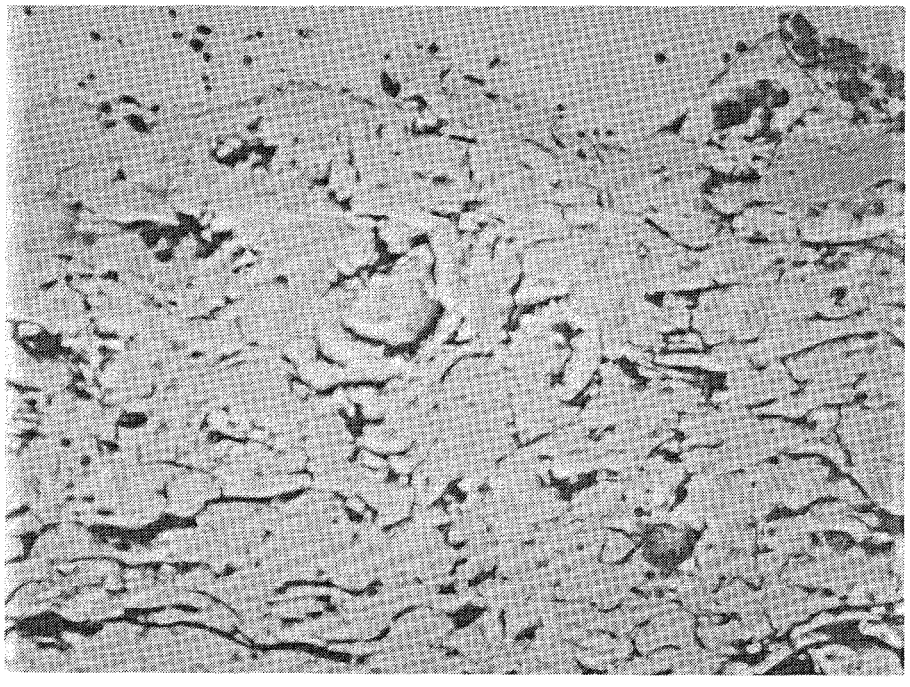

Magnification: 100X

Figure 30. Thermal Barrier Coating With Plasma Arc Current of 350 Amperes

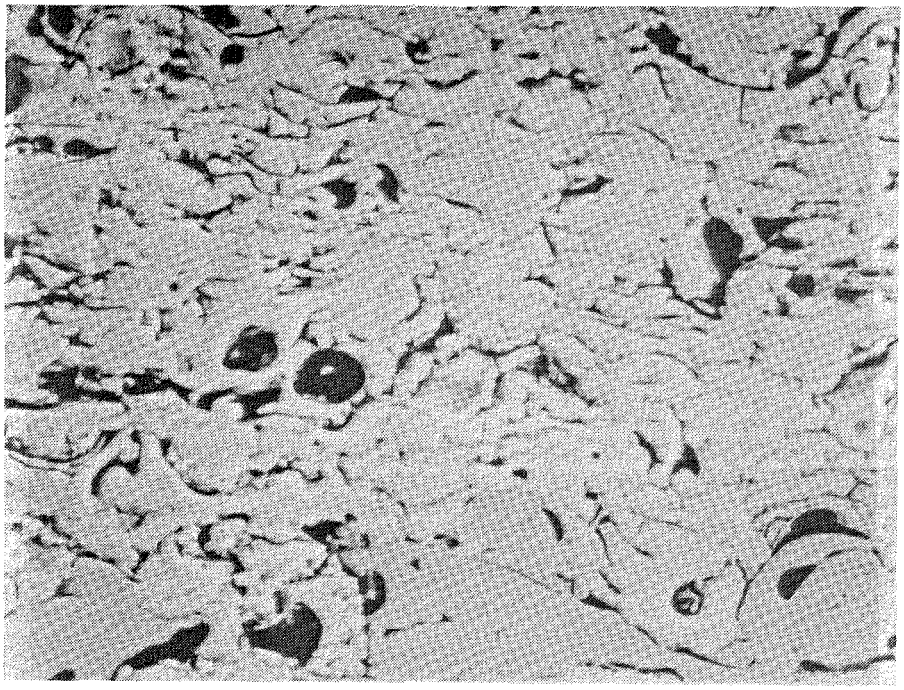

Magnification: 1000X

Figure 31. Thermal Barrier Coating With Plasma Arc Current of 475 Amperes

were performed as described separately in Section 3.1.6. These entailed the use of a different anode to allow operation at 80 kW where other modifications to the operating parameters masked the effect of arc current alone.

3.1.5 Anode Selection Effects

The water cooled copper anode used in a plasma spray gun also functions as a nozzle for controlling and ducting the plasma gas flow. Design of this component is one of the primary factors in determining the exit gas velocity and maximum arc current that can be used. The data in Table 7 was supplied by Metco Inc. as a guide for evaluating the performance characteristics of the various anodes available for the 7M system.

Trial coatings were sprayed with two of these anodes using the parameters given in Table 8. Manufacturer recommended parameters were used in each case. A baseline coating deposited with the GH anode is shown in Figure 32. This structure is typical of the thin coatings developed during this study.

The type 700 anode is similar to the GH but is operated at higher power levels. A bond coat deposited using this anode is shown in Figure 33. Coating thickness developed more rapidly using the 700 anode than with the type GH anode. The deposit also evidenced greater porosity and oxidation than the baseline (GH anode) coating. No obvious benefit in coating quality was observed with

Table 7

Plasma Spray Anode Performance Characteristics

Anode	Gas System	Maximum Electrical Parameters			Plasma Exit Velocity	Nozzle Life (hrs)
		kW	Amps	Volts		
GH	A/H_2	37	500	75	1829	25
700	A/H_2	42	600	70	1768	20
703	A/H_2	45	600	75	2621	15
704	A	58	1000	58	2835	30

Table 8

Effect of Anode Selection

Coating	Anode	Current (amperes)	Voltage (volts)	Power kW	Standoff (cm)	Thickness (mm)
Bond	GH	500	65	32	10.0	0.025
Ceramic	GH	450	50	22	7.6	0.025
Bond	GH	400	50	20	10.0	0.051
Ceramic	704	1000	54	54	7.6	0.025
Bond	704	1000	52	52	10.0	0.130

this anode. Operating the 700 anode at lower power levels produced coatings similar to those obtained with the type GH anode.

The type 703 anode operated at 45 kW produced excessive substrate oxidation as shown in Figure 34. Severe oxidation pits are visible in the copper substrate, and unmelted particles are evident where particle melting and vacuum fusion of the NiCrAlY produced entrapped voids. The laminar structure normally seen in these structures is not evident.

Two examples of coatings applied with the type 704 anode are shown in Figures 35 and 36. A zirconia coating applied over a standard bond coat is shown in Figure 35, and Figure 36 shows just a NiCrAlY bond coat applied with the type 704 anode. In both tests the deposit rate was low, and thin dense coatings resulted. Severe oxidation occurred at the bond coat-substrate interface, indicating overheating. The bond coat applied under these conditions was also rich in oxides. No indications of coating improvment were obtained with these special anodes and it was decided to continue tests with the standard GH anode.

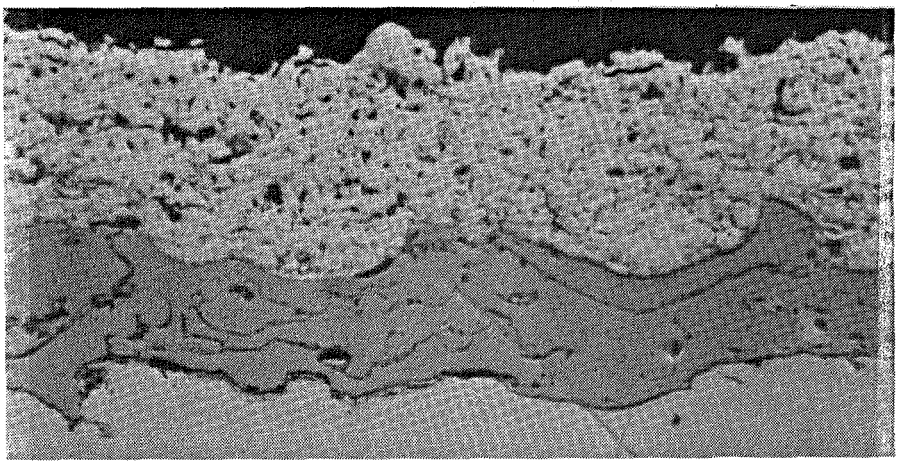

Magnification: 500X

Figure 32. Baseline Coating Applied with a GH Anode

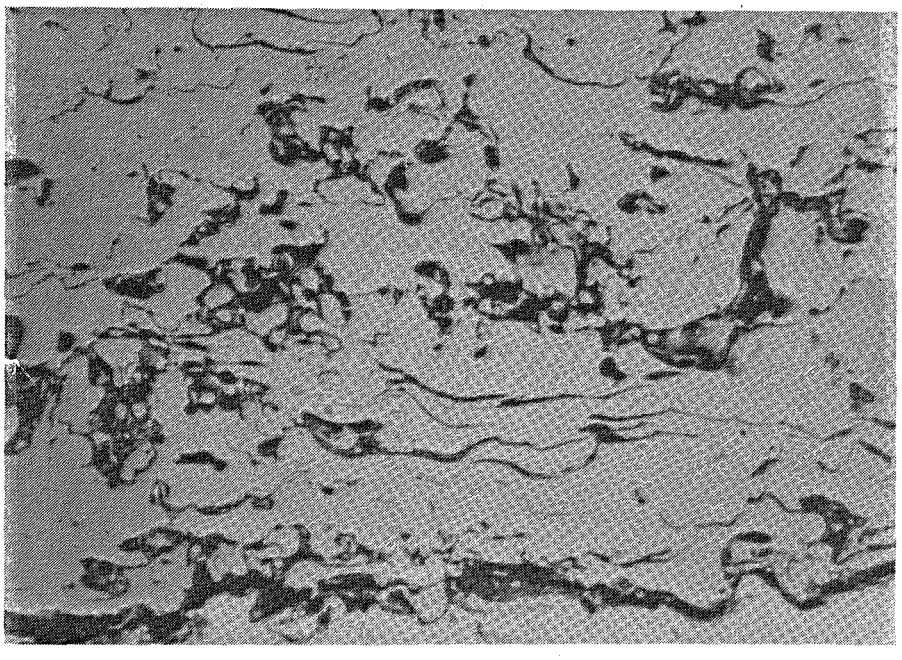

Magnification: 500X

Figure 33. Bond Coat Deposited at 42 kW With A Type 700 Anode

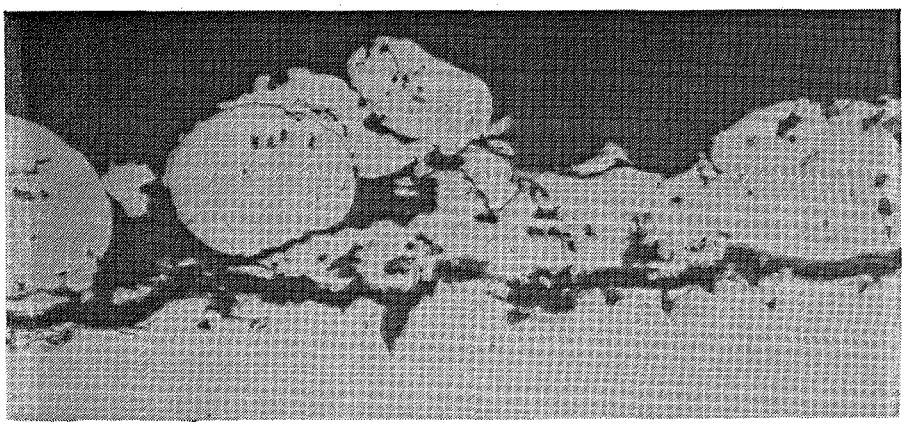

Magnification: 500X

Figure 34. Bond Coat Applied at 45 kw With a Type 703 Anode

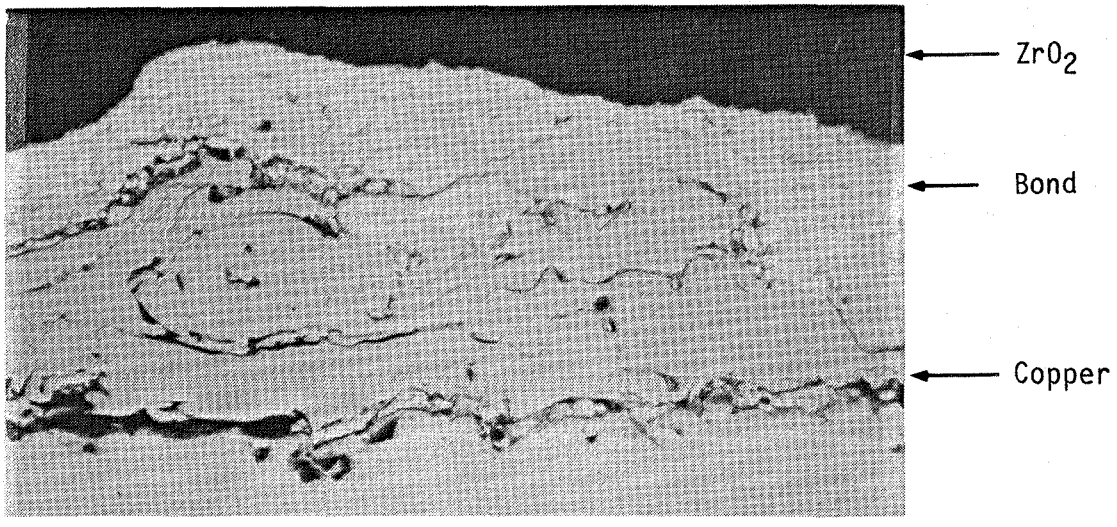

Magnification: 500X

Figure 35. Zirconia Applied to the Baseline Bond Coat With a 704 Anode at 58 kW

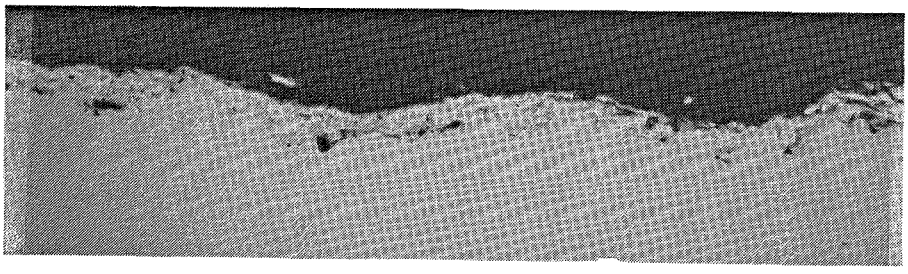

Figure 36. Bond Coat Applied With a Type 704 Anode at 58 kw

3.1.6 Effect of Traverse Rate

The baseline traverse rate used in these tests was 2.5 cm/sec. This was reduced incrementally to 1.2 cm/s. No visible change was found in the coating microstructure. However, as traverse rate was decreased, substrate temperature increased. At 1.2 cm/s this increase amounted to 12°C. This slight increase in substrate temperature did not visibly affect bond quality.

3.1.7 Powder Feed Rate

Zirconia feed rate was varied over the range of 0.04 to 0.09 gm/s. The baseline value was 0.05 gm/sec. Reproducible feed rates lower than 0.04 gm/s could not be achieved. The reduction in feed rate below baseline (Fig. 37) did not affect the coating microstructure. As feed rates were increased, laminar voids developed as shown in Figures 38 and 39. At feed rates higher than 0.09 gm/s deposit efficiency decreased, as evidenced by visible, unmelted particles bouncing off the fixture and substrate. Generally, it was found that the lower the feed rate the more uniform the coating, with a corresponding reduction in unmelted particles in the coating.

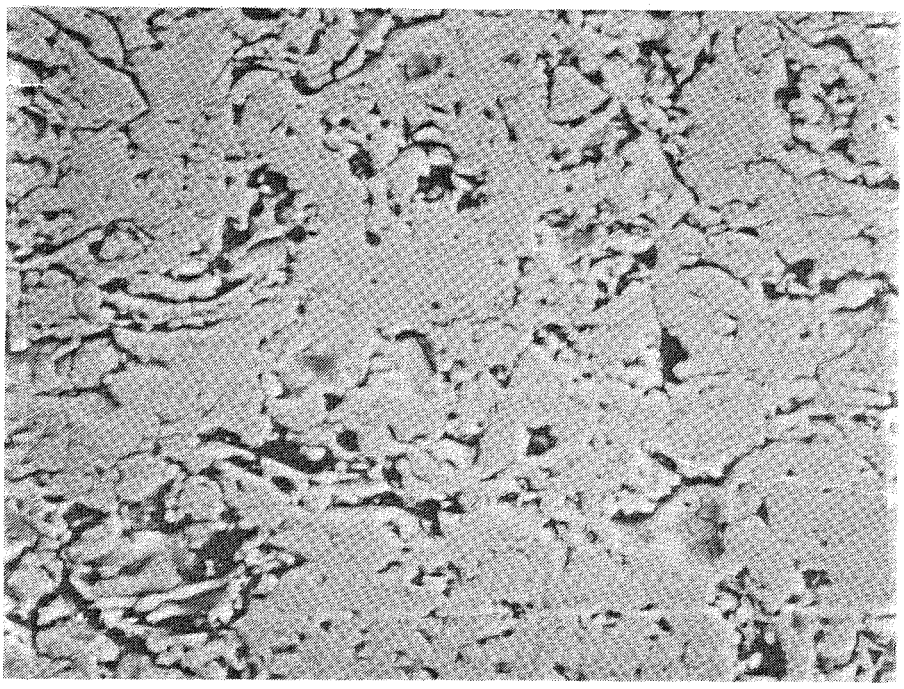

Magnification: 1000X

Figure 37. Thermal Barrier Coating With Powder Feed Rate of 0.04 gms/sec

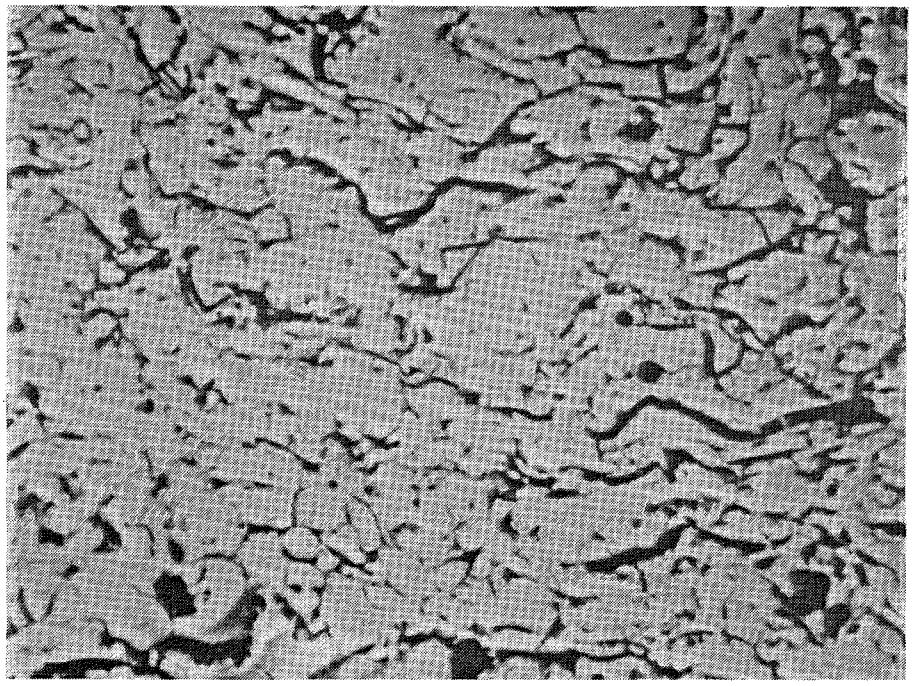

Magnification: 1000X

Figure 38. Thermal Barrier Coating With Powder Feed RAte of 0.062 gms/sec

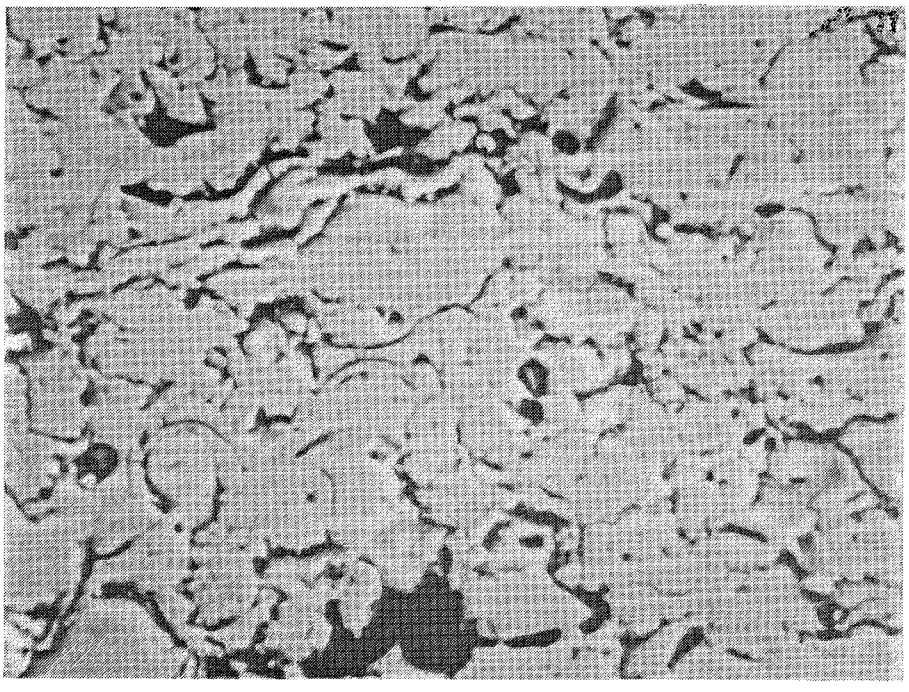

Magnification: 1000X

Figure 39. Thermal Barrier Coating With Powder Feed RAte of 0.09 gms/sec

3.2 PROPERTY MEASUREMENT

Based on the laboratory data from the studies performed in Section 2, three sets of ceramics and one set of bond coat deposition parameters were selected for further study. The parameters are given in Table 9. Examples of coated specimens used for property measurement testing are shown in Appendix 3.

Table 9

Plasma Spray Parameters Selected for Coating Property Measurements

	Ceramic Coating #1	Ceramic Coating #2	Ceramic Coating #3	Bond Coat
Current (amps)	400	500	600	500
Voltage (volts)	50	65	70	65
Power (kW)	20	32	42	32
Argon (m^3/hr)	2.97	2.97	4.25	5.66
Hydrogen (m^3/hr)	0.085	0.14	0.20	0.11
Stand-Off (cm)	6.4	6.4	6.4	
Plasma Velocity (m/s)	25.4	30.5	43.7	32.5
Powder Port	No. 2	No. 2	No. 3	No. 2
Cooling Air (kPa)	551	551	551	551
Nozzle	GH	GH	703	GH

The same bond coat parameters were used in all tests to apply a nominal 0.025 mm coating to the copper substrate. Substrate temperatures were held within the range of 97 to 120°C during coating application. Higher substrate temperatures caused excessive oxide formation at the bond coat-copper interface. The first system (Fig. 40) used the standard bond coat and the zirconia-8% yttria was applied at 20 kW. The 32 kW coating is shown is Figure 41 and the 40 kW coating is shown in Figure 42.

As the power level increased the coatings exhibited a reduction in pore size and an increase in porosity. It was found that the coatings produced at 20 and 40 kW could be duplicated readily. However, those produced at 32 kW varied in density and other properties as discussed in Section 3.5. Generally, as anode wear increased the coating tended to become less dense. This effect was only evident on the 32 kW coatings and no quantitative relationship could be established. Anode usage was limited to four hours to minimize anode wear effects but they could not be eliminated from the 32 kW coatings. Because of this variation, the property data reported in this section is limited to values obtained from specimens produced with new anodes unless otherwise noted.

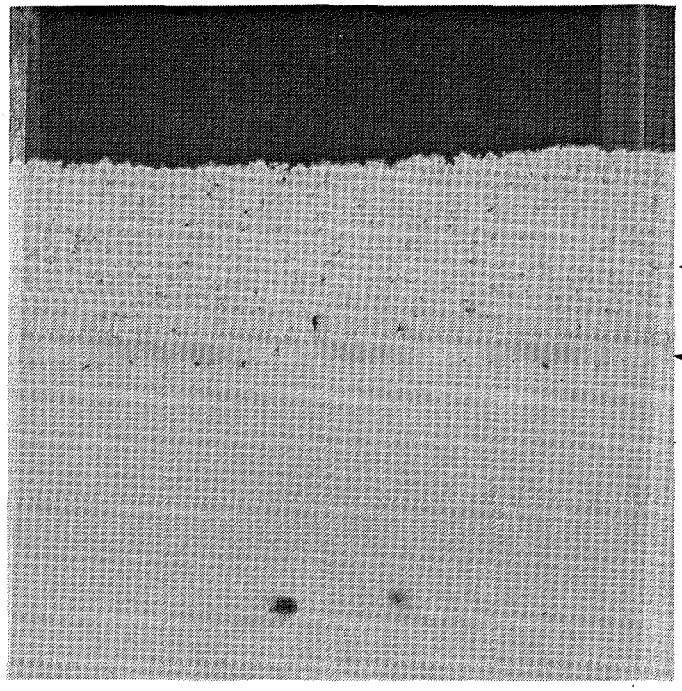

Figure 40. Thermal Barrier Coating Applied at 20 kW (System 1)

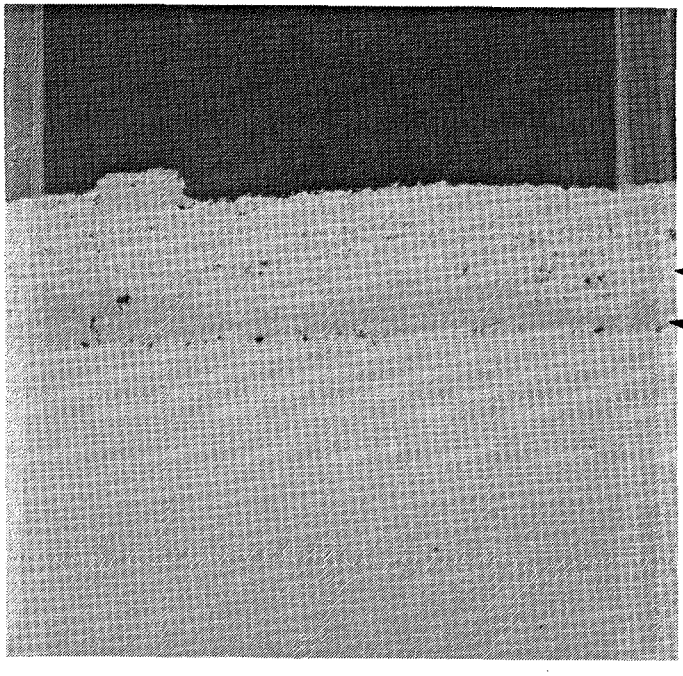

Figure 41. Thermal Barrier Coating Applied at 32 kw

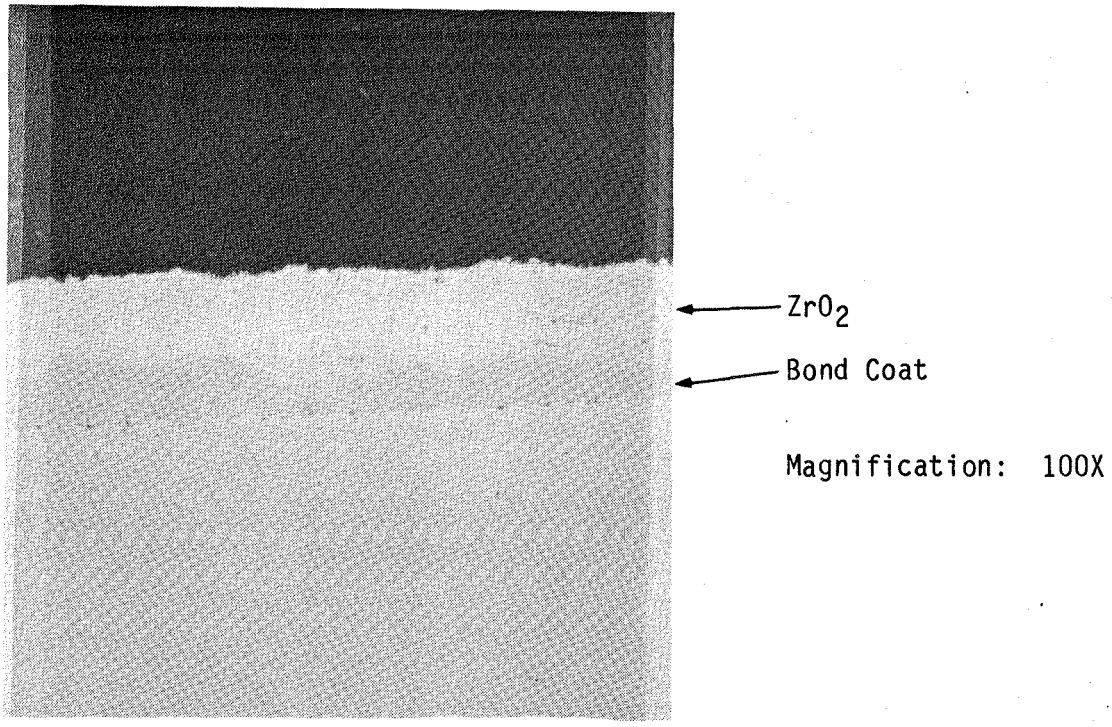

Figure 42. Thermal Barrier Coating Applied at 40 kw

3.2.1 Density

Coating density was determined by three methods:

- Visual inspection of a 100X photomicrograph
- Photometric evaluation of 50X photomicrographs
- Weighing and measuring a sample of the coating

The following average values were obtained:

$ZrO_2 \cdot 8Y_2O_3$ Density Values

	Visual (% Theory)	Photometric (% Theory)	Weight (g/cc)
Coating System 1	85	80	4.8
Coating System 2	92	90	5.2
Coating System 3	95	95	5.3

3.2.2 Thickness Control

Because of the extreme thinness of the coatings required in this program (0.013 to 0.10 mm) control of the application parameters was considered an important factor. Conventional coatings vary by ±0.02 mm or more from the nominal thickness. For the coatings evaluated in this study, this could amount to ±12% of the thickest coatings while producing completely uncoated areas with the thinner coatings. To assure a precise and uniform coating, it was found that low powder feedrates, in the range of 0.05 to 0.10 gm/s, were required. Under these conditions typical build-up rates were 0.0025 to 0.008 mm per traverse. The low powder feed also provided a more uniform ceramic deposit, free of entrapped particles. Under these conditions coatings 0.025 mm thick could be produced to an accuracy of ±0.005 mm.

3.2.3 Thermal Diffusivity and Conductivity

Thermal conductivity and diffusivity of the coatings were measured as described previously. The values obtained are reported in Table 10 and in Figures 43 and 44.

The coatings applied at 20 and 40 kW show an increase in thermal conductivity with increased gun power. The 32 kW coating is inconsistent in that it does not lie between the other two values as would be anticipated. In other tests the 32 kW coating responded as if it were less dense than the 20 kW coating. The source of this erratic performance at 32 kW has not been identified. Apparently at this power level the plasma flame is sensitive to minor variations in anode wear and gas flow, at levels below the sensitiity of the process controls. Because of this fluctuation, the 20 and 40 kW coatings were selected for coating the experimental thrust chambers.

3.2.4 Surface Finish

Surface finish did not appear to be a function of plasma spray gun parameters. When surface finish values of the as-sprayed coatings were checked, arithmetic average values of 5-10 micrometers were obtained. Generally these values appeared to be the result of initial particle size rather than power levels, once a uniform coating was obtained.

3.2.5 Crystal Structure

X-ray diffraction measurements of the coatings gave nominal values of 94-98% cubic and tetragonal with the remainder being monoclinic. The initial powder was reported as 10% monoclinic with the balance cubic. This transformation of the monoclinic zirconia to cubic/tetragonal was similar in all cases. There appeared to be less monoclinic zirconia (about 3%) in the 20 kW coatings

Table 10

Thermal Diffusivity and Conductivity of $ZrO_2Y_2O_3$ Layers

Sample	Temperature (°C)	Thickness (cm)	Density ($gm\ cm^{-3}$)	Specific Heat ($W\ s\ gm^{-1}K^{-1}$)	Half-Time (sec)	Diffusivity ($cm^2\ sec^{-1}$)	Conductivity ($W\ cm^{-1}K^{-1}$)	Conductivity ($Btu\ in\ hr^{-1}ft^{-2}F^{-1}$)
20 kW	23	0.0254	4.8	0.457	0.0775	0.00298	0.00654	4.53
	100	0.0254	4.8	0.491	0.0891	0.00250	0.00590	4.09
	200	0.0254	4.8	0.522	0.0924	0.00238	0.00596	4.13
	300	0.0254	4.8	0.541	0.0965	0.00229	0.00593	4.11
	400	0.0254	4.8	0.552	0.0101	0.00219	0.00581	4.03
	500	0.0254	4.8	0.567	0.1009	0.00218	0.00591	4.10
32 kW	23	0.0178	5.2	0.457	0.0337	0.00413	0.00981	6.80
	100	0.0178	5.2	0.491	0.0338	0.00397	0.01010	7.00
	200	0.0178	5.2	0.522	0.0354	0.00372	0.01010	7.00
	300	0.0178	5.2	0.541	0.0365	0.00363	0.01020	7.07
	400	0.0178	5.2	0.552	0.0380	0.00345	0.00991	6.81
	500	0.0178	5.2	0.567	0.0383	0.00342	0.01910	7.00
40 kW	23	0.0178	5.2	0.457	0.0339	0.00379	0.00901	6.25
	100	0.0178	5.2	0.491	0.0353	0.00356	0.00909	6.30
	200	0.0178	5.2	0.522	0.0384	0.00321	0.00871	6.04
	300	0.0178	5.2	0.541	0.0397	0.00311	0.00875	6.07
	400	0.0178	5.2	0.552	0.0408	0.00302	0.00866	6.00
	500	0.0178	5.2	0.557	0.0421	0.00292	0.00860	5.96

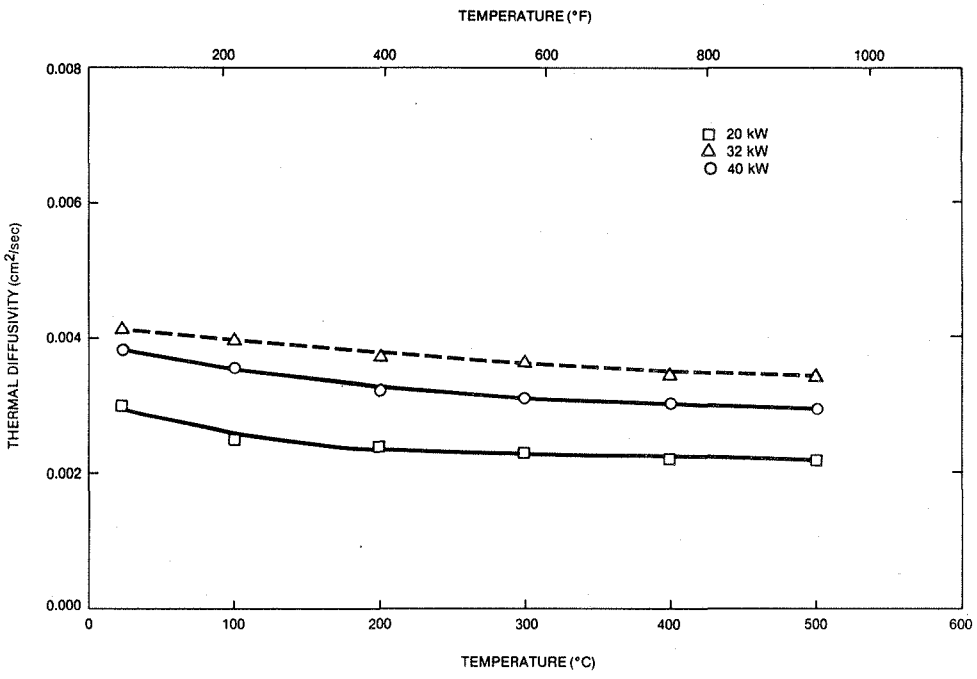

Figure 43. Thermal Diffusivity of $ZrO_2Y_2O_3$ Layers

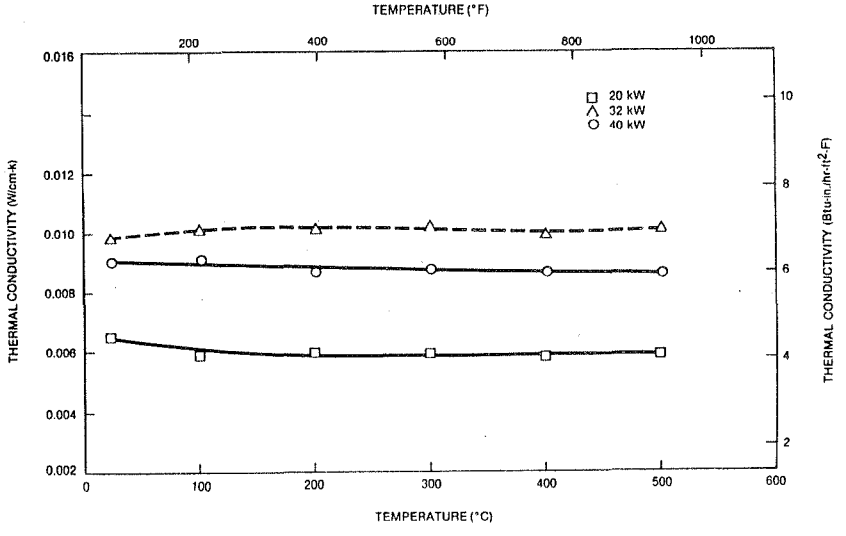

Figure 44. Thermal Conductivity of $ZrO_2Y_2O_3$ Layers

than in the 40 kW coating, but this variation was within the error limits of the analysis and it could not verified.

3.2.6 Calorimeter Tests

The 1.27 cm calorimeter probe is shown in Figure 45 and the test surface installed in a guard is shown in Figure 46. Some loss of insulation between the probe and guard is visible in the second figure. When this loss occurred the change in outlet temperature was less than 0.5°C and the results remained within experimental accuracy.

In operation the plasma flame was directed at the 1.27 cm diameter face of the calorimeter. Water flow and the T between the inlet and outlet water

temperatures were recorded for calculating the total heat input to the cold face calorimeter. Both coated and uncoated calorimeters were tested.

The appearance of a zirconia coated calorimeter is shown in Figure 47. The coating was applied to a thickness of 0.10 mm at 40 kW. In this test, the calorimeter was exposed to a 32 kW plasma flame. The relationship between power level and gun distance to heat flux is shown in Figure 48. Input to the calorimeter was measured for three sets of gun parameters as shown, and plotted as a function of distance. The gun parameters were given previously in Table 9.

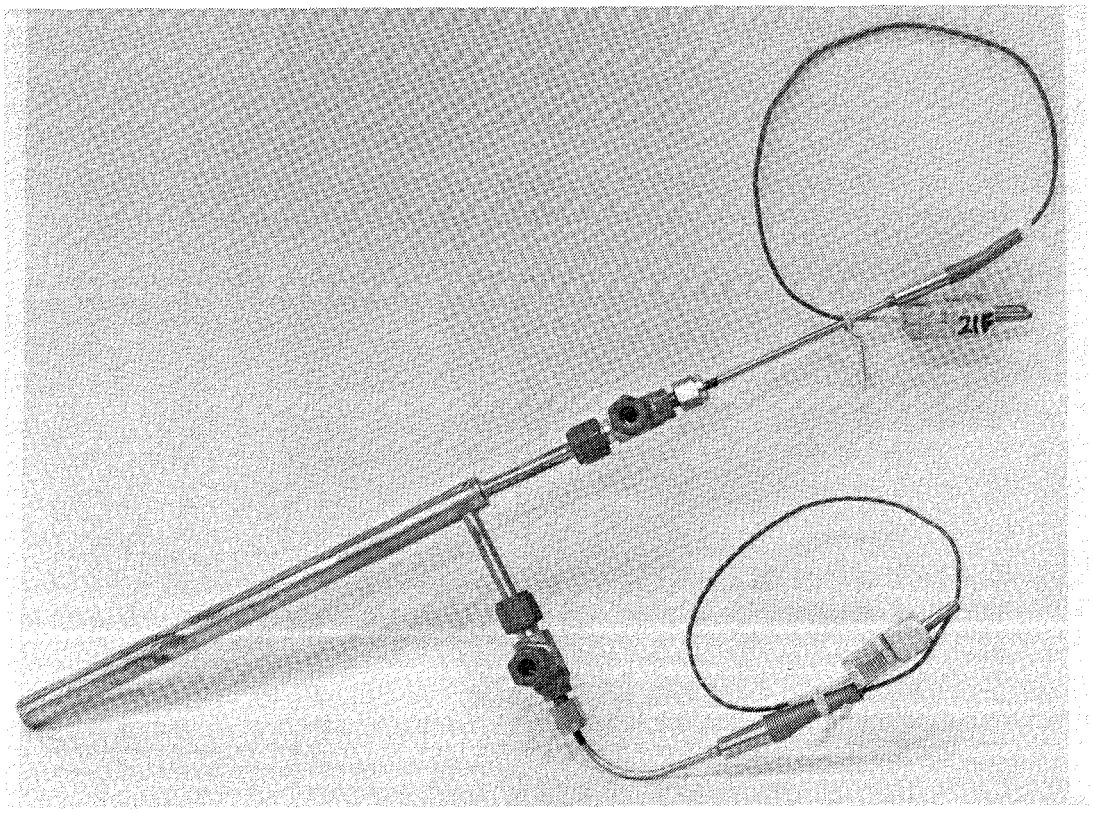

Figure 45. Water Cooled Calorimeter Probe

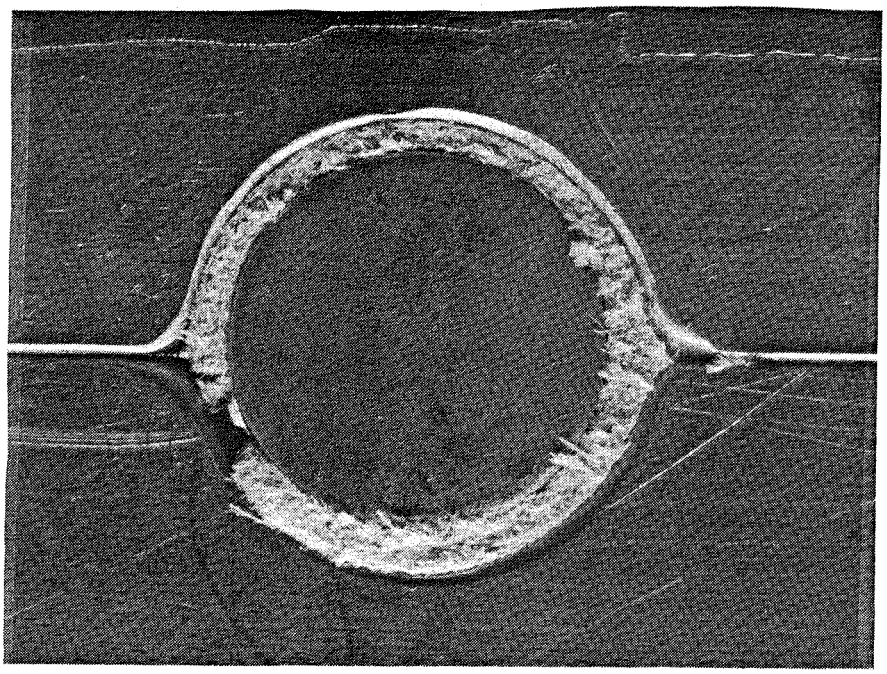

Figure 46. Calorimeter Face in Guard Shield

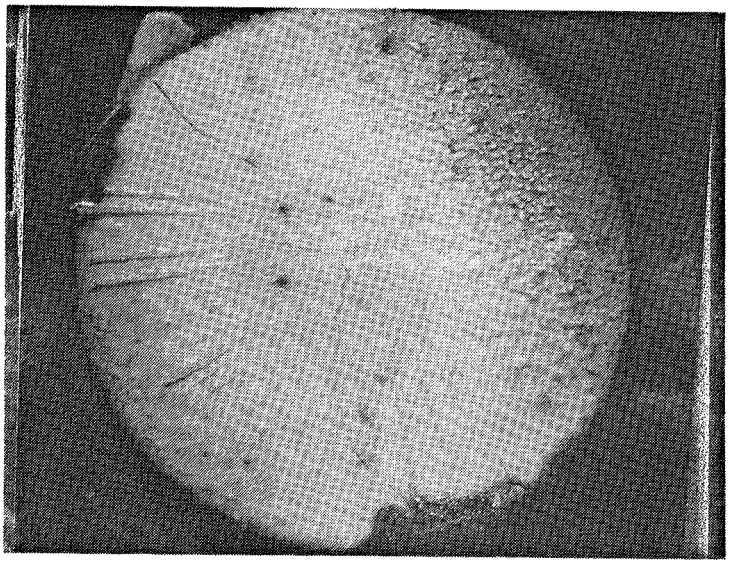

Figure 47. Calorimeter Face With 40 kW $ZrO_2Y_2O_3$ Coating 0.10 mm Thick Exposed to a Heat Flux of 9.15 watts/mm^2

Heating appears to be more sensitivite to voltage (hydrogen flow) than to current. The current increased by 100 amperes for each increase in power. The 15 volt increase between 20 and 32 kW shows a far greater increase in heat input than the 5 volt increase between 32 and 40 kW.

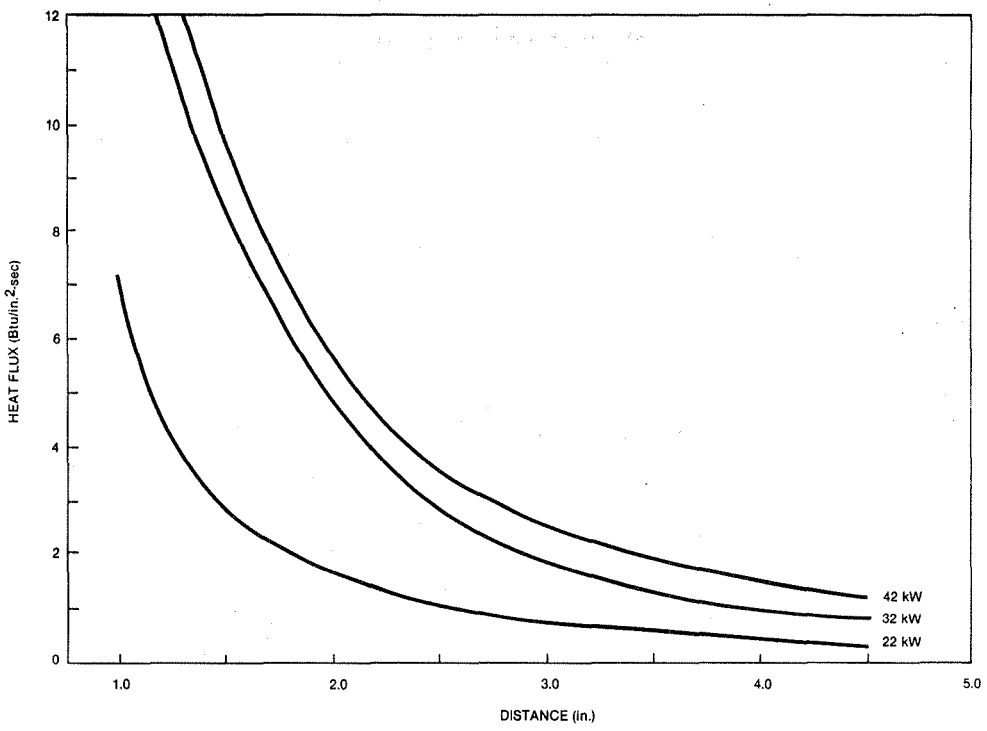

Figure 48. Heat Flux From a Plasma Torch as a Function of Distance at Selected Power Levels

The effect of the zirconia coatings on heat input to the calorimeter is reported in Figure 49 through 51. The 20 kW coating provided the greatest reduction in heat input to the calorimeter. The coating remained intact until the heat flux through the coating reached 8.2 watts/mm^2 at which point surface melting occurred. When the 32 kW coating was tested failure occurred at a heat input of 9.0 watts/mm^2 through spallation of the coating. The third coating, 40 kW zirconia, survived until surface melting occurred at an input of approximately 16.3 watts/mm^2 or twice that of the 20 kW coating. Failure of this coating also occurred as a result of melting. Some cracking normal to the surface occurred that may also have contributed to the low insulative value obtained with this coating.

Generally, the tests confirmed the thermal conductivity values previously measured and showed that the coatings could be retained up to the point of surface melting. The poor performance of the 32 kW coating supported the selection of the 20 and 40 kW for the coating of test thrust chambers.

3.2.7 Residual Stress and Stress Free Temperature

Several flat copper strip specimens were coated for residual stress and stress free temperature measurement. A copper thickness of 0.8128 mm and a bond coat thickness of 0.0508 mm were used for these tests. Density, residual stress

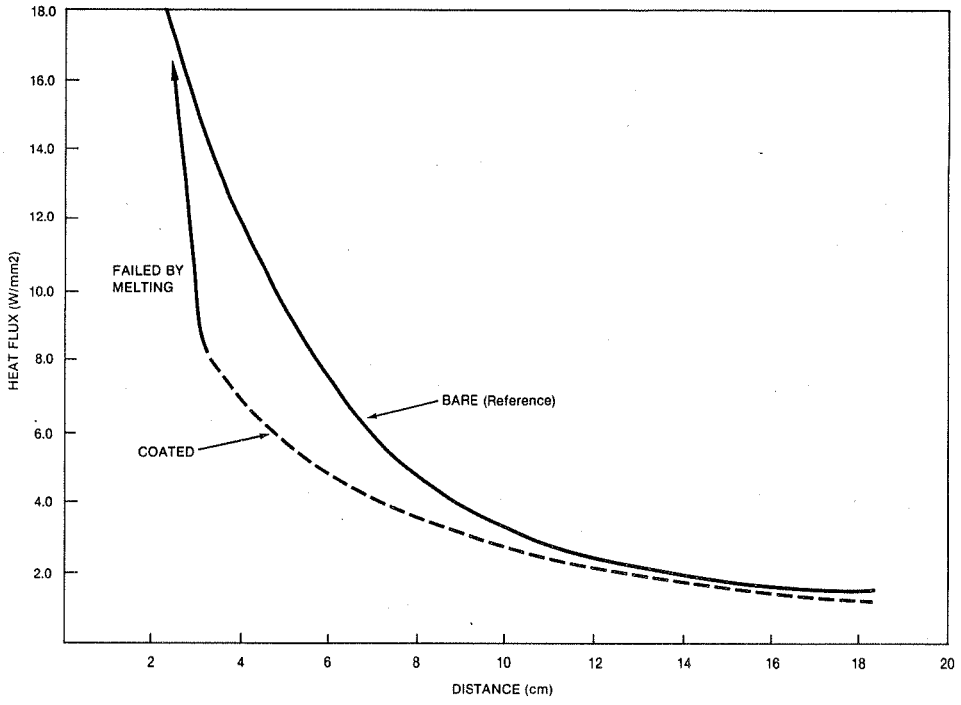

Figure 49. Heat Flux Transmitted to a Copper Calorimeter at 32 kW Through a 0.1 mm 20 kW Zirconia Coating

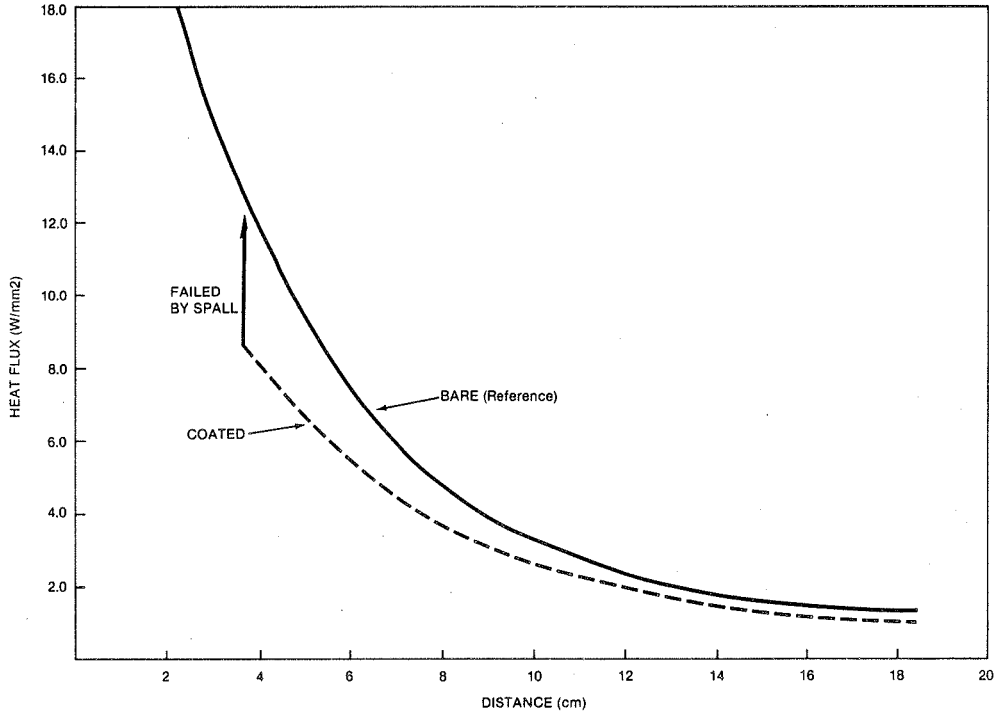

Figure 50. Heat Flux Transmitted to a Copper Caloriometer at 32 kW Through a 0.10 mm, 32 kW Zirconia Coating

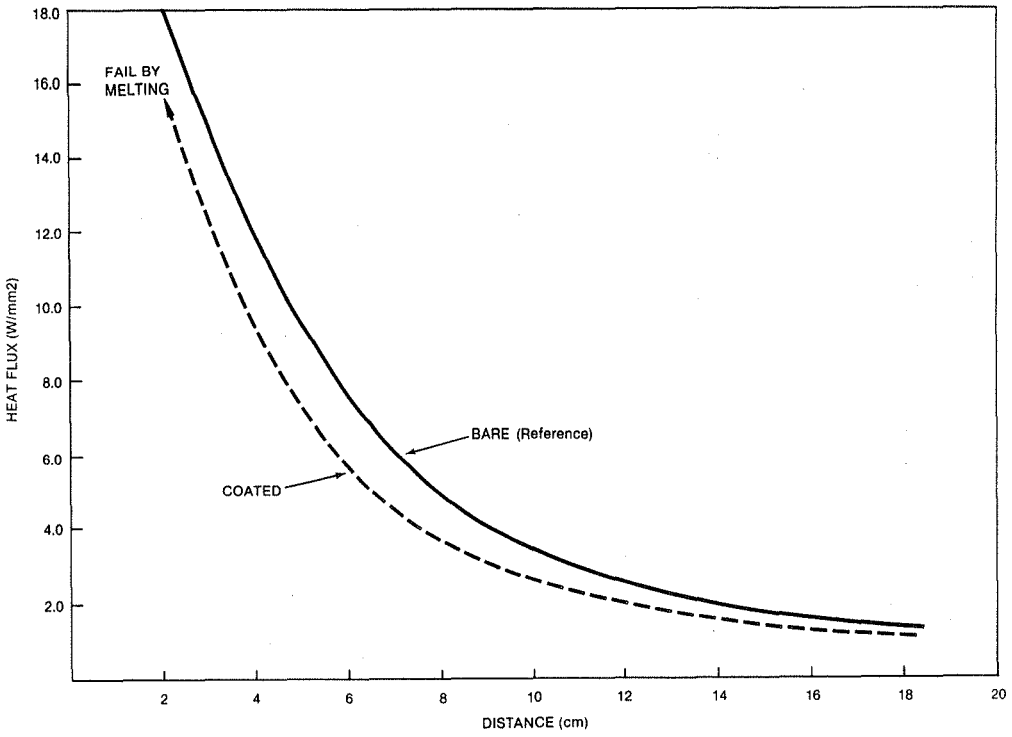

Figure 51. Heat Flux Transmitted to a Copper Calorimeter at 32 kW Through a 0.10 mm, 40 kW Zirconia Coating

and stress free temperature (SFT) were measured as described in the previous section. The results are shown in Table 1. The spray parameters for these coatings are given in Table 9.

These data show an increase in density and a rather constant residual stress and SFT with an increase in gun power from 20 kW to 32 kW. A substantial increase in residual stress and SFT was observed when the gun power was increased further, to 42 kW, although the desnsity remained constant. Increasing the coating thickness from 0.0965 mm to 0.254 mm also caused a significant increase in residual stress and SFT. No density measurement was made on this latter coating.

It is interesting to note that these data show the coating to incur a compressive residual stress during plasma spraying. This could effectively weaken the coating in service since compressive spallation is the predominant coating failure mode. However, the data generated thus far is rather limited and does not warrant conclusive interpretation.

The coatings produced in this study were strength tested in their as-sprayed condition (e.g., no annealing). Thus, the strength data generated reflects any effect of residual stress on coating strength. Reduction of residual stresses may present a practical means of increasing coating strength. This concept, although not pursued on this program, may be worthy of future coating development studies.

Table 11

Residual Stress and Stress Free Temperature Results From Coated Flat Specimens (0.8128 mm copper and 0.0508 mm NiCrAlY bond)

Coating Type*	Deposit Rate (mils/ pass)	Weight Gain (gms)	δ (mm)	α_1 (mm)	L (mm)	S (MPa)	T_{SF} (C)	Density (%)
I	0.1	0.3990	0.1778	0.09652	50.8	-7.2	58	88.6
	0.1	0.3778	0.3048	0.09652	50.8	-12.3	84	84.0
II	0.6	0.4341	0.2540	0.09652	50.8	-10.3	74	96.5
	0.6	0.4315	0.2794	0.09652	50.8	-11.3	79	96.0
	-	--	5.4864	0.02540	55.12	-60.2	447	--
III	0.4	0.5209	1.9812	0.1016	50.8	-75.6	437	93.0

3.3 ANALYTICAL MODELING

3.3.1 Thrust Chamber Model Development

Initial finite element performance analyses of the thrust chamber coating system were subcontracted to Control Data Corporation. This initial work included the model construction, preliminary test runs, and several coating analyses. All later finite element analyses were performed at Solar.

The original thrust chamber coating system model was 50.8 mm long and was divided into six elements axially. This resulted in an element aspect ratio (length/width) of 667 for the bond coat elements, which are the most extreme. The model length was later changed to 0.229 mm, which reduced the bond coat element aspect ratio to 3. This change caused no difference in the thermal analyses and less than a three percent variation in the calculated stresses. The shorter model was used for all of the final coating analyses.

The finite element model of the thrust chamber coating system was used to evaluate typical coating performance under selected operating conditions. Material properties from the literature were used in these analyses (Table 1). The selected operating conditions included a hot ceramic surface temperature of 1650°C (the maximum desirable ceramic operating temperature), cold copper surface temperatures of -240, -18 and 204°C, and a specified heat flux of 18 W/mm^2. These temperature selections were explained earlier but this heat flux was selected inadvertently due to an error in the original analyses performed by CDC. The heat flux was originally intended to be 49 W/mm^2 but the units were misinterpreted to be W rather than W/mm^2. Nonetheless, these

analyses were useful in developing the coating model and observing the general behavior of the coating system under potential operating conditions.

These initial coating systems analyses used a constant ceramic coating thickness of 0.10 mm. Steady state analyses were performed to evaluate the temperature distributions, heat fluxes and stress profiles through the coatings.

One series of coating system analyses used a constant hot surface temperature of 1650°C and three cold side temperatures: -240, -18 and 204°C. The resulting temperature gradients are shown in Figure 52. This figure shows that the bulk of the temperature drop occurs through the thin ceramic layer, subjecting the copper to a relatively low temperature gradient. The temperature gradients through the coating and the copper do not appear to be significantly influenced by the cold side temperature, although the overall temperature difference was increased by 31% from the smallest value to the largest.

The stress profiles resulting from the temperature gradients shown in Figure 52 are presented next. The hoop (or circumferential) stresses are equal to the axial stresses (due to the radial temperature gradient) and are shown in Figure 53. The radial stress profiles are shown in Figure 54. Step discontinuities in these stress profiles occur at the interfaces of different materials in the coating system. These discontinuities result from the changes in elastic moduli between materials, since the analyses assume continuous strain across the interfaces.

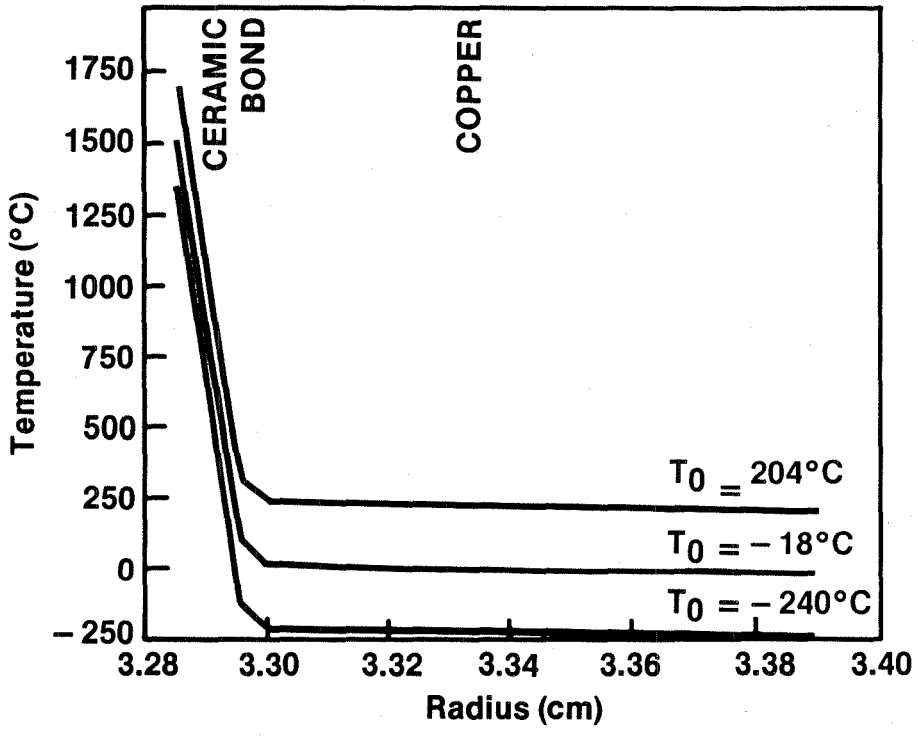

Figure 52. Temperature Radient for 1650°C Wall Temperature

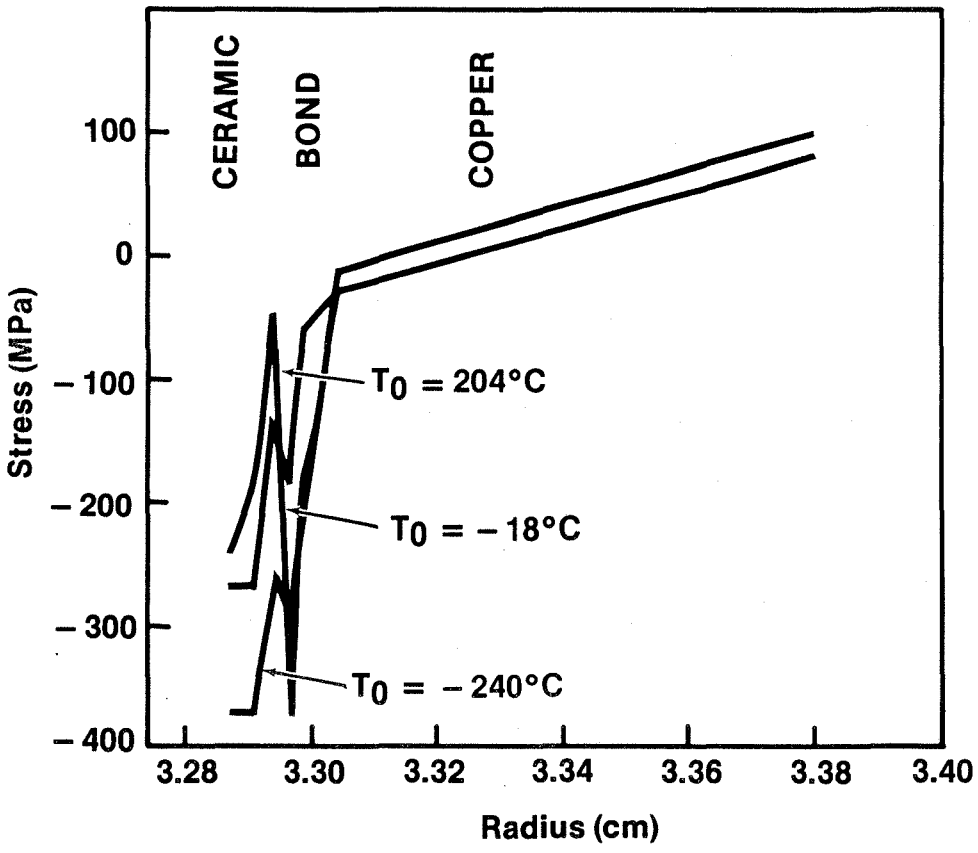

Figure 53. Axial Stress Gradient for 1650°F Wall Temperature

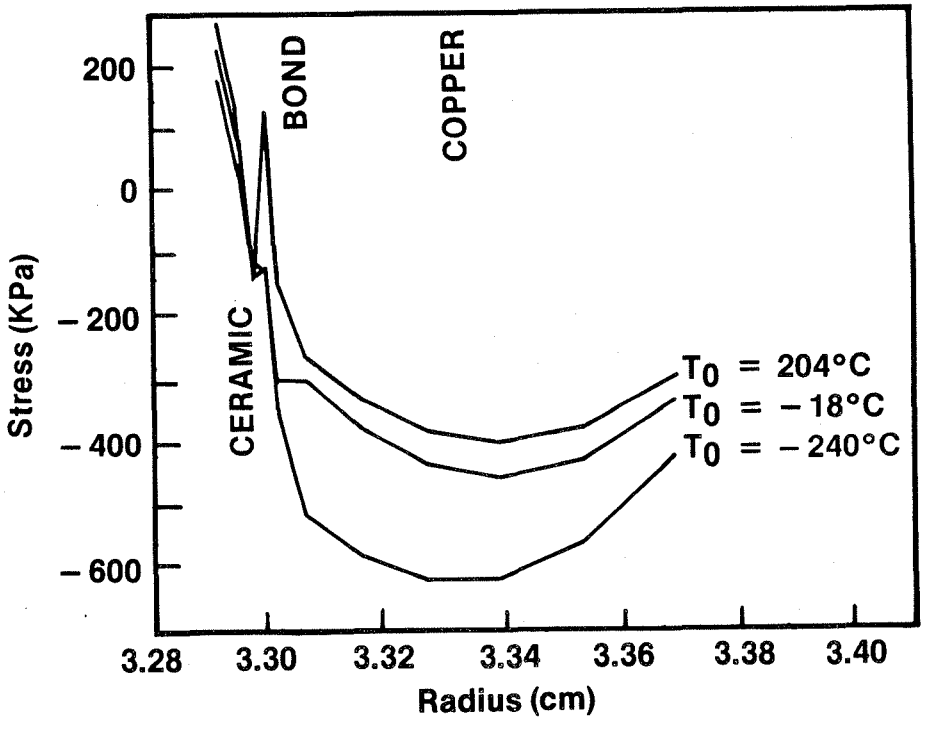

Figure 54. Thrust Chamber Radial Stress Gradient for 1650°C Inner Wall Temperature

The hoop and axial stresses in the coating are shown to be compressive; the maximum values occurring at the coating surface with a linear reduction through the thickness. The stresses in the bond coat are again compressive, while the stresses in the copper change from compressive to tensile. The coating stresses are of significant magnitude, with the maximum stresses on the order of -240 to -400 MPa. Stresses in the copper wall range from -31 to +110 MPa. The maximum tensile stress in the copper falls between the yield strengths of annealed and hardened oxygen-free copper.

The radial stresses through the coating system are much less severe than the hoop and axial stresses. Thus, the coating system is essentially in a biaxial stress state during operation. Radial stresses in the ceramic are approximately 0.5 MPa maximum, while the radial stresses in the copper are on the order of -0.9 to -1.6 MPa, maximum.

The cold surface temperature appears to have a significant effect on the hoop and axial stresses in the coating. A cold temperature change from 204 to -240°C (a 31% increase in overall temperature differential) results in a 60% increase in the maximum compressive coating stress. The effect on the hoop and axial stresses in the copper is less pronounced, with approximately a 45% increase in stress observed for the same change in cold side temperature. Cold side temperature also had an effect on the radial stresses, but the stress magnitude remained relatively insignificant.

A second set of coating system analyses used a constant radial heat flux of 18 W/mm^2 through the coating and the same three cold surface temperatures as before: -240, -18 and 204°C. The resulting temperature gradients are shown in Figure 55. The heat flux specified for these analyses was similar to the resulting heat fluxes in the previous analyses. In fact, the two cases having a 204°C cold side temperature are nearly identical.

As expected, the hot surface temperature decreases with decreasing cold surface temperature, since the heat flux is constant. It is interesting to note that the decrease in hot surface temperature (333°C) is approximately 25% less than the decrease in cold surface temperature (444°C), over the range evaluated. This is attributed to temperature affects on the material properties. As in the previous analyses, most of the temperature drop occurs through the ceramic coating, subjecting the bond and substrate to to relatively small thermal gradients.

The hoop and axial stress profiles resulting from the temperature gradients in Figure 55 are shown in Figure 56. These stress profiles are quite similar to those of the previous analyses, again showing the ceramic coating under very high compressive stress. The copper is subjected to slight compressive stresses at the bond interface and moderate tensile stresses at the outer surface.

These first two series of analyses were conducted to exercise the thrust chamber coating system model, and to evaluate the general behavior of the coating system under typical rocket engine operating conditions. The model was found to operate acceptably and the coating system behavior was found to be reasonable.

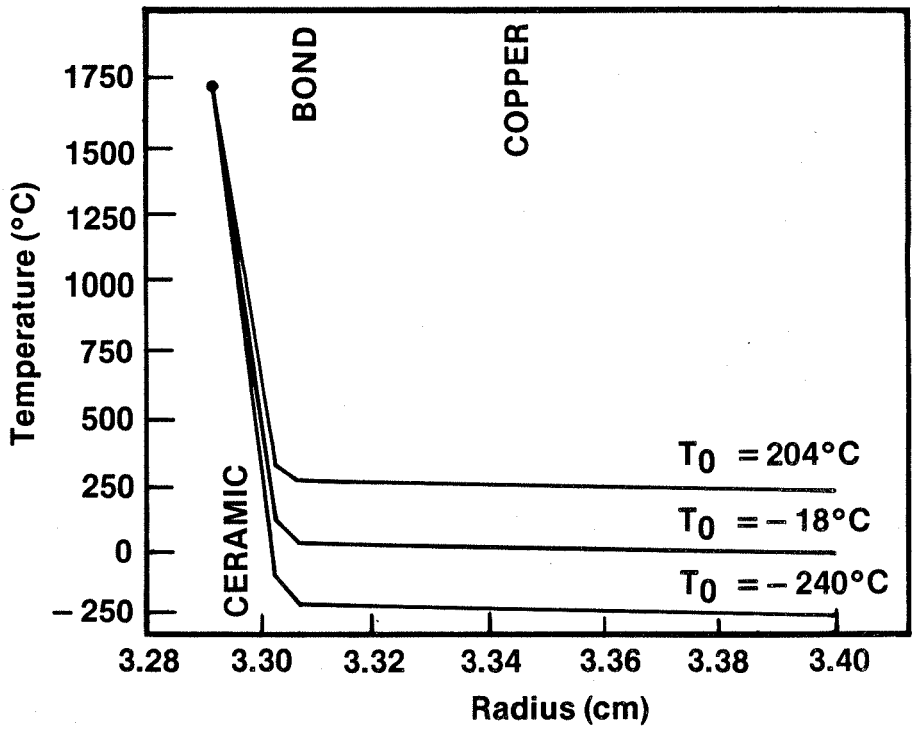

Figure 55. Thrust Chamber Temperature Gradient for 1650°C Inner Wall Temperature

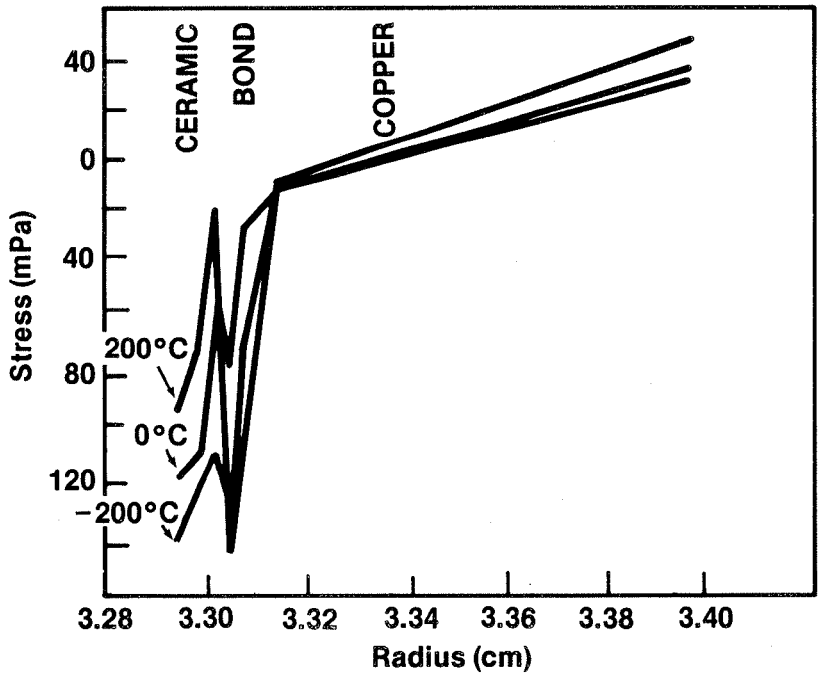

Figure 56. Thrust Chamber Axial Stress Gradient for 1650°C Inner Wall Temperature

This model was then used to evaluate the effect of thickness on the predicted coating temperatures and stresses in the thrust chamber environment. These analyses again used literature values for material properties. The purpose of these analyses was to observe the general effect of coating thickness on coating stress and temperature, and to establish a probable range of the coating thickness required for rocket thrust chamber application.

Figure 57 shows both surface temperature (left scale) and hoop (or axial) stress (right scale) in the coating for a constant heat flux (20 w/mm^2). This heat flux is at the lower end of a typical thrust chamber operating range. Both coating temperature and stress increase linearly with coating thickness.

This analysis indicates that a coating thickness of less than 0.13 mm may be required to maintain an acceptable coating temperature (2000°C) at this heat flux condition. The compressive coating stresses in this thickness range would be less than 400 MPa. The significance of this was not known at the time of these analyses.

Figure 58 shows the effect of coating thickness on heat flux for a fixed temperature gradient. The hot surface temperature (1650°C) used for this analysis is a desirable upper limit for the coating. The cold temperature (-18°C) is a reasonable anticipated operating value. This curve shows the heat flux is inversely proportional to coating thickness. At very low thicknesses, the heat flux is very sensitive to coating thickness. Again, the

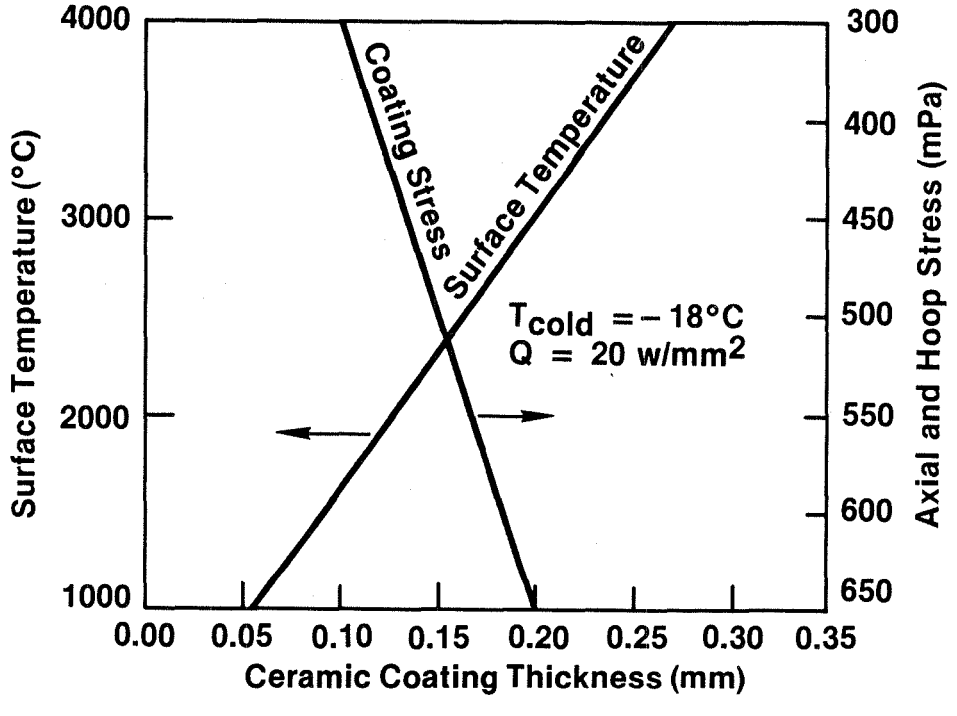

Figure 57. Relationship of Coating Surface Temperature and Stress to Coating Thickness to Constant Heat Flux

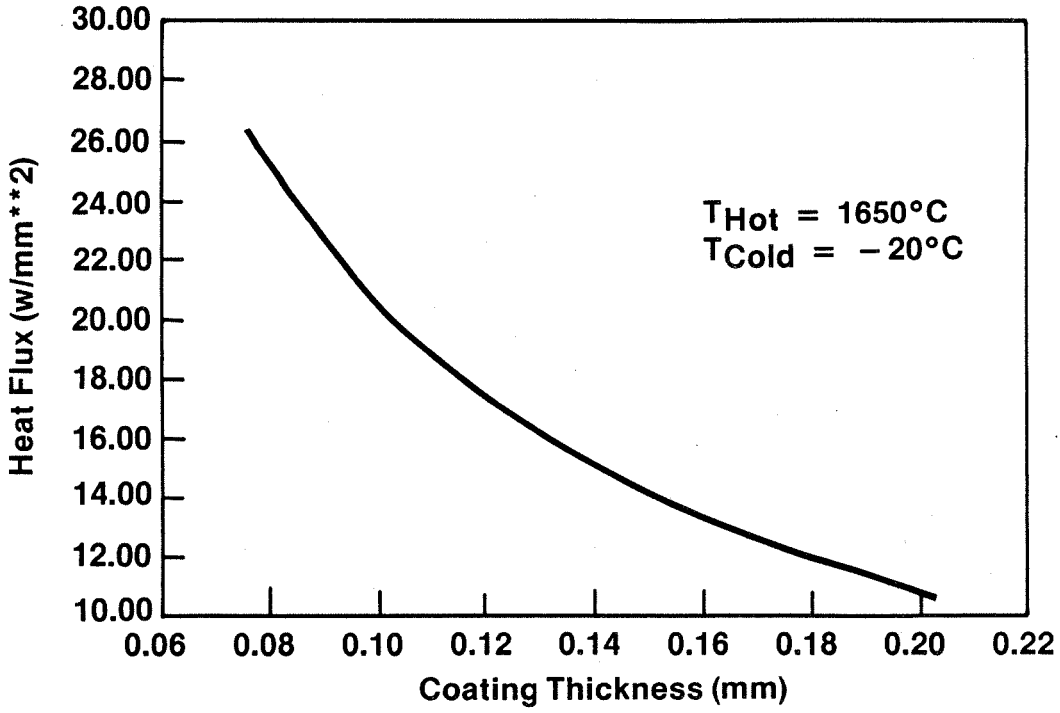

Figure 58. Initial Predicted Heat Flux Versus Coating Thickness at Constant ΔT

range of heat fluxes covered by this graph is in the moderate operating regime. This analysis indicates that coating thicknesses of less than 0.075 mm may be required to accommodate the high heat flux conditions without excessive temperature. The maximum compressive coating stress for this case is constant with varying coating thickness and is 350 MPa.

3.3.2 Coating Structure Model Development

Finite Element Model of Porous Coating

A variety of coating structures were evaluated using the finite element model shown in Figure 5. These structures included a variety of pore dimension ratios (D_r), total porosities (P_t), and pore sizes (P_i). An attempt was made to establish a relationship between these three coating parameters (Dr, Pt, Pi) and the effective thermal conductivity of the coating system (k).

An evaluation of the significance of radiation to the overall heat flow through a TBC was conducted. This was accomplished by comparing the heat flux through one coating model, with and without radiation across the pores. A negligible effect was observed. Thus, radiation was omitted from further analyses, to reduce the required computer time.

Figure 59 shows plots of effective thermal conductivity vs. pore dimension ratio for various combinations of total porosity and individual pore size.

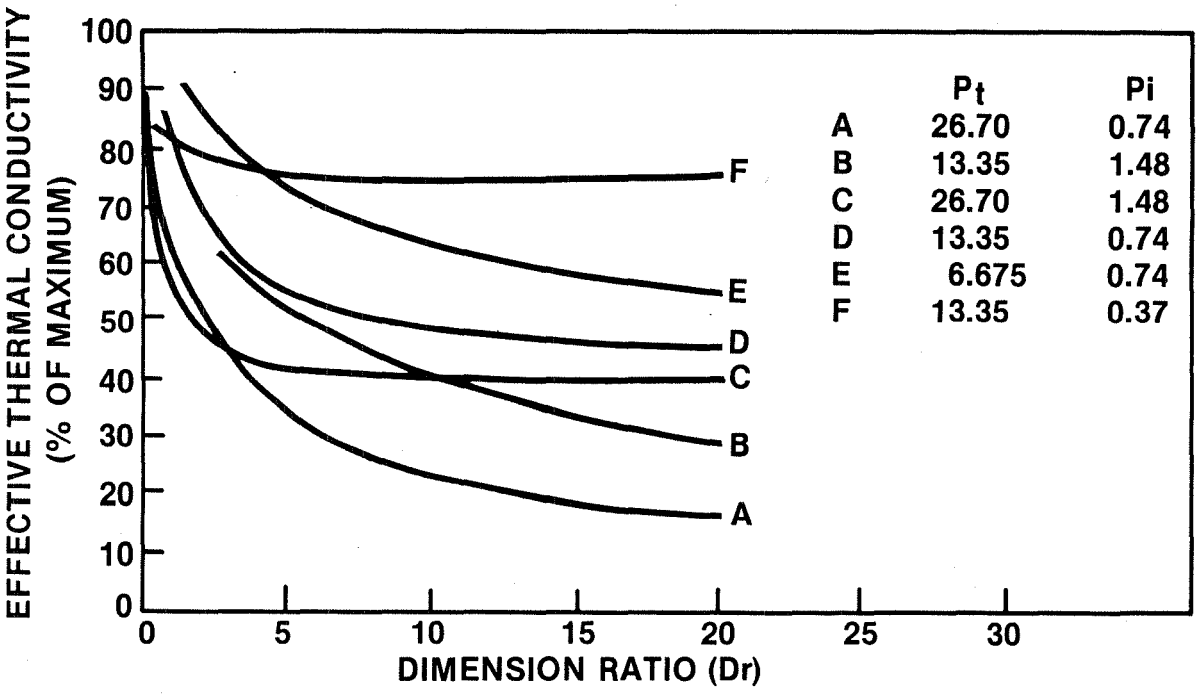

Figure 59. Influence of Microstructure on Effective Thermal Conductivity

Inspection of these curves shows a consistent trend towards higher thermal conductivity with decreasing dimension ratio (D_r). This trend is most pronounced for small values of D_r and tends to level off at large values of D_r. Also evident from this figure are inconsistencies in the effects of both porosity and pore size on effective conductivity. For example, curves A, D and E show a consistent pattern of increasing conductivity with decreasing porosity. (This trend is intuitively understandable.) However, curves B and C depict the opposite effect; that is, a decreasing conductivity with decreasing porosity. Similarly, curves B, D and F indicate an increase in conductivity with decreasing pore size, while curves A and C show the opposite effect.

Numerical regression analyses were performed to establish mathematical expressions for effective thermal conductivity in terms of one and two coating parameters. Due to the inconsistencies just described, it was not possible at this point to establish expressions containing all three coating parameters. It is believed that different coating parameters must be established, to replace or compliment the three parameters initially selected, in order to adequately and uniquely characterize a coating structure. Limited regression analyses were performed however, to illustrate the approach and methodology employed to establish an analytical thermal model of a porous coating structure.

All of the curves in Figure 59 appear to have an approximately exponential form. One-variable regression analyses were performed to establish mathematical expressions for curves A, D and E. Curves A and E were found to best fit an exponential relationship, while curve D was found to best fit an

inverse D_r (D_r being the independent variable) relationship. Curve D can also be expressed in exponential form with slightly less accuracy. These expressions and their respective correlation coefficients (r) are presented here:

$$\text{Curve A} \quad k = 56.94 - 13.82\ \ell n\ (D_r) \quad (r = 0.996) \tag{10}$$

$$\text{Curve E} \quad k = 94.13 - 13.26\ \ell n\ (D_r) \quad (r = 1.000) \tag{11}$$

$$\text{Curve D} \quad k = 67.46 - 7.74\ \ell n\ (D_r) \quad (r = 0.975) \tag{12}$$

$$k = (42.59\ D_r + 59.35)/D_r \quad (r = 0.999) \tag{13}$$

Two-variable regression analyses were performed on two sets of curves in Figure 59. Each set used dimension ratio as one variable. The first set showed a consistent decrease in conductivity with increasing porosity and contained curves A, D and E. The second set showed a consistent decrease in conductivity with increasing pore size, and contained curves B, D and F. The following expressions were established for k:

$$k = 526.8\ P_t^{-0.70}\ D_r^{-0.32} \quad (r_m = 0.906) \tag{14}$$

for a pore size of $P_i = 0.74$ and

$$k = 65.4\ P_i^{-0.31}\ D_r^{-0.13} \quad (r_m = 0.767) \tag{15}$$

for a porosity of $P_t = 13.35$; r_m is the multiple regression correlation coefficient.

Some of the analytical "data" generated using the finite element porous coating model were used to create the plot of effective thermal conductivity versus porosity shown in Figure 60. All of the curves presented show the same general trend of decreasing thermal conductivity with increasing porosity, except for curve G, which shows a slight rise in conductivity when the porosity is increased from 15 to 25 percent. It should be noted that curve G still lies in the range of "scatter" of the other curves.

Curiously, curve G also most closely matches the experimental data, plotted as curve H, for porosities less than 15 percent. The experimental data is derived from measured values of coating conductivities and porosities (reported earlier) and an assumed value for the thermal conductivity of the solid ceramic of 2.06 W/mC, which is one of the commonly reported literature values. It appears from Figure 60 that the finite element model of a porous coating generally predicts the same effect of porosity on thermal conductivity as observed experimentally. Although the experimental data falls outside of the analytical results, the shape of the curve is basically consistent. The objective of the analytical model was to simulate the effects of coating structure parameters on thermal conductivity, and then to empirically adjust the model to accurately calculate the actual value of a coating's thermal conductivity.

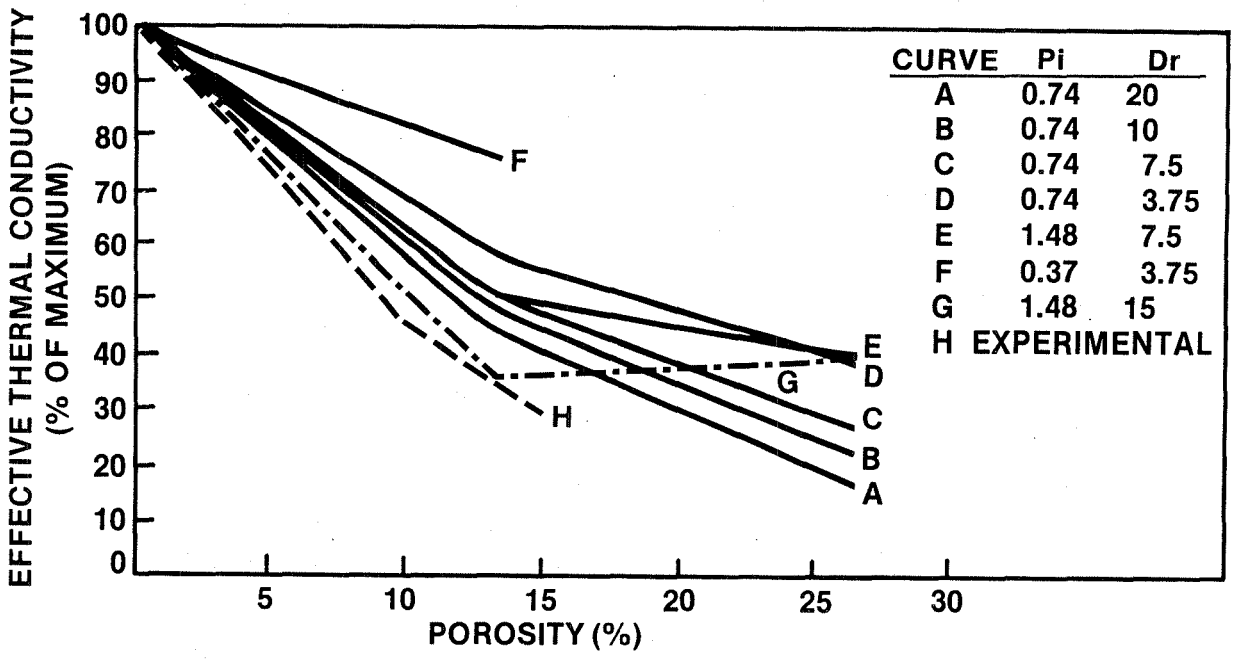

Figure 60. Finite Element Analysis of Porosity Effect on Effective Thermal Conductivity of Coatings

Due to the inconsistencies in the analytical model results described earlier, no attempt to empirically adjust the model was made. The results thus far support the contention that such a model can be empirically modified to produce accurate results. However, the basic model must first accurately represent all of the critical structural parameters of a porous coating. Therefore, additional work is required to establish more appropriate coating characterization parameters before a useful analytical model can be developed.

Theoretical Thermal Conductivity Predictions for Porous Coatings

Much work has been done to theoretically predict the properties of mixtures of materials (Refs. 6, 7). This work encompasses mixtures of all numbers and types of phases. All binary mixtures can be divided into three basic classes: (1) one-phase miscible mixtures, (2) two-phase systems with one continuous phase and one dispersed phase and (3) two-phase systems with two continuous phases. There are general mixture rules for each of these classes of mixtures for predicting material properties. It is most often necessary to combine empirical data with theoretical equations to accurately predict specific properties of a particular mixture.

A porous ceramic coating may be characterized as a mixture with one solid continuous phase (the ceramic) and one gaseous dispersed phase (the pores). In this case, the continuous phase is considered to be the "hard" phase and the dispersed phase is the "soft" phase. In addition, the continuous phase in a porous ceramic is most likely the major phase; that is, the phase com-

prising the largest volume fraction. Figure 61 illustrates this type of mixture.

The thermal conductivity of mixtures such as that depicted in Figure 61 have been evaluated by Maxwell and applied by Eucken (Ref. 6). Eucken suggests an expression for the resultant thermal conductivity of a mixture (k_m) as

$$k_m = k_c \left[\frac{1 + 2\, v_d\, (1 - k_c/k_d)/(2k_c/k_d + 1)}{1 - v_d\, (1 - k_c/k_d)/(k_c/k_d + 1)} \right] \tag{16}$$

where k is the thermal conductivity, v is the volume fraction and the subscripts c and d stand for the continuous and dispersed phases, respectively. When $k_c \gg k_d$, the expression for resultant conductivity can be simplified to

$$k_m = k_c\, [(1 - v_d)/(1 + v_d)] \tag{17}$$

and if $k_d \gg k_c$ the expression simplifies to

$$k_m \approx k_c\, [(1 + 2v_d)/(1 - v_d)] \tag{18}$$

Note that Equation (18) expresses the resultant (or effective) thermal conductivity of a mixture solely in terms of the conductivities and volume fractions of each component in the mixture. There is evidence to suggest that other factors are of equal importance in determining effective conductivity (Ref. 7). For example, some two-phase systems, such as Al_2O_3-ZrO_3 and MgO-$MgAl_2O_4$, can exhibit thermal conductivities lower than either single phase. This results from flat microcracks which open along grain boundaries during thermal cycling due to differences in the thermal expansion coefficient within the material. The small fraction of porosity which results from this cracking may

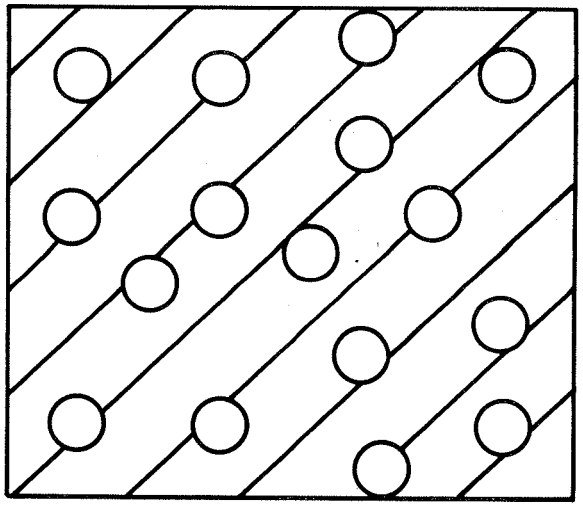

Figure 61. Illustration of Mixture Having a Continuous Major Phase and Dispersed Minor Phase

cause a significant reduction in thermal conductivity when the porosity occurs as a continuous phase perpendicular to the heat flow path. Similarly, the thermal conductivities of other oxides can be significantly altered by heat treating, with little change in porosity or grain size.

Thermal cycling of some two-phase solid mixtures has been observed to continuously change the effective thermal conductivity due to crack growth during cooling and crack annealing during heating. The opening and closing of such cracks have caused hysteresis in conductivity measurements of some materials (e.g., aluminum titanate) (Ref. 7). This type of effect from thermal cycling may be pertinent to the behavior of thermal barrier coatings, especially those subjected to high heat fluxes. No reference of this behavior has been found for TBC's in particular, but the phenomena is worthy of note.

Temperature may also influence the thermal conductivity of a mixture by affecting the conductivity of each phase. In the case of pores containing air, not only does the true thermal conductivity of air increase sharply with temperature, but so does the effective thermal conductivity due to radiation heat transfer. This is illustrated in Figure 62 where the effective thermal conductivity, due to radiation, of a pore having a thickness dp, is shown as a function of temperature. The thermal conductivity of solid ZrO_2 is shown also, for comparison. It is interesting to note that a pore having a thickness on the same order of magnitude as the coating thicknesses being investigated in this study (0.10 mm), even at high temperatures (1600°C), has an effective thermal conductivity of only 3 percent that of solid ZrO_2. This agrees with the previous conclusion that radiation across the individual pores makes a negligible contribution to the overall heat flux through a porous coating.

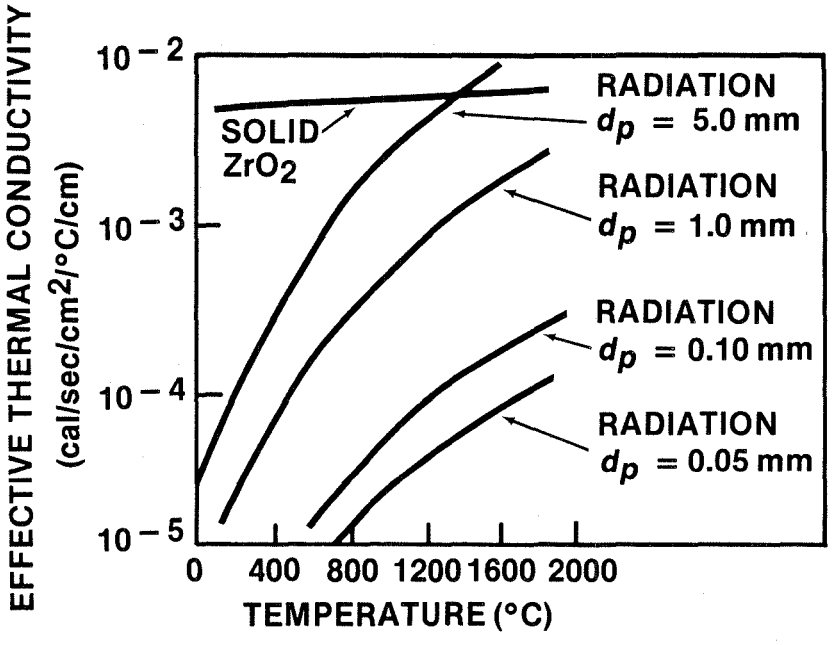

Figure 62. Radiation

The nature of the interface between two phases in a mixure may also affect the properties of the mixture. In porous ceramic coatings this effect may influence the resultant thermal conductivity, since heat transfer across the interface must occur by natural convection.

Other factors that have been considered in their effect on the properties of two-phase mixtures having one dispersed phase are the maximum packing fraction and the shape, agglomeration, orientation and distribution of the dispersed particles. The packing fraction accounts for the fact that the dispersed phase cannot pack in such a manner as to completely fill a space. Nielsen (Ref. 7) has described an analytical approach for calculating the properties of mixtures which takes into account these latter factors.
The general mixture rule proposed by Nielsen is:

$$\frac{P_c}{P_m} = \frac{1 + A\,B\,v_d}{1 - B\,\psi v_d} \tag{19}$$

where $$A = 1/(K_E - 1) \tag{20}$$

$$B = \frac{P_c/P_d - 1}{P_c/P_d + A} \tag{21}$$

$$= 1 + \left(\frac{1 - m}{\phi_m{}^2}\right)\phi d \tag{22}$$

and P_c = property of continuous phase
P_d = property of dispersed phase
P_m = property of mixture
K_E = Einstein coefficient
v_d = volume fraction of dispersed phase
ϕ_m = maximum packing fraction

The constant A depends upon the shape of the dispersed particles, their state of agglomeration, their orientation and the nature of the interface. "A" can vary from zero to infinity and is related to the Einstein coefficient which can be calculated theoretically or derived empirically. The factor ψ takes into account the maximum packing fraction which is defined as:

$$\phi_m = \frac{\text{true particle volume}}{\text{volume occupied by particles}}$$

Values of m can be estimated or measured in a variety of ways.

Table 12 presents some values of ϕ_m which were derived largely from theory. Table 13 presents some values of K_E derived for mechanical properties of mixtures. In general, values of K_E are usually slightly greater for thermal properties than for mechanical properties, but often only small errors will result from using the mechanical values for thermal calculations.

Table 12

Values of ϕ_m for Various Mixtures

Particles	Type of Packing	ϕ_m
Spheres	Hexagonal close packing	0.7405
Spheres	Face centered cubic	0.7405
Spheres	Body centered cubic	0.60
Spheres	Simple cubic	0.5236
Spheres	Random close packing	0.637
Spheres	Random loose packing	0.601
Fibers	Parallel hexagonal	0.907
Fibers	Parallel cubic	0.785
Fibers	Parallel random	0.82
Cubes	Random	0.70
Rods	L/D = 4, random three dimensional (approx.)	0.625
Rods	L/D = 8, random three dimensional (approx.)	0.48
Rods	L/D = 16, random three dimensional (approx.)	0.30
Rods	L/D = 40, random three dimensional (approx.)	0.13
Rods	L/D = 70, random three dimensional (approx.)	0.065

The original Einstein equation, derived for the viscosity of suspensions of rigid spheres, can be generally expressed as:

$$P_m/P_c = 1 + K_E\, v_d \tag{23}$$

for low concentrations of the dispersed phase when P_d/P_c is very large. This form of the equation may be applied to porous coatings if P is used to represent thermal resistivity, since the resistivity of air is much greater than that of the ceramic. This expression provides a simple method of determining K_E from experimental data. Equation (23) can thus be transformed to:

$$k_m/k_c = 1/(1 + K_E\, v_d) \tag{24}$$

for low values of v_d and large values of k_c/k_d. This is referred to here as the simplified Einstein equation.

Table 13

Values of K_E for Various Mixtures

Type of Dispersed Phase	Orientation of Particles and Type of Stress	K_E
Dispersed spheres	Any. No slippage	2.50
Dispersed spheres	Any. Slippage	1.0
Spherical aggregates of spheres	Any. $\phi_a = \phi_m$ of spheres within aggregate	$2.5/\phi_a$
Cubes	Random (approximate)	3.1
Uniaxially oriented fibers	Fibers parallel to tensile stress component	2L/D
Uniaxially oriented fibers	Fibers perpendicular to tensile stress component	1.50
Uniaxially oriented fibers	Longitudinal-transverse shear	2.0
Uniaxially oriented fibers	Traverse-transverse shear	1.5
Uniaxially oriented fibers	Bulk modulus	1.0
Fibers randomly oriented in three dimension	Shear. (Approximate)	L/2D

Comparison of Theoretical Conductivity Calculations and Experimental Data

Three methods of calculating the theoretical thermal conductivity of a porous coating have been suggested: (1) the Maxwell theory, (2) the Einstein equation and (3) the simplified Einstein equation. Each of these methods was applied to a porous zirconium oxide coating to predict effective thermal conductivity as a function of porosity. Thermal conductivity values from the literature were used for solid $ZrO_2 8Y_2O_3$ and air, both at 1200°K. The results of these analyses are presented in Figure 63 and are compared to the experimental data presented earlier.

Theoretical curve A in Figure 63 was calculated from equation (16) based on Maxwell's mixture theory. This equation expresses the effective thermal

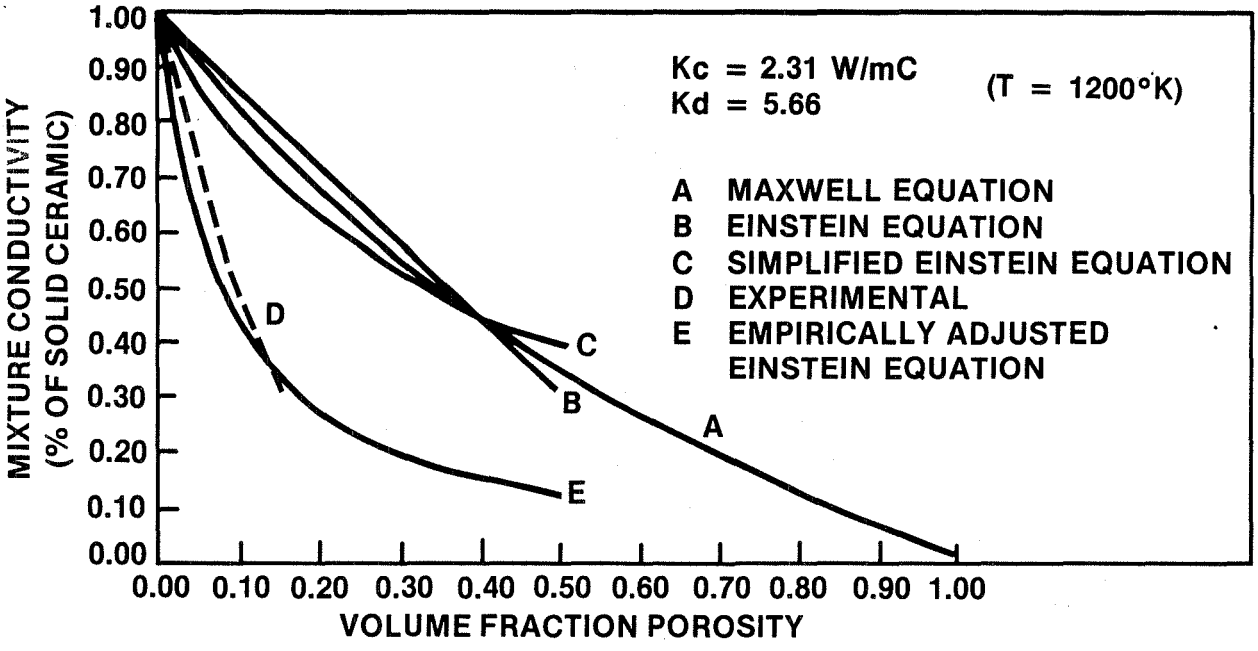

Figure 63. Theoretical Thermal Conductivity of Porous Coating

conductivity of the mixture in terms of the conductivities and volume fractions of the individual phases. It does not account for pore size, distribution, agglomeration, orientation, or interface effects.

Theoretical curve B was established using equation (19) (the Einstein equation). It was necessary to estimate values of K_E and ϕ_m to apply this equation. A value of $K_E = 3.5$ was selected based on the value of K_E for random cubes presented in Table 13. The selected value of K_E is slightly greater than the value in the table for mechanical properties, to compensate for the difference between K_E values for mechanical and thermal properties. A value of $\phi_m = 0.70$ was selected based on the value for random cubes presented in Table 12.

The properties, P, in equation (19) represent thermal conductivities for this analysis. This equation presumably accounts for the distribution, agglomeration, orientation and interface effects of the dispersed pores. It is recognized that the assumed values of K_E and ϕ_m are educated guesses and should be investigated in more detail if this analytical approach is pursued further.

Theoretical curve C was established using equation (24) (the simplified Einstein equation). Only a value for K_E was needed for this analysis. Again, this value was selected as $K_E = 3.5$.

Curve D in Figure 63 represents the experimental data generated earlier. The value of solid ceramic conductivity used to generate this curve is a commonly quoted literature value, $k_c = 2.06$ W/mC. It should be noted that besides the possible error in the value used for k_c ($\pm$ 9% based on reported data) this

experimental data curve also represents two measured values, k_m and P_t, which are subject to experimental error.

It is obvious from Figure 63 that the experimental data does not agree well with the theoretical analyses. The three theoretical models all agree fairly well with each other in the low porosity region; the largest discrepancy (about 15% difference) being between the two versions of the Einstein equation. The Maxwell conductivity curve lies midway between these two.

The fifth curve in Figure 63 represents an empirically adjusted Einstein equation. In this case two values of K_E were calculated from the experimental data using equation (24). These values are:

K_E = 11.74 @ 10% porosity
K_E = 16.32 @ 15% porosity
K_E = 14 average

The average value of K_E was used in equation (24) to construct curve E, which matches the experimental data reasonably well (within 9.5%). Although this value of K_E is larger than values quoted in the literature, it is acceptable since there is no theoretical upper limit to the value of K_E. The equation for curve E is:

$$k_m/k_c = 1/(1 + 14\ v_d) \qquad (25)$$

Equation (19) (the Einstein equation) was also used to generate an empirically calibrated expression for effective thermal conductivity. In this case a value of ϕ_m = 0.70 was assumed and values of K_E were calculated using the experimental thermal conductivity data in equations (19) through (22). This analysis yielded an average value of K_E = 1.06, which was used with the assumed value of ϕ_m to calculate a curve of thermal conductivity vs. porosity. The resulting curve fell almost exactly on the empirically adjusted curve created previously using the simplified Einstein equation.

No attempt to empirically calibrate equation (18) was made. This expression has no inherent variables which can be manipulated. It appears from Figure 63 that the difference between this equation (curve A) and the experimenal data is more than just a constant, and therefore, would probably involve an exponential factor of some form.

Overall, equation (25) appears to provide the simplest, reasonably accurate expression for calculating the effective thermal conductivities of the ceramic coatings in this study. It is recognized that the experimental data base should be expanded to provide further verification of this relationship. It is likely that a more accurate value of K_E may be determined through additional testing, but that the form of equation (25) will still apply.

3.3.3 Discussion of Model Development

A practical method for analytically modelling TBC's has been developed. This method basically consists of two parts. First, the material properties of the TBC are determined, either experimentally or analytically. Second, these material properties are used in a finite element model of the coating system to predict the thermo-mechanical response of the coating to specific operating conditions. This model can also be used to predict the effects of coating process parameters on coating performance. This requires that the effect of the process parameters on the coating properties first be determined. Then, these material property changes can be incorporated into the finite element model, to evaluate the effects on coating performance.

The material properties used in this study were either measured or taken from the literature. A more complete analytical model could be constructed if the material properties were analytically derived. This could be accomplished by establishing empirical relationships between coating properties and coating deposition parameters. Coating properties could then be predicted by monitoring the coating deposition parameters. An alternative approach might be to relate all coating properties to easily measured coating characteristics, such as porosity.

The objective of the porous coating model was to establish an analytical method of predicting the thermal conducitivity of a coating based on porosity. Thermal conductivity was selected for this investigation since it is one of the most critical properties in these analyses. It was intended to uniquely define the porous structure of a coating in terms of geometric parameters, and relate these parameters to thermal conductivity. These relationships would then be empirically adjusted. A real coating could then be defined in terms of these geometric parameters and it's thermal conductivity calculated.

The porous coating model was intended to be developed one step further. A relationship between coating deposition parameters and the geometric coating parameters was to be established empirically. This model could then be used to predict the thermal conductivity of a coating based on its deposition parameters.

However, the porous coating model was not sufficiently developed to achieve these results. The geometric parameters selected to characterize a porous coating structure proved inadequate. Despite the obvious inconsistencies in the model, however, much of the analysis was consistent and produced logical results. It is believed that the basic model concept is sound, but requires further development. The geometric coating parameters need to be re-evaluated and perhaps redefined or expanded.

The theoretical models for coating thermal conductivity appear to have merit. Empirical adjustment of the Einstein equation produced a reasonably accurate expression for thermal conductivity in terms of porosity. However, additional empirical data is required to fully evaluate these models.

3.4 COMPUTER ANALYSES

3.4.1 Coating Strength Data Analyses

Coating strength data were generated using the four-point flexure test, for the three coating types previously described: those applied at the 20, 30 and 40 kW power levels. These are referred to as coating types A, B and C, respectively. Two sets of coating strength data were generated at different points in time. Each set tested three thicknesses of each coating type. Set number 1 tested coatings of thicknesses 0.0508, 0.1016 and 0.1524 mm; set number 2 tested coatings of thicknesses 0.0254, 0.0508 and 0.1016 mm. Three specimens were tested for each coating type and thickness combination. The strength data is presented in Table 14a and 14b, along with the measured loads and deflections at failure and calculated radii of the neutral axes. Coating strength is defined here as the maximum compressive strain in the coating at the time of failure (ε_m). Also reported is the strain at the bond interface of the coating (ε_b), and at the coating mid-thickness (ε_c).

The coating strength data is plotted in Figure 64 as maximum coating strain vs. coating thickness. Although coating thickness was not known to affect coating strength, it did provide a convenient graphical means for comparison of coating strengths. Curves A, B and C represent the original data set and curves D, E and F represent the second data set. Each data point represents the average of three strength tests.

It is difficult to make intuitive conclusions about the relative strengths of the three coating types, based on the data presented in Figure 64. The strengths of each coating type overlap each other, within each data set, and exhibit inconsistent trends as functions of thickness. It is apparent, however, that the strengths of the coatings in the second set were significantly higher than those in the first. The reason for this has not been determined. Although the coating application parameters were the same for both coating specimen sets, there may have been a subtle improvement in the application process for set #2 due to the experience of coating set #1.

The apparently inconsistent results from the coating strength tests are not unreasonable. Rarely do ceramic materials of any type exhibit deterministic strengths (Ref. 8). It is often convenient to employ statistics in evaluating the strength of ceramic materials. Thus, statistical analyses of the coating strength data were used to compare the strengths of the three coating types.

Because of the obvious difference in strengths between the two sets of coating tests, each set was evaluated individually. A matched-pair t test (Ref. 9) was used to compare the strengths of the three coatings in each set. This statistical method is used to make inference about the mean of the difference between two matched groups. In this case the strengths of coatings having the same thickness were matched to form pairs of data. This minimized the possible influence of thickness on the strength comparison.

Table 14a

Four-Point Bend Specimen Results - Data Set 1

Number	Coating Type	t Thickness (mm)	P Load (kg)	Y Deflection (mm)	R_1 Inner Radius (mm)	ϵ_b Interface Strain x 10^{-2}	ϵ_c Coating Strain x 10^{-2}	ϵ_m Surface Strain x 10^{-2}	R Neutral Radius (mm)
1	A	0.0508	15.5	5.18	33.27	-0.801	-0.877	-0.952	33.59
2			16.0	5.59	31.24	-0.840	-0.921	-1.001	31.56
3			16.5	6.10	28.96	-0.889	-0.976	-1.063	38.66
4		0.1016	21.0	6.58	27.18	-0.703	-0.888	-1.073	27.47
5			22.5	6.58	27.18	-0.703	-0.888	-1.073	27.47
6			20.5	6.38	27.94	-0.691	-0.871	-1.051	28.24
7		0.1524	27.0	8.18	23.11	-0.575	-0.900	-1.226	23.40
8			28.7	8.18	23.11	-0.575	-0.900	-1.226	23.40
9			27.5	7.19	25.40	-0.550	-0.847	-1.143	25.69
10	B	0.0508	17.0	5.79	30.23	-0.861	-0.944	-1.027	30.54
11			18.0	5.99	29.46	-0.870	-0.963	-1.048	29.78
12			18.0	5.79	30.23	-0.861	-0.944	-1.143	25.69
13		0.1016	29.0	7.39	24.89	-0.742	-0.943	-1.145	25.18
14			24.0	8.18	23.11	-0.775	-0.992	-1.209	23.40
15			28.7	7.87	23.62	-0.765	-0.978	-1.190	23.91
16		0.1524	26.8	7.19	25.40	-0.550	-0.847	-1.143	25.69
17			25.0	6.20	28.70	-0.519	-0.782	-1.044	29.00
18			27.1	7.77	23.88	-0.566	-0.882	-1.197	24.17
19	C	0.0508	8.3	8.69	22.10	-1.082	-1.196	-1.309	22.39
20			10.6	6.99	25.91	-0.965	-1.062	-1.159	26.21
21			--	--	--	--	--	--	--
22		0.1016	23.0	8.99	21.59	-0.807	-1.039	-1.271	21.87
23			22.5	6.58	27.18	-0.703	-0.888	-1.073	27.47
24			21.5	7.29	25.15	-0.737	-0.937	-1.137	25.44
25		0.1524	35.0	7.49	24.64	-0.558	-0.864	-1.169	24.93
26			22.0	11.18	18.80	-0.627	-1.027	-1.427	19.07
27			21.0	8.38	22.61	-0.580	-0.913	-1.246	22.89

Table 14b

Four-Point Bend Specimen Results - Data Set 2

Number	Coating Type	t Thickness (mm)	P Load (kg)	Y Deflection (mm)	R_1 Inner Radius (mm)	ϵ_b Interface Strain x 10^{-2}	ϵ_c Coating Strain x 10^{-2}	ϵ_m Surface Strain x 10^{-2}	R Neutral Radius (mm)
1	A	0.0254	15.3	8.13	23.18	1.252	1.306	1.360	23.50
2			14.6	7.87	23.73	1.229	1.281	1.334	24.05
3			13.8	8.13	23.18	1.252	1.306	1.360	23.50
4		0.0508	13.7	7.62	24.32	1.204	1.256	1.308	24.64
5			13.8	7.37	24.95	1.180	1.230	1.280	25.27
6			13.7	6.86	26.38	1.127	1.175	1.222	26.70
7		0.1016	14.8	7.62	24.32	1.204	1.256	1.308	24.64
8			17.3	8.13	23.18	1.252	1.306	1.360	23.50
9			16.0	7.37	24.95	1.180	1.230	1.280	25.27
10	B	0.0254	14.0	8.13	23.18	1.046	1.154	1.262	23.47
11			13.6	8.13	23.18	1.046	1.154	1.262	23.47
12			--	--	--	--	--	--	--
13		0.0508	17.5	8.38	22.67	1.063	1.173	1.284	22.96
14			17.1	8.13	23.18	1.046	1.154	1.262	23.47
15			17.7	8.13	23.18	1.046	1.154	1.262	23.47
16		0.1016	20.0	10.67	19.31	1.190	1.319	1.449	19.60
17			20.1	10.67	19.31	1.190	1.319	1.449	19.60
18			19.8	9.65	20.58	1.138	1.260	1.382	20.85
19	C	0.0254	20.0	9.91	20.23	0.837	1.085	1.333	20.50
20			19.5	9.14	21.33	0.812	1.047	1.282	21.61
21			17.0	8.64	22.19	0.794	1.020	1.246	22.48
22		0.0508	22.2	9.65	20.58	0.829	1.073	1.317	20.85
23			22.0	7.37	24.95	0.741	0.942	1.143	25.25
24			21.0	9.65	20.58	0.829	1.073	1.317	20.85
25		0.1016	23.3	9.40	20.94	0.821	1.060	1.300	21.21
26			19.3	6.86	26.38	0.716	0.907	1.097	26.67
27			20.7	6.86	26.38	0.716	0.907	1.097	26.67

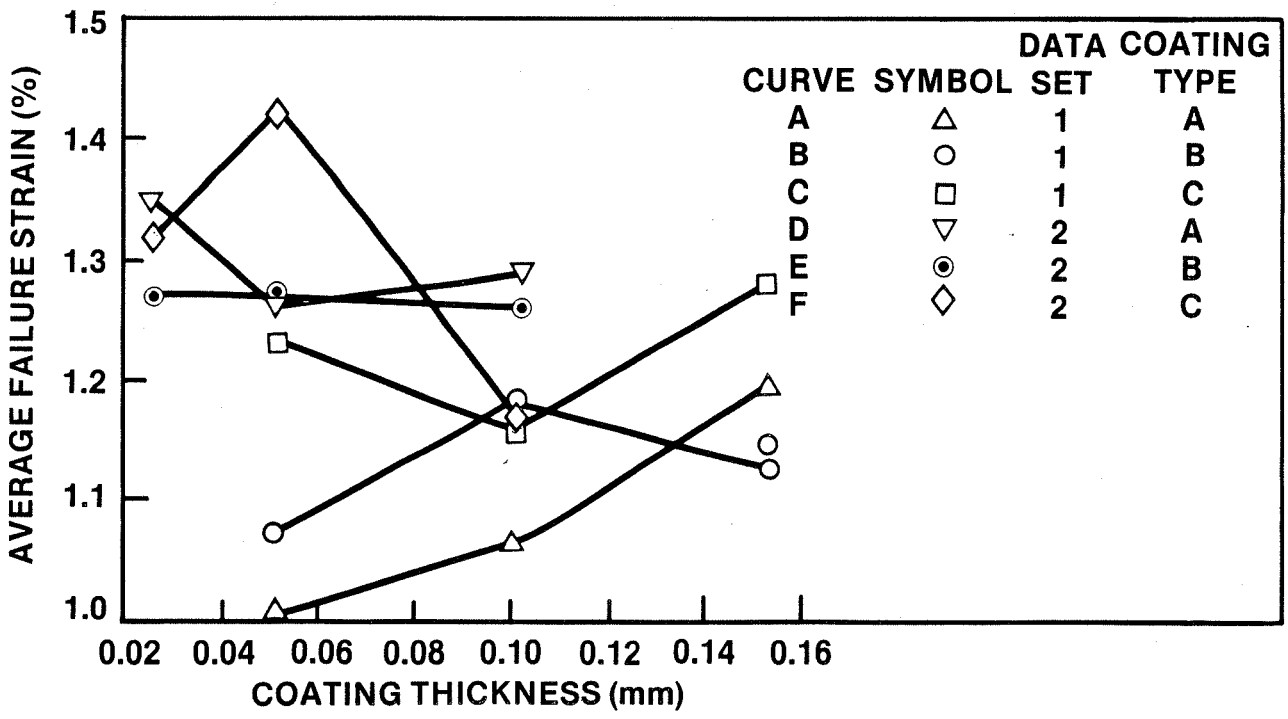

Figure 64. Coating strength Data From Four-Point Flexure Tests

The Student's t distributions may be used for inference about the mean of a sample group when (1) the population distribution is normal (or at least symmetrical and unimodal), (2) the population variance is unknown and estimated by the sample variance and (3) the sample is random. The latter two conditions are inherently met by the nature of the coating strength tests. However, the strengths of ceramics do not necessarily exhibit a normal distribution. Thus, condition (1) may not be satisfied. To determine how well the coating strength data generated in this study matched a normal distribution, a Chi-squared goodness-of-fit test (Ref. 9) was employed. A 95 percent confidence level was selected to evaluate the hypothesis that the coating strength samples were from a normal distribution. These tests indicated that the hypothesis could not be rejected for data set 2 and could be rejected for data set 1. The calculated value of Chi-squared for data set 2 was actually quite close to the rejection limit. Thus, little evidence of a normal distribution was detected through these analyses.

Despite this result, condition (1) may be reasonably satisfied by applying the central limit theorem. This theorem states that even if a population is not normal, the sampling distribution of averages for that population is approximately normal for a large number of samples (>30). The sampling distribution of averages is the probability distribution associated with the sample average ($\bar{y}$). This distribution consists of all possible values of $\bar{y}$, for a fixed sample size, and the probabilities associated with these values of the random variable.

In the case of the coating strength data generated for this program, only nine strength values per coating type, per data set, were obtained. Although

this does not meet the minimum sample size recommended to approximate a normal distribution, it was used for this analysis and this factor should be considered when evaluating the results. The three coating strengths measured for each coating thickness/type combination were averaged to create the data base for this analysis.

The null hypothesis used in these analyses was $H_0:\mu_d = 0$ and the alternative hypothesis was $H_a:\mu_d \neq 0$ in which μ_d is the population mean for the difference in strength between two coatings. This hypothesis was tested to compare pairs of coating strength data; three tests were required for each data set: A vs. B, A vs. C and B vs. C. The Student's t values were calculated as follows:

$$\bar{y}_d = y_d/n$$

$$s_d^2 = \frac{\varepsilon y_d^2 - (\varepsilon y_d)^2/n}{n - 1}$$

$$t = \frac{\bar{y}_d - \mu_{do}}{s_d/\sqrt{n}}$$

where n = number of pairs
y_d = strength difference
$\bar{y}_d$ = average strength difference
s_d = sample variance
μ_{do} = mean strength difference assumed by the null hypothesis

A confidence limit of 95 percent was used for these analyses. Thus, $\alpha = 0.05$ where α corresponds to the probability that t exceeds a corresponding value in the Student's t tables. The degree of freedom ($\gamma = n - 1$) for these tests was always 2. The t values are therefore $t_{0.025,2} = 4.303$ and $t_{0.975,2} = -4.303$. In summary, the probability that $-4.303 < t < 4.303$ if $\gamma = 2$ is 95 percent, assuming the null hypothesis is correct.

The coating strength data used in these analyses are shown in Table 15. The t statistics, and some of the intermediate calculated values, for these data are presented in Table 16.

Inspection of the calculated t statistics for data set 1 suggests the following:

- The strength of coating A is not significantly different from the strength of coating B.
- The strength of coating A is significantly different from the strength of coating C.
- The strength of coating B is not significantly different from the strength of coating C.

Table 15

Coating Strength Data for Statistical t-Test Analysis

Data Set Number	Thickness (mm)	Average Compressive Failure Strain (%)		
		Coating A	Coating B	Coating C
1	0.0508 0.1016 0.1524	1.005 1.066 1.198	1.073 1.181 1.128	1.234 1.160 1.281
2	0.0254 0.0508 0.1016	1.350 1.260 1.290	1.270 1.270 1.260	1.320 1.430 1.170

Table 16a

Matched Pair t-Test Calculations - Data Set 1

Thickness (mm)	A vs. B		A vs. C		B vs. C	
	Difference y_{d1}	(Difference)^2 y_{d1}^2	Difference y_{d2}	(Difference)^2 y_{d2}^2	Difference y_{d3}	(Difference)^2 y_{d3}^2
0.0508	-0.068	0.004624	-0.229	0.052441	-0.161	0.025921
0.1016	-0.115	0.013225	-0.094	0.008836	0.021	0.000441
0.1524	0.07	0.0049	-0.083	0.006889	-0.153	0.023409
$\sum$	-0.113	0.022749	-0.406	0.068166	-0.293	0.049771
Average difference $\bar{y}_d$	-0.0377		-0.1356		-0.09767	
(Sample variance)^2 s_d^2	-0.007779		0.00661		0.01058	
test statistic t	2.219		-8.649		-1.645	

Table 16b

Matched Pair t-Test Calculations - Data Set 2

Thickness (mm)	A vs. B		A vs. C		B vs. C	
	Difference y_{d1}	(Difference)^2 y_{d1}^2	Difference y_{d2}	(Difference)^2 y_{d2}^2	Difference y_{d3}	(Difference^2) y_{d3}^2
0.0254	0.08	0.0064	0.03	0.0009	-0.05	0.0025
0.0508	-0.01	0.0001	-0.17	0.0289	-0.16	0.0256
0.1016	0.03	0.0009	0.12	0.0144	0.09	0.0081
$\sum$	0.10	0.0074	-0.02	0.0442	-0.12	0.0362
Average difference $\bar{y}_d$	0.03333		-0.00667		-0.04	
(Sample variance)^2 s_d^2	0.00203		0.02203		0.00577	
test statistic t	1.281		-0.0778		-0.912	

These statistical conclusions can be interpreted to indicate that there is a strength difference among the three coating types. Since A and C are probably different, and B cannot be distinguished from either A or C, it can be assumed that B has a strength somewhere between A and C. Thus, these results suggest that there was an increase in coating strength associated with an increase in plasma spray power level for the coatings in data set 1.

Assuming that the conclusions made from the analysis of data set 1 are valid, a plot of average failure strain vs. power level was constructed; see Figure 65. Table 16 shows the pertinent data for this curve. This figure serves to illustrate the results of the data set 1 strength analysis and is not intended to be taken conclusively.

Inspection of the calculated t statistics for data set 2 suggest the following:

- The strength of coating A is not significantly different from the strength of coating B or C.
- The strength of coating B is not significantly different from the strength of coating A or C.

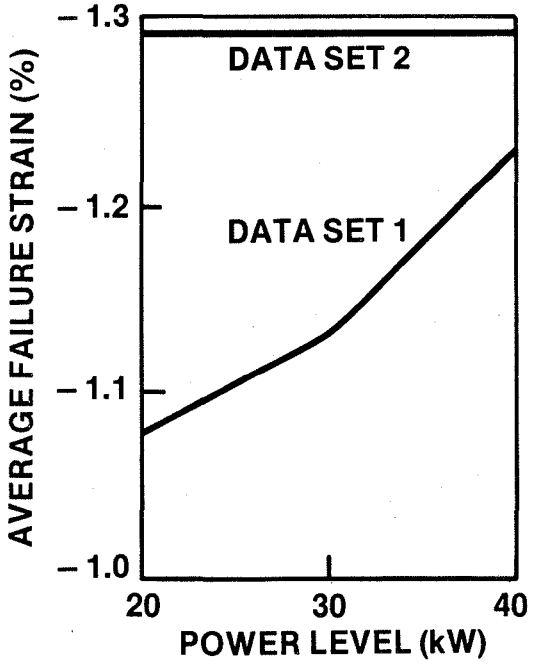

Figure 65.

Average Coating Failure Strain Versus Plasma Spray Power Level

These statistical conclusions indicate that there was no difference in strength among the three coating types in data set 2. This analysis suggests, therefore, that there was no effect of power level on the strengths of the coatings in data set 2. The average of all coating failure strains in data set 2 was calculated as -1.29 percent. This result was added to the data set 1 results in Table 17 and Figure 65.

The results of the strength data analyses for data sets 1 and 2 are basically inconsistent. Data set 1 indicates an effect of power level on coating strength whereas data set 2 does not. In addition, data set 2 shows a significantly greater coating strength than data set 1. These inconsistencies suggest that additional testing is required before any conclusions can be made about the true strength of these coatings or the effect of power level on coating strength.

If we assume that power level does not have an effect on coating strength, then each data set represents a characteristic strength distribution for the coating system tested. Although the difference in strength between each data set is obvious, it is currently unexplained. Thus, although each data set theoretically represents the same coating system, they will be evaluated separately, without assuming that either one is incorrect.

The strength data from data sets 1 and 2 were used to evaluate the probability of coating survival vs. coating strain. The coating strength data from each set was ranked according to value. The probability of survival (P_S) for each data point was then calculated from:

$$P_S = 1 - R/(N + 1) \qquad (26)$$

Table 17

Average Coating Strength as a Function of Plasma Spray Power Level

Data Set	Coating Type	Power Level (kW)	Average Failure Strain (%)	Range
1	A	20	-1.09	-0.952 to -1.226
	B	30	-1.13	-1.027 to -1.209
	C	40	-1.23	-1.073 to -1.427
2	A,B,C	20,30,40	-1.29	-1.170 to -1.430

where R is the rank of the strength value and N is the number of specimens in each set. This data is shown plotted in Figure 66. The difference in strengths between the two data sets is illustrated clearly in this figure.

Computerized regression analyses were used to fit fourth order polynominal equations to this data. These resulting equations are:

data set 1: $(r = 0.991)$

$$P_s = -83.2 + 272.1e - 319.0\, e^2 + 160.4e^3 - 29.3e^4 \quad (27)$$

data set 2: $(r = 0.989)$

$$P_s = 693.1 - 2331.1e + 2926.9e^2 - 1622.4e^3 + 334.7e^4 \quad (28)$$

where e is the strain in percent, and r is the correlation coefficient.

Other probability distributions were also evaluated for their applicability to the coating strength data. For example, the Weibull relationship (Ref. 8), which is often found applicable to ceramic strength data, was investigated. The Weibull relationship is:

$$\ell n \ell n\, [1/(1 - F)] = m\, \ell n\, (e/e_0) \quad (29)$$

where F is the probability of failure, m and e_0 are constants, and e is the failure strain. Thus, a plot of $\ell n \ell n\, [1/(1 - F)]$ vs. $\ell n(e)$ should yield a straight line if this relationship is valid. Figure 67 shows the strength data from data sets 1 and 2 plotted in this manner. Linear regression analyses were used to mathematically model the data. The resulting equations for the two data sets are:

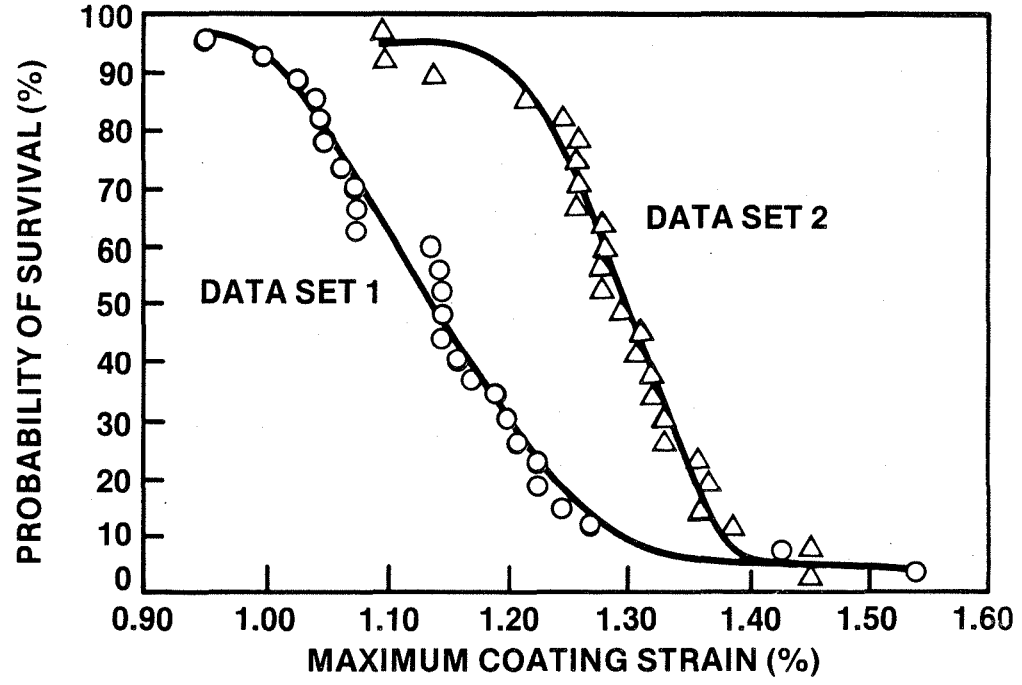

Figure 66. Survival Probablility Versus Coating Strain

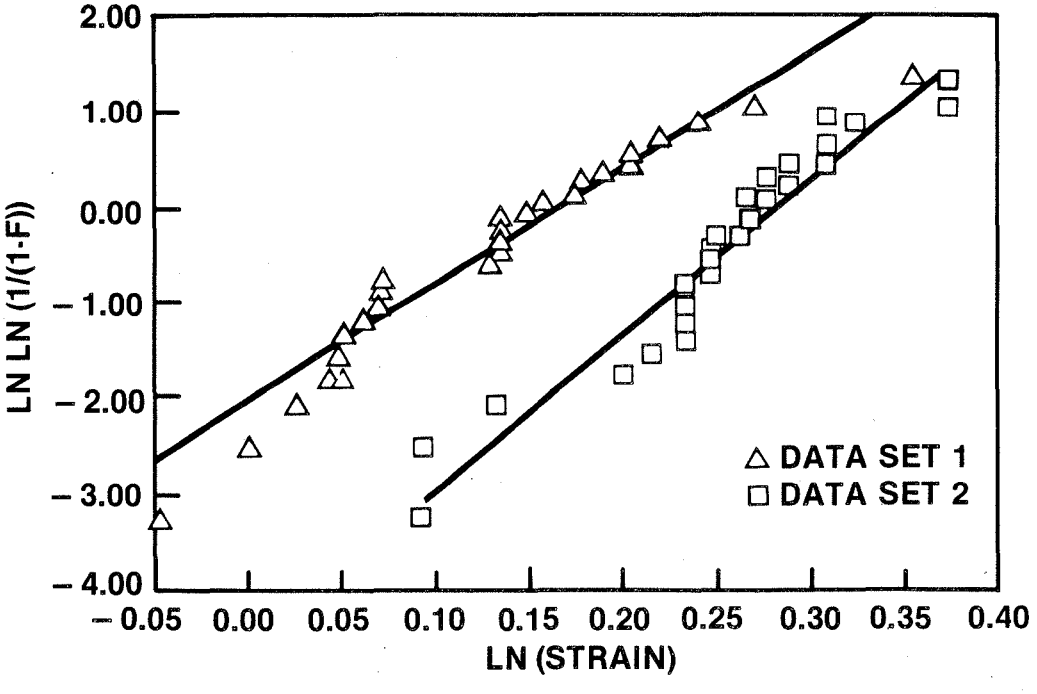

Figure 67. Coating Strength Weibull Plots

data set 1 ($r = 0.965$ $m = 12$)

$$\ell n \ell n(1/(1- F) = 12.12\ \ell n(e) - 2.075 \quad (30)$$

data set 2 ($r = 0.970$ $m = 16$)

$$\ell n \ell n\ (1\ /(1 - F) = 16.16\ \ell n(e) - 4.577 \quad (31)$$

where r is the correlation coefficient, and m is the slope of the curve (or the Weibull modulus).

Inspection of Figure 67 shows the marked difference in strength observed between data sets 1 and 2. There is also a slight difference in the slopes of the two curves. The slopes of these curves are referred to as the Weibull moduli ["m" in equation (29)]. A large value of m indicates a small spread in strength values. Therefore, Figure 67 indicates that data set 2 was not only stronger but also had a narrower strength distribution. This again may be attributed to subtle improvements in the coating application process between the two specimen sets.

The Weibull probability of failure plots have quite acceptable correlation coefficients. Also, the Weibull moduli calculated from this data are in the range of values quoted in the literature for many monolithic ceramics (m = 4 to 20). The significance of this has not been determined.

Either of the probability of failure distributions presented for coating strain can be used (graphically or mathematically) to predict coating reliability under specific operating conditions. Alternatively, the limiting operating conditions for a coating can be established for a desired survival probability. These analyses first require a thermomechanical model of the coating system, to calculate the strain in the coating. This strain can then be used to predict the probability of coating survival, using the probability distributions just presented.

3.4.2 Performance Analyses of Actual TBCs

Performance predictions for the thermal barrier coatings produced in this study were made using the thrust chamber model described earlier in this report. A range of steady state operating conditions was analyzed which included a variety of heat fluxes, temperature gradients and coating thicknesses. Measured material properties of the coatings were used; each coating type was unique in its value of thermal conductivity. An average thermal conductivity was used in some analyses, to predict the effects of other parameters.

Material properties other than the thermal conductivity of the coating were obtained from the literature. These properties are listed in Table 1. Since thermal conductivity is the only coating property of consequence for steady state thermal analyses, the thermal analyses of these coatings are expected to be quite accurate.

The structural analyses depend upon values for the coefficient of thermal expansion, Poisson's ratio and the elastic modulus. Although literature values were used for these properties, little discrepancy between the structural analytical results and the true behavior of these coatings is expected. The coefficients of thermal expansion measured in this study agreed well with the literature values, thus giving confidence in the use of the literature values in the analyses. The literature values were used because they were defined as functions of temperature whereas the measured values were obtained at a specific temperature. Furthermore, the use of the elastic modulus was often eliminated by evaluating coating strength in terms of strain. Thus, Poisson's ratio, which is of secondary importance, remains as the only material property of any uncertainty in the structural analyses. Future studies may focus on obtaining accurate measurements of this property, as well as better measurements of the other properties, to improve the overall coating model.

Three values of thermal conductivity were used for the coatings in these analyses: 0.60, 0.935 and 1.0 W/mC. These represent the highest and lowest measured values of the three coating types tested, and an average of the 30 and 40 kW coatings. This average was taken from the most consistent experimental data that was obtained.

The cold surface temperature for these analyses was 200°C, unless otherwise stated. This temperature was thought to be most representative of a steady state rocket engine operation. Some analyses were performed with a -20°C cold surface temperature.

Parametric coating systems analyses were conducted using four specific heat fluxes: 16, 49, 82 and 164 W/mm^2. These heat fluxes cover the range of values typically encountered in uncoated copper rocket thrust chamber walls, the highest value representing an extreme condition at the throat section. Applying a TBC will implement a reduction in heat flux through the wall, by increasing the operating wall surface temperature and thus decreasing the temperature difference between the gas and the wall.

A simple analysis indicates that this reduction in heat flux may be significant. For example, let us assume that the heat flux to the hot surface of the thrust chamber is due only to convection of the hot gases, and that the heat transfer coefficient and surface area are constant. Then, any change in the temperature difference between the gas and the hot surface will result in a proportional change in heat flux.

Let us assume that the hot gas temperature is 3000°C. Data from NASA indicates that the heat flux through a bare copper thrust chamber wall may reach 164 W/mm^2. Let us further assume that the surface of the copper wall reaches its melting point of 1100°C at this condition (extreme case). We can now calculate the expected heat flux through a coated thrust chamber wall operating with an acceptable surface temperature of 2000°C from

$$Q_c = Q_b (T_g - T_s)_c/(T_g - T_s)_b \qquad (32)$$

where Q = heat flux
T_g = gas temperature
T_s = surface temperature

and the subscripts c and b refer to the coated and bare thrust chamber walls, respectively. This calculation indicates that the heat flux through the coated wall may be only 53 percent of the heat flux through an uncoated wall, or 86 W/mm^2 at the maximum condition.

Based on this calculation, it is assumed that the heat flux value of 82 W/mm^2 used in these analyses is representative of the maximum actual heat flux in the throat section of a coated high pressure rocket thrust chamber. The lower heat flux values are expected to represent the non-throat sections of the coated wall, or part-load operating conditions. The analyses using a heat flux of 164 W/mm^2 are useful in establishing trends from the parametric study results.

Figure 68 shows the temperature profiles through a coating system having a 0.0254 mm TBC with average thermal conductivity, for two heat fluxes: 49 and 82 W/mm^2. These are medium and high heat flux values for a coated high pressure rocket thrust chamber. It is obvious that most of the temperature drop occurs across the TBC, subjecting the bond and substrate to a relatively small thermal gradient, as intended. As also expected, the thermal gradient through the coating is greater, and the surface temperature much higher, with the higher heat flux. The lower heat flux requires a surface temperature approximately equal to the maximum desirable ceramic temperature (~1900°C).

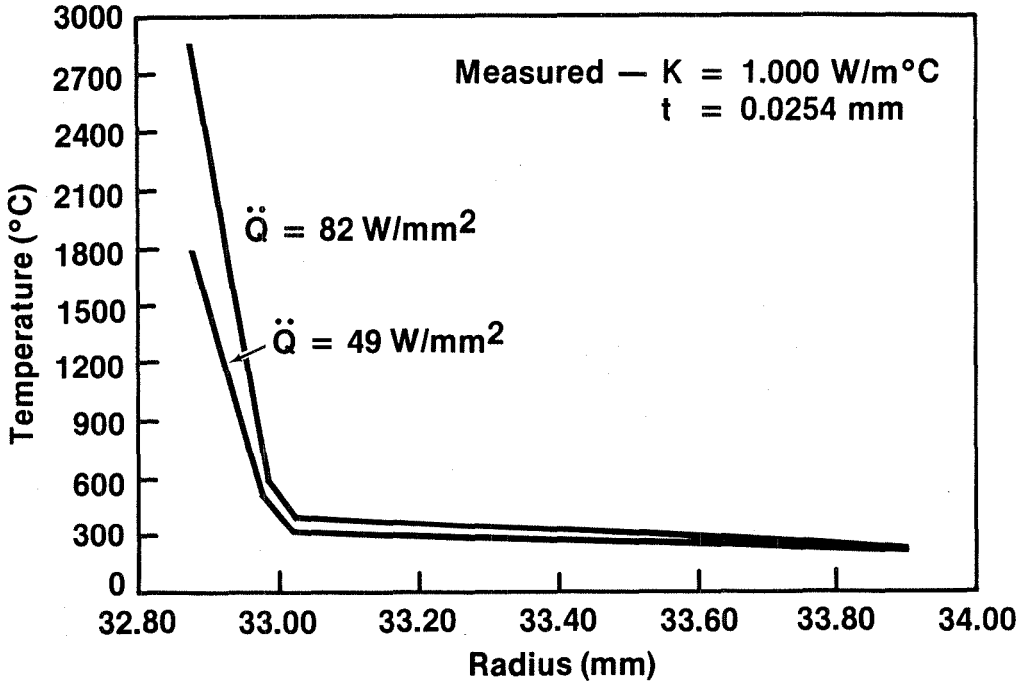

Figure 68. Predicted Coating Temperature Profile

Figure 69 shows the hoop (or axial) stress profile that results in this coating system from the imposed thermal gradients. These curves show the TBC and bond coat in compression and the substrate primarily in tension. The higher heat flux induces higher compressive stresses in the ceramic and higher tensile stresses in the substrate, than the lower heat flux. These differences are approximately proportional to the difference in temperature drop between the two cases. The magnitudes of the coating stresses are relatively high, on the order of 500 MPa. The significance of these stresses will be discussed later.

Figure 70 shows the radial stress profile through the same coating system. The magnitude of these stresses are quite small, (0-3 MPa), but are greatest in the copper substrate. Also, the effect of heat flux is most significant in the substrate, whereas the temperatures, hoop and axial stresses were most affected in the coating.

Figure 71 represents the temperature profiles through two coating systems having a 0.0254 mm TBC with different thermal conductivities: 0.6 and 1.0 W/mC. The heat flux through these coatings is 82 W/mm^2. The thermal gradient and surface temperature of the ceramic coating are much greater with the lower value of k. No difference was calculated in the thermal gradients of the bond and substrate between the two cases, and again, this thermal gradient is relatively small. In this case, both of the ceramic surface temperatures exceed the maximum desirable ceramic operating temperature.

Figure 72 shows the hoop (or axial) stress profiles through the same coating system. Again, the TBC is shown under significant compressive stress (500-800

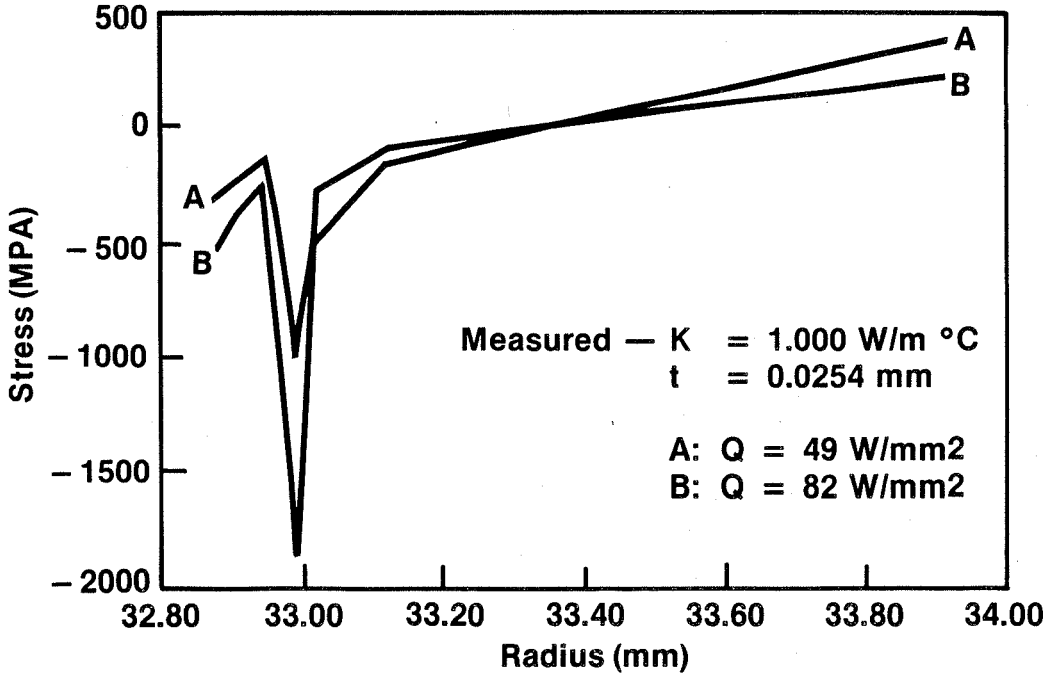

Figure 69. Predicted Hoop and Axial Coating Stress Profile

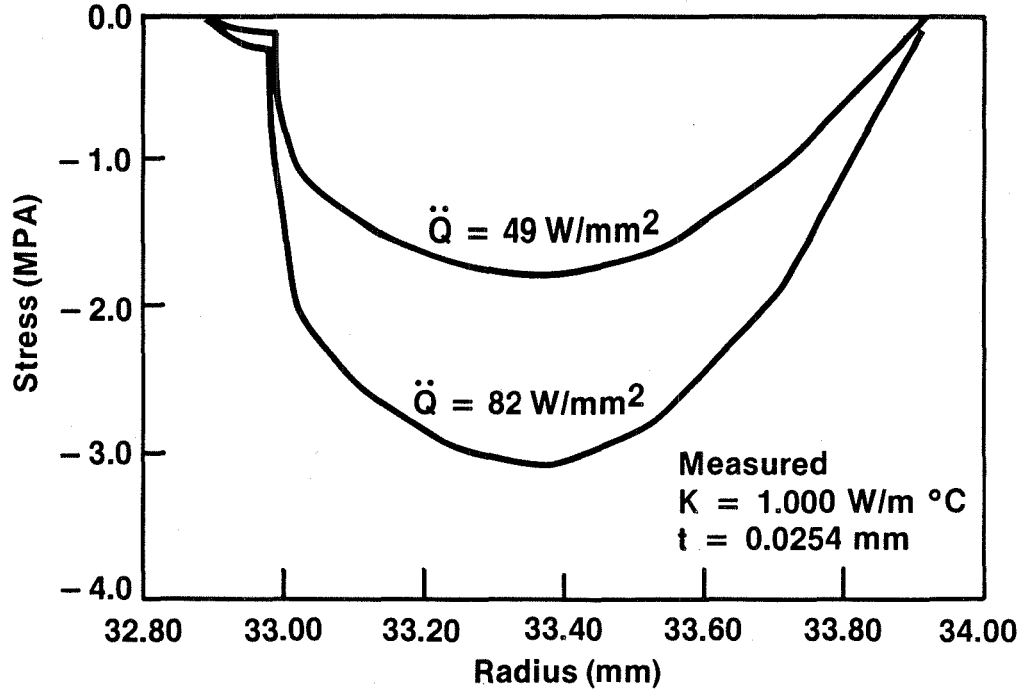

Figure 70. Predicted Radial Stress Profile Through Coating Using Average Measured Thermal Conductivity

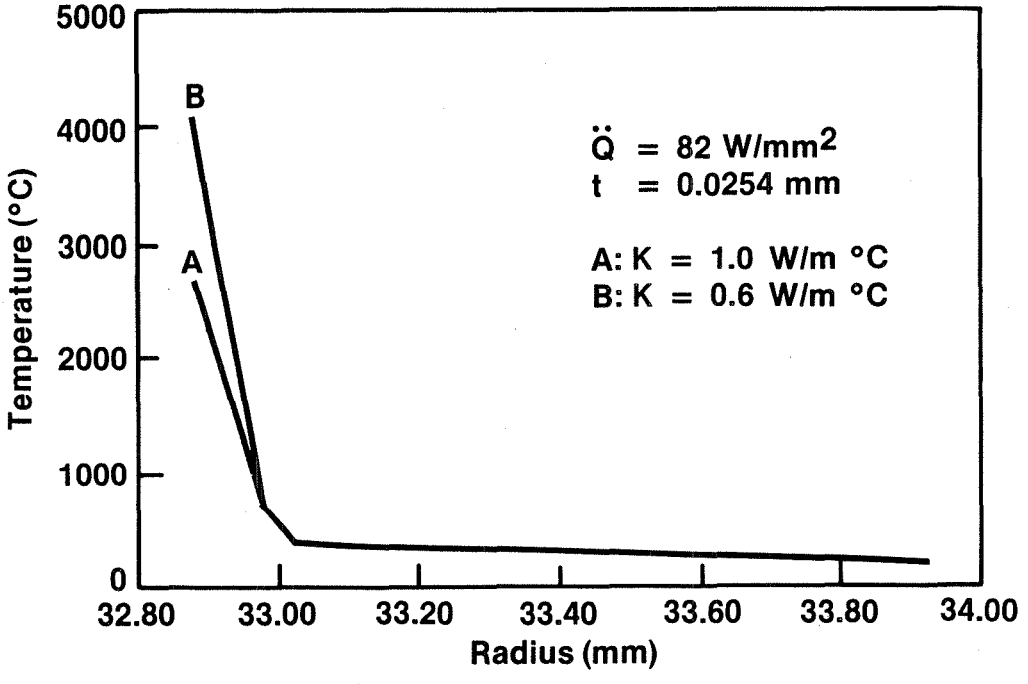

Figure 71. Coating Temperature Profile

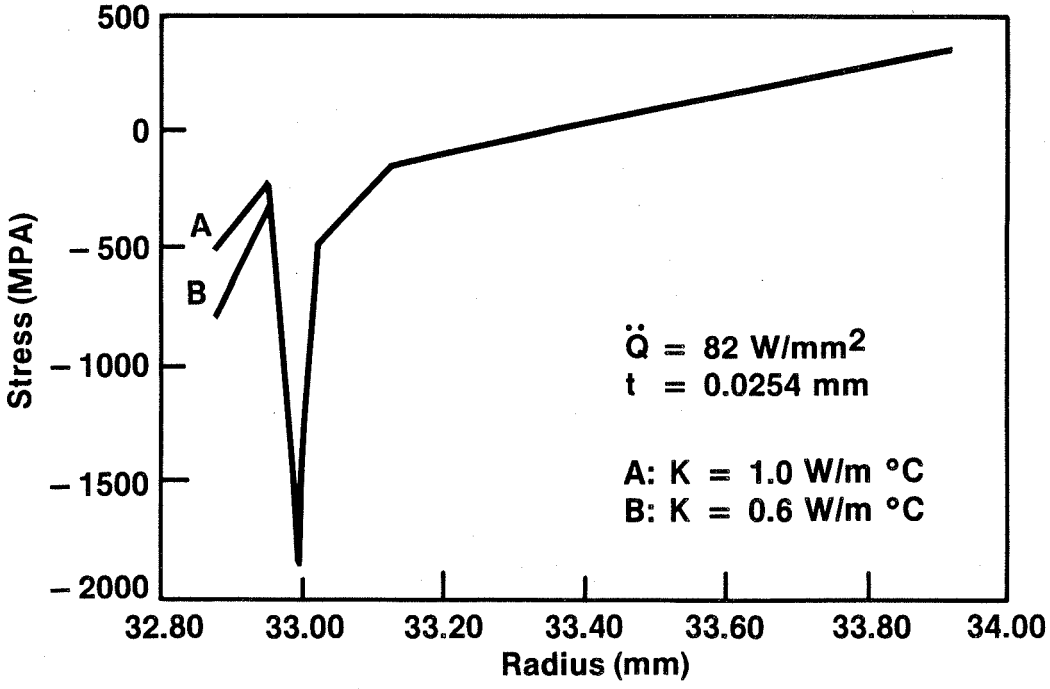

Figure 72. Hoop and Axial Coating Stress

MPa). The bond and some of the substrate are also in compression, while most of the substrate is in tension. The coating with higher thermal conductivity is seen to incur significantly less stress than the other coating, while the remainder of the coating systems stresses are identical.

These initial analyses indicated that a coating thickness of 0.0254 mm may be inadequate for very high heat flux conditions. Thus, a series of analyses were conducted to determine the effect of coating thickness on coating surface temperature at the maximum heat flux condition expected in a typical high pressure rocket thrust chamber: 82 W/mm^2. The results of these analyses are presented in Figure 73, for two values of coating thermal conductivity: 0.6 and 1.0 W/mC. A desirable maximum ceramic operating temperature is shown here as 1900°C.

Inspection of Figure 73 is very informative. This analysis demonstrates the importance of accurately knowing the thermal conductivity of a TBC and of the ability to accurately, and precisely, control coating thickness. For example, suppose that a 0.015 mm coating with k = 1.0 W/mC is specified for this high heat flux application, to operate at the limiting surface temperature. If the conductivity of the coating is actually 0.6 W/mC, the ceramic surface temperature must be increased to approximately 2600°C to accommodate the same heat flux.

Similarly, assume that a 0.009 mm coating with k = 0.6 W/mC is specified for this same application, again to operate at the limiting surface temperature. If a portion of this coating turns out to be 0.015 mm thick, the ceramic temperature may exceed the desired limit in that area if the heat flux is

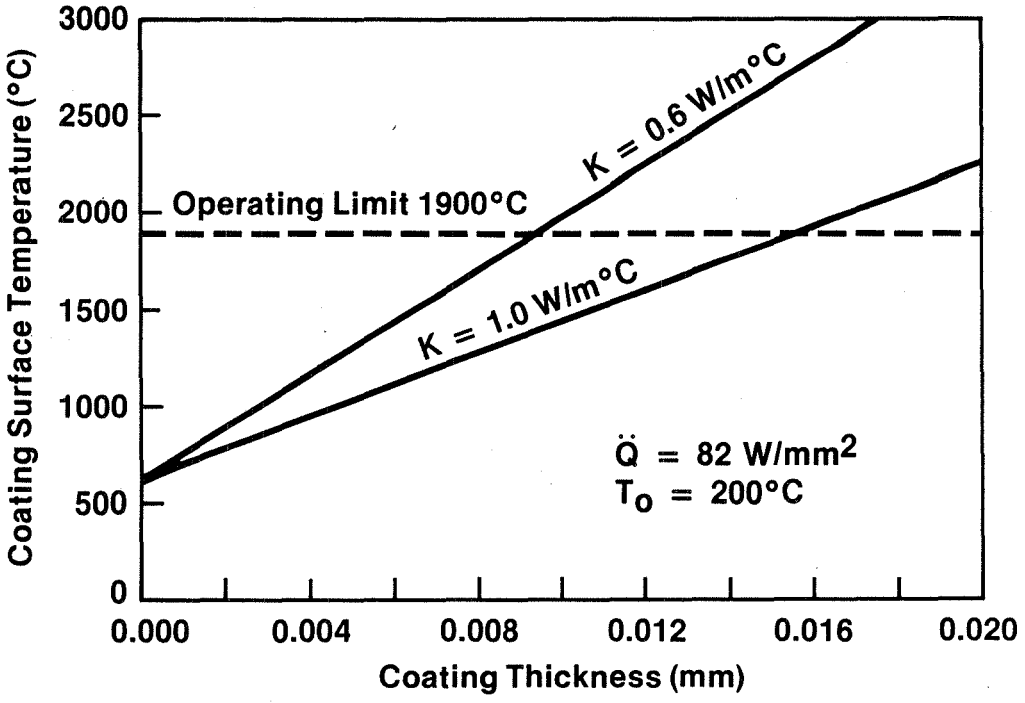

Figure 73. Effect of Coating Thickness on Surface Temperature for Fixed Heat Flux

maintained. The effect of thickness is seen to be more pronounced for the lower thermal conductivity coating, as its slope in Figure 73 is steeper than the other.

Figure 74 shows the effect of coating thickness on the maximum compressive coating strain in the TBC, for two coating thermal conductivities (0.6 and 1.0 W/mC) and a heat flux of 82 W/mm^2. Coating strain is seen to increase with coating thickness, and at a faster rate for the lower thermal conductivity coating. Again, the significance of thermal conductivity is demonstrated in this figure. For example, a 0.010 mm coating with k = 1.0 W/mC operating at this condition would experience a compressive strain of approximately 0.95%. If the coating actually had a conductivity of 0.6 W/mC, the coating strain would increase to 1.50%, for the same heat flux. Thus, coating strain may be significantly affected by thermal conductivity, with the effect being more pronounced at higher thicknesses.

Figures 73 and 74 demonstrate the sensitivity of coating performance to thickness and material property variations. Thickness variations are significant due to the thin values required for high heat flux applications. Thus, although the variation required to cause failure may amount to a 100% increase in coating thickness, the absolute value may only be on the order of 0.01 mm. Control of coating thickness to this degree may be very challenging. Also, thermal conductivity measurements made earlier were found to vary by up to 15%, for one particular coating type. This variation may have a significant effect on coating performance. The point to be made is that the acceptable operating conditions for a particular coating system may be signifi-

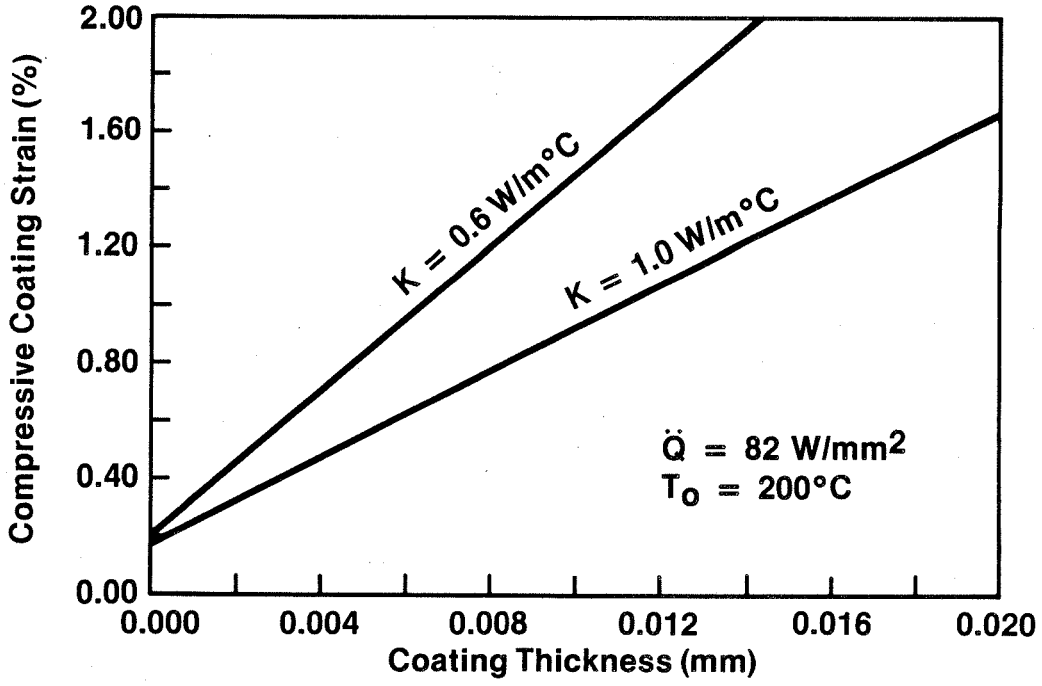

Figure 74. Effect of Coating Thickness on Maximum Compressive Coating Strain

cantly limited by the accuracy and precision of the coating application process.

The curves in Figures 73 and 74 were constructed for a specific heat flux. These curves are useful for preliminary coating system evaluations, if the heat flux is approximately correct. However, the true effect of TBC variations on coating performance requires an extended heat transfer analysis. For example, an increase in coating thickness will most likely cause a decrease in heat flux due to an increase in surface temperature. Thus, more detailed analyses are required to accurately evaluate a particular coating system for a specific application.

For example, a simple evaluation of the relationship between heat flux and coating thickness can be made as follows. Let us assume that the following parameters are constant: gas temperature (Tg), cold surface temperature (Tc), heat flow area (A), hot surface heat transfer coefficient (h), and the coating thermal conductivity (k). For a steady state thrust chamber condition, we can write:

$$Q/A = h(Tg - Ts) = k(Ts - Tc)/t \quad (33)$$

where t is the coating thickness.

Solving for t:

$$t = k(Ts - tc)/h(Tg - Ts) \quad (34)$$

If we let ta represent the actual coating thickness and td represent the design coating thickness, we can evaluate the effect of thickness variations on the coating surface temperature:

$$ta/td = (Ts_a - Tc)(Tg - Ts_d/(Ts_d - Tc)(Tg - Ts_a) \quad (35)$$

where the subscripts a and d represent actual and design conditions respectively. Assuming reasonable values for Tg (3000°C) and Tc (200°C) we can plot coating surface temperature versus normalized thickness (ta/td) for various design surface temperatures (see Fig. 75). Note that at a normalized thickness of 1.0, the actual coating surface temperature equals the design surface temperature. Actual surface temperature then increases non-linearly with coating thickness, rapidly at first, and gradually approaches a maximum value. It is interesting to note that coating surface temperature is especially sensitive to thickness variations around the design point.

Curves like those in Figure 75 can be used to select a nominal coating design thickness, based on a maximum allowable coating temperature and a probable thickness variation. By locating the point defined by (1) a normalized thickness based on the maximum possible coating thickness and (2) a maximum allowable coating temperature, one can define the coating design temperature and thus the nominal coating thickness. For example, if we select a maximum allowable coating temperature of 2000°C, and suspect the coating may be 100% thicker than the design thickness in some areas (Ta/Td = 2), then the coating should be designed for a surface temperature of approximately 1450°C.

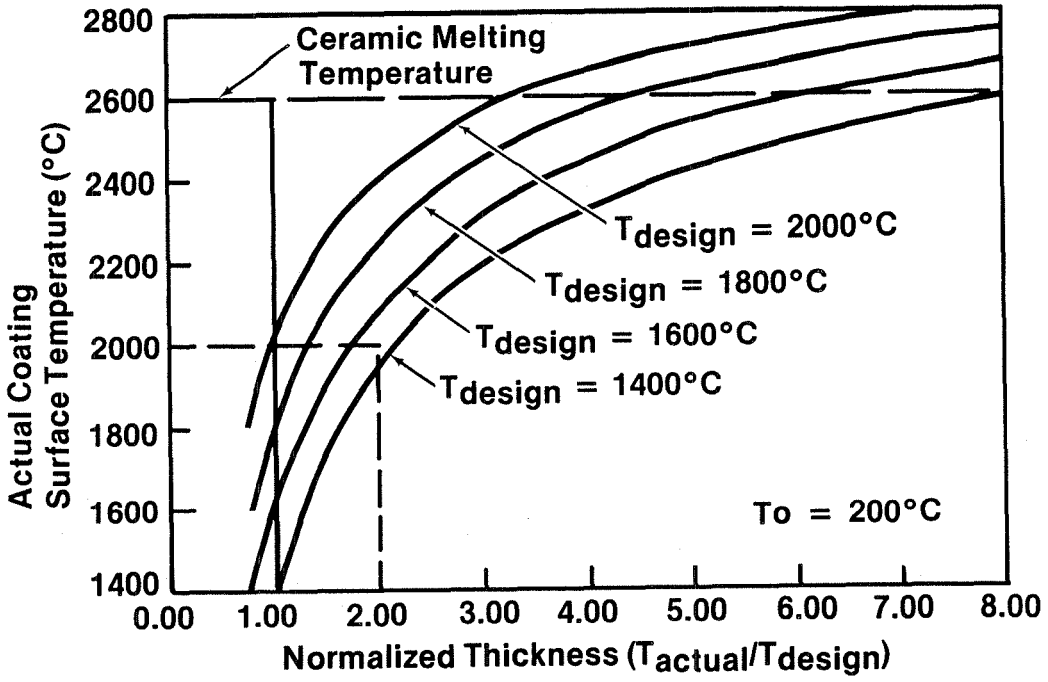

Figure 75. Effect of Thickness Variations on Surface Temperature

The analytical results shown in Figures 73 and 74 indicate that the TBC's under study must be very thin to survive the high heat fluxes anticipated in high pressure rocket engine thrust chambers. Figure 73 indicates that a coating thickness less than 0.015 mm is required to prevent surface melting at the highest heat flux evaluated. These analyses also indicate that the coatings under study are likely to fail structurally prior to melting. For example, Figure 73 shows that a 0.015 mm thick coating with k = 1.0 W/mC would operate at the maximum desirable surface temperature of 1900°C. However, Figure 74 shows that this coating would incur a compressive strain of approximately 1.30 percent at this condition. This strain corresponds to a 10 to 50 percent survival probability, depending on which strength data set is used in Figure 66.

Figure 76 shows the effect of coating thickness on surface temperature for a coating with an average thermal conductivity of 0.935 W/mC, over a range of heat fluxes. This effect is linear for a constant heat flux. This analysis demonstrates that surface temperature is much more sensitive to coating thickness changes at high heat fluxes, than at low heat fluxes. The heat fluxes shown in this figure cover the range of anticipated operating conditions for a typical high pressure thrust chamber application. Again, it can be seen that a very thin coating (less than 0.02 mm) is required to accommodate

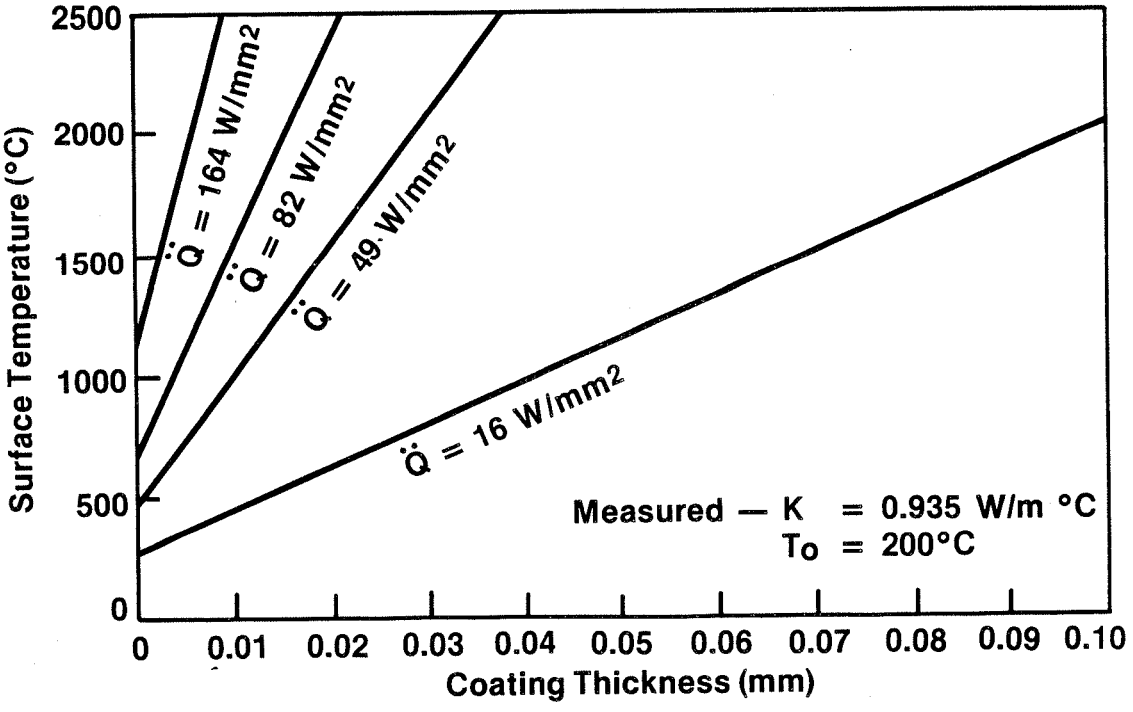

Figure 76. Coating Surface Temperature Versus Coating Thickness for Various Heat Fluxes Using Average Measured Thermal Conductivity

the high anticipated rocket engine heat fluxes (82 W/mm^2) without excessive surface temperatures (<2000°C) for this coating.

Figure 77 shows the effect of coating thickness on maximum compressive coating strain for the same conditions as just described. This effect is linear for a constant heat flux. Coating strain is most sensitive to coating thickness at the high heat flux conditions. At the highest anticipated rocket engine heat flux condition, 82 W/mm^2, the predicted coating strain is quite high compared to the survival probability curves shown in Figure 66. Coating thicknesses of this coating type which incur reasonable strains (say <1.0%)at this heat flux are quite thin (~0.01 mm).

Figure 78 shows the effect of coating thickness and thermal conductivity on heat flux for a specified ceramic surface temperature of 1927°C and a cold surface temperature of -18°C. This hot surface temperature is a desirable operating limit for the ceramic coating. Heat flux is inversely proportional to coating thickness and directly proportional to thermal conductivity. The heat flux values shown in this figure cover the range of heat fluxes expected in most rocket thrust chambers. The coating thicknesses required to maintain an acceptable surface temperature at the most severe rocket engine conditions are again quite small (<0.02 mm), even for the coating with the highest measured thermal conductivity.

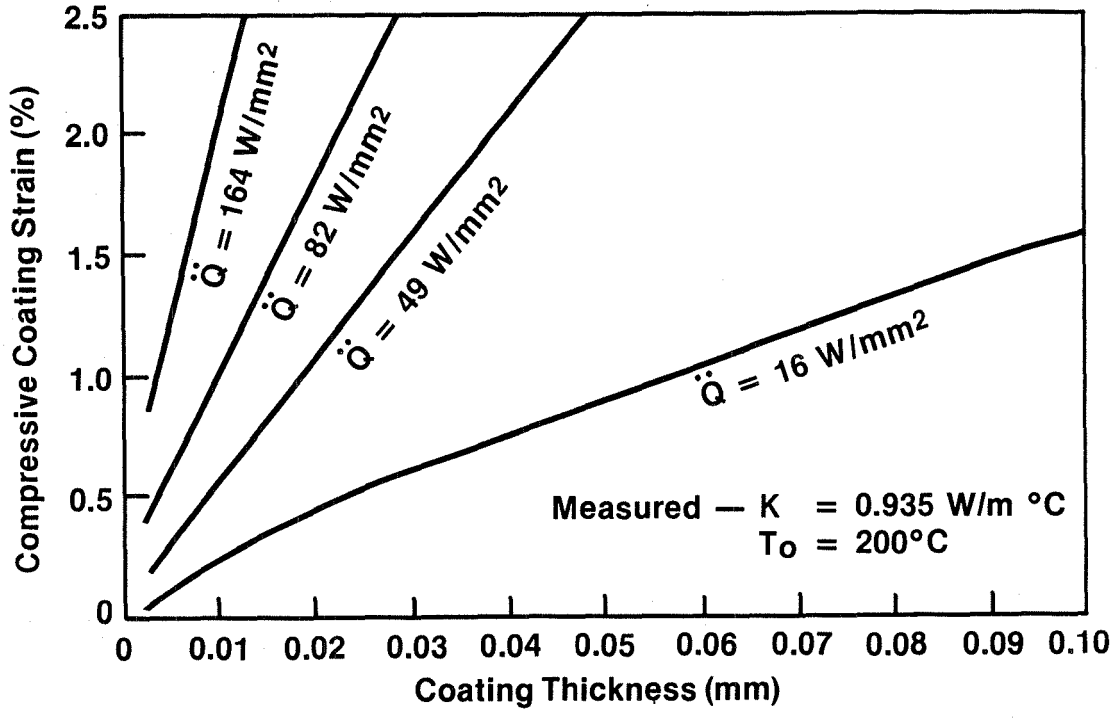

Figure 77. Coating Strain Versus Coating Thickness for Various Heat Fluxes

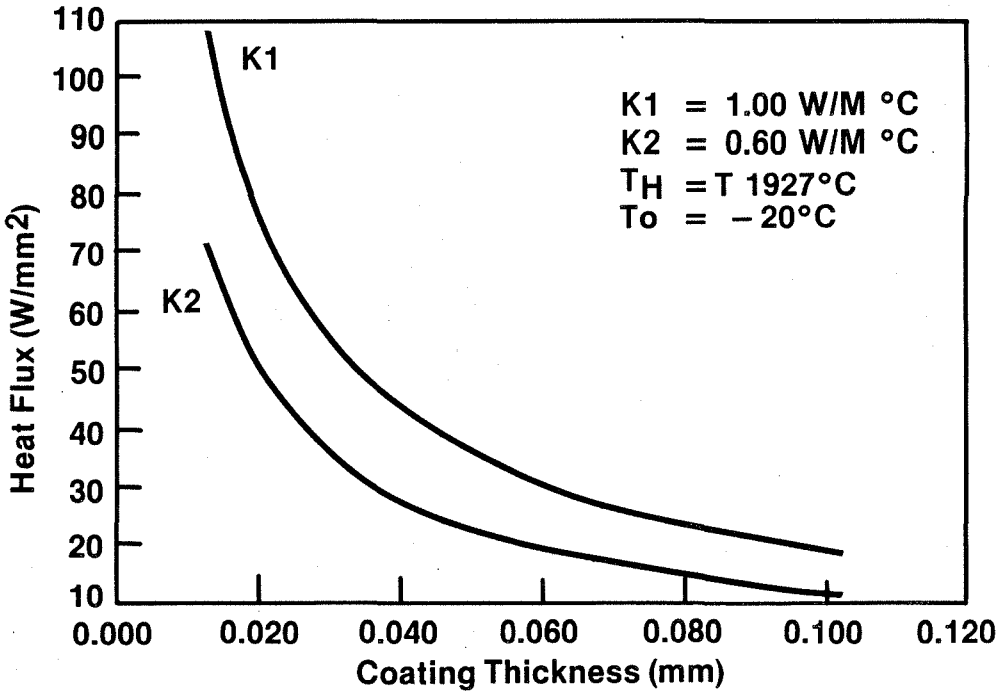

Figure 78. Heat Flux Versus Coating at Constant ΔT

Figure 79 shows the effect of coating thickness and temperature differential on the heat flux through a coating having an average measured thermal conductivity of 0.935 W/mc. The cold surface temperature for these analyses is -18°C. The ceramic surface temperature associated with the upper curve is 2200°C, which is greater than the desired maximum coating temperature, but less than the ceramic melting point. The lower curve represents a moderate ceramic surface temperature. Heat flux is inversely proportional to coating thickness and directly proportional to the temperature differential. The heat fluxes in this figure cover the range of values expected in the rocket engine thrust chambers. Again, the coating thicknesses required to accommodate the higher heat fluxes, even with an excessive ceramic temperature, under these conditions, is very small.

The performance curves presented in this section can be used to evaluate the general behavior of the TBC's produced in this study, under anticipated high pressure rocket thrust chamber operating conditions. These curves are also useful for demonstrating the effects of various parameters on coating performance. The analytical thrust chamber model can easily be used to evaluate a particular coating system under more specific operating conditions, and can be readily refined to incorporate more accurate material properties and/or boundary conditions as they become available.

3.4.3 Coating Design Technique

To illustrate an analytical coating design technique, the models described in this report were used to establish design criteria for the coatings produced

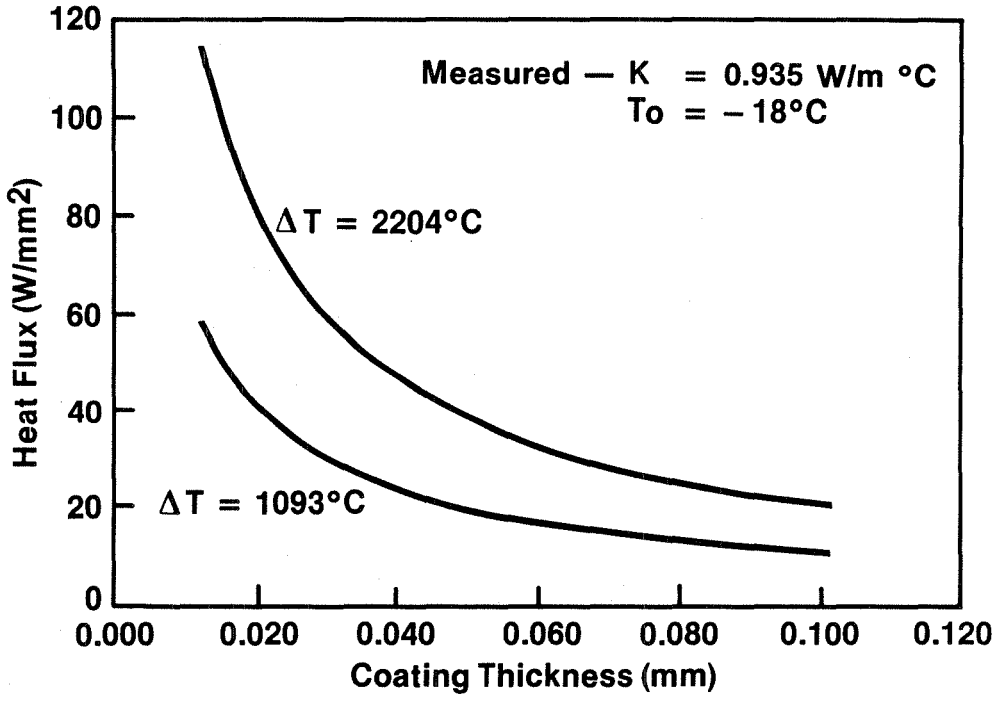

Figure 79. Heat Flux Versus Coating Thickness for Two ΔTs

in this study for rocket thrust chambers. These design criteria are essentially operating limitations and coating thickness limitations which must not be exceeded, to assure successful operation of the TBC. The physical limitations of the coating dictate the design criteria. The physical limitations considered for these analsyses were maximum compressive coating strain and maximum coating temperature.

The maximum allowable coating strain was established using Figure 66. Strength data from the first, and weaker, specimen set were used to evaluate the "worst" case. A survival probability of 95 percent was arbitrarily selected as a design criterion for the coating. Using the curve in Figure 66 for data set 1, a maximum allowable coating strain of one percent was established. A coating temperature limitation of 2000°C was also selected, based on information from the literature and past experience at Solar.

The coating system model of a rocket thrust chamber wall was used to evaluate the performance of the TBC's under steady state operating conditions. Various operating conditions, coating thicknesses and coating types were evaluated to define those combinations that cause excessive strain or temperature in the coating. A constant cold surface temperature of 200°C was maintained for these analyses and a range of heat fluxes was investigated.

Two coating types, A and C, were evaluated. These represent the 20 and 40 kW coatings respectively. For these analyses, the coating types were differentiated only by the thermal conductivity of the coating. It was assumed that both coating types reflect the same strength distribution.

It was found that coating strain, rather than temperature, was always the limiting factor in these analyses. The results are presented in Figure 80 which shows maximum allowable heat flux through the coating vs. coating thickness for the two coating types. These results corroborate past experience which indicates that thin coatings can tolerate greater heat fluxes than thick coatings, without failing. These analyses show the inverse relationship between maximum allowable heat flux and coating thickness.

It is again noted that the high heat fluxes anticipated in high presure rocket engines ($\sim$82 W/mm^2) require an extremely thin coating (<0.02 mm) for structural integrity. Also of interest is the significant effect that coating properties and coating thickness can have on the allowable heat flux for thin coatings.

3.4.4 Discussion of Analytical Results

Coating systems analyses were conducted to establish the performance characteristics and operating limitations of the TBCs produced in this study for high heat flux applications. The finite element model that was used in these analyses simulated the coated throat section of a thrust chamber, which experiences an extremely high heat load. Previous calibration of the finite element model, including an evaluation of the significance of element aspect

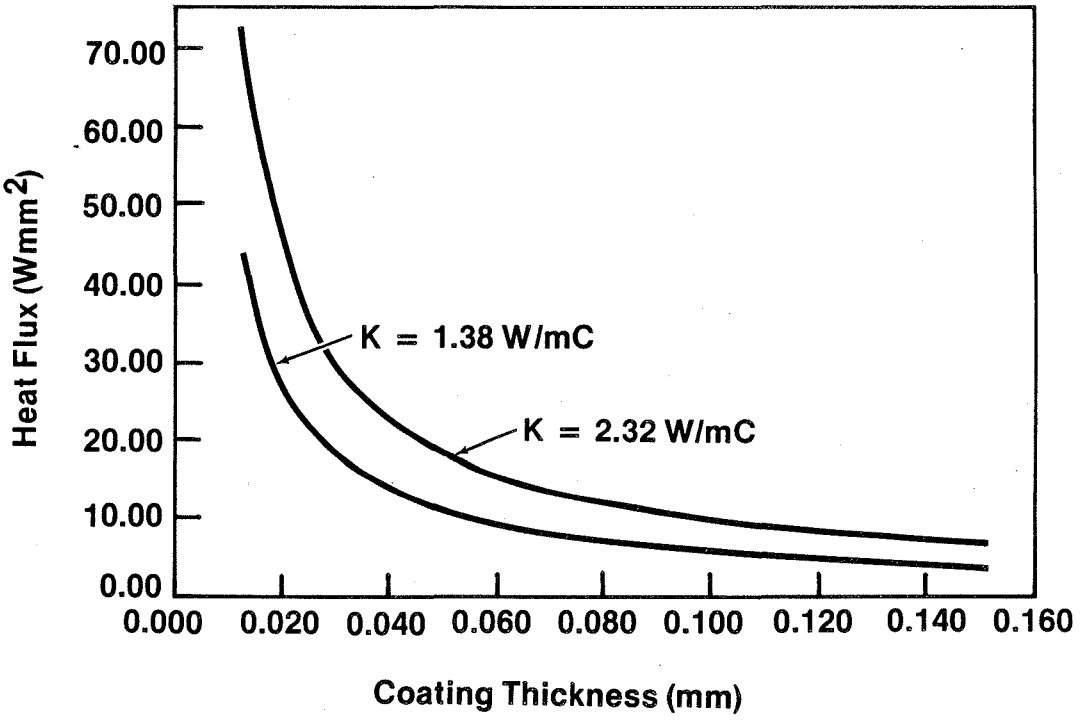

Figure 80. Maximum Heat Flux Versus Coating Thickness at 1% Strain

ratio, provides confidence that the model works properly. However, the accuracy of these results ultimately depends upon how closely the model simulates the actual coating system. This is determined largely by the accuracy of the geometry, boundary conditions and material properties.

The geometry of the finite element model is that of a cylinder. Although the actual thrust chamber throat is a curved surface, it is expected that the model geometry accurately represents a very small length at the middle of the throat, where the slope of the surface is parallel to the gas flow. The boundary conditions selected for these analyses covered ranges of anticipated operating conditions, based on the best information available from NASA. The most accurate material property data available were used in this model, and were specified as functions of temperature. The results of these analyses are therefore thought to be reasonably accurate.

These results suggest that the coatings evaluated in this study must be very thin to be practical for rocket thrust chamber applications. The thicknesses required to assure structural integrity at the high heat flux operating conditions are on the order of 0.010 mm. (This is based on the assumption that coating failure results from compressive thermal stress.)

Furthermore, it is obvious from these analyses that variations in coating thickness and material properties may significantly affect the performance of very thin coatings. Precise control over coating thickness and accurate knowledge of the coating properties may be essential to the successful operation of TBCs in high heat flux environments. Because of the thinness of these coatings, adequate control of the coating thickness may present a formidable challenge. Methods of accurately predicting coating material properties and precisely controlling coating thickness may each require a significant development effort.

Two basic approaches for making these coatings more compatible with the high pressure rocket thrust chamber requirements have been defined:

1. Develop a stronger coating to insure that surface temperature, rather than coating strain, is the primary limitation for heat flux. Then, by maintaining the lowest cold surface temperature practical, the heat flux through the coating can be maximized for a given coating thickness.

2. Develop a technique for controlling coating thermal conductivity. Then heat flux can be regulated within the material limitations of the coating system.

Both of these approaches require additional coating development work.

3.5 TEST THRUST CHAMBER COATING

A test thrust chamber is shown in Figure 81. This chamber has an inner diameter of 6.6 cm. Coating of this inner diameter required the use of different equipment than had been used in the previous program development

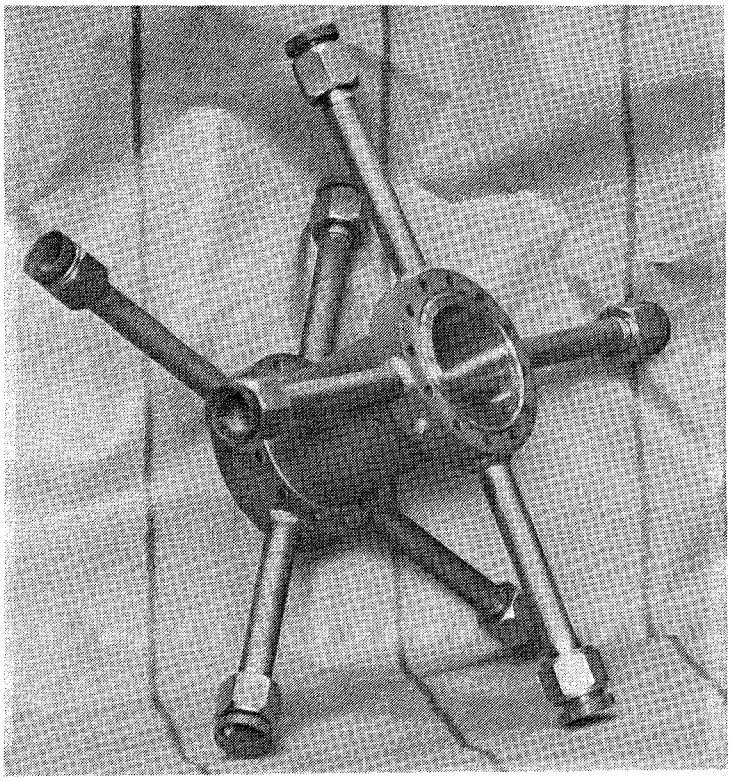

Figure 81. NASA Thrust Chamber for Test Coating

steps which employed a standard 7M gun configuration. The gun was changed to use a 7MBT-12 angle extension. The anode for this unit is designed to deflect the plasma gas at an angle of 45 degrees to the gun axis for coating the internal surfaces of small cylinders.

The equipment changeover required minor adjustments in the deposition process to achieve coatings equivalent to those initially established. Copper rings, 6.6 cm in diameter by 1.25 cm long, were fabricated from 0.81 mm copper sheet. The rings were mounted in a rotating fixture and the inner surfaces were coated. Forty-two rings were coated initially. Arbitrary adjustments to the gun parameters were made until coating appearance and deposit rates appeared similar to those obtained with the standard equipment. Initially, wide variations in coating quality were observed. These were traced to rapid anode wear. Normally these variations would not be significant when conventional coating thickness were being applied. However, the very thin coatings required for this application were sensitive to minor changes in gun characteristics. Anode usage was then limited to three hours.

Twenty-eight additional rings were then coated and metallurgically sectioned to further refine the coating process. The parametric variations are given in Table 18. These tests included minor adjustments to the spray parameters and thickness variations to verify consistent coating application.

Table 18

Specimen Definition in Final Ring Coating Tests

Ring Specimen	Volts-amps	Volts-amps	Thick (mil)		Gas flow (cfh)	
			Bond	Ceramic	Bond	Ceramic
43	65-500	70-600	1	4	60	80
44	65-500	55-400	1	4	60	50
46	65-500	55-400	1	4	60	50
47	70-600	70-600	1	4	80	80
48	70-600	70-600	1	4	100	80
49	70-600	55-400	2	4	80	50
50	70-600	65-500	2	4	80	60
51	70-600	65-500	2	4	80	60
52	70-600	65-500	1	0.5	80	60
53	70-600	65-500	1	0.5	80	60
54	70-600	65-500	1	0.5	80	60
55	70-600	65-500	1	1	80	60
56	70-600	65-500	1	1	80	60
57	70-600	65-500	1	1	80	60
58	70-600	65-500	1	2	80	60
59	70-600	65-500	1	2	80	60
60	70-600	65-500	1	2	80	60
61	70-600	N/A	1.5	N/A	70	N/A
62	70-600	70-600	1.5	1	70	80
63	70-600	70-600	1.5	0.5	70	80
64	70-600	70-600	1.5	2	70	80
65	70-600	70-600	1.5	4	70	80
66	60-500	N/A	1.5	N/A	70	N/A
67	70-600	70-600	1.5	0.5	70	80
68	70-600	70-600	1.5	1	70	80
69	70-600	70-600	1.5	2	70	80
70	70-600	70-600	1.5	4	70	80

The bond coat selected for these test chambers is shown in Figure 82. This bond coat was applied at 42 kW as indicated for ring #49 in Table 18. The ceramic applied to this ring was not considered to be suitable, so the ceramic coating parameters of ring 47, Figure 83, were selected for the 42 kW ceramic coating. Table 19 shows the parameters used to spray the cylindrical thrust chambers and the original flat test specimens.

The effect of increasing plasma gas flow and the bond coat can be seen by comparing Figure 82 and 83, both were applied at the same parameters except for plasma gas flow. The higher flow used for ring #47 caused overheating and oxidation of the substrate and poor deposition of the NiCrAlY. However, for the zirconia coating it was found necessary to use a higher power level and gas flow to achieve the desired coating structure. The coating applied at 32 kW with a lower gas flow had a nonuniform structure with numerous large voids.

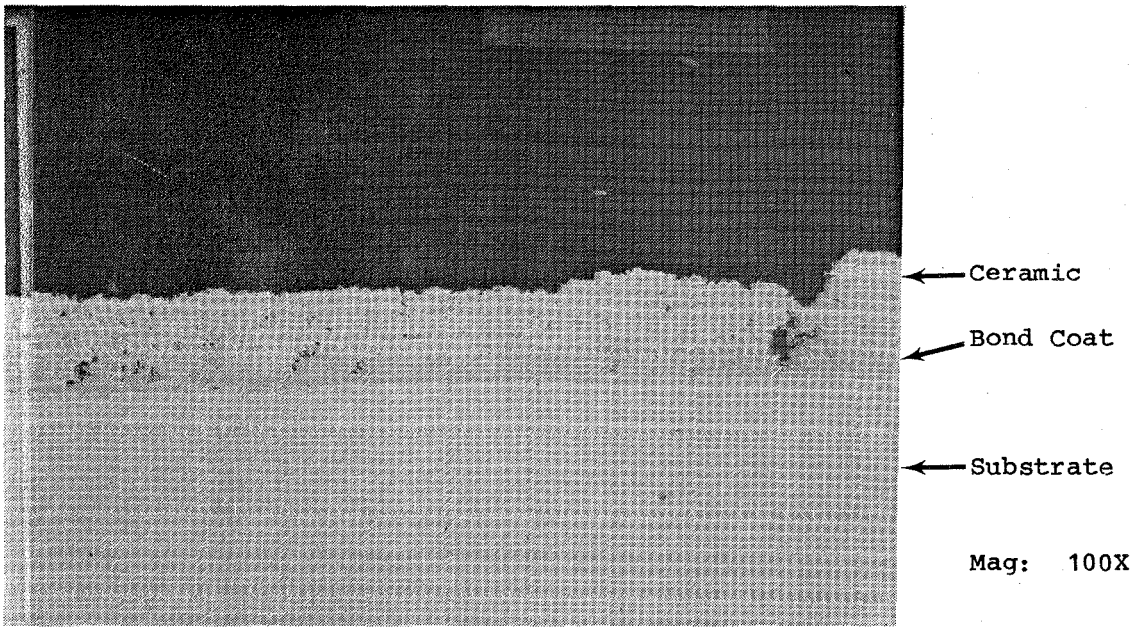

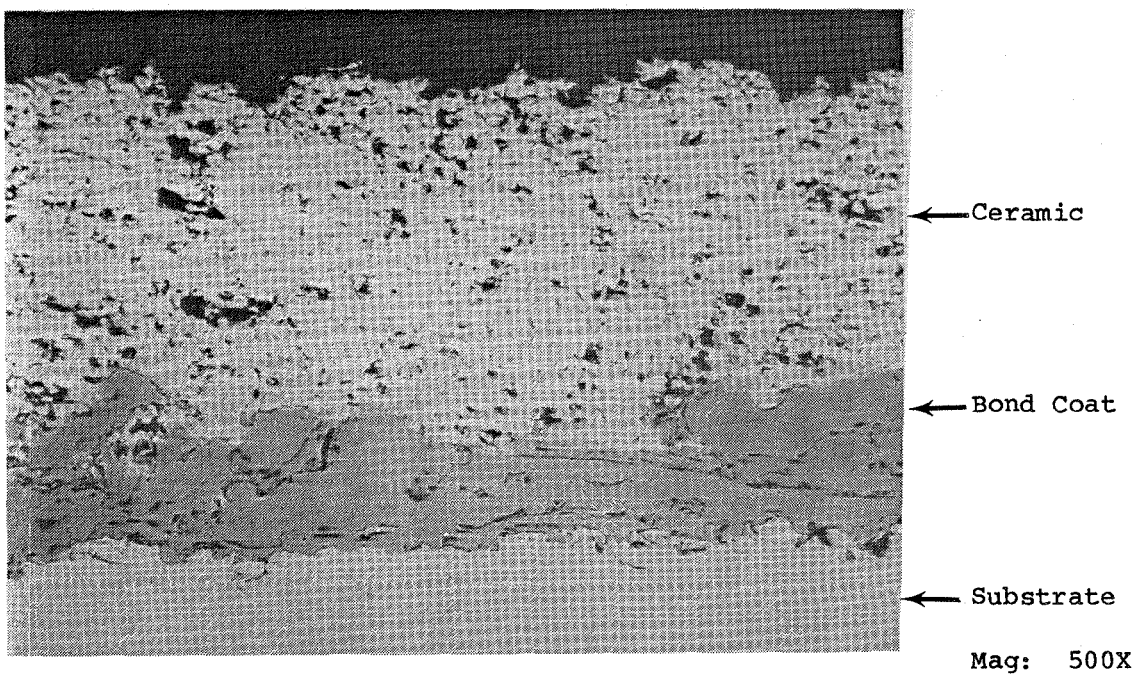

Figure 82. Photomicrographs of 42 kW Bond Coat (Ring 49)

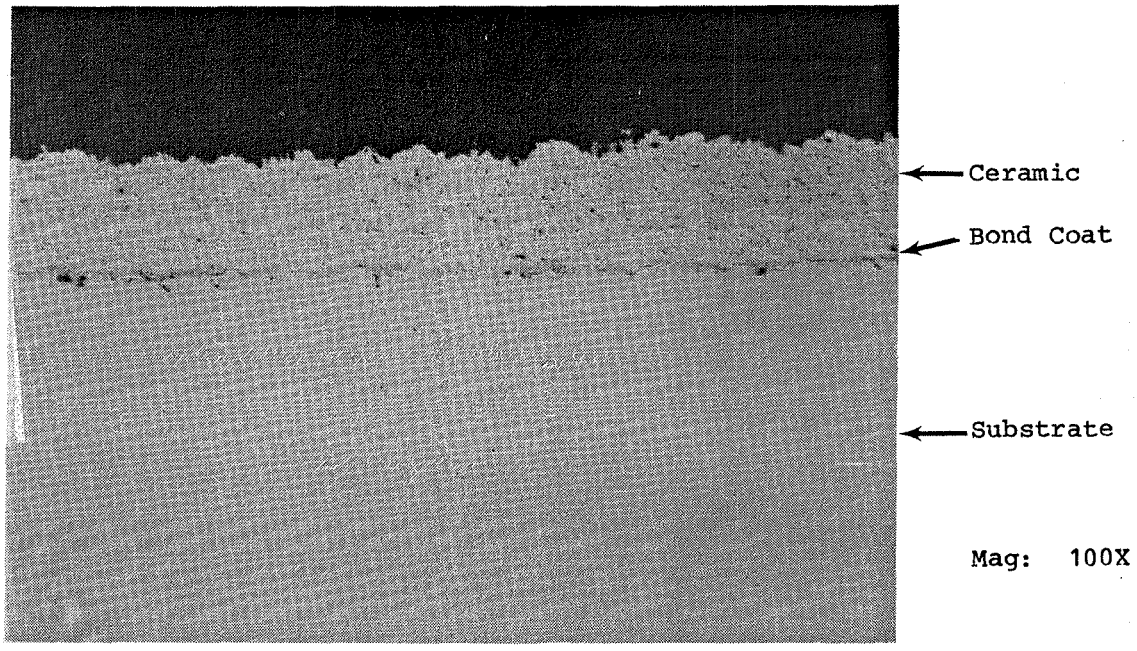

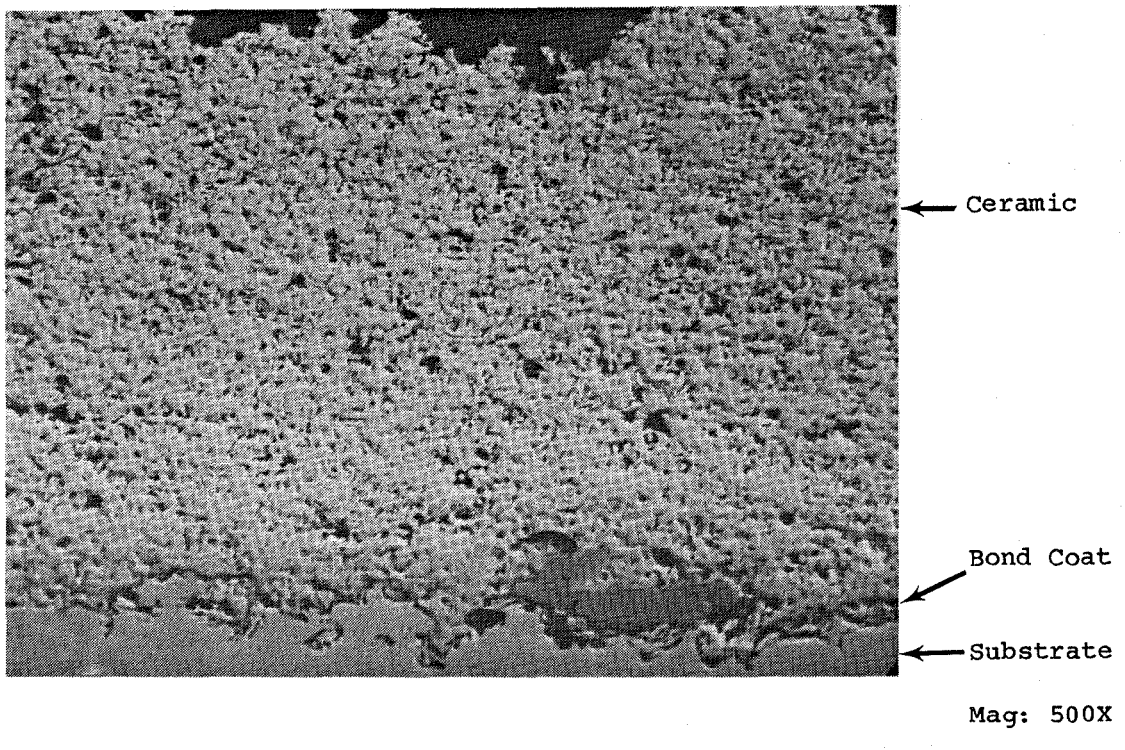

Figure 83. Photomicrograph of 42 kW Zirconia-8% Yttria Coating for Ring 47

Table 19

Plasma Spray Parameters for Flat and Ring Specimens

	Flat Ceramic Coating #1	Flat Ceramic Coating #2	Flat Ceramic Coating #3	Flat Bond Coat	Ring Ceramic Coating	Ring Bond Coating
Current (amps)	400	500	600	500	600	600
Voltage (volts)	50	65	70	65	70	70
Power (kW)	20	32	42	32	42	42
Argon (m^3/hr)	2.97	2.97	4.25	5.66	2.27	2.27
Hydrogen (m^3/hr)	0.085	0.14	0.20	0.11	0.425	0.453
Stand-Off (cm)	6.4	6.4	6.4	6.4	3.18	3.18
Plasma Velocity (m/s)	25.4	30.5	43.7	32.5	--	--
Power Port	No. 2	No. 2	No. 3	No. 2	No. 2	No. 2
Cooling Air (kPa)	551	551	551	551	538	538
Nozzle	GH	GH	703	GH	713	713

Having selected the specific parameters for coating the thrust chamber, a fixture was constructed for rotating and cooling the chamber during coating application. The set-up is shown in Figures 84 and 85. A standoff support was constructed to allow the plasma gun to exit from the chamber at each end of every traverse. This platform was then mounted on the end of a hollow shaft. Cooling air for the chamber was introduced into the hollow shaft through radial holes and a concentric manifold. This air was then introduced into the chamber fuel passages through tubing connected to the fuel lines, and used to cool the substrate during coating. A collector ring, not shown in the photographs, was added to catch the cooling air and direct it over a thermocouple for monitoring cooling air temperature during coating. The entire unit was then coupled to a variable speed drive for rotation during spraying. Rotational speed was 73.5 rpm which produced a surface speed of 15.2 m/min.

The first cylinder was coated to a nominal ceramic coating thickness of 0.025 mm. Telatemp Recorders (Telatemp, Fullertin, CA) were usd to determine the maximum substrate temperature during coating. A concentric flange with a 6.3 mm wall was attached to the end of the cylinder for metallurgical sectioning after coating. The cylinder was coated and a section made of the test specimen. It was found that the coating shown in Figure 86, was unacceptable. The directional effects of the 45 degree extension gun are evident. The coating section shows a shadowing effect from the initial particles much like a snow fence with inconsistent voids and uncoated areas. To prevent this, it was decided to reverse the cylinder with respect to gun traverse to provide a more uniform coating buildup. The effect of this on the ceramic phase is evident in Figure 87 with a uniform deposit of zirconia on each side of the bond coat projections. Backside cooling of the substrate was inadvertently reduced during this test and substrate overheating resulted in excessive oxidation and poor adherence.

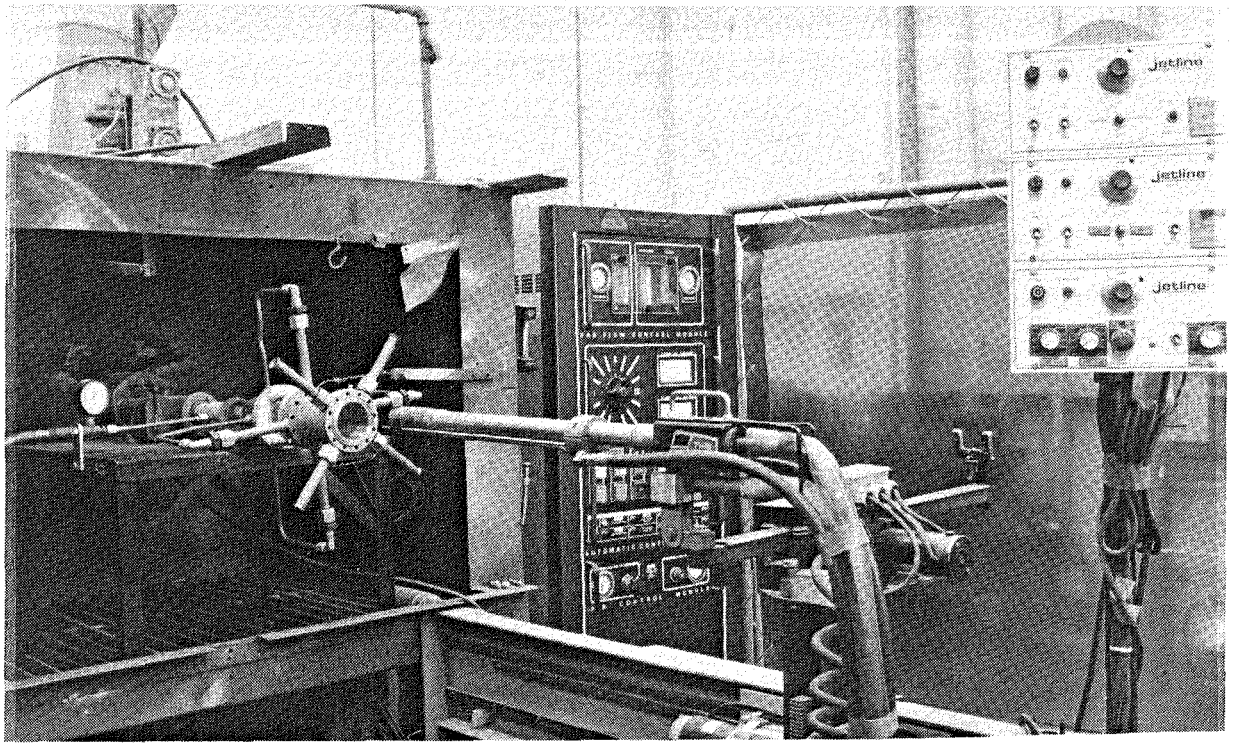

Figure 84. Overall Thrust Chamber Coating Set-Up

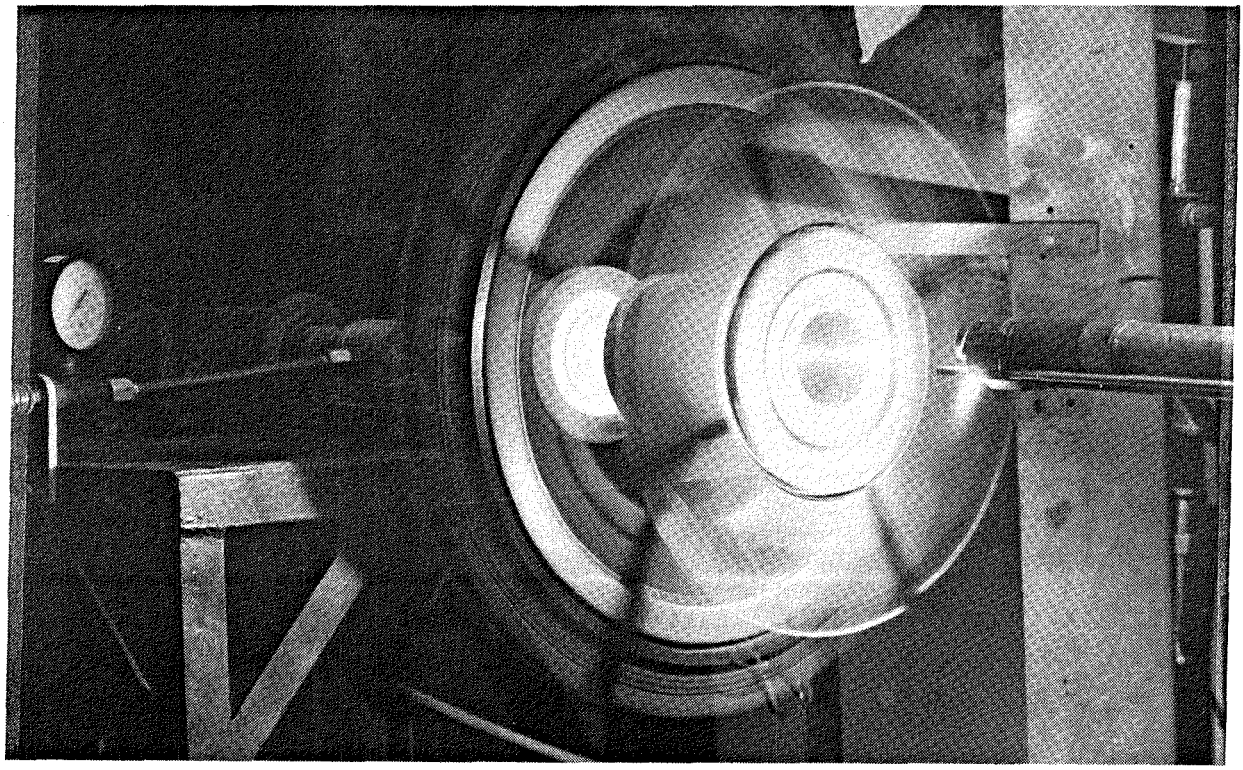

Figure 85. Coating Thrust Chamber

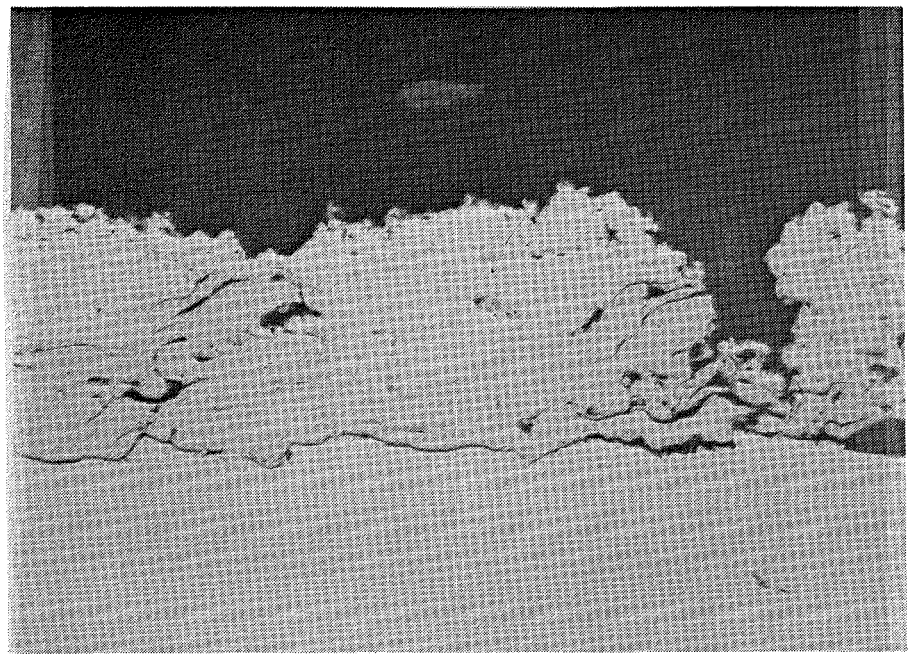

(Magnification: 500X)

Figure 86. First Coating Applied to a Thrust Chamber With a 7MBT Extension

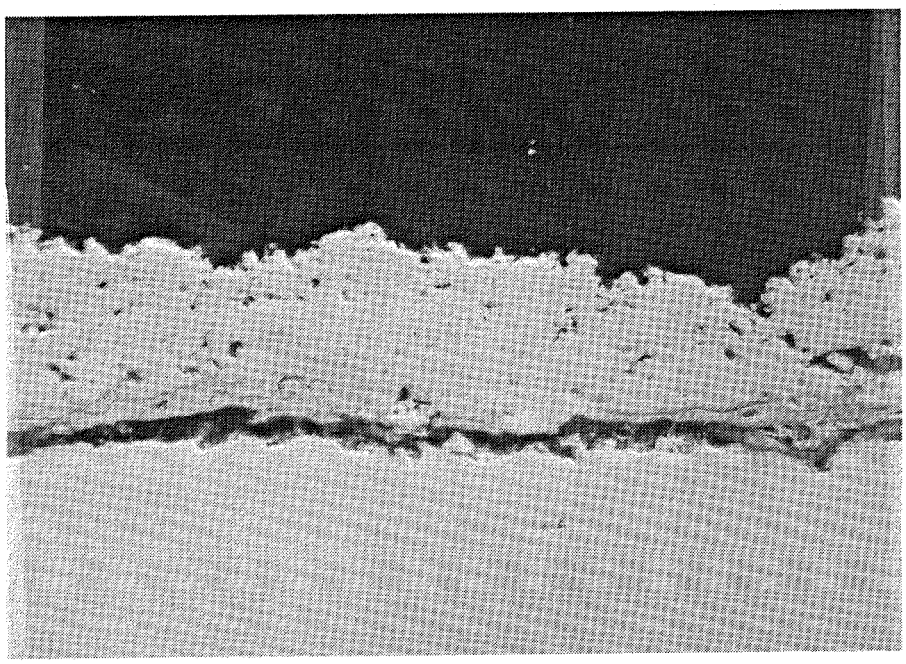

(Mgnification: 500X)

Figure 87. Coating Applied With Periodic Reversing of Cylinder

The initial cylinder was stripped and recoated with cyclic reversal. The maximum temperature of the unit was found to be 121°C using the data from the Telatemp recorders. A test section showed the coating thickness to be between 0.019 and 0.025 mm which is within the error expected for a nominal 0.025 mm coating.

The second cylinder was coated in the same manner to a nominal ceramic coating thickness of 0.013 mm. This coating thickness was found to range between 0.013 mm and 0.019 mm with the majority of the coating being close to the lower limit. This coating closely followed the contours of the bond coating without the leveling effects of the thicker coatings (see Fig. 88). It is expected that this might create a heat transfer problem in the anticipated service environment.

The third cylinder was coated to a thickness of 0.076 mm in the same manner as the previous two. No significant change in coating characteristics was observed. The fourth cylinder was coated to a thickness of 0.025 mm. This coating appeared to be slightly more porous than the previous specimens, but in the thin coating no quantitative differentiation could be made.

The change from flat specimens and rings, used for initial studies, to a small diameter cylinder introduced variations in the coating procedure. The limited access prevented using gun standoff as a process parameter and required adopting previously developed parameters in a new gun configuration. Also, parameters developed for gun power levels at significantly higher values than 40 kW could not be used.

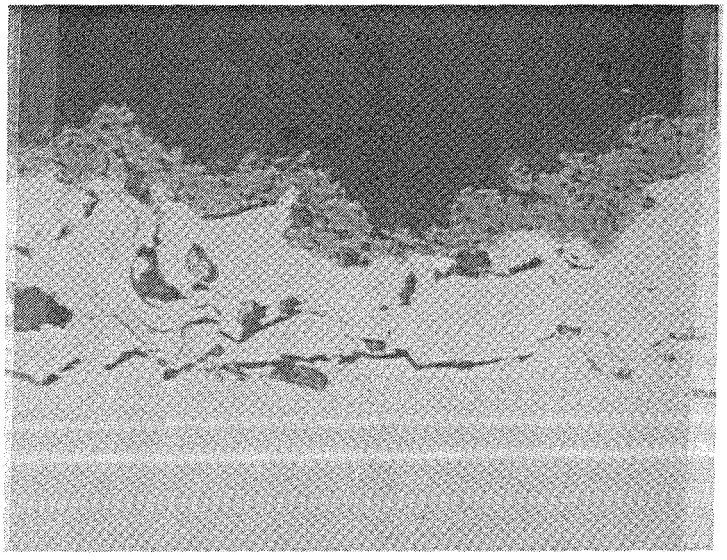

(Magnification: 500X)

Figure 88. Coating Applied to a Planned Thickness of 0.013 mm

In practice, the coating power levels developed for the ceramic coating proved to be effective. It was necessary to adjust powder and plasma gas flow to provide a duplicate zirconia coating. Applying a reliable NiCrAlY bond coat was less successful and this process needs to be improved. The gases entrapped in the cylinder during spraying reacted to minor disturbances and unmelted oxidized particles were entrapped in the bond coat, preventing proper adherance. Bonding of the NiCrAlY to the copper substrate was not fully reliable and no nondestructive test was found. Throughout the cylinder coating tests this bond was found to be the weak point of the system and generated several problems in reliability that have not yet been resolved.

Four additional test chambers were coated at a later date. These coatings were applied with several process modifications to reduce substrate oxidation. The modifications consisted of improved substrate cooling, inert gas injection at the plasma gun tip, increased powder feed to reduce the time required to apply the bond coat, and improved substrate surface preparation using a larger grit size.

All of the coated test chambers are more fully documented in a separate lab report issued to the NASA program manager: Solar Report No. SR85-R-2151-00 (01/31/85).

4

CONCLUSIONS

1. A practical analytical model of a TBC has been developed. This model combines empirical material property data with finite element analyses to predict the performance of the coating in service. This model can be used to evaluate the effect of coating deposition parameters on coating performance by first determining the effect of these parameters on the coating properties.

2. An analytical model of a porous coating structure was partially developed. This model requires additional development but appears to have potential for ultimately correlating coating thermal conductivity with deposition parameters.

3. Theoretical models of mixtures appear to have potential for predicting the thermal conductivities of TBC's. These models require empirical adjustment but may provide an accurate and practical method of calculating coating thermal conductivity as a function of porosity.

4. A practical method of testing coating strength has been developed. The four point flexure tests provide a simple and economical method of measuring coating strengths. Plastic deformation of the copper substrate causes complications in the strain analyses and contributes to the experimental error of the measurements. Due to the statistical nature of ceramic strengths, sets of 30 specimens are recommended per test to obtain reliable results.

5. A convenient method of utilizing the coating strength data is to establish a failure probability distribution for each coating type. Comparison of strength distributions can reveal differences between coating types. These failure probabilities can be used to statistically predict coating failure.

6. The coating stregth data generated in this study produced conflicting results. Two sets of data were generated at different times. The second set showed a significant increase in strength and a narrower strength distribution. Also, the first data set indicated an effect of plasma gun power level on coating strength whereas the second set did not. No conclusions are drawn as to the effect of power level or about the true strength of these coatings.

7. Performance analyses of the coatings produced in this study indicate that extremely thin (<0.02 mm) coatings may be required to operate reliably in the high heat flux environment of a high pressure rocket thrust chamber.

8. These performance analyses indicate that structural failure is likely to occur before the coating melts, for the coatings evaluated.

9. Two methods of improving the applicability of these coatings to rocket thrust chamber applications are (1) increase coating strength so that surface temperature becomes the limiting factor rather than strain and (2) increase the thermal conductivity of the coating to accommodate higher heat fluxes.

10. These analyses have demonstrated that coating performance is extremely sensitive to coating thickness and thermal conductivity at the very high heat flux conditions. The need for very accurate knowledge of the coating properties and precise control of the coating thickness is apparent at these high heat fluxes.

11. A practical coating design technique has been demonstrated. This technique uses the coating performance model to calculate the maximum allowable heat flux through the coating, as a function of thickness, based on physical coating limitations (strain, temperature). This provides a convenient plot of the recommended operating envelope for a specified coating reliability.

12. Coating tests indicate that the weak point in these coatings may be the bond-to-substrate interface.

5

RECOMMENDATION

1. Additional strength data should be generated to resolve the conflicting results obtained to date, and to establish a reliable failure probability distribution for these coatings. A method of eliminating plastic deformation of the substrate should be investigated to eliminate a source of experimental error. Testing specimens made with a stronger substrate (e.g., steel) should be tried.

2. A method of measuring Poisson's ratio and the elastic modulus of these coatings should be explored, to improve the basic coating model.

3. The porous coating model should be developed further. Alternative methods of characterizing a coating structure to accommodate analytical modeling should be explored.

4. Experimental coating development should be conducted to improve the strength of these coatings and perhaps to control their thermal conductivities. The analytical model of the porous coating may be useful in developing a technique for controlling the thermal conductivity of the coating.

5. Performance analyses of these coatings should be conducted for transient thermal conditions. These conditions may induce higher strains than those calculated for steady state conditions.

6. Coating strength should be measured as a function of time and temperature. This could be done by subjecting groups of specimens to high temperature environments for specified lengths of time and testing their strength with the four-point flexure test. These results could then be incorporated into the coating model to predict coating life during a specified operating cycle.

REFERENCES

1. Taylor, Raymond E., "High Temperatures - High Pressures", 1979, Volume II, pp. 43-58.

2. Andrews, Andrew I., "Porcelain Enamels", 2nd Ed., The Garrard Press, Champaign, IL, 1961.

3. Price, H. G., et al., "Reliability and Effective Thermal Conductivity of Three Metallic-Ceramic Composite Insulating Coatings on Cooled Hydrogen-Oxygen Rockets", NASA Technical Note, NASA TN D-7392, November 1973.

4. Liebert, C. H. and Gaugler, R. E., "Significance of Thermal Contact Resistance in Two-Layer Thermal-Barrier-Coated Turbine Vanes", NASA Technical Memorandum 81483, 1980.

5. NASA/PWA - 4-Point Testing . . .

6. Kingery, Bowen, Uhlmann, Introduction to Ceramics, 2nd Ed., John Wiley and Sons, 1976.

7. Nielson, L. E., Predicting the Properties of Mixtures: Mixture Rules in Science and Engineering, Marcel Dekker, Inc., New York, 1978.

8. Ritter, J. R., "Engineering Design and Fatigue Failure of Brittle Materials", Fracture Mechanics of Ceramics, Vol. 4, Plenum Publishing Corp., 1978.

9. Dowdy, S. and Wearden, S., Statistics for Research, John Wiley & Sons, 1983.

10. Stepka, Francis S., "NASA Thermal Barrier Coatings - Summary and Update", NASA Technical Memorandum 790, September 1978.

11. Amos, D. J., "Analytical Investigation of Thermal Barrier Coatings on Advanced Power Generation Gas Turbines", Westinghouse Electric Corp., NASA CR-135146, July 1977.

12. Andress, D. E., "Analytical Study of Thermal Barrier Coated First Stage Blades in an F100 Engine," NASA CR-135359, February 1978.

13. Liebert, C. H. and Gaugler, R. E., "Significance of Thermal Coating Resistance in Two-Layer Thermal Barrier Coated Turbine Vanes", NASA Technical Memorandum, 81483.

14. Esposito, John J and Zabora, Ronald F., "Thrust Chamber Life Prediction - Vol. 1 - Mechanical and Physical Properties of High Performance Rocket Nozzle Materials", NASA-CR-134805, Boeing Aerospace Company, March 1975.

15. Wikes, K. E., et al., "Thermophysical Properties of Plasma Sprayed Coatings", Battelle Columbus Laboratories NASA CR-121144, March 1973.

APPENDIX 1

COATING STRESS/STRAIN ANALYSIS FOR FOUR POINT FLEXURE TEST

Plastic deformation of the copper substrate during strength testing required that a sophisticated stress analysis be developed to calculate the true strains in the coating at failure. The premise of this analysis is that the neutral axis of the coated beam specimen shifts towards the ceramic coating as the copper plastically yields. The location of the neutral axis must be determined to evaluate the strain in the coating. The neutral axis is defined as the plane which experiences no axial dimensional change, thus the sum of the bending moments about this axis is zero. This provides a method of locating the neutral axis by using a moment balance.

It is assumed for this analysis that the copper substrate behaves as a perfectly plastic material (strain hardening is neglected) and possesses equal properties in tension and compression. Material property values for the copper and the ceramic were obtained from the literature (Refs. 10-16). These properties are:

Yield strength, copper	YS_{cu}	= 70 MPa
Elastic modulus, copper	E_{cu}	= 1.12×10^5 MPa
Elastic modulus, ceramic	E_{cer}	= 4.48×10^4 MPa

The bond coat was neglected in these analyses.

The stress distribution in the coated flexure specimen during testing is shown in Figure 89. The stress in the copper substrate increases linearly with distance from the neutral axis, until the yield stress is reached. The stress beyond this point remains constant and equal to the yield strength of the copper. The strain in the ceramic coating is assumed to be elastic until the point of failure. Thus, the stress in the coating is assumed to remain directly proportional to the distance from the neutral axis.

Three dimensions are required for this analysis: R_1 (or R_2), t_1 and t_2 which are defined in Figure 89. An arbitrary approximation for the radius of curvature of the neutral axis (R) is used to begin an iterative solution procedure. Each iteration involves calculating the extent of the elastic zone (e) and the net moment about the neutral axis. If the calculated net moment is not sufficiently close to zero, a new value of R is selected and the next iteration performed. The true neutral axis is found by iterating until the net moment is essentially zero.

The computer program created for this analysis uses the midpoint of the beam specimen, $(t_1 + t_2)/2$, as the initial "guess" for R. An iteration procedure is then used to converge on the true R, subtracting increments of DR (typically 2.54×10^{-6} mm) from R for each iteration. Convergence on a solution is determined when the sense of the net moment changes sign. The true neutral axis is calculated as the average of the last two radii evaluated. The strain in the ceramic coating (ε_c) is then calculated from

$$\varepsilon_c = c/R$$

where c is the distance from the neutral axis to the point of interest.

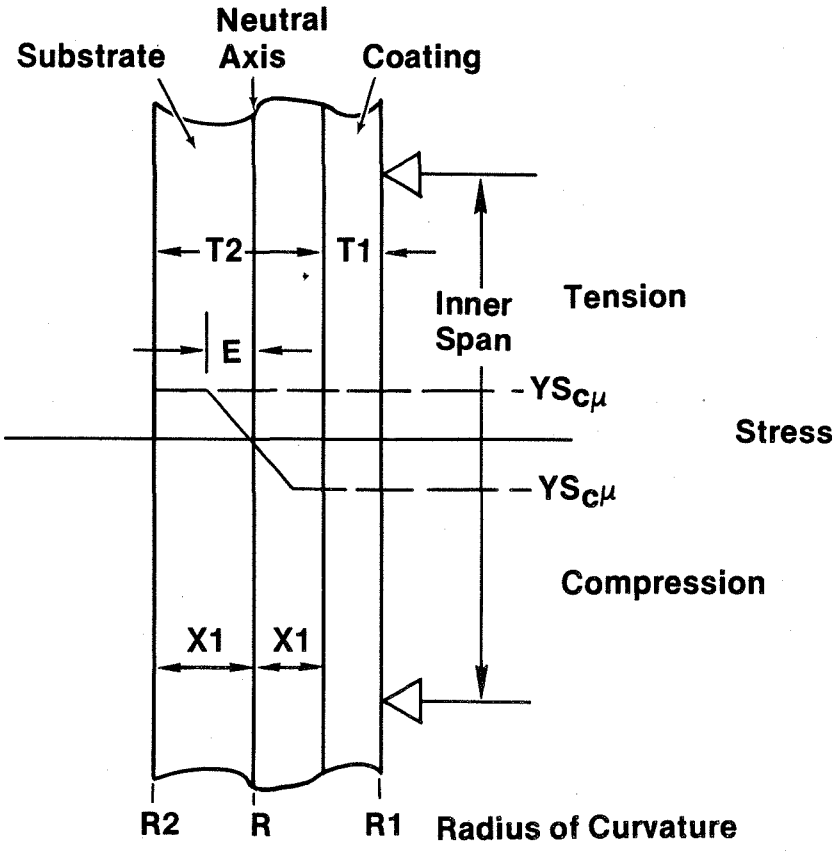

Figure 89. Stress/Strain Model for Plastically Deforming Four-Point Bend Specimen

APPENDIX 2

EXAMPLES OF FINITE ELEMENT THRUST CHAMBER ANALYSES INPUT AND OUTPUT

(THERMAL AND STRESS)

INTRODUCTION

This appendix documents the basic thermo-mechanical coating system computer analyses used to evaluate thrust chamber coating performance on this program.

Representative input and output files for use with the ANSYS computer code are presented. A thermal analysis input file is listed on page 121. The associated output for this file is listed on pages 122 through 136.

A stress analysis input file is listed on page 138. The associated output for this file is listed on pages 139 through 154.

Post processing input and output files are listed on pages 155 and 156. This analysis calculates stresses at the nodes in the finite element mode.

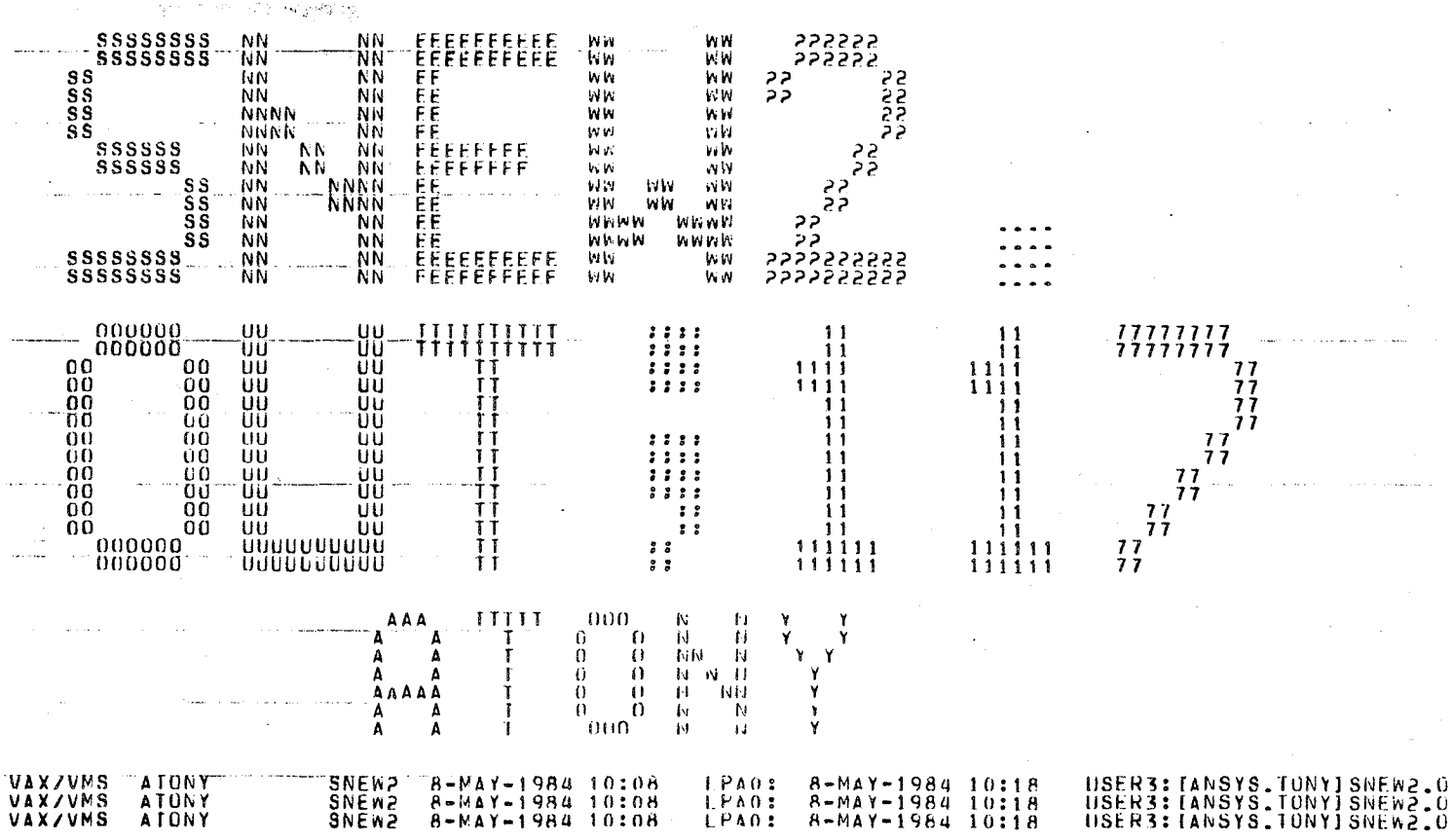
SSSSSSSS NN NN EEEEEEEEEE WW WW 222222
SSSSSSSS NN NN EEEEEEEEEE WW WW 222222
SS NN NN EE WW WW 22 22
SS NN NN EE WW WW 22 22
SS NNNN NN EE WW WW 22
SS NNNN NN EE WW WW 22
SSSSSS NN NN NN EEEEEEEE WW WW 22
SSSSSS NN NN NN EEEEEEEE WW WW 22
SS NN NNNN EE WW WW WW 22
SS NN NNNN EE WW WW WW 22
SS NN NN EE WWWW WWWW 22
SS NN NN EE WWWW WWWW 22
SSSSSSSS NN NN EEEEEEEEEE WW WW 2222222222
SSSSSSSS NN NN EEEEEEEEEE WW WW 2222222222
000000 UU UU TTTTTTTTTT ;;;; 11 11 77777777
000000 UU UU TTTTTTTTTT ;;;; 11 11 77777777
00 00 UU UU TT ;;;; 1111 1111 77
00 00 UU UU TT ;;;; 1111 1111 77
00 00 UU UU TT 11 11 77
00 00 UU UU TT 11 11 77
00 00 UU UU TT ;;;; 11 11 77
00 00 UU UU TT ;;;; 11 11 77
00 00 UU UU TT ;;;; 11 11 77
00 00 UU UU TT ;;;; 11 11 77
00 00 UU UU TT ;; 11 11 77
00 00 UU UU TT ;; 11 11 77
000000 UUUUUUUUUU TT ;; 111111 111111 77
000000 UUUUUUUUUU TT ;; 111111 111111 77
AAA TTTTT 000 N N Y Y
A A T 0 0 NN N Y Y
A A T 0 0 N N N Y
AAAAA T 0 0 N NN Y
A A T 0 0 N N Y
A A T 000 N N Y
VAX/VMS ATONY SNEW2 8-MAY-1984 10:08 LPA0: 8-MAY-1984 10:18 USER3:[ANSYS.TONY]SNEW2.OUT;117
VAX/VMS ATONY SNEW2 8-MAY-1984 10:08 LPA0: 8-MAY-1984 10:18 USER3:[ANSYS.TONY]SNEW2.OUT;117
VAX/VMS ATONY SNEW2 8-MAY-1984 10:08 LPA0: 8-MAY-1984 10:18 USER3:[ANSYS.TONY]SNEW2.OUT;117

********** ANSYS INPUT DATA LISTING (FILE18) ******

```
            6     12     18     24     30     36     42     48     54     60
            V      V      V      V      V      V      V      V      V      V
 1  /PREP7
 2  /TITLE THRUST CHAMBER MODEL
 3  /GOPR
 4  KAN,-1
 5  TOFFST,460
 6  ET,1,55,2,,1
 7  KXX,1,,.0000125
 8  KXX,2,,.000118,,.0000000618
 9  KXX,3,,.0052314
10  C,1,1
11  C,2,1
12  C,3,1
13  DENS,1,1
14  DENS,2,1
15  DENS,3,1
16  N,1,1,2945,,.009
17  N,7,1,2945,0.
18  FILL
19  NGEN,4,7,1,7,1,0,.0013333333
20  NGEN,4,7,22,28,1,,.0005
21  N,50,1,3038889,,.009
22  N,56,1,3038889,0.
23  FILL
24  N,57,1,3085556,,.009
25  N,63,1,3085556,0.
26  FILL
27  N,64,1,314,,.009
28  N,70,1,314,0.
29  FILL
30  N,71,1,3202222,,.009
31  N,77,1,3202222,0.
32  FILL
33  N,78,1,3272222,,.009
34  N,84,1,3272222,0.
35  FILL
36  N,85,1,335,,.009
37  N,91,1,335,0.
38  FILL
39  MAT,1
40  E,2,9,8,1
41  EGEN,6,1,1
42  EGEN,3,7,1,6
43  MAT,2
44  E,23,30,29,22
45  EGEN,6,1,19
46  EGEN,3,7,19,24
47  MAT,3
48  E,44,51,50,43
49  EGEN,6,1,37
50  EGEN,6,7,37,42

51  ITER,-10,10
52  KBC,1
53  KRF,1
54  HFLOW,1,HEAT,00,0097088,,7,6
55  HFLOW,2,HEAT,0,0194175,,6,1
56  NT,85,TEMP,400,,,91
57  AFWRIT,1,1
58  FINISH
59  /INPUT,27
60  /GOPR
61  FINISH
62  /EOF
```

copper Btu/sinF

```
ANSYS - ENGINEERING ANALYSIS SYSTEM  REVISION 4.0 E2      SOLAR TURBINES    AUG-1,1981
SWANSON ANALYSIS SYSTEMS, INC.        HOUSTON, PENNSYLVANIA 15342   PHONE (412)746-3304  TWX 51
 TITLE                                                              10.0986    5/ 8/84 CP

        ***** ANSYS ANALYSIS DEFINITION (PREP7) *****

 NEW TITLE=  THRUST CHAMBER MODEL

 PRINTOUT RESUMED BY /GOP

 ANALYSIS TYPE= -1

 TEMPERATURE OFFSET FROM ABSOLUTE ZERO= 460.000

 ELEMENT TYPE  1 USES STIF55
  KEYOPT(1-9)=   2   0   1     0   0   0      0   0   0  INCTPR= 0  NUMBER OF NODES=   4

 TSOPAR, THERMAL SOLID, 2-D

 CURRENT NODAL DOF SET IS  TEMP

 TWO-DIMENSIONAL STRUCTURE

  MATERIAL    1          COEFFICIENTS OF KXX  VS. TEMP EQUATION
   C0 =  0.1250000E-04

 PROPERTY TABLE,KXX    MAT=    1  NUM. POINTS=   2
       ,TEMPERATURE      DATA          TEMPERATURE      DATA
      0.0000000E+00 0.1250000E-04  2300.000      0.1250000E-04

  MATERIAL    2          COEFFICIENTS OF KXX  VS. TEMP EQUATION
   C0 =  0.1180000E-03  C1 =  0.6180000E-07  C2 =  0.0000000E+00
   C3 =  0.0000000E+00  C4 =  0.0000000E+00

 PROPERTY TABLE,KXX    MAT=    2  NUM. POINTS=   2
       ,TEMPERATURE      DATA          TEMPERATURE      DATA
      0.0000000E+00 0.1180000E-03  2300.000      0.2601400E-03

  MATERIAL    3          COEFFICIENTS OF KXX  VS. TEMP EQUATION
   C0 =  0.5231400E-02

 PROPERTY TABLE,KXX    MAT=    3  NUM. POINTS=   2
       TEMPERATURE       DATA          TEMPERATURE      DATA
      0.0000000E+00 0.5231400E-02  2300.000      0.5231400E-02

  MATERIAL    1          COEFFICIENTS OF C    VS. TEMP EQUATION
   C0 =  1.000000

 PROPERTY TABLE,C      MAT=    1  NUM. POINTS=   2
       ,TEMPERATURE      DATA          TEMPERATURE      DATA
      0.0000000E+00  1.000000       2300.000       1.000000

  MATERIAL    2          COEFFICIENTS OF C    VS. TEMP EQUATION
   C0 =  1.000000

 PROPERTY TABLE,C      MAT=    2  NUM. POINTS=   2
       ,TEMPERATURE      DATA          TEMPERATURE      DATA
      0.0000000E+00  1.000000       2300.000       1.000000

  MATERIAL    3          COEFFICIENTS OF C    VS. TEMP EQUATION
   C0 =  1.000000

 PROPERTY TABLE,C      MAT=    3  NUM. POINTS=   2
       ,TEMPERATURE      DATA          TEMPERATURE      DATA
      0.0000000E+00  1.000000       2300.000       1.000000

  MATERIAL    1          COEFFICIENTS OF DENS VS. TEMP EQUATION
   C0 =  1.000000

 PROPERTY TABLE,DENS   MAT=    1  NUM. POINTS=   2
       ,TEMPERATURE      DATA          TEMPERATURE      DATA
      0.0000000E+00  1.000000       2300.000       1.000000

  MATERIAL    2          COEFFICIENTS OF DENS VS. TEMP EQUATION
   C0 =  1.000000

 PROPERTY TABLE,DENS   MAT=    2  NUM. POINTS=   2
       ,TEMPERATURE      DATA          TEMPERATURE      DATA
      0.0000000E+00  1.000000       2300.000       1.000000

  MATERIAL    3          COEFFICIENTS OF DENS VS. TEMP EQUATION
   C0 =  1.000000
```

```
PROPERTY TABLE,DENS  MAT=    3  NUM. POINTS=   2
      TEMPERATURE        DATA        TEMPERATURE        DATA
    0.0000000E+00   1.000000       2300.000        1.000000

NODE     1  KCS= 0  X,Y,Z=  1.2945      0.90000E-02 0.00000E+00

NODE     7  KCS= 0  X,Y,Z=  1.2945      0.00000E+00 0.00000E+00

FILL    5 POINTS BETWEEN NODE     1 AND NODE     7
  START WITH NODE     2 AND INCREMENT BY    1

GENERATE    4 TOTAL SETS OF NODES WITH INCREMENT      7
  SET IS FROM     1 TO     7 IN STEPS OF    1
  GEOMETRY INCREMENTS ARE 0.13333E-02 0.00000E+00 0.00000E+00

GENERATE    4 TOTAL SETS OF NODES WITH INCREMENT      7
  SET IS FROM    22 TO    28 IN STEPS OF    1
  GEOMETRY INCREMENTS ARE 0.50000E-03 0.00000E+00 0.00000E+00

NODE    50  KCS= 0  X,Y,Z=  1.3039      0.90000E-02 0.00000E+00

NODE    56  KCS= 0  X,Y,Z=  1.3039      0.00000E+00 0.00000E+00

FILL    5 POINTS BETWEEN NODE    50 AND NODE    56
  START WITH NODE    51 AND INCREMENT BY    1

NODE    57  KCS= 0  X,Y,Z=  1.3086      0.90000E-02 0.00000E+00

NODE    63  KCS= 0  X,Y,Z=  1.3086      0.00000E+00 0.00000E+00

FILL    5 POINTS BETWEEN NODE    57 AND NODE    63
  START WITH NODE    58 AND INCREMENT BY    1

NODE    64  KCS= 0  X,Y,Z=  1.3140      0.90000E-02 0.00000E+00

NODE    70  KCS= 0  X,Y,Z=  1.3140      0.00000E+00 0.00000E+00

FILL    5 POINTS BETWEEN NODE    64 AND NODE    70
  START WITH NODE    65 AND INCREMENT BY    1

NODE    71  KCS= 0  X,Y,Z=  1.3202      0.90000E-02 0.00000E+00

NODE    77  KCS= 0  X,Y,Z=  1.3202      0.00000E+00 0.00000E+00

FILL    5 POINTS BETWEEN NODE    71 AND NODE    77
  START WITH NODE    72 AND INCREMENT BY    1

NODE    78  KCS= 0  X,Y,Z=  1.3272      0.90000E-02 0.00000E+00

NODE    84  KCS= 0  X,Y,Z=  1.3272      0.00000E+00 0.00000E+00

FILL    5 POINTS BETWEEN NODE    78 AND NODE    84
  START WITH NODE    79 AND INCREMENT BY    1

NODE    85  KCS= 0  X,Y,Z=  1.3350      0.90000E-02 0.00000E+00

NODE    91  KCS= 0  X,Y,Z=  1.3350      0.00000E+00 0.00000E+00

FILL    5 POINTS BETWEEN NODE    85 AND NODE    91
  START WITH NODE    86 AND INCREMENT BY    1

MATERIAL NUMBER SET TO  1
ELEMENT     1       2       9       8       1

GENERATE    6 TOTAL SETS OF ELEMENTS WITH NODE INCREMENT OF     1
  SET IS    1 TO    1 IN STEPS OF   1
NUMBER OF ELEMENTS=     6

GENERATE    3 TOTAL SETS OF ELEMENTS WITH NODE INCREMENT OF     7
  SET IS    1 TO    6 IN STEPS OF   1
NUMBER OF ELEMENTS=    18

MATERIAL NUMBER SET TO  2
ELEMENT    19      23      30      29      22

GENERATE    6 TOTAL SETS OF ELEMENTS WITH NODE INCREMENT OF     1
  SET IS   19 TO   19 IN STEPS OF   1
NUMBER OF ELEMENTS=    24

GENERATE    3 TOTAL SETS OF ELEMENTS WITH NODE INCREMENT OF     7
  SET IS   19 TO   24 IN STEPS OF   1
NUMBER OF ELEMENTS=    36
```

```
 MATERIAL NUMBER SET TO    3
 ELEMENT   37      44      51      50      43

 GENERATE    6 TOTAL SETS OF ELEMENTS WITH NODE INCREMENT OF     1
   SET IS   37 TO   37 IN STEPS OF   1
 NUMBER OF ELEMENTS=     42

 GENERATE    6 TOTAL SETS OF ELEMENTS WITH NODE INCREMENT OF     7
   SET IS   37 TO   42 IN STEPS OF   1
 NUMBER OF ELEMENTS=     72

 NITTER=    -10  NPRINT=     10  NPOST=     10

 ALL PRINT CONTROLS RESET TO     10

 ALL POST DATA FILE CONTROLS RESET TO     10

 STEP BOUNDARY CONDITION KEY= 1

 REACTION FORCE KEY= 1

 SPECIFIED HEAT FLOW DEFINITION FOR HEAT FROM NODE      1 TO NODE      7 IN STEPS OF      6
  VALUES= 0.97088E-02

 SPECIFIED HEAT FLOW DEFINITION FOR HEAT FROM NODE      2 TO NODE      6 IN STEPS OF      1
  VALUES= 0.19418E-01

 SPECIFIED TEMP. DEFINITION FOR TEMP FROM NODE     85 TO NODE     91 IN STEPS OF      1
  VALUES=  400.00       ADDITIONAL DOFS=

 DATA CHECKED - NO FATAL ERRORS FOUND.
 CHECK OUTPUT FOR POSSIBLE WARNING MESSAGES.

 ANALYSIS DATA WRITTEN ON FILE27 (    229 LINES)

 ALL CURRENT PREP7 DATA WRITTEN TO FILE16
  FOR POSSIBLE RESUME FROM THIS POINT

 ***** ROUTINE COMPLETED *****  CP =          7.350

 ***** INPUT FILE SWITCHED FROM FILE18 TO FILE27
```



```
      ***** NOTICE *****  THIS IS THE ANSYS GENERAL PURPOSE
      FINITE ELEMENT COMPUTER PROGRAM.  NEITHER SWANSON ANALYSIS
      SYSTEMS, INC. NOR THE CORPORATION SUPPLYING THE COMPUTER
      FACILITIES FOR THIS ANALYSIS ASSUME ANY RESPONSIBILITY FOR
      THE VALIDITY, ACCURACY, OR APPLICABILITY OF ANY RESULTS
      OBTAINED FROM THE ANSYS SYSTEM.  THE USER MUST VERIFY HIS
      OWN RESULTS.

      SWANSON ANALYSIS SYSTEMS,INC. IS ENDEAVORING TO MAKE THE
      ANSYS PROGRAM AS COMPLETE, ACCURATE, AND EASY TO USE AS
      POSSIBLE.  SUGGESTIONS AND COMMENTS ARE WELCOMED.  ANY
      ERRORS ENCOUNTERED IN EITHER THE DOCUMENTATION OR THE
      RESULTS SHOULD BE IMMEDIATELY BROUGHT TO OUR ATTENTION.

      ***** ANALYSIS OPTIONS *****

                                        VALUE
 ANALYSIS TYPE . . . . . .               -1
 ELEMENT CONSTANT TABLE . . .             6
 NODAL HEAT FLOW KEY . . . . .            1
 MASTER DOF READ KEY . . . . .            1
 MATERIAL TABLE ENTRIES. . . .            2

 UNIFORM TEMPERATURE . . . . .         0.00
 TEMPERATURE ZERO SHIFT . . .        460.00

      ***** ELEMENT TYPES *****

 TYPE  STIF   DESCRIPTION                  KEY OPTIONS                    NJ   INOTPR
                                           1  2  3   4  5  6   7  8  9
   1    55   ISOPAR. THERMAL SOLID, 2-D    2  0  1   0  0  0   0  0  0    0      0
 NUMBER OF ELEMENT TYPES=   1

      ***** TABLE OF ELEMENT REAL CONSTANTS *****
 NO.

 NUMBER OF REAL CONSTANT SETS=   0
```

***** ELEMENT DEFINITIONS *****

ELEMENT	NODES					MAT	TYPE	CLASS
1	2	9	8	1		1	1	0
2	3	10	9	2		1	1	0
3	4	11	10	3		1	1	0
4	5	12	11	4		1	1	0
5	6	13	12	5		1	1	0
6	7	14	13	6		1	1	0
7	9	16	15	8		1	1	0
8	10	17	16	9		1	1	0
9	11	18	17	10		1	1	0
10	12	19	18	11		1	1	0
11	13	20	19	12		1	1	0
12	14	21	20	13		1	1	0
13	16	23	22	15		1	1	0
14	17	24	23	16		1	1	0
15	18	25	24	17		1	1	0
16	19	26	25	18		1	1	0
17	20	27	26	19		1	1	0
18	21	28	27	20		1	1	0
19	23	30	29	22		2	1	0
20	24	31	30	23		2	1	0
21	25	32	31	24		2	1	0
22	26	33	32	25		2	1	0
23	27	34	33	26		2	1	0
24	28	35	34	27		2	1	0
25	30	37	36	29		2	1	0
26	31	38	37	30		2	1	0
27	32	39	38	31		2	1	0
28	33	40	39	32		2	1	0
29	34	41	40	33		2	1	0
30	35	42	41	34		2	1	0
31	37	44	43	36		2	1	0
32	38	45	44	37		2	1	0
33	39	46	45	38		2	1	0
34	40	47	46	39		2	1	0
35	41	48	47	40		2	1	0
36	42	49	48	41		2	1	0
37	44	51	50	43		3	1	0
38	45	52	51	44		3	1	0
39	46	53	52	45		3	1	0
40	47	54	53	46		3	1	0
41	48	55	54	47		3	1	0
42	49	56	55	48		3	1	0
43	51	58	57	50		3	1	0
44	52	59	58	51		3	1	0
45	53	60	59	52		3	1	0
46	54	61	60	53		3	1	0
47	55	62	61	54		3	1	0
48	56	63	62	55		3	1	0
49	58	65	64	57		3	1	0
50	59	66	65	58		3	1	0
51	60	67	66	59		3	1	0
52	61	68	67	60		3	1	0
53	62	69	68	61		3	1	0
54	63	70	69	62		3	1	0
55	65	72	71	64		3	1	0
56	66	73	72	65		3	1	0
57	67	74	73	66		3	1	0
58	68	75	74	67		3	1	0
59	69	76	75	68		3	1	0
60	70	77	76	69		3	1	0
61	72	79	78	71		3	1	0
62	73	80	79	72		3	1	0
63	74	81	80	73		3	1	0
64	75	82	81	74		3	1	0
65	76	83	82	75		3	1	0
66	77	84	83	76		3	1	0
67	79	86	85	78		3	1	0
68	80	87	86	79		3	1	0
69	81	88	87	80		3	1	0
70	82	89	88	81		3	1	0
71	83	90	89	82		3	1	0
72	84	91	90	83		3	1	0

INTEGER STORAGE REQUIREMENTS FOR ELEMENT INPUT CP= 10.800 TIME= 10
MEMORY I= 1001 MEMORY II= 182 TOTAL = 1183 MEMORY AVAILABLE= 340000
MAXIMUM NODE NUMBER FOR AVAILABLE AUXILIARY MEMORY SIZE= 169498

NUMBER OF ELEMENTS = 72 MAXIMUM NODE NUMBER USED = 91

LOCATION ROTATION (DEGREES)

NODE	X (OR R)	Y (OR THETA)	THXY (OR RT)
1	1.2945	0.90000E-02	0.00000E+00
2	1.2945	0.75000E-02	0.00000E+00
3	1.2945	0.60000E-02	0.00000E+00
4	1.2945	0.45000E-02	0.00000E+00
5	1.2945	0.30000E-02	0.00000E+00
6	1.2945	0.15000E-02	0.00000E+00
7	1.2945	0.00000E+00	0.00000E+00
8	1.2958	0.90000E-02	0.00000E+00
9	1.2958	0.75000E-02	0.00000E+00
10	1.2958	0.60000E-02	0.00000E+00
11	1.2958	0.45000E-02	0.00000E+00
12	1.2958	0.30000E-02	0.00000E+00
13	1.2958	0.15000E-02	0.00000E+00
14	1.2958	0.00000E+00	0.00000E+00
15	1.2972	0.90000E-02	0.00000E+00
16	1.2972	0.75000E-02	0.00000E+00
17	1.2972	0.60000E-02	0.00000E+00
18	1.2972	0.45000E-02	0.00000E+00
19	1.2972	0.30000E-02	0.00000E+00
20	1.2972	0.15000E-02	0.00000E+00
21	1.2972	0.00000E+00	0.00000E+00
22	1.2985	0.90000E-02	0.00000E+00
23	1.2985	0.75000E-02	0.00000E+00
24	1.2985	0.60000E-02	0.00000E+00
25	1.2985	0.45000E-02	0.00000E+00
26	1.2985	0.30000E-02	0.00000E+00
27	1.2985	0.15000E-02	0.00000E+00
28	1.2985	0.00000E+00	0.00000E+00
29	1.2990	0.90000E-02	0.00000E+00
30	1.2990	0.75000E-02	0.00000E+00
31	1.2990	0.60000E-02	0.00000E+00
32	1.2990	0.45000E-02	0.00000E+00
33	1.2990	0.30000E-02	0.00000E+00
34	1.2990	0.15000E-02	0.00000E+00
35	1.2990	0.00000E+00	0.00000E+00
36	1.2995	0.90000E-02	0.00000E+00
37	1.2995	0.75000E-02	0.00000E+00
38	1.2995	0.60000E-02	0.00000E+00
39	1.2995	0.45000E-02	0.00000E+00
40	1.2995	0.30000E-02	0.00000E+00
41	1.2995	0.15000E-02	0.00000E+00
42	1.2995	0.00000E+00	0.00000E+00
43	1.3000	0.90000E-02	0.00000E+00
44	1.3000	0.75000E-02	0.00000E+00
45	1.3000	0.60000E-02	0.00000E+00
46	1.3000	0.45000E-02	0.00000E+00
47	1.3000	0.30000E-02	0.00000E+00
48	1.3000	0.15000E-02	0.00000E+00
49	1.3000	0.00000E+00	0.00000E+00
50	1.3039	0.90000E-02	0.00000E+00
51	1.3039	0.75000E-02	0.00000E+00
52	1.3039	0.60000E-02	0.00000E+00
53	1.3039	0.45000E-02	0.00000E+00
54	1.3039	0.30000E-02	0.00000E+00
55	1.3039	0.15000E-02	0.00000E+00
56	1.3039	0.00000E+00	0.00000E+00
57	1.3086	0.90000E-02	0.00000E+00
58	1.3086	0.75000E-02	0.00000E+00
59	1.3086	0.60000E-02	0.00000E+00
60	1.3086	0.45000E-02	0.00000E+00
61	1.3086	0.30000E-02	0.00000E+00
62	1.3086	0.15000E-02	0.00000E+00
63	1.3086	0.00000E+00	0.00000E+00
64	1.3140	0.90000E-02	0.00000E+00
65	1.3140	0.75000E-02	0.00000E+00
66	1.3140	0.60000E-02	0.00000E+00
67	1.3140	0.45000E-02	0.00000E+00
68	1.3140	0.30000E-02	0.00000E+00
69	1.3140	0.15000E-02	0.00000E+00
70	1.3140	0.00000E+00	0.00000E+00
71	1.3202	0.90000E-02	0.00000E+00
72	1.3202	0.75000E-02	0.00000E+00
73	1.3202	0.60000E-02	0.00000E+00
74	1.3202	0.45000E-02	0.00000E+00
75	1.3202	0.30000E-02	0.00000E+00
76	1.3202	0.15000E-02	0.00000E+00
77	1.3202	0.00000E+00	0.00000E+00
78	1.3272	0.90000E-02	0.00000E+00
79	1.3272	0.75000E-02	0.00000E+00
80	1.3272	0.60000E-02	0.00000E+00
81	1.3272	0.45000E-02	0.00000E+00
82	1.3272	0.30000E-02	0.00000E+00
83	1.3272	0.15000E-02	0.00000E+00
84	1.3272	0.00000E+00	0.00000E+00
85	1.3350	0.90000E-02	0.00000E+00
86	1.3350	0.75000E-02	0.00000E+00
87	1.3350	0.60000E-02	0.00000E+00
88	1.3350	0.45000E-02	0.00000E+00
89	1.3350	0.30000E-02	0.00000E+00
90	1.3350	0.15000E-02	0.00000E+00
91	1.3350	0.00000E+00	0.00000E+00

XMIN= 1.295 XMAX= 1.335 YMIN= 0.0000E+00 YMAX= 0.9000E-02 ZMIN= 0.0000E+00

INTEGER STORAGE REQUIREMENTS FOR NODE INPUT CP= 14.650 TIME= 10.1
MEMORY I= 0 MEMORY II= 546 TOTAL= 546 MEMORY AVAILABLE= 340000
MAXIMUM NODE NUMBER FOR AVAILABLE AUXILIARY MEMORY SIZE= 113333

***** MATERIAL PROPERTIES *****

MATERIAL 1

KXX PROPERTY TABLE (LINEAR INTERPOLATION)

TEMP	KXX	TEMP	KXX
0.0	0.12500E-04	2300.0	0.12500E-04

MATERIAL 2

KXX PROPERTY TABLE (LINEAR INTERPOLATION)

TEMP	KXX	TEMP	KXX
0.0	0.11800E-03	2300.0	0.26014E-03

MATERIAL 3

KXX PROPERTY TABLE (LINEAR INTERPOLATION)

TEMP	KXX	TEMP	KXX
0.0	0.52314E-02	2300.0	0.52314E-02

MATERIAL 1

C PROPERTY TABLE (LINEAR INTERPOLATION)

TEMP	C	TEMP	C
0.0	1.0000	2300.0	1.0000

MATERIAL 2

C PROPERTY TABLE (LINEAR INTERPOLATION)

TEMP	C	TEMP	C
0.0	1.0000	2300.0	1.0000

MATERIAL 3

C PROPERTY TABLE (LINEAR INTERPOLATION)

TEMP	C	TEMP	C
0.0	1.0000	2300.0	1.0000

MATERIAL 1

DENS PROPERTY TABLE (LINEAR INTERPOLATION)

TEMP	DENS	TEMP	DENS
0.0	1.0000	2300.0	1.0000

MATERIAL 2

DENS PROPERTY TABLE (LINEAR INTERPOLATION)

TEMP	DENS	TEMP	DENS
0.0	1.0000	2300.0	1.0000

MATERIAL 3

DENS PROPERTY TABLE (LINEAR INTERPOLATION)

TEMP	DENS	TEMP	DENS
0.0	1.0000	2300.0	1.0000

MAXIMUM MATERIAL NUMBER= 3

```
          ***** MASTER DEGREES OF FREEDOM  *****
  NODE        DEGREES OF FREEDOM LIST

NUMBER OF SPECIFIED MASTER D.O.F.=      0
TOTAL NUMBER OF MASTER D.O.F.    =      0

 INTEGER STORAGE REQUIREMENTS FOR MATERIALS, ETC. INPUT          CP=     16.940  TIME= 10.10826
MEMORY I=       92  MEMORY II=        0  TOTAL=       92  MEMORY AVAILABLE=  340000

*** LOAD STEP    1  OPTIONS SPECIFICATIONS

NITTER=     -10  NPRINT=      10  NPOST=      10

ALL PRINT CONTROLS RESET TO     10

ALL POST DATA FILE CONTROLS RESET TO     10

ACEL= 0.00000E+00 0.00000E+00 0.00000E+00

OMEGA= 0.00000E+00 0.00000E+00 0.00000E+00

DOMEGA= 0.00000E+00 0.00000E+00 0.00000E+00

CGLOC= 0.00000E+00 0.00000E+00 0.00000E+00

CGOMEGA= 0.00000E+00 0.00000E+00 0.00000E+00

DOMEGA= 0.00000E+00 0.00000E+00 0.00000E+00

KTEMP=       0       0

ALL TEMPERATURES SET TO TUNIF=      0.000

STEADY STATE CONVERGENCE CRITERION=  1.0000
TRANSIENT OPTIMIZATION CRITERIA=  5.0000
TEMPERATURE LIMIT= 0.00000E+00
KEY TO TERMINATE RUN IF NO CONVERGENCE=      0.

LOADS STEPPED TO FINAL VALUES FOR ALL ITERATIONS (KRC= 1)

REACTION FORCE KEY= 1

UNIFORM TEMPERATURE=     0.000  (TREF=     0.000)

BOUNDARY CONDITION PRINT KEY= 0
```

```
LOAD STEP NUMBER =    1

  *** LOAD OPTIONS SUMMARY

TIME= 0.00000E+00   NITTER=     -10

ACEL   = 0.00000E+00 0.00000E+00 0.00000E+00
OMEGA  = 0.00000E+00 0.00000E+00 0.00000E+00
DOMEGA= 0.00000E+00 0.00000E+00 0.00000E+00
CGLOC  = 0.00000E+00 0.00000E+00 0.00000E+00
CGOMEG= 0.00000E+00 0.00000E+00 0.00000E+00
DCGOME= 0.00000E+00 0.00000E+00 0.00000E+00
TEMPERATURE (KTEMP) LOAD STEP=      0   ITERATION=      0
STIFFNESS REUSE KEY (KUSE)=   0

UNIFORM TEMPERATURE=     0.000   (TREF=     0.000)

PRINT ELEMENT FORCES AND REACTION FORCES (KRF=1)

LOADS STEPPED TO FINAL VALUES FOR ALL ITERATIONS (KBC= 1)
STEADY STATE CONVERG. CRIT.=  1.0000
TRANSIENT OPT. CRITERIA=   5.0000
TEMPERATURE LIMIT= 0.00000E+00
KEY TO TERMINATE RUN IF NO CONVERGENCE=     0.
MODE=     0   ISYM=     1

NPRINT=     10   NPOST=     10   REACTION PRINT FREQ=     10
 DISP. POST DATA FREQ=     10  REACT. POST DATA FREQ=     10

 DISPLACEMENT PRINT FREQUENCIES
   FREQ   NSTRT   NSTOP    NINC
     10       1   32000       1

 ELEMENT PRINT AND POST DATA FREQUENCIES
  TYPE   STIFF   STRESS  FORCE    STRESS    DATA   FORCE
         NO.     PRINT  PRINT     DATA     LEVEL  DATA
    1     55       10     10        10        3     10


          ***** SPECIFIED TEMPERATURES *****

   NODE       TEMP

   85      400.000
   86      400.000
   87      400.000
   88      400.000
   89      400.000
   90      400.000
   91      400.000


          ***** SPECIFIED HEAT FLOW RATES *****

   NO.      NODE   D. OF FR.        VALUE

    1          1      HEAT     0.970880E-02
    2          7      HEAT     0.970880E-02
    3          2      HEAT     0.194175E-01
    4          3      HEAT     0.194175E-01
    5          4      HEAT     0.194175E-01
    6          5      HEAT     0.194175E-01
    7          6      HEAT     0.194175E-01


***** LOAD SUMMARY -       7 TEMPERATURES       7 HEAT FLOWS     0 CONVECTIONS      *****


 INTEGER STORAGE REQUIREMENTS FOR LOAD DATA INPUT                    CP=     21.240   TIME= 10.11101
MEMORY I=      216   MEMORY II=        0   TOTAL=      216  MEMORY AVAILABLE=   340000

 RANGE OF ELEMENT MAXIMUM CONDUCTIVITY IN GLOBAL COORDINATES
MAXIMUM= 0.125014E-01  AT ELEMENT      72
MINIMUM= 0.108696E-04  AT ELEMENT       6
```

```
 INTEGER STORAGE REQUIREMENTS FOR ELEMENT FORMULATION              CP=     26.520  TIME= 10.11[illegible]
MEMORY I=      214  MEMORY II=        0  TOTAL=      214  MEMORY AVAILABLE=  340000

  *** ELEMENT STIFFNESS FORMULATION TIMES
 TYPE  NUMBER  STIF  TOTAL CP   AVE CP

    1      72    55     4.550     0.063

 TIME AT END OF ELEMENT STIFFNESS FORMULATION   CP =      26.540

 MAXIMUM IN-CORE WAVE FRONT ALLOWED FOR REQUESTED MEMORY SIZE=  580

 INTEGER STORAGE REQUIREMENTS FOR WAVE FRONT MATRIX SOLUTION       CP=     29.730  TIME= 10.11592
MEMORY I=      214  MEMORY II=      121  TOTAL=      335  MEMORY AVAILABLE=  340000

 MAXIMUM IN-CORE WAVE FRONT (EQUATIONS) USED=    9

  *** MATRIX SOLUTION TIMES
 READ IN ELEMENT STIFFNESSES    CP=            1.430
 NODAL COORD. TRANSFORMATION    CP=            0.120
 MATRIX TRIANGULARIZATION       CP=            0.880

 TIME AT END OF MATRIX TRIANGULARIZATION   CP=          29.750

 INTEGER STORAGE REQUIREMENTS FOR BACK SUBSTITUTION                CP=     30.180  TIME= 10.11[illegible]
MEMORY I=      214  MEMORY II=      186  TOTAL=      400  MEMORY AVAILABLE=  340000

  *** ELEM. HT. FLOW CALC. TIMES
 TYPE  NUMBER  STIF  TOTAL CP   AVE CP

    1      72    55     2.390     0.033

  *** NODAL HT. FLOW CALC. TIMES
 TYPE  NUMBER  STIF  TOTAL CP   AVE CP

    1      72    55     0.260     0.004

 *** LOAD STEP     1   ITER      1  COMPLETED.  TIME=  0.000000E+00  KUSE= 0  CUM. ITER.=     1

 INTEGER STORAGE REQUIREMENTS FOR HEAT FLOW CALCULATIONS           CP=     33.890  TIME= 10.11827
MEMORY I=      214  MEMORY II=      364  TOTAL=      578  MEMORY AVAILABLE=  340000

  *** STORAGE REQUIREMENT SUMMARY
 MAXIMUM CENTRAL MEMORY USED   =     1001
 MAXIMUM AUXILIARY MEMORY USED=      546
 MAXIMUM TOTAL MEMORY USED     =     1183
 MAXIMUM AUXILIARY AVAILABLE   =   339784

  *** PROBLEM STATISTICS
 NO. OF ACTIVE DEGREES OF FREEDOM =      84
 R.M.S. WAVEFRONT SIZE =       7.5

  *** ANSYS BINARY FILE STATISTICS
 BUFFER SIZE USED= 2040
 POST DATA WRITTEN ON FILE12
 RESTART DATA WRITTEN ON FILE 3    (    18426 WORDS)
 TEMPERATURES WRITTEN ON FILE 4

 *** LOAD STEP     1   ITER      2  COMPLETED.  TIME=  0.000000E+00  KUSE= 0  CUM. ITER.=     2
 STEADY STATE CONVERGENCE VALUE =  27.4601  AT NODE     22     CRITERION =    1.0000

 *** LOAD STEP     1   ITER      3  COMPLETED.  TIME=  0.000000E+00  KUSE= 0  CUM. ITER.=     3
 STEADY STATE CONVERGENCE VALUE =   0.5384  AT NODE     22     CRITERION =    1.0000

 *** SOLUTION CONVERGED - LOAD STEP    1  CONVERGED AFTER ITERATION      3  CUM. ITER.=     3
       NEXT ITERATION (IDENTIFIED AS ITERATION    10) SATISFIES PRINTOUT OR POST DATA REQUEST.
```

***** TEMPERATURE SOLUTION ***** TIME = 0.00000E+00 LOAD STEP= 1 ITERATION= 10 CUM. ITE

NODE	TEMP	NODE	TEMP	NODE	TEMP	NODE	TEMP	NODE	TE
1	3760.5	2	3760.5	3	3760.5	4	3760.5	5	376
6	3760.5	7	3760.5	8	2694.7	9	2694.7	10	269
11	2694.7	12	2694.7	13	2694.7	14	2694.7	15	162
16	1629.1	17	1629.1	18	1629.1	19	1629.1	20	162
21	1629.1	22	565.47	23	565.47	24	565.47	25	565
26	565.47	27	565.47	28	565.47	29	532.67	30	532
31	532.67	32	532.67	33	532.67	34	532.67	35	532
36	499.43	37	499.43	38	499.43	39	499.43	40	499
41	499.43	42	499.43	43	465.74	44	465.74	45	465
46	465.74	47	465.74	48	465.74	49	465.74	50	458
51	458.35	52	458.35	53	458.35	54	458.35	55	458
56	458.35	57	449.51	58	449.51	59	449.51	60	449
61	449.51	62	449.51	63	449.51	64	439.23	65	439
66	439.23	67	439.23	68	439.23	69	439.23	70	439
71	427.54	72	427.54	73	427.54	74	427.54	75	427
76	427.54	77	427.54	78	414.46	79	414.46	80	414
81	414.46	82	414.46	83	414.46	84	414.46	85	400
86	400.00	87	400.00	88	400.00	89	400.00	90	400
91	400.00								

MAXIMUM TEMPERATURE= 3760.5 AT NODE 1
MINIMUM TEMPERATURE= 400.00 AT NODE 91

***** ELEMENT HEAT FLOW RATES ***** TIME = 0.000000E+00 LOAD STEP= 1 ITER.= 10 CUM. ITER.

ELEMENT 1
HEAT FLOW INTO NODE 2 -0.970874E-02
HEAT FLOW INTO NODE 9 0.970878E-02
HEAT FLOW INTO NODE 8 0.970876E-02
HEAT FLOW INTO NODE 1 -0.970880E-02

ELEMENT 2
HEAT FLOW INTO NODE 3 -0.970875E-02
HEAT FLOW INTO NODE 10 0.970876E-02
HEAT FLOW INTO NODE 9 0.970875E-02
HEAT FLOW INTO NODE 2 -0.970876E-02

ELEMENT 3
HEAT FLOW INTO NODE 4 -0.970875E-02
HEAT FLOW INTO NODE 11 0.970875E-02
HEAT FLOW INTO NODE 10 0.970875E-02
HEAT FLOW INTO NODE 3 -0.970875E-02

ELEMENT 4
HEAT FLOW INTO NODE 5 -0.970875E-02
HEAT FLOW INTO NODE 12 0.970875E-02
HEAT FLOW INTO NODE 11 0.970875E-02
HEAT FLOW INTO NODE 4 -0.970875E-02

ELEMENT 5
HEAT FLOW INTO NODE 6 -0.970876E-02
HEAT FLOW INTO NODE 13 0.970875E-02
HEAT FLOW INTO NODE 12 0.970876E-02
HEAT FLOW INTO NODE 5 -0.970875E-02

ELEMENT 6
HEAT FLOW INTO NODE 7 -0.970880E-02
HEAT FLOW INTO NODE 14 0.970876E-02
HEAT FLOW INTO NODE 13 0.970878E-02
HEAT FLOW INTO NODE 6 -0.970874E-02

ELEMENT 7
HEAT FLOW INTO NODE 9 -0.970876E-02
HEAT FLOW INTO NODE 16 0.970876E-02
HEAT FLOW INTO NODE 15 0.970876E-02
HEAT FLOW INTO NODE 8 -0.970876E-02

ELEMENT 8
HEAT FLOW INTO NODE 10 -0.970875E-02
HEAT FLOW INTO NODE 17 0.970876E-02
HEAT FLOW INTO NODE 16 0.970876E-02
HEAT FLOW INTO NODE 9 -0.970876E-02

ELEMENT 9
HEAT FLOW INTO NODE 11 -0.970875E-02

```
HEAT FLOW INTO NODE    16  0.970875E-02
HEAT FLOW INTO NODE    17  0.970875E-02
HEAT FLOW INTO NODE    10 -0.970876E-02

ELEMENT    10
HEAT FLOW INTO NODE    12 -0.970876E-02
HEAT FLOW INTO NODE    19  0.970875E-02
HEAT FLOW INTO NODE    18  0.970876E-02
HEAT FLOW INTO NODE    11 -0.970875E-02

ELEMENT    11
HEAT FLOW INTO NODE    13 -0.970876E-02
HEAT FLOW INTO NODE    20  0.970876E-02
HEAT FLOW INTO NODE    19  0.970876E-02
HEAT FLOW INTO NODE    12 -0.970875E-02

ELEMENT    12
HEAT FLOW INTO NODE    14 -0.970876E-02
HEAT FLOW INTO NODE    21  0.970876E-02
HEAT FLOW INTO NODE    20  0.970876E-02
HEAT FLOW INTO NODE    13 -0.970876E-02

ELEMENT    13
HEAT FLOW INTO NODE    16 -0.970876E-02
HEAT FLOW INTO NODE    23  0.970876E-02
HEAT FLOW INTO NODE    22  0.970876E-02
HEAT FLOW INTO NODE    15 -0.970876E-02

ELEMENT    14
HEAT FLOW INTO NODE    17 -0.970876E-02
HEAT FLOW INTO NODE    24  0.970876E-02
HEAT FLOW INTO NODE    23  0.970876E-02
HEAT FLOW INTO NODE    16 -0.970876E-02

ELEMENT    15
HEAT FLOW INTO NODE    18 -0.970876E-02
HEAT FLOW INTO NODE    25  0.970876E-02
HEAT FLOW INTO NODE    24  0.970876E-02
HEAT FLOW INTO NODE    17 -0.970876E-02

ELEMENT    16
HEAT FLOW INTO NODE    19 -0.970876E-02
HEAT FLOW INTO NODE    26  0.970876E-02
HEAT FLOW INTO NODE    25  0.970876E-02
HEAT FLOW INTO NODE    18 -0.970876E-02

ELEMENT    17
HEAT FLOW INTO NODE    20 -0.970876E-02
HEAT FLOW INTO NODE    27  0.970876E-02
HEAT FLOW INTO NODE    26  0.970876E-02
HEAT FLOW INTO NODE    19 -0.970876E-02

ELEMENT    18
HEAT FLOW INTO NODE    21 -0.970876E-02
HEAT FLOW INTO NODE    28  0.970876E-02
HEAT FLOW INTO NODE    27  0.970876E-02
HEAT FLOW INTO NODE    20 -0.970876E-02

ELEMENT    19
HEAT FLOW INTO NODE    23 -0.970876E-02
HEAT FLOW INTO NODE    30  0.970876E-02
HEAT FLOW INTO NODE    29  0.970876E-02
HEAT FLOW INTO NODE    22 -0.970876E-02

ELEMENT    20
HEAT FLOW INTO NODE    24 -0.970876E-02
HEAT FLOW INTO NODE    31  0.970876E-02
HEAT FLOW INTO NODE    30  0.970876E-02
HEAT FLOW INTO NODE    23 -0.970876E-02

ELEMENT    21
HEAT FLOW INTO NODE    25 -0.970876E-02
HEAT FLOW INTO NODE    32  0.970876E-02
HEAT FLOW INTO NODE    31  0.970876E-02
HEAT FLOW INTO NODE    24 -0.970876E-02

ELEMENT    22
HEAT FLOW INTO NODE    26 -0.970876E-02
HEAT FLOW INTO NODE    33  0.970876E-02
HEAT FLOW INTO NODE    32  0.970876E-02
HEAT FLOW INTO NODE    25 -0.970876E-02

ELEMENT    23
HEAT FLOW INTO NODE    27 -0.970876E-02
```

```
HEAT FLOW INTO NODE    34  0.970876E-02
HEAT FLOW INTO NODE    33  0.970876E-02
HEAT FLOW INTO NODE    26 -0.970876E-02

ELEMENT    24
HEAT FLOW INTO NODE    28 -0.970876E-02
HEAT FLOW INTO NODE    35  0.970876E-02
HEAT FLOW INTO NODE    34  0.970876E-02
HEAT FLOW INTO NODE    27 -0.970876E-02

ELEMENT    25
HEAT FLOW INTO NODE    30 -0.970876E-02
HEAT FLOW INTO NODE    37  0.970876E-02
HEAT FLOW INTO NODE    36  0.970876E-02
HEAT FLOW INTO NODE    29 -0.970876E-02

ELEMENT    26
HEAT FLOW INTO NODE    31 -0.970876E-02
HEAT FLOW INTO NODE    38  0.970876E-02
HEAT FLOW INTO NODE    37  0.970876E-02
HEAT FLOW INTO NODE    30 -0.970876E-02

ELEMENT    27
HEAT FLOW INTO NODE    32 -0.970876E-02
HEAT FLOW INTO NODE    39  0.970876E-02
HEAT FLOW INTO NODE    38  0.970876E-02
HEAT FLOW INTO NODE    31 -0.970876E-02

ELEMENT    28
HEAT FLOW INTO NODE    33 -0.970876E-02
HEAT FLOW INTO NODE    40  0.970876E-02
HEAT FLOW INTO NODE    39  0.970876E-02
HEAT FLOW INTO NODE    32 -0.970876E-02

ELEMENT    29
HEAT FLOW INTO NODE    34 -0.970876E-02
HEAT FLOW INTO NODE    41  0.970876E-02
HEAT FLOW INTO NODE    40  0.970876E-02
HEAT FLOW INTO NODE    33 -0.970876E-02

ELEMENT    30
HEAT FLOW INTO NODE    35 -0.970876E-02
HEAT FLOW INTO NODE    42  0.970876E-02
HEAT FLOW INTO NODE    41  0.970876E-02
HEAT FLOW INTO NODE    34 -0.970876E-02

ELEMENT    31
HEAT FLOW INTO NODE    37 -0.970876E-02
HEAT FLOW INTO NODE    44  0.970876E-02
HEAT FLOW INTO NODE    43  0.970876E-02
HEAT FLOW INTO NODE    36 -0.970876E-02

ELEMENT    32
HEAT FLOW INTO NODE    38 -0.970876E-02
HEAT FLOW INTO NODE    45  0.970876E-02
HEAT FLOW INTO NODE    44  0.970876E-02
HEAT FLOW INTO NODE    37 -0.970876E-02

ELEMENT    33
HEAT FLOW INTO NODE    39 -0.970876E-02
HEAT FLOW INTO NODE    46  0.970876E-02
HEAT FLOW INTO NODE    45  0.970876E-02
HEAT FLOW INTO NODE    38 -0.970876E-02

ELEMENT    34
HEAT FLOW INTO NODE    40 -0.970876E-02
HEAT FLOW INTO NODE    47  0.970876E-02
HEAT FLOW INTO NODE    46  0.970876E-02
HEAT FLOW INTO NODE    39 -0.970876E-02

ELEMENT    35
HEAT FLOW INTO NODE    41 -0.970876E-02
HEAT FLOW INTO NODE    48  0.970876E-02
HEAT FLOW INTO NODE    47  0.970876E-02
HEAT FLOW INTO NODE    40 -0.970876E-02

ELEMENT    36
HEAT FLOW INTO NODE    42 -0.970876E-02
HEAT FLOW INTO NODE    49  0.970876E-02
HEAT FLOW INTO NODE    48  0.970876E-02
HEAT FLOW INTO NODE    41 -0.970876E-02

ELEMENT    37
HEAT FLOW INTO NODE    44 -0.970876E-02
```

```
HEAT FLOW INTO NODE    51  0.970876E-02
HEAT FLOW INTO NODE    50  0.970876E-02
HEAT FLOW INTO NODE    43 -0.970876E-02

ELEMENT    38
HEAT FLOW INTO NODE    45 -0.970876E-02
HEAT FLOW INTO NODE    52  0.970876E-02
HEAT FLOW INTO NODE    51  0.970876E-02
HEAT FLOW INTO NODE    44 -0.970876E-02

ELEMENT    39
HEAT FLOW INTO NODE    46 -0.970876E-02
HEAT FLOW INTO NODE    53  0.970876E-02
HEAT FLOW INTO NODE    52  0.970876E-02
HEAT FLOW INTO NODE    45 -0.970876E-02

ELEMENT    40
HEAT FLOW INTO NODE    47 -0.970876E-02
HEAT FLOW INTO NODE    54  0.970876E-02
HEAT FLOW INTO NODE    53  0.970876E-02
HEAT FLOW INTO NODE    46 -0.970876E-02

ELEMENT    41
HEAT FLOW INTO NODE    48 -0.970876E-02
HEAT FLOW INTO NODE    55  0.970876E-02
HEAT FLOW INTO NODE    54  0.970876E-02
HEAT FLOW INTO NODE    47 -0.970876E-02

ELEMENT    42
HEAT FLOW INTO NODE    49 -0.970876E-02
HEAT FLOW INTO NODE    56  0.970876E-02
HEAT FLOW INTO NODE    55  0.970876E-02
HEAT FLOW INTO NODE    48 -0.970876E-02

ELEMENT    43
HEAT FLOW INTO NODE    51 -0.970876E-02
HEAT FLOW INTO NODE    58  0.970876E-02
HEAT FLOW INTO NODE    57  0.970876E-02
HEAT FLOW INTO NODE    50 -0.970876E-02

ELEMENT    44
HEAT FLOW INTO NODE    52 -0.970876E-02
HEAT FLOW INTO NODE    59  0.970876E-02
HEAT FLOW INTO NODE    58  0.970876E-02
HEAT FLOW INTO NODE    51 -0.970876E-02

ELEMENT    45
HEAT FLOW INTO NODE    53 -0.970876E-02
HEAT FLOW INTO NODE    60  0.970876E-02
HEAT FLOW INTO NODE    59  0.970876E-02
HEAT FLOW INTO NODE    52 -0.970876E-02

ELEMENT    46
HEAT FLOW INTO NODE    54 -0.970876E-02
HEAT FLOW INTO NODE    61  0.970876E-02
HEAT FLOW INTO NODE    60  0.970876E-02
HEAT FLOW INTO NODE    53 -0.970876E-02

ELEMENT    47
HEAT FLOW INTO NODE    55 -0.970876E-02
HEAT FLOW INTO NODE    62  0.970876E-02
HEAT FLOW INTO NODE    61  0.970876E-02
HEAT FLOW INTO NODE    54 -0.970876E-02

ELEMENT    48
HEAT FLOW INTO NODE    56 -0.970876E-02
HEAT FLOW INTO NODE    63  0.970876E-02
HEAT FLOW INTO NODE    62  0.970876E-02
HEAT FLOW INTO NODE    55 -0.970876E-02

ELEMENT    49
HEAT FLOW INTO NODE    58 -0.970876E-02
HEAT FLOW INTO NODE    65  0.970876E-02
HEAT FLOW INTO NODE    64  0.970876E-02
HEAT FLOW INTO NODE    57 -0.970876E-02

ELEMENT    50
HEAT FLOW INTO NODE    59 -0.970876E-02
HEAT FLOW INTO NODE    66  0.970876E-02
HEAT FLOW INTO NODE    65  0.970876E-02
HEAT FLOW INTO NODE    58 -0.970876E-02

ELEMENT    51
HEAT FLOW INTO NODE    60 -0.970876E-02
```

```
HEAT FLOW INTO NODE    67  0.970876E-02
HEAT FLOW INTO NODE    66  0.970876E-02
HEAT FLOW INTO NODE    59 -0.970876E-02

ELEMENT    52
HEAT FLOW INTO NODE    61 -0.970876E-02
HEAT FLOW INTO NODE    68  0.970876E-02
HEAT FLOW INTO NODE    67  0.970876E-02
HEAT FLOW INTO NODE    60 -0.970876E-02

ELEMENT    53
HEAT FLOW INTO NODE    62 -0.970876E-02
HEAT FLOW INTO NODE    69  0.970876E-02
HEAT FLOW INTO NODE    68  0.970876E-02
HEAT FLOW INTO NODE    61 -0.970876E-02

ELEMENT    54
HEAT FLOW INTO NODE    63 -0.970876E-02
HEAT FLOW INTO NODE    70  0.970876E-02
HEAT FLOW INTO NODE    69  0.970876E-02
HEAT FLOW INTO NODE    62 -0.970876E-02

ELEMENT    55
HEAT FLOW INTO NODE    65 -0.970876E-02
HEAT FLOW INTO NODE    72  0.970876E-02
HEAT FLOW INTO NODE    71  0.970876E-02
HEAT FLOW INTO NODE    64 -0.970876E-02

ELEMENT    56
HEAT FLOW INTO NODE    66 -0.970876E-02
HEAT FLOW INTO NODE    73  0.970876E-02
HEAT FLOW INTO NODE    72  0.970876E-02
HEAT FLOW INTO NODE    65 -0.970876E-02

ELEMENT    57
HEAT FLOW INTO NODE    67 -0.970876E-02
HEAT FLOW INTO NODE    74  0.970876E-02
HEAT FLOW INTO NODE    73  0.970876E-02
HEAT FLOW INTO NODE    66 -0.970876E-02

ELEMENT    58
HEAT FLOW INTO NODE    68 -0.970876E-02
HEAT FLOW INTO NODE    75  0.970876E-02
HEAT FLOW INTO NODE    74  0.970876E-02
HEAT FLOW INTO NODE    67 -0.970876E-02

ELEMENT    59
HEAT FLOW INTO NODE    69 -0.970876E-02
HEAT FLOW INTO NODE    76  0.970876E-02
HEAT FLOW INTO NODE    75  0.970876E-02
HEAT FLOW INTO NODE    68 -0.970876E-02

ELEMENT    60
HEAT FLOW INTO NODE    70 -0.970876E-02
HEAT FLOW INTO NODE    77  0.970876E-02
HEAT FLOW INTO NODE    76  0.970876E-02
HEAT FLOW INTO NODE    69 -0.970876E-02

ELEMENT    61
HEAT FLOW INTO NODE    72 -0.970876E-02
HEAT FLOW INTO NODE    79  0.970876E-02
HEAT FLOW INTO NODE    78  0.970876E-02
HEAT FLOW INTO NODE    71 -0.970876E-02

ELEMENT    62
HEAT FLOW INTO NODE    73 -0.970876E-02
HEAT FLOW INTO NODE    80  0.970876E-02
HEAT FLOW INTO NODE    79  0.970876E-02
HEAT FLOW INTO NODE    72 -0.970876E-02

ELEMENT    63
HEAT FLOW INTO NODE    74 -0.970876E-02
HEAT FLOW INTO NODE    81  0.970876E-02
HEAT FLOW INTO NODE    80  0.970876E-02
HEAT FLOW INTO NODE    73 -0.970876E-02

ELEMENT    64
HEAT FLOW INTO NODE    75 -0.970876E-02
HEAT FLOW INTO NODE    82  0.970876E-02
HEAT FLOW INTO NODE    81  0.970876E-02
HEAT FLOW INTO NODE    74 -0.970876E-02

ELEMENT    65
HEAT FLOW INTO NODE    76 -0.970876E-02
```

```
 HEAT FLOW INTO NODE    65  0.970876E-02
 HEAT FLOW INTO NODE    82  0.970876E-02
 HEAT FLOW INTO NODE    75 -0.970876E-02

 ELEMENT    66
 HEAT FLOW INTO NODE    77 -0.970876E-02
 HEAT FLOW INTO NODE    84  0.970876E-02
 HEAT FLOW INTO NODE    83  0.970876E-02
 HEAT FLOW INTO NODE    76 -0.970876E-02

 ELEMENT    67
 HEAT FLOW INTO NODE    79 -0.970876E-02
 HEAT FLOW INTO NODE    86  0.970876E-02
 HEAT FLOW INTO NODE    85  0.970876E-02
 HEAT FLOW INTO NODE    78 -0.970876E-02

 ELEMENT    68
 HEAT FLOW INTO NODE    80 -0.970876E-02
 HEAT FLOW INTO NODE    87  0.970876E-02
 HEAT FLOW INTO NODE    86  0.970876E-02
 HEAT FLOW INTO NODE    79 -0.970876E-02

 ELEMENT    69
 HEAT FLOW INTO NODE    81 -0.970876E-02
 HEAT FLOW INTO NODE    88  0.970876E-02
 HEAT FLOW INTO NODE    87  0.970876E-02
 HEAT FLOW INTO NODE    80 -0.970876E-02

 ELEMENT    70
 HEAT FLOW INTO NODE    82 -0.970876E-02
 HEAT FLOW INTO NODE    89  0.970876E-02
 HEAT FLOW INTO NODE    88  0.970876E-02
 HEAT FLOW INTO NODE    81 -0.970876E-02

 ELEMENT    71
 HEAT FLOW INTO NODE    83 -0.970876E-02
 HEAT FLOW INTO NODE    90  0.970876E-02
 HEAT FLOW INTO NODE    89  0.970876E-02
 HEAT FLOW INTO NODE    82 -0.970876E-02

 ELEMENT    72
 HEAT FLOW INTO NODE    84 -0.970876E-02
 HEAT FLOW INTO NODE    91  0.970876E-02
 HEAT FLOW INTO NODE    90  0.970876E-02
 HEAT FLOW INTO NODE    83 -0.970876E-02
```

```
          ANSYS - ENGINEERING ANALYSIS SYSTEM  REVISION 4.0 E2      SOLAR TURBINES    AUG 1,1981
     SWANSON ANALYSIS SYSTEMS, INC.          HOUSTON, PENNSYLVANIA 15342   PHONE (412)746-3304  TWX 510

  THRUST CHAMBER MODEL                                                    10.1357    5/ 8/84 CP

   ***** NODAL HEAT FLOW RATES *****    TIME =  0.00000E+00  LOAD STEP=   1  ITERATION= 10  CUM. ITER.=

  NOTE - HEAT FLOW RATES ARE POSITIVE INTO THE NODE

    NODE       HEAT

     85    -0.970876E-02
     86    -0.194175E-01
     87    -0.194175E-01
     88    -0.194175E-01
     89    -0.194175E-01
     90    -0.194175E-01
     91    -0.970876E-02

  TOTAL    -0.116505

  *** LOAD STEP    1   ITER    10   COMPLETED.   TIME=  0.000000E+00  KUSE= 0  CUM. ITER.=    4
   STEADY STATE CONVERGENCE VALUE =   0.5384   AT NODE     22     CRITERION =   1.0000

  END OF INPUT ENCOUNTERED ON FILE27

  ***** INPUT FILE SWITCHED FROM FILE27 TO FILE18

  PRINTOUT RESUMED BY /GOP


  ***** ROUTINE COMPLETED *****  CP =        65.440

  /EOF ENCOUNTERED ON FILE18


  ***** RUN COMPLETED *****  CP=        65.4800    TIME=   10.1360
```

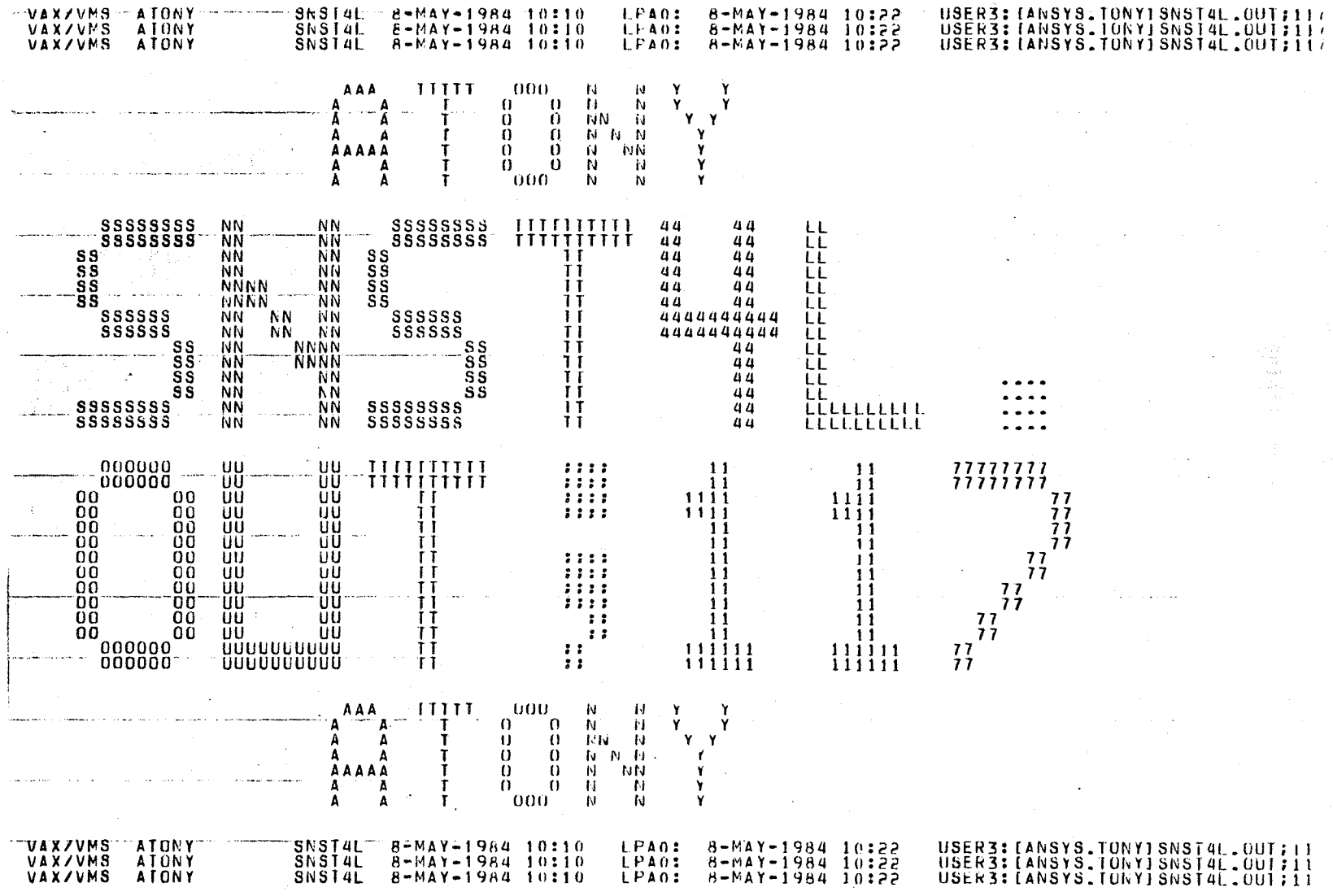
VAX/VMS ATONY SNST4L 8-MAY-1984 10:10 LPA0: 8-MAY-1984 10:22 USER3:[ANSYS.TONY]SNST4L.OUT;11
VAX/VMS ATONY SNST4L 8-MAY-1984 10:10 LPA0: 8-MAY-1984 10:22 USER3:[ANSYS.TONY]SNST4L.OUT;11
VAX/VMS ATONY SNST4L 8-MAY-1984 10:10 LPA0: 8-MAY-1984 10:22 USER3:[ANSYS.TONY]SNST4L.OUT;11
ANSYS
TONY
SNST4L
8-MAY-1984 10:10
LPA0:
8-MAY-1984 10:22
USER3:[ANSYS.TONY]SNST4L.OUT;11
VAX/VMS ATONY SNST4L 8-MAY-1984 10:10 LPA0: 8-MAY-1984 10:22 USER3:[ANSYS.TONY]SNST4L.OUT;11
VAX/VMS ATONY SNST4L 8-MAY-1984 10:10 LPA0: 8-MAY-1984 10:22 USER3:[ANSYS.TONY]SNST4L.OUT;11
VAX/VMS ATONY SNST4L 8-MAY-1984 10:10 LPA0: 8-MAY-1984 10:22 USER3:[ANSYS.TONY]SNST4L.OUT;11

```
          ********** ANSYS INPUT DATA LISTING (FILE18) **********

          6     12     18     24     30     36     42     48     54     60     66     72     78
          V     V      V      V      V      V      V      V      V      V      V      V      V
  1   /PREP7
  2   /TITLE THRUST CHAMBER MODEL
  3   /GOPR
  4   KAN,0
  5   TOFFST,0
  6   TREF,70.
  7   ET,1,42,,,1,2
  8   EX,1,6.6E6,-.002E6
  9   EX,2,18.25E6,.0012E6
 10   EX,3,17E6
 11   ALPX,1,3.97E-6,.0012E-6
 12   ALPX,2,7.529E-6,4.383E-9,1.007E-11,-7.202E-15,1.786E-18
 13   ALPX,3,9.8E-6
 14   DENS,1,1
 15   DENS,2,1
 16   DENS,3,1
 17   NUXY,1,.23
 18   NUXY,2,.23
 19   NUXY,3,.355
 20   N,1,1.2945,.009
 21   N,7,1.2945,0.
 22   FILL
 23   NGEN,4,7,1,7,1,0.0013333333
 24   NGEN,4,7,22,28,1,.0005
 25   N,50,1.3038889,.009
 26   N,56,1.3038889,0.
 27   FILL
 28   N,57,1.3085556,.009
 29   N,63,1.3085556,0.
 30   FILL
 31   N,64,1.314,.009
 32   N,70,1.314,0.
 33   FILL
 34   N,71,1.3202222,.009
 35   N,77,1.3202222,0.
 36   FILL
 37   N,78,1.3272222,.009
 38   N,84,1.3272222,0.
 39   FILL
 40   N,85,1.335,.009
 41   N,91,1.335,0.
 42   FILL
 43   MAT,1
 44   E,2,9,8,1
 45   EGEN,6,1,1
 46   EGEN,3,7,1,6
 47   MAT,2
 48   E,23,30,29,22
 49   EGEN,6,1,19
 50   EGEN,3,7,19,24

 51   MAT,3
 52   E,44,51,50,43
 53   EGEN,6,1,37
 54   EGEN,6,7,37,42
 55   ITER,-10,10
 56   KTEMP,1,10
 57   KBC,1
 58   KRF,1
 59   D,7,UY,0,,91,7
 60   CPSIZE,20
 61   CPNGEN,1,UY,1,85,7
 62   AFWRIT,1,1
 63   FINISH
 64   /INPUT,27
 65   /GOPR
 66   FINISH
 67   /EOF
 68
```

```
 MATERIAL    1              COEFFICIENTS OF DENS VS. TEMP EQUATION
  C0 =    1.000000

PROPERTY TABLE,DENS   MAT=    1  NUM. POINTS=  2
      ,TEMPERATURE      DATA          TEMPERATURE      DATA
     0.0000000E+00  1.000000        2300.000        1.000000

 MATERIAL    2              COEFFICIENTS OF DENS VS. TEMP EQUATION
  C0 =    1.000000

PROPERTY TABLE,DENS   MAT=    2  NUM. POINTS=  2
      ,TEMPERATURE      DATA          TEMPERATURE      DATA
     0.0000000E+00  1.000000        2300.000        1.000000

 MATERIAL    3              COEFFICIENTS OF DENS VS. TEMP EQUATION
  C0 =    1.000000

PROPERTY TABLE,DENS   MAT=    3  NUM. POINTS=  2
      ,TEMPERATURE      DATA          TEMPERATURE      DATA
     0.0000000E+00  1.000000        2300.000        1.000000

 MATERIAL    1              COEFFICIENTS OF NUXY VS. TEMP EQUATION
  C0 =    0.2300000

PROPERTY TABLE,NUXY   MAT=    1  NUM. POINTS=  2
       TEMPERATURE      DATA          TEMPERATURE      DATA
     0.0000000E+00 0.2300000        2300.000        0.2300000

 MATERIAL    2              COEFFICIENTS OF NUXY VS. TEMP EQUATION
  C0 =    0.2300000

PROPERTY TABLE,NUXY   MAT=    2  NUM. POINTS=  2
      ,TEMPERATURE      DATA          TEMPERATURE      DATA
     0.0000000E+00 0.2300000        2300.000        0.2300000

 MATERIAL    3              COEFFICIENTS OF NUXY VS. TEMP EQUATION
  C0 =    0.3550000

PROPERTY TABLE,NUXY   MAT=    3  NUM. POINTS=  2
      ,TEMPERATURE      DATA          TEMPERATURE      DATA
     0.0000000E+00 0.3550000        2300.000        0.3550000

NODE     1  KCS= 0  X,Y,Z=  1.2945      0.90000E-02 0.00000E+00

NODE     7  KCS= 0  X,Y,Z=  1.2945      0.00000E+00 0.00000E+00

FILL    5 POINTS BETWEEN NODE     1 AND NODE     7
  START WITH NODE     2 AND INCREMENT BY    1

GENERATE    4 TOTAL SETS OF NODES WITH INCREMENT     7
  SET IS FROM     1 TO     7 IN STEPS OF     1
  GEOMETRY INCREMENTS ARE 0.13333E-02 0.00000E+00 0.00000E+00

GENERATE    4 TOTAL SETS OF NODES WITH INCREMENT     7
  SET IS FROM    22 TO    28 IN STEPS OF     1
  GEOMETRY INCREMENTS ARE 0.50000E-03 0.00000E+00 0.00000E+00

NODE    50  KCS= 0  X,Y,Z=  1.3039      0.90000E-02 0.00000E+00

NODE    56  KCS= 0  X,Y,Z=  1.3039      0.00000E+00 0.00000E+00

FILL    5 POINTS BETWEEN NODE    50 AND NODE    56
  START WITH NODE    51 AND INCREMENT BY    1

NODE    57  KCS= 0  X,Y,Z=  1.3086      0.90000E-02 0.00000E+00

NODE    63  KCS= 0  X,Y,Z=  1.3086      0.00000E+00 0.00000E+00

FILL    5 POINTS BETWEEN NODE    57 AND NODE    63
  START WITH NODE    58 AND INCREMENT BY    1

NODE    64  KCS= 0  X,Y,Z=  1.3140      0.90000E-02 0.00000E+00

NODE    70  KCS= 0  X,Y,Z=  1.3140      0.00000E+00 0.00000E+00

FILL    5 POINTS BETWEEN NODE    64 AND NODE    70
  START WITH NODE    65 AND INCREMENT BY    1

NODE    71  KCS= 0  X,Y,Z=  1.3202      0.90000E-02 0.00000E+00

NODE    77  KCS= 0  X,Y,Z=  1.3202      0.00000E+00 0.00000E+00

FILL    5 POINTS BETWEEN NODE    71 AND NODE    77
  START WITH NODE    72 AND INCREMENT BY    1
```

```
     ANSYS - ENGINEERING ANALYSIS SYSTEM  REVISION 4.0 E2      SOLAR TURBINES   AUG 1,1981
   SWANSON ANALYSIS SYSTEMS, INC.        HOUSTON, PENNSYLVANIA 15342   PHONE (412)746-3304  TWX 5
 TITLE                                                                  10.1389    5/ 8/84 (

       ***** ANSYS ANALYSIS DEFINITION (PREP7) *****

 NEW TITLE=  THRUST CHAMBER MODEL

 PRINTOUT RESUMED BY /GOP

 ANALYSIS TYPE=  0

 TEMPERATURE OFFSET FROM ABSOLUTE ZERO=    0.000

 REFERENCE TEMPERATURE=  70.000  (TUNIF=  70.000)

 ELEMENT TYPE  1 USES STIF42
  KEYOPT(1-9)=   0   0   1     2   0   0       0   0   0  INOTPR= 0  NUMBER OF NODES=    4

 ISOPAR, STRESS SOLID, 2-D

 CURRENT NODAL DOF SET IS  UX    UY

 TWO-DIMENSIONAL STRUCTURE

  MATERIAL    1          COEFFICIENTS OF EX    VS. TEMP EQUATION
   C0 =    6600000.      C1 =   -2000.000      C2 =  0.0000000E+00
   C3 =  0.0000000E+00   C4 =   0.0000000E+00

 PROPERTY TABLE,EX    MAT=   1  NUM. POINTS=  2
       TEMPERATURE      DATA          TEMPERATURE      DATA
     0.0000000E+00   6600000.        2300.000       2000000.

  MATERIAL    2          COEFFICIENTS OF EX    VS. TEMP EQUATION
   C0 =  0.1825000E+08   C1 =    1200.000      C2 =  0.0000000E+00
   C3 =  0.0000000E+00   C4 =   0.0000000E+00

 PROPERTY TABLE,EX    MAT=   2  NUM. POINTS=  2
       TEMPERATURE      DATA          TEMPERATURE      DATA
     0.0000000E+00 0.1825000E+08   2300.000      0.2101000E+08

  MATERIAL    3          COEFFICIENTS OF EX    VS. TEMP EQUATION
   C0 =  0.1700000E+08

 PROPERTY TABLE,EX    MAT=   3  NUM. POINTS=  2
       TEMPERATURE      DATA          TEMPERATURE      DATA
     0.0000000E+00 0.1700000E+08   2300.000      0.1700000E+08

  MATERIAL    1          COEFFICIENTS OF ALPX VS. TEMP EQUATION
   C0 =  0.3970000E-05   C1 =  0.1200000E-08   C2 =  0.0000000E+00
   C3 =  0.0000000E+00   C4 =   0.0000000E+00

 PROPERTY TABLE,ALPX  MAT=   1  NUM. POINTS=  2
       TEMPERATURE      DATA          TEMPERATURE      DATA
     0.0000000E+00 0.3970000E-05   2300.000      0.6730000E-05

  MATERIAL    2          COEFFICIENTS OF ALPX VS. TEMP EQUATION
   C0 =  0.7529000E-05   C1 =  0.4383000E-08   C2 =  0.1007000E-10
   C3 = -0.7202000E-14   C4 =   0.1786000E-17

 PROPERTY TABLE,ALPX  MAT=   2  NUM. POINTS= 24
       TEMPERATURE      DATA          TEMPERATURE      DATA
     0.0000000E+00 0.7529000E-05    100.0000      0.8060977E-05
      200.0000      0.8753642E-05    300.0000      0.9570213E-05
      400.0000      0.1047819E-04    500.0000      0.1144938E-04
      600.0000      0.1245983E-04    700.0000      0.1348993E-04
      800.0000      0.1452432E-04    900.0000      0.1555194E-04
      1000.000      0.1656600E-04    1100.000      0.1756402E-04
      1200.000      0.1854779E-04    1300.000      0.1952340E-04
      1400.000      0.2050121E-04    1500.000      0.2149588E-04
      1600.000      0.2252634E-04    1700.000      0.2361582E-04
      1800.000      0.2479185E-04    1900.000      0.2608621E-04
      2000.000      0.2753500E-04    2100.000      0.2917858E-04
      2200.000      0.3106163E-04    2300.000      0.3323307E-04

  MATERIAL    3          COEFFICIENTS OF ALPX VS. TEMP EQUATION
   C0 =  0.9800000E-05

 PROPERTY TABLE,ALPX  MAT=   3  NUM. POINTS=  2
       TEMPERATURE      DATA          TEMPERATURE      DATA
     0.0000000E+00 0.9800000E-05   2300.000      0.9800000E-05
```

```
 NODE    78  KCS= 0  X,Y,Z=  1.3272      0.90000E-02 0.00000E+00

 NODE    84  KCS= 0  X,Y,Z=  1.3272      0.00000E+00 0.00000E+00

 FILL    5 POINTS BETWEEN NODE    78 AND NODE    84
  START WITH NODE    79 AND INCREMENT BY    1

 NODE    85  KCS= 0  X,Y,Z=  1.3350      0.90000E-02 0.00000E+00

 NODE    91  KCS= 0  X,Y,Z=  1.3350      0.00000E+00 0.00000E+00

 FILL    5 POINTS BETWEEN NODE    85 AND NODE    91
  START WITH NODE    86 AND INCREMENT BY    1

 MATERIAL NUMBER SET TO  1
 ELEMENT     1       2       9       8       1

 GENERATE    6 TOTAL SETS OF ELEMENTS WITH NODE INCREMENT OF     1
    SET IS    1 TO    1 IN STEPS OF  1
 NUMBER OF ELEMENTS=      6

 GENERATE    3 TOTAL SETS OF ELEMENTS WITH NODE INCREMENT OF     7
    SET IS    1 TO    6 IN STEPS OF  1
 NUMBER OF ELEMENTS=     18

 MATERIAL NUMBER SET TO  2
 ELEMENT    19      23      30      29      22

 GENERATE    6 TOTAL SETS OF ELEMENTS WITH NODE INCREMENT OF     1
    SET IS   19 TO   19 IN STEPS OF  1
 NUMBER OF ELEMENTS=     24

 GENERATE    3 TOTAL SETS OF ELEMENTS WITH NODE INCREMENT OF     7
    SET IS   19 TO   24 IN STEPS OF  1
 NUMBER OF ELEMENTS=     36

 MATERIAL NUMBER SET TO  3
 ELEMENT    37      44      51      50      43

 GENERATE    6 TOTAL SETS OF ELEMENTS WITH NODE INCREMENT OF     1
    SET IS   37 TO   37 IN STEPS OF  1
 NUMBER OF ELEMENTS=     42

 GENERATE    6 TOTAL SETS OF ELEMENTS WITH NODE INCREMENT OF     7
    SET IS   37 TO   42 IN STEPS OF  1
 NUMBER OF ELEMENTS=     72

 NITTER=    -10  NPRINT=     10  NPOST=     10
 BOUNDARY CONDITIONS STEPPED DUE TO NEGATIVE NITTER

 ALL PRINT CONTROLS RESET TO     10

 ALL POST DATA FILE CONTROLS RESET TO     10

 KTEMP=      1     10

 TEMPERATURES FROM LOAD STEP=      1  ITERATION=     10

 STEP BOUNDARY CONDITION KEY= 1

 REACTION FORCE KEY= 1

 SPECIFIED DISP UY    FROM NODE       7 TO NODE      91 IN STEPS OF      7
  VALUES= 0.00000E+00 0.00000E+00  ADDITIONAL DOFS=

 SET MAXIMUM COUPLED NODE SET SIZE TO  20

 GENERATE ADDITIONAL NODES ON SET=      1  DIRECTION= UY
 STARTING NODE=      1  ENDING NODE=     85  NODE INC.=      7

 COUPLED SET=      1  DIRECTION= UY     TOTAL NODES=     13
 NODES=      1       8      15      22      29      36      43      50      57      64
            71      78      85

 MAXIMUM COUPLED SET NUMBER=    1

 DATA CHECKED - NO FATAL ERRORS FOUND.
 CHECK OUTPUT FOR POSSIBLE WARNING MESSAGES.

 ANALYSIS DATA WRITTEN ON FILE27 (   246 LINES)

 ALL CURRENT PREP7 DATA WRITTEN TO FILE16
  FOR POSSIBLE RESUME FROM THIS POINT
```

```
***** NOTICE ***** THIS IS THE ANSYS GENERAL PURPOSE
FINITE ELEMENT COMPUTER PROGRAM. NEITHER SWANSON ANALYSIS
SYSTEMS, INC. NOR THE CORPORATION SUPPLYING THE COMPUTER
FACILITIES FOR THIS ANALYSIS ASSUME ANY RESPONSIBILITY FOR
THE VALIDITY, ACCURACY, OR APPLICABILITY OF ANY RESULTS
OBTAINED FROM THE ANSYS SYSTEM. THE USER MUST VERIFY HIS
OWN RESULTS.

SWANSON ANALYSIS SYSTEMS,INC. IS ENDEAVORING TO MAKE THE
ANSYS PROGRAM AS COMPLETE, ACCURATE, AND EASY TO USE AS
POSSIBLE. SUGGESTIONS AND COMMENTS ARE WELCOMED. ANY
ERRORS ENCOUNTERED IN EITHER THE DOCUMENTATION OR THE
RESULTS SHOULD BE IMMEDIATELY BROUGHT TO OUR ATTENTION.

***** ANALYSIS OPTIONS *****

                                    VALUE

ANALYSIS TYPE . . . . . .          0
COUPLED DEGREES OF FREEDOM KEY     1
ELEMENT CONSTANT TABLE . . .       6
REACTION FORCE KEY . . . . .       1
MASTER DOF READ KEY . . . . .      1
MATERIAL TABLE ENTRIES. . . .     24

REFERENCE TEMPERATURE . . . .   70.00
UNIFORM TEMPERATURE . . . . .   70.00

***** ELEMENT TYPES *****

TYPE  STIF        DESCRIPTION                KEY OPTIONS                    NJ   INOTP
                                             1  2  3   4  5  6   7  8  9

  1    42   ISOPAR. STRESS SOLID, P-D        0  0  1   2  0  0   0  0  0    0     0

NUMBER OF ELEMENT TYPES=   1

NO.       ***** TABLE OF ELEMENT REAL CONSTANTS *****

NUMBER OF REAL CONSTANT SETS=    0
```

***** ELEMENT DEFINITIONS *****

ELEMENT	NODES				MAT	TYPE	CLASS	ELEMENT REAL CONSTANTS
1	2	9	8	1	1	1	0	
2	3	10	9	2	1	1	0	
3	4	11	10	3	1	1	0	
4	5	12	11	4	1	1	0	
5	6	13	12	5	1	1	0	
6	7	14	13	6	1	1	0	
7	9	16	15	8	1	1	0	
8	10	17	16	9	1	1	0	
9	11	18	17	10	1	1	0	
10	12	19	18	11	1	1	0	
11	13	20	19	12	1	1	0	
12	14	21	20	13	1	1	0	
13	16	23	22	15	1	1	0	
14	17	24	23	16	1	1	0	
15	18	25	24	17	1	1	0	
16	19	26	25	18	1	1	0	
17	20	27	26	19	1	1	0	
18	21	28	27	20	1	1	0	
19	23	30	29	22	2	1	0	
20	24	31	30	23	2	1	0	
21	25	32	31	24	2	1	0	
22	26	33	32	25	2	1	0	
23	27	34	33	26	2	1	0	
24	28	35	34	27	2	1	0	
25	30	37	36	29	2	1	0	
26	31	38	37	30	2	1	0	
27	32	39	38	31	2	1	0	
28	33	40	39	32	2	1	0	
29	34	41	40	33	2	1	0	
30	35	42	41	34	2	1	0	
31	37	44	43	36	2	1	0	
32	38	45	44	37	2	1	0	
33	39	46	45	38	2	1	0	
34	40	47	46	39	2	1	0	
35	41	48	47	40	2	1	0	
36	42	49	48	41	2	1	0	
37	44	51	50	43	3	1	0	
38	45	52	51	44	3	1	0	
39	46	53	52	45	3	1	0	
40	47	54	53	46	3	1	0	
41	48	55	54	47	3	1	0	
42	49	56	55	48	3	1	0	
43	51	58	57	50	3	1	0	
44	52	59	58	51	3	1	0	
45	53	60	59	52	3	1	0	
46	54	61	60	53	3	1	0	
47	55	62	61	54	3	1	0	
48	56	63	62	55	3	1	0	
49	58	65	64	57	3	1	0	
50	59	66	65	58	3	1	0	
51	60	67	66	59	3	1	0	
52	61	68	67	60	3	1	0	
53	62	69	68	61	3	1	0	
54	63	70	69	62	3	1	0	
55	65	72	71	64	3	1	0	
56	66	73	72	65	3	1	0	
57	67	74	73	66	3	1	0	
58	68	75	74	67	3	1	0	
59	69	76	75	68	3	1	0	
60	70	77	76	69	3	1	0	
61	72	79	78	71	3	1	0	
62	73	80	79	72	3	1	0	
63	74	81	80	73	3	1	0	
64	75	82	81	74	3	1	0	
65	76	83	82	75	3	1	0	
66	77	84	83	76	3	1	0	
67	79	86	85	78	3	1	0	
68	80	87	86	79	3	1	0	
69	81	88	87	80	3	1	0	
70	82	89	88	81	3	1	0	
71	83	90	89	82	3	1	0	
72	84	91	90	83	3	1	0	

INTEGER STORAGE REQUIREMENTS FOR ELEMENT INPUT CP= 11.140 TIME= 10.14551
MEMORY I= 1001 MEMORY II= 182 TOTAL= 1183 MEMORY AVAILABLE= 340000
MAXIMUM NODE NUMBER FOR AVAILABLE AUXILIARY MEMORY SIZE= 169498

NUMBER OF ELEMENTS = 72 MAXIMUM NODE NUMBER USED = 91

LOCATION ROTATION

NODE	X (OR R)	Y (OR THETA)	THXY (OR RT)
1	1.2945	0.90000E-02	0.00000E+00
2	1.2945	0.75000E-02	0.00000E+00
3	1.2945	0.60000E-02	0.00000E+00
4	1.2945	0.45000E-02	0.00000E+00
5	1.2945	0.30000E-02	0.00000E+00
6	1.2945	0.15000E-02	0.00000E+00
7	1.2945	0.00000E+00	0.00000E+00
8	1.2958	0.90000E-02	0.00000E+00
9	1.2958	0.75000E-02	0.00000E+00
10	1.2958	0.60000E-02	0.00000E+00
11	1.2958	0.45000E-02	0.00000E+00
12	1.2958	0.30000E-02	0.00000E+00
13	1.2958	0.15000E-02	0.00000E+00
14	1.2958	0.00000E+00	0.00000E+00
15	1.2972	0.90000E-02	0.00000E+00
16	1.2972	0.75000E-02	0.00000E+00
17	1.2972	0.60000E-02	0.00000E+00
18	1.2972	0.45000E-02	0.00000E+00
19	1.2972	0.30000E-02	0.00000E+00
20	1.2972	0.15000E-02	0.00000E+00
21	1.2972	0.00000E+00	0.00000E+00
22	1.2985	0.90000E-02	0.00000E+00
23	1.2985	0.75000E-02	0.00000E+00
24	1.2985	0.60000E-02	0.00000E+00
25	1.2985	0.45000E-02	0.00000E+00
26	1.2985	0.30000E-02	0.00000E+00
27	1.2985	0.15000E-02	0.00000E+00
28	1.2985	0.00000E+00	0.00000E+00
29	1.2990	0.90000E-02	0.00000E+00
30	1.2990	0.75000E-02	0.00000E+00
31	1.2990	0.60000E-02	0.00000E+00
32	1.2990	0.45000E-02	0.00000E+00
33	1.2990	0.30000E-02	0.00000E+00
34	1.2990	0.15000E-02	0.00000E+00
35	1.2990	0.00000E+00	0.00000E+00
36	1.2995	0.90000E-02	0.00000E+00
37	1.2995	0.75000E-02	0.00000E+00
38	1.2995	0.60000E-02	0.00000E+00
39	1.2995	0.45000E-02	0.00000E+00
40	1.2995	0.30000E-02	0.00000E+00
41	1.2995	0.15000E-02	0.00000E+00
42	1.2995	0.00000E+00	0.00000E+00
43	1.3000	0.90000E-02	0.00000E+00
44	1.3000	0.75000E-02	0.00000E+00
45	1.3000	0.60000E-02	0.00000E+00
46	1.3000	0.45000E-02	0.00000E+00
47	1.3000	0.30000E-02	0.00000E+00
48	1.3000	0.15000E-02	0.00000E+00
49	1.3000	0.00000E+00	0.00000E+00
50	1.3039	0.90000E-02	0.00000E+00
51	1.3039	0.75000E-02	0.00000E+00
52	1.3039	0.60000E-02	0.00000E+00
53	1.3039	0.45000E-02	0.00000E+00
54	1.3039	0.30000E-02	0.00000E+00
55	1.3039	0.15000E-02	0.00000E+00
56	1.3039	0.00000E+00	0.00000E+00
57	1.3086	0.90000E-02	0.00000E+00
58	1.3086	0.75000E-02	0.00000E+00
59	1.3086	0.60000E-02	0.00000E+00
60	1.3086	0.45000E-02	0.00000E+00
61	1.3086	0.30000E-02	0.00000E+00
62	1.3086	0.15000E-02	0.00000E+00
63	1.3086	0.00000E+00	0.00000E+00
64	1.3140	0.90000E-02	0.00000E+00
65	1.3140	0.75000E-02	0.00000E+00
66	1.3140	0.60000E-02	0.00000E+00
67	1.3140	0.45000E-02	0.00000E+00
68	1.3140	0.30000E-02	0.00000E+00
69	1.3140	0.15000E-02	0.00000E+00
70	1.3140	0.00000E+00	0.00000E+00
71	1.3202	0.90000E-02	0.00000E+00
72	1.3202	0.75000E-02	0.00000E+00
73	1.3202	0.60000E-02	0.00000E+00
74	1.3202	0.45000E-02	0.00000E+00
75	1.3202	0.30000E-02	0.00000E+00
76	1.3202	0.15000E-02	0.00000E+00
77	1.3202	0.00000E+00	0.00000E+00
78	1.3272	0.90000E-02	0.00000E+00
79	1.3272	0.75000E-02	0.00000E+00
80	1.3272	0.60000E-02	0.00000E+00
81	1.3272	0.45000E-02	0.00000E+00
82	1.3272	0.30000E-02	0.00000E+00
83	1.3272	0.15000E-02	0.00000E+00
84	1.3272	0.00000E+00	0.00000E+00
85	1.3350	0.90000E-02	0.00000E+00
86	1.3350	0.75000E-02	0.00000E+00
87	1.3350	0.60000E-02	0.00000E+00
88	1.3350	0.45000E-02	0.00000E+00
89	1.3350	0.30000E-02	0.00000E+00
90	1.3350	0.15000E-02	0.00000E+00
91	1.3350	0.00000E+00	0.00000E+00

XMIN= 1.295 XMAX= 1.335 YMIN= 0.0000E+00 YMAX= 0.9000E-02 ZMIN= 0.0000E+00 ZMAX=

INTEGER STORAGE REQUIREMENTS FOR NODE INPUT CP= 14.970 TIME= 10.14771
MEMORY I= 0 MEMORY II= 546 TOTAL= 546 MEMORY AVAILABLE= 340000
MAXIMUM NODE NUMBER FOR AVAILABLE AUXILIARY MEMORY SIZE= 113333

***** MATERIAL PROPERTIES *****

TERIAL 1

X PROPERTY TABLE (LINEAR INTERPOLATION)

MP	EX	TEMP	EX	TEMP	EX	TEMP	EX	TEMP	EX
0.0	0.66000E+07	2300.0	0.20000E+07						

TERIAL 2

X PROPERTY TABLE (LINEAR INTERPOLATION)

MP	EX	TEMP	EX	TEMP	EX	TEMP	EX	TEMP	EX
0.0	0.18250E+08	2300.0	0.21010E+08						

TERIAL 3

X PROPERTY TABLE (LINEAR INTERPOLATION)

MP	EX	TEMP	EX	TEMP	EX	TEMP	EX	TEMP	EX
0.0	0.17000E+08	2300.0	0.17000E+08						

TERIAL 1

LPX PROPERTY TABLE (LINEAR INTERPOLATION)

MP	ALPX	TEMP	ALPX	TEMP	ALPX	TEMP	ALPX	TEMP	ALPX
0.0	0.39700E-05	2300.0	0.67300E-05						

TERIAL 2

LPX PROPERTY TABLE (LINEAR INTERPOLATION)

MP	ALPX	TEMP	ALPX	TEMP	ALPX	TEMP	ALPX	TEMP	ALPX
0.0	0.75290E-05	100.0	0.80610E-05	200.0	0.87536E-05	300.0	0.95702E-05	400.0	0.10478E-
500.0	0.11449E-04	600.0	0.12460E-04	700.0	0.13490E-04	800.0	0.14524E-04	900.0	0.15552E-
000.0	0.16566E-04	1100.0	0.17564E-04	1200.0	0.18548E-04	1300.0	0.19523E-04	1400.0	0.20501E-
500.0	0.21496E-04	1600.0	0.22526E-04	1700.0	0.23616E-04	1800.0	0.24792E-04	1900.0	0.26086E-
000.0	0.27535E-04	2100.0	0.29179E-04	2200.0	0.31062E-04	2300.0	0.33233E-04		

TERIAL 3

LPX PROPERTY TABLE (LINEAR INTERPOLATION)

MP	ALPX	TEMP	ALPX	TEMP	ALPX	TEMP	ALPX	TEMP	ALPX
0.0	0.98000E-05	2300.0	0.98000E-05						

TERIAL 1

ENS PROPERTY TABLE (LINEAR INTERPOLATION)

MP	DENS	TEMP	DENS	TEMP	DENS	TEMP	DENS	TEMP	DENS
0.0	1.0000	2300.0	1.0000						

TERIAL 2

ENS PROPERTY TABLE (LINEAR INTERPOLATION)

MP	DENS	TEMP	DENS	TEMP	DENS	TEMP	DENS	TEMP	DENS
0.0	1.0000	2300.0	1.0000						

TERIAL 3

ENS PROPERTY TABLE (LINEAR INTERPOLATION)

MP	DENS	TEMP	DENS	TEMP	DENS	TEMP	DENS	TEMP	DENS
0.0	1.0000	2300.0	1.0000						

```
 MATERIAL    1

  NUXY PROPERTY TABLE (LINEAR INTERPOLATION)
 TEMP        NUXY        TEMP        NUXY        TEMP        NUXY        TEMP        NUXY        TEMP
------------------------------------------------------------------------------------------------------
     0.0  0.23000        2300.0  0.23000

 MATERIAL    2

------------------------------------------------------------------------------------------------------
  NUXY PROPERTY TABLE (LINEAR INTERPOLATION)
 TEMP        NUXY        TEMP        NUXY        TEMP        NUXY        TEMP        NUXY        TEMP
------------------------------------------------------------------------------------------------------
     0.0  0.23000        2300.0  0.23000

 MATERIAL    3

------------------------------------------------------------------------------------------------------
  NUXY PROPERTY TABLE (LINEAR INTERPOLATION)
 TEMP        NUXY        TEMP        NUXY        TEMP        NUXY        TEMP        NUXY        TEMP
------------------------------------------------------------------------------------------------------
     0.0  0.35500        2300.0  0.35500

MAXIMUM MATERIAL NUMBER=    3

------------------------------------------------------------------------------------------------------
            ***** COUPLED DEG. OF FR. DEFINITIONS *****

  SET   D.O.F.        NUMBER          COUPLED NODES
------------------------------------------------------------------------------------------------------
    1   UY              13              1       8      15      22      29      36      43      50      57
                                       71      78      85

NUMBER OF COUPLED SETS=    1

------------------------------------------------------------------------------------------------------
            ***** MASTER DEGREES OF FREEDOM *****

   NODF        DEGREES OF FREEDOM LIST

NUMBER OF SPECIFIED MASTER D.O.F.=      0
TOTAL NUMBER OF MASTER D.O.F.    =      0

 INTEGER STORAGE REQUIREMENTS FOR MATERIALS, ETC. INPUT          CP=     17.870   TIME= 10.14935
MEMORY I=     2172  MEMORY II=        0  TOTAL=     2172  MEMORY AVAILABLE=   340000

*** LOAD STEP    1  OPTIONS SPECIFICATIONS

NITTER=     -10  NPRINT=     10  NPOST=     10

ALL PRINT CONTROLS RESET TO     10

ALL POST DATA FILE CONTROLS RESET TO     10

ACEL= 0.00000E+00 0.00000E+00 0.00000E+00

OMEGA= 0.00000E+00 0.00000E+00 0.00000E+00

DOMEGA= 0.00000E+00 0.00000E+00 0.00000E+00

CGLOC= 0.00000E+00 0.00000E+00 0.00000E+00

CGOMEGA= 0.00000E+00 0.00000E+00 0.00000E+00

DOMEGA= 0.00000E+00 0.00000E+00 0.00000E+00

KTEMP=      1     10

TEMPERATURES FROM LOAD STEP=      1  ITERATION=     10

PLASTICITY CONVERGENCE CRITERION=      0.0100
CREEP OPTIMIZATION CRITERIA=      0.1000
LARGE DEFL. CONVERGENCE CRITERIA=     0.001000
DISPLACEMENT LIMIT= 0.00000E+00
KEY TO TERMINATE RUN IF NO CONVERGENCE=     0.

REACTION FORCE KEY= 1

UNIFORM TEMPERATURE=    70.000   (TREF=    70.000)
```

THRUST CHAMBER MODEL 10.1499 5/ 8/80

LOAD STEP NUMBER = 1

*** LOAD OPTIONS SUMMARY

TIME= 0.00000E+00 NITTER= -10

ACEL = 0.00000E+00 0.00000E+00 0.00000E+00
OMEGA = 0.00000E+00 0.00000E+00 0.00000E+00
DOMEGA= 0.00000E+00 0.00000E+00 0.00000E+00
CGLOC = 0.00000E+00 0.00000E+00 0.00000E+00
CGOMEG= 0.00000E+00 0.00000E+00 0.00000E+00
DCGOME= 0.00000E+00 0.00000E+00 0.00000E+00
TEMPERATURE (KTEMP) LOAD STEP= 1 ITERATION= 10
STIFFNESS REUSE KEY (KUSE)= 0

UNIFORM TEMPERATURE= 70.000 (TREF= 70.000)

PRINT ELEMENT FORCES AND REACTION FORCES (KRF=1)

LOADS STEPPED TO FINAL VALUES FOR ALL ITERATIONS (KBC= 1)
PLASTIC CONVERG. CRITERION= 0.0100
CREEP OPTIMUM. CRITERION= 0.1000
LARGE DEFL. CONVERG. CRITERION= 0.001000
DISPLACEMENT LIMIT= 0.00000E+00
KEY TO TERMINATE RUN IF NO CONVERGENCE= 0.
MODE= 0 ISYM= 1

NPRINT= 10 NPOST= 10 REACTION PRINT FREQ= 10
DISP. POST DATA FREQ= 10 REACT. POST DATA FREQ= 10

DISPLACEMENT PRINT FREQUENCIES

FREQ	NSTRT	NSTOP	NINC
10	1	32000	1

ELEMENT PRINT AND POST DATA FREQUENCIES

TYPE NO.	STIFF PRINT	STRESS PRINT	FORCE PRINT	STRESS DATA	DATA LEVEL	FORCE DATA
1	42	10	10	10	3	10

***** SPECIFIED DISPLACEMENTS *****

NODE	UX	UY
7		0.000000E+00
14		0.000000E+00
21		0.000000E+00
28		0.000000E+00
35		0.000000E+00
42		0.000000E+00
49		0.000000E+00
56		0.000000E+00
63		0.000000E+00
70		0.000000E+00
77		0.000000E+00
84		0.000000E+00
91		0.000000E+00

TEMPERATURE DATA READ FROM LOAD STEP= 1 ITER= 10 CUM. ITER= 4 ON FILE 4

***** LOAD SUMMARY - 13 DISPLACEMENTS 0 FORCES 0 PRESSURES *****

INTEGER STORAGE REQUIREMENTS FOR LOAD DATA INPUT CP= 23.430 TIME= 10.15279
MEMORY I= 1316 MEMORY II= 0 TOTAL= 1316 MEMORY AVAILABLE= 340000

***** CENTROID, MASS, AND MASS MOMENTS OF INERTIA *****

CALCULATIONS ASSUME ELEMENT MASS AT ELEMENT CENTROID

TOTAL MASS = 0.30111E-02

```
MASS AND MOMENT VALUES ARE EVALUATED FOR A 360. DEGREE MODEL.
THE BELOW TABLE IS BASED ON A WEIGHTED(MASS PROPORTIONAL TO RADIUS) AXISYMMETRIC SECTION.

                FIRST          FIRST MOMENT/MASS        SECOND      SQUARE ROOT OF
                MOMENT           (CENTROID)             MOMENT      SECOND MOMENT/MASS
                                                                    (RADIUS OF GYR.)

RADIAL       0.3959E-02          1.3149              0.5206E-02          1.315
AXIAL        0.1355E-04        0.45000E-02

  *** MASS SUMMARY BY ELEMENT TYPE ***

 TYPE        MASS
    1   0.301107E-02

 RANGE OF ELEMENT MAXIMUM STIFFNESS IN GLOBAL COORDINATES
MAXIMUM= 0.598372E+08   AT ELEMENT      72
MINIMUM= 0.133552E+07   AT ELEMENT       3

 INTEGER STORAGE REQUIREMENTS FOR ELEMENT FORMULATION              CP=     39.670  TIME= 10.15987
MEMORY I=     1314  MEMORY II=        0  TOTAL=     1314  MEMORY AVAILABLE=   340000

  *** ELEMENT STIFFNESS FORMULATION TIMES
 TYPE  NUMBER  STIF  TOTAL CP    AVE CP

    1      72     42     15.360     0.213

 TIME AT END OF ELEMENT STIFFNESS FORMULATION   CP =      39.690

 MAXIMUM IN-CORE WAVE FRONT ALLOWED FOR REQUESTED MEMORY SIZE=  579

 INTEGER STORAGE REQUIREMENTS FOR WAVE FRONT MATRIX SOLUTION       CP=     45.640  TIME= 10.16166
MEMORY I=     1314  MEMORY II=      361  TOTAL=     1675  MEMORY AVAILABLE=   340000

MAXIMUM IN-CORE WAVE FRONT (EQUATIONS) USED=  17

  *** MATRIX SOLUTION TIMES
 READ IN ELEMENT STIFFNESSES    CP=            3.170
 NODAL COORD. TRANSFORMATION    CP=            0.060
 MATRIX TRIANGULARIZATION       CP=            2.060

TIME AT END OF MATRIX TRIANGULARIZATION   CP=          45.660

 INTEGER STORAGE REQUIREMENTS FOR BACK SUBSTITUTION                CP=     46.400  TIME= 10.16193
MEMORY I=     1314  MEMORY II=      370  TOTAL=     1684  MEMORY AVAILABLE=   340000

  *** ELEM. STRESS CALC. TIMES
 TYPE  NUMBER  STIF  TOTAL CP    AVE CP

    1      72     42      6.230     0.087

  *** NODAL FORCE CALC. TIMES
 TYPE  NUMBER  STIF  TOTAL CP    AVE CP

    1      72     42      0.340     0.005

  *** LOAD STEP     1    ITER      1  COMPLETED.  TIME=  0.000000E+00  KUSE= 0  CUM. ITER.=     1

  *** SOLUTION CONVERGED - LOAD STEP    1  CONVERGED AFTER ITERATION     1  CUM. ITER.=     1
      NEXT ITERATION (IDENTIFIED AS ITERATION    10) SATISFIES PRINTOUT OR POST DATA REQUEST.
```

**** DISPLACEMENT SOLUTION ***** TIME = 0.00000E+00 LOAD STEP= 1 ITERATION= 10

NODE	UX	UY
1	0.477796E-02	0.335788E-04
2	0.477796E-02	0.279823E-04
3	0.477796E-02	0.223859E-04
4	0.477796E-02	0.167894E-04
5	0.477796E-02	0.111930E-04
6	0.477796E-02	0.559650E-05
7	0.477796E-02	0.000000E+00
8	0.482023E-02	0.335788E-04
9	0.482023E-02	0.279823E-04
10	0.482023E-02	0.223859E-04
11	0.482023E-02	0.167894E-04
12	0.482023E-02	0.111929E-04
13	0.482023E-02	0.559647E-05
14	0.482023E-02	0.000000E+00
15	0.484649E-02	0.335788E-04
16	0.484649E-02	0.279823E-04
17	0.484649E-02	0.223859E-04
18	0.484649E-02	0.167894E-04
19	0.484649E-02	0.111929E-04
20	0.484649E-02	0.559647E-05
21	0.484649E-02	0.000000E+00
22	0.485506E-02	0.335788E-04
23	0.485506E-02	0.279823E-04
24	0.485506E-02	0.223859E-04
25	0.485506E-02	0.167894E-04
26	0.485506E-02	0.111929E-04
27	0.485506E-02	0.559647E-05
28	0.485506E-02	0.000000E+00
29	0.485851E-02	0.335788E-04
30	0.485851E-02	0.279823E-04
31	0.485851E-02	0.223859E-04
32	0.485851E-02	0.167894E-04
33	0.485851E-02	0.111929E-04
34	0.485851E-02	0.559647E-05
35	0.485851E-02	0.000000E+00
36	0.486153E-02	0.335788E-04
37	0.486153E-02	0.279823E-04
38	0.486153E-02	0.223859E-04
39	0.486153E-02	0.167894E-04
40	0.486153E-02	0.111929E-04
41	0.486153E-02	0.559647E-05
42	0.486153E-02	0.000000E+00
43	0.486412E-02	0.335788E-04
44	0.486412E-02	0.279823E-04
45	0.486412E-02	0.223859E-04
46	0.486412E-02	0.167894E-04
47	0.486412E-02	0.111929E-04
48	0.486412E-02	0.559647E-05
49	0.486412E-02	0.000000E+00
50	0.487950E-02	0.335788E-04
51	0.487950E-02	0.279823E-04
52	0.487950E-02	0.223859E-04
53	0.487950E-02	0.167894E-04
54	0.487950E-02	0.111929E-04
55	0.487950E-02	0.559647E-05
56	0.487950E-02	0.000000E+00
57	0.489717E-02	0.335788E-04
58	0.489717E-02	0.279823E-04
59	0.489717E-02	0.223859E-04
60	0.489717E-02	0.167894E-04
61	0.489717E-02	0.111929E-04
62	0.489717E-02	0.559647E-05
63	0.489717E-02	0.000000E+00
64	0.491671E-02	0.335788E-04
65	0.491671E-02	0.279823E-04
66	0.491671E-02	0.223859E-04
67	0.491671E-02	0.167894E-04
68	0.491671E-02	0.111929E-04
69	0.491671E-02	0.559647E-05
70	0.491671E-02	0.000000E+00
71	0.493764E-02	0.335788E-04
72	0.493764E-02	0.279823E-04
73	0.493764E-02	0.223859E-04
74	0.493764E-02	0.167894E-04
75	0.493764E-02	0.111929E-04
76	0.493764E-02	0.559647E-05
77	0.493764E-02	0.000000E+00
78	0.495943E-02	0.335788E-04
79	0.495943E-02	0.279823E-04
80	0.495943E-02	0.223859E-04
81	0.495943E-02	0.167894E-04
82	0.495943E-02	0.111929E-04
83	0.495943E-02	0.559647E-05
84	0.495943E-02	0.000000E+00
85	0.498146E-02	0.335788E-04
86	0.498146E-02	0.279823E-04
87	0.498146E-02	0.223859E-04
88	0.498146E-02	0.167894E-04
89	0.498146E-02	0.111929E-04
90	0.498146E-02	0.559647E-05
91	0.498146E-02	0.000000E+00

MAXIMUMS		
NODE	88	1
VALUE	0.498146E-02	0.335788E-04

***** ELEMENT STRESSES ***** TIME = 0.000000E+00 LOAD STEP= 1 ITERATION= 10 CUM. ITER.= 2

E= 1 NODES= 2 9 8 1 , MAT= 1 VOL= 0.2590E-05 2-D SOLID
EC.YC= 1.295 0.8250E-02 TEMP=3227.6, SX.SY.SXY.SZ= -24.701 -45525. -0.11062E-02 -45564.
SIG1.SIG2.SIG3= -24.701 -45525. -45564. S.I.= 45539. SIGE= 45520.
STATIC FORCES ON NODE 2 -0.510869E-06 -41.9627
STATIC FORCES ON NODE 9 0.455526E-01 -36.6321
STATIC FORCES ON NODE 8 0.455559E-01 36.6321
STATIC FORCES ON NODE 1 0.199640E-13 41.9627

E= 2 NODES= 3 10 9 2 , MAT= 1 VOL= 0.2590E-05 2-D SOLID
EC.YC= 1.295 0.6750E-02 TEMP=3227.6 SX.SY.SXY.SZ= -24.700 -45525. 0.72755E-03 -45564.
SIG1.SIG2.SIG3= -24.700 -45525. -45564. S.I.= 45539. SIGE= 45520.
STATIC FORCES ON NODE 3 0.743681E-06 -41.9627
STATIC FORCES ON NODE 10 0.455544E-01 -36.6321
STATIC FORCES ON NODE 9 0.455522E-01 36.6321
STATIC FORCES ON NODE 2 0.510869E-06 41.9627

E= 3 NODES= 4 11 10 3 , MAT= 1 VOL= 0.2590E-05 2-D SOLID
EC.YC= 1.295 0.5250E-02 TEMP=3227.6 SX.SY.SXY.SZ= -24.701 -45525. 0.39518E-03 -45564.
SIG1.SIG2.SIG3= -24.701 -45525. -45564. S.I.= 45539. SIGE= 45520.
STATIC FORCES ON NODE 4 0.218991E-13 -41.9627
STATIC FORCES ON NODE 11 0.455546E-01 -36.6321
STATIC FORCES ON NODE 10 0.455540E-01 36.6321
STATIC FORCES ON NODE 3 -0.743682E-06 41.9627

E= 4 NODES= 5 12 11 4 , MAT= 1 VOL= 0.2590E-05 2-D SOLID
EC.YC= 1.295 0.3750E-02 TEMP=3227.6 SX.SY.SXY.SZ= -24.701 -45525. -0.39518E-03 -45564.
SIG1.SIG2.SIG3= -24.701 -45525. -45564. S.I.= 45539. SIGE= 45520.
STATIC FORCES ON NODE 5 -0.743681E-06 -41.9627
STATIC FORCES ON NODE 12 0.455540E-01 -36.6321
STATIC FORCES ON NODE 11 0.455546E-01 36.6321
STATIC FORCES ON NODE 4 -0.142331E-12 41.9627

E= 5 NODES= 6 13 12 5 , MAT= 1 VOL= 0.2590E-05 2-D SOLID
EC.YC= 1.295 0.2250E-02 TEMP=3227.6, SX.SY.SXY.SZ= -24.700 -45525. -0.72755E-03 -45564.
SIG1.SIG2.SIG3= -24.700 -45525. -45564. S.I.= 45539. SIGE= 45520.
STATIC FORCES ON NODE 6 0.510870E-06 -41.9627
STATIC FORCES ON NODE 13 0.455522E-01 -36.6321
STATIC FORCES ON NODE 12 0.455544E-01 36.6321
STATIC FORCES ON NODE 5 0.743681E-06 41.9627

E= 6 NODES= 7 14 13 6 , MAT= 1 VOL= 0.2590E-05 2-D SOLID
EC.YC= 1.295 0.7500E-03 TEMP=3227.6, SX.SY.SXY.SZ= -24.701 -45525. 0.11062E-02 -45564.
SIG1.SIG2.SIG3= -24.701 -45525. -45564. S.I.= 45539. SIGE= 45520.
STATIC FORCES ON NODE 7 0.363945E-13 -41.9627
STATIC FORCES ON NODE 14 0.455559E-01 -36.6321
STATIC FORCES ON NODE 13 0.455526E-01 36.6321
STATIC FORCES ON NODE 6 -0.510870E-06 41.9627

E= 7 NODES= 9 16 15 8 , MAT= 1 VOL= 0.2594E-05 2-D SOLID
EC.YC= 1.297 0.8250E-02 TEMP=2161.9, SX.SY.SXY.SZ= -63.463 -29583. 0.47900E-03 -29586.
SIG1.SIG2.SIG3= -63.463 -29583. -29586. S.I.= 29523. SIGE= 29521.
STATIC FORCES ON NODE 9 -0.455544E-01 -28.5516
STATIC FORCES ON NODE 16 0.751574E-01 -22.6113
STATIC FORCES ON NODE 15 0.751573E-01 22.6113
STATIC FORCES ON NODE 8 -0.455559E-01 28.5516

E= 8 NODES= 10 17 16 9 , MAT= 1 VOL= 0.2594E-05 2-D SOLID
EC.YC= 1.297 0.6750E-02 TEMP=2161.9, SX.SY.SXY.SZ= -63.461 -29583. -0.13724E-02 -29586.
SIG1.SIG2.SIG3= -63.461 -29583. -29586. S.I.= 29523. SIGE= 29521.
STATIC FORCES ON NODE 10 -0.455553E-01 -28.5516
STATIC FORCES ON NODE 17 0.751551E-01 -22.6113
STATIC FORCES ON NODE 16 0.751549E-01 22.6113
STATIC FORCES ON NODE 9 -0.455503E-01 28.5516

E= 9 NODES= 11 18 17 10 , MAT= 1 VOL= 0.2594E-05 2-D SOLID
EC.YC= 1.297 0.5250E-02 TEMP=2161.9, SX.SY.SXY.SZ= -63.462 -29583. -0.31594E-03 -29586.
SIG1.SIG2.SIG3= -63.462 -29583. -29586. S.I.= 29523. SIGE= 29521.
STATIC FORCES ON NODE 11 -0.455546E-01 -28.5516
STATIC FORCES ON NODE 18 0.751563E-01 -22.6113
STATIC FORCES ON NODE 17 0.751559E-01 22.6113
STATIC FORCES ON NODE 10 -0.455531E-01 28.5516

E= 10 NODES= 12 19 18 11 , MAT= 1 VOL= 0.2594E-05 2-D SOLID
EC.YC= 1.297 0.3750E-02 TEMP=2161.9, SX.SY.SXY.SZ= -63.462 -29583. 0.31594E-03 -29586.
SIG1.SIG2.SIG3= -63.462 -29583. -29586. S.I.= 29523. SIGE= 29521.
STATIC FORCES ON NODE 12 -0.455531E-01 -28.5516
STATIC FORCES ON NODE 19 0.751559E-01 -22.6113
STATIC FORCES ON NODE 18 0.751563E-01 22.6113
STATIC FORCES ON NODE 11 -0.455546E-01 28.5516

E= 11 NODES= 13 20 19 12 , MAT= 1 VOL= 0.2594E-05 2-D SOLID
EC.YC= 1.297 0.2250E-02 TEMP=2161.9 SX.SY.SXY.SZ= -63.461 -29583. 0.13724E-02 -29586.
SIG1.SIG2.SIG3= -63.461 -29583. -29586. S.I.= 29523. SIGE= 29521.
STATIC FORCES ON NODE 13 -0.455503E-01 -28.5516
STATIC FORCES ON NODE 20 0.751549E-01 -22.6113
STATIC FORCES ON NODE 19 0.751551E-01 22.6113
STATIC FORCES ON NODE 12 -0.455553E-01 28.5516

E= 12 NODES= 14 21 20 13 , MAT= 1 VOL= 0.2594E-05 2-D SOLID
EC.YC= 1.297 0.7500E-03 TEMP=2161.9, SX.SY.SXY.SZ= -63.463 -29583. -0.47900E-03 -29586.
SIG1.SIG2.SIG3= -63.463 -29583. -29586. S.I.= 29523. SIGE= 29521.
STATIC FORCES ON NODE 14 -0.455559E-01 -28.5516
STATIC FORCES ON NODE 21 0.751573E-01 -22.6113
STATIC FORCES ON NODE 20 0.751574E-01 22.6113
STATIC FORCES ON NODE 13 -0.455544E-01 28.5516

E= 13 NODES= 16 23 22 15 , MAT= 1 VOL= 0.2595E-05 2-D SOLID
EC.YC= 1.298 0.8250E-02 TEMP=1097.3 SX.SY.SXY.SZ= -84.370 -9743.8 -0.55892E-04 -9716.0
SIG1.SIG2.SIG3= -84.370 -9716.0 -9743.8 S.I.= 9659.5 SIGE= 9645.6
STATIC FORCES ON NODE 16 -0.751572E-01 -13.0616
STATIC FORCES ON NODE 23 0.848726E-01 -3.79159
STATIC FORCES ON NODE 22 0.848729E-01 3.79159
STATIC FORCES ON NODE 15 -0.751573E-01 13.0616

E= 14 NODES= 17 24 23 16 , MAT= 1 VOL= 0.2595E-05 2-D SOLID
EC.YC= 1.298 0.6750E-02 TEMP=1097.3 SX.SY.SXY.SZ= -84.368 -9743.8 -0.56978E-03 -9716.0
SIG1.SIG2.SIG3= -84.368 -9716.0 -9743.8 S.I.= 9659.5 SIGE= 9645.6
STATIC FORCES ON NODE 17 -0.751564E-01 -13.0616
STATIC FORCES ON NODE 24 0.848710E-01 -3.79159
STATIC FORCES ON NODE 23 0.848717E-01 3.79159
STATIC FORCES ON NODE 16 -0.751552E-01 13.0616

```
STATIC FORCES ON NODE      25  0.848707E-01   -3.79159
STATIC FORCES ON NODE      24  0.848712E-01    3.79159
STATIC FORCES ON NODE      17 -0.751546E-01   13.0616

=   16  NODES=   19   26   25   18 ,  MAT=  1   VOL= 0.2595E-05                                                    2-D SOLID
.YC=  1.298      0.3750E-02  TEMP=1097.3  SX.SY.SXY.SZ=  -84.368       -9743.8       0.62783E-03  -9716.0
SIG1.SIG2.SIG3=    -84.368        -9716.0        -9743.8   S.I.=        9659.5   SIGE=        9645.6
STATIC FORCES ON NODE      19 -0.751546E-01   -13.0616
STATIC FORCES ON NODE      26  0.848712E-01   -3.79159
STATIC FORCES ON NODE      25  0.848707E-01    3.79159
STATIC FORCES ON NODE      18 -0.751563E-01   13.0616

=   17  NODES=   20   27   26   19 ,  MAT=  1   VOL= 0.2595E-05                                                    2-D SOLID
.YC=  1.298      0.2250E-02  TEMP=1097.3  SX.SY.SXY.SZ=  -84.368       -9743.8       0.56978E-03  -9716.0
SIG1.SIG2.SIG3=    -84.368        -9716.0        -9743.8   S.I.=        9659.5   SIGE=        9645.6
STATIC FORCES ON NODE      20 -0.751552E-01   -13.0616
STATIC FORCES ON NODE      27  0.848717E-01   -3.79159
STATIC FORCES ON NODE      26  0.848710E-01    3.79159
STATIC FORCES ON NODE      19 -0.751564E-01   13.0616

=   18  NODES=   21   28   27   20 ,  MAT=  1   VOL= 0.2595E-05                                                    2-D SOLID
.YC=  1.298      0.7500E-03  TEMP=1097.3  SX.SY.SXY.SZ=  -84.370       -9743.8       0.55891E-04  -9716.0
SIG1.SIG2.SIG3=    -84.370        -9716.0        -9743.8   S.I.=        9659.5   SIGE=        9645.6
STATIC FORCES ON NODE      21 -0.751573E-01   -13.0616
STATIC FORCES ON NODE      28  0.848729E-01   -3.79159
STATIC FORCES ON NODE      27  0.848726E-01    3.79159
STATIC FORCES ON NODE      20 -0.751572E-01   13.0616

=   19  NODES=   23   30   29   22 ,  MAT=  2   VOL= 0.9741E-06                                                    2-D SOLID
.YC=  1.299      0.8250E-02  TEMP= 549.1  SX.SY.SXY.SZ=  -96.760       -48895.       0.44283E-03  -48763.
SIG1.SIG2.SIG3=    -96.760        -48763.        -48895.   S.I.=        48799.   SIGE=        48732.
STATIC FORCES ON NODE      23 -0.848726E-01   -16.3862
STATIC FORCES ON NODE      30  0.103159        15.3650
STATIC FORCES ON NODE      29  0.103159        15.3650
STATIC FORCES ON NODE      22 -0.848729E-01   16.3862

=   20  NODES=   24   31   30   23 ,  MAT=  2   VOL= 0.9741E-06                                                    2-D SOLID
.YC=  1.299      0.6750E-02  TEMP= 549.1  SX.SY.SXY.SZ=  -96.758       -48895.       0.68331E-03  -48763.
SIG1.SIG2.SIG3=    -96.758        -48763.        -48895.   S.I.=        48799.   SIGE=        48732.
STATIC FORCES ON NODE      24 -0.848715E-01   -16.3862
STATIC FORCES ON NODE      31  0.103158        15.3650
STATIC FORCES ON NODE      30  0.103157        15.3650
STATIC FORCES ON NODE      23 -0.848714E-01   16.3862

=   21  NODES=   25   32   31   24 ,  MAT=  2   VOL= 0.9741E-06                                                    2-D SOLID
YC=  1.299      0.5250E-02  TEMP= 549.1  SX.SY.SXY.SZ=  -96.758       -48895.       0.26697E-03  -48763.
G1.SIG2.SIG3=    -96.758        -48763.        -48895.   S.I.=        48799.   SIGE=        48732.
ATIC FORCES ON NODE      25 -0.848707E-01   -16.3862
ATIC FORCES ON NODE      32  0.103157        15.3650
ATIC FORCES ON NODE      31  0.103157        15.3650
ATIC FORCES ON NODE      24 -0.848708E-01   16.3862

=   22  NODES=   26   33   32   25 ,  MAT=  2   VOL= 0.9741E-06                                                    2-D SOLID  42
YC=  1.299      0.3750E-02  TEMP= 549.1  SX.SY.SXY.SZ=  -96.758       -48895.      -0.26698E-03  -48763.
G1.SIG2.SIG3=    -96.758        -48763.        -48895.   S.I.=        48799.   SIGE=        48732.
ATIC FORCES ON NODE      26 -0.848708E-01   -16.3862
ATIC FORCES ON NODE      33  0.103157        15.3650
ATIC FORCES ON NODE      32  0.103157        15.3650
ATIC FORCES ON NODE      25 -0.848707E-01   16.3862

=   23  NODES=   27   34   33   26 ,  MAT=  2   VOL= 0.9741E-06                                                    2-D SOLID  42
YC=  1.299      0.2250E-02  TEMP= 549.1  SX.SY.SXY.SZ=  -96.758       -48895.      -0.68331E-03  -48763.
G1.SIG2.SIG3=    -96.758        -48763.        -48895.   S.I.=        48799.   SIGE=        48732.
ATIC FORCES ON NODE      27 -0.848714E-01   -16.3862
ATIC FORCES ON NODE      34  0.103157        15.3650
ATIC FORCES ON NODE      33  0.103158        15.3650
ATIC FORCES ON NODE      26 -0.848715E-01   16.3862

=   24  NODES=   28   35   34   27 ,  MAT=  2   VOL= 0.9741E-06                                                    2-D SOLID  42
YC=  1.299      0.7500E-03  TEMP= 549.1  SX.SY.SXY.SZ=  -96.760       -48895.      -0.44284E-03  -48763.
G1.SIG2.SIG3=    -96.760        -48763.        -48895.   S.I.=        48799.   SIGE=        48732.
ATIC FORCES ON NODE      28 -0.848729E-01   -16.3862
ATIC FORCES ON NODE      35  0.103159        15.3650
ATIC FORCES ON NODE      34  0.103159        15.3650
ATIC FORCES ON NODE      27 -0.848726E-01   16.3862

=   25  NODES=   30   37   36   29 ,  MAT=  2   VOL= 0.9744E-06                                                    2-D SOLID  42
YC=  1.299      0.8250E-02  TEMP= 516.0  SX.SY.SXY.SZ=  -112.90       -35477.       0.52424E-03  -35329.
G1.SIG2.SIG3=    -112.90        -35329.        -35477.   S.I.=        35365.   SIGE=        35290.
ATIC FORCES ON NODE      30 -0.103158        12.0281
ATIC FORCES ON NODE      37  0.116407        11.0188
ATIC FORCES ON NODE      36  0.116407        11.0188
ATIC FORCES ON NODE      29 -0.103159        12.0281

=   26  NODES=   31   38   37   30 ,  MAT=  2   VOL= 0.9744E-06                                                    2-D SOLID  42
YC=  1.299      0.6750E-02  TEMP= 516.0  SX.SY.SXY.SZ=  -112.90       -35477.       0.94951E-03  -35329.
G1.SIG2.SIG3=    -112.90        -35329.        -35477.   S.I.=        35365.   SIGE=        35290.
ATIC FORCES ON NODE      31 -0.103157        12.0281
ATIC FORCES ON NODE      38  0.116406        11.0188
ATIC FORCES ON NODE      37  0.116406        11.0188
ATIC FORCES ON NODE      30 -0.103158        12.0281

=   27  NODES=   32   39   38   31 ,  MAT=  2   VOL= 0.9744E-06                                                    2-D SOLID  42
YC=  1.299      0.5250E-02  TEMP= 516.0  SX.SY.SXY.SZ=  -112.90       -35477.       0.43595E-03  -35329.
G1.SIG2.SIG3=    -112.90        -35329.        -35477.   S.I.=        35365.   SIGE=        35290.
ATIC FORCES ON NODE      32 -0.103157        12.0281
ATIC FORCES ON NODE      39  0.116406        11.0188
ATIC FORCES ON NODE      38  0.116405        11.0188
ATIC FORCES ON NODE      31 -0.103157        12.0281

=   28  NODES=   33   40   39   32 ,  MAT=  2   VOL= 0.9744E-06                                                    2-D SOLID  42
YC=  1.299      0.3750E-02  TEMP= 516.0  SX.SY.SXY.SZ=  -112.90       -35477.      -0.43596E-03  -35329.
G1.SIG2.SIG3=    -112.90        -35329.        -35477.   S.I.=        35365.   SIGE=        35290.
ATIC FORCES ON NODE      33 -0.103157        12.0281
ATIC FORCES ON NODE      40  0.116405        11.0188
ATIC FORCES ON NODE      39  0.116406        11.0188
ATIC FORCES ON NODE      32 -0.103157        12.0281

=   29  NODES=   34   41   40   33 ,  MAT=  2   VOL= 0.9744E-06                                                    2-D SOLID  42
YC=  1.299      0.2250E-02  TEMP= 516.0  SX.SY.SXY.SZ=  -112.90       -35477.      -0.94951E-03  -35329.
G1.SIG2.SIG3=    -112.90        -35329.        -35477.   S.I.=        35365.   SIGE=        35290.
ATIC FORCES ON NODE      34 -0.103158        12.0281
ATIC FORCES ON NODE      41  0.116406        11.0188
ATIC FORCES ON NODE      40  0.116406        11.0188
ATIC FORCES ON NODE      33 -0.103157        12.0281

=   30  NODES=   35   42   41   34 ,  MAT=  2   VOL= 0.9744E-06                                                    2-D SOLID  42
YC=  1.299      0.7500E-03  TEMP= 516.0  SX.SY.SXY.SZ=  -112.90       -35477.      -0.52424E-03  -35329.
G1.SIG2.SIG3=    -112.90        -35329.        -35477.   S.I.=        35365.   SIGE=        35290.
ATIC FORCES ON NODE      35 -0.103159        12.0281
ATIC FORCES ON NODE      42  0.116407        11.0188
ATIC FORCES ON NODE      41  0.116407        11.0188
ATIC FORCES ON NODE      34 -0.103158        12.0281

=   31  NODES=   37   44   43   36 ,  MAT=  2   VOL= 0.9748E-06                                                    2-D SOLID  42
YC=  1.300      0.8250E-02  TEMP= 482.6  SX.SY.SXY.SZ=  -123.96       -22558.       0.48380E-03  -22399.
G1.SIG2.SIG3=    -123.96        -22399.        -22558.   S.I.=        22434.   SIGE=        22355.
ATIC FORCES ON NODE      37 -0.116406        -7.82839
ATIC FORCES ON NODE      44  0.124806        -6.83127
```

```
STATIC FORCES ON NODE      43 -0.124806        6.83127
STATIC FORCES ON NODE      36 -0.116407        7.82839

EL=   32  NODES=   38   45   44   37      MAT=  2   VOL= 0.9748E-06                                                    2-D SOLID
XC,YC=  1.300     0.6750E-02  TEMP= 482.6  SX,SY,SXY,SZ=  -123.96        -22558.      0.91239E-03  -22399.
 SIG1,SIG2,SIG3=     -123.96        -22399.        -22558.     S.I.=      22434.     SIGE=      22355.
 STATIC FORCES ON NODE      38 -0.116406        7.82839
 STATIC FORCES ON NODE      45  0.124806        6.83127
 STATIC FORCES ON NODE      44  0.124806        6.83127
 STATIC FORCES ON NODE      37 -0.116407        7.82839

EL=   33  NODES=   39   46   45   38      MAT=  2   VOL= 0.9748E-06                                                    2-D SOLID
XC,YC=  1.300     0.5250E-02  TEMP= 482.6  SX,SY,SXY,SZ=  -123.96        -22558.      0.43320E-03  -22399.
 SIG1,SIG2,SIG3=     -123.96        -22399.        -22558.     S.I.=      22434.     SIGE=      22355.
 STATIC FORCES ON NODE      39 -0.116406        7.82839
 STATIC FORCES ON NODE      46  0.124806        6.83127
 STATIC FORCES ON NODE      45  0.124805        6.83127
 STATIC FORCES ON NODE      38 -0.116406        7.82839

EL=   34  NODES=   40   47   46   39      MAT=  2   VOL= 0.9748E-06                                                    2-D SOLID
XC,YC=  1.300     0.3750E-02  TEMP= 482.6  SX,SY,SXY,SZ=  -123.96        -22558.     -0.43320E-03  -22399.
 SIG1,SIG2,SIG3=     -123.96        -22399.        -22558.     S.I.=      22434.     SIGE=      22355.
 STATIC FORCES ON NODE      40 -0.116406        7.82839
 STATIC FORCES ON NODE      47  0.124805        6.83127
 STATIC FORCES ON NODE      46  0.124806        6.83127
 STATIC FORCES ON NODE      39 -0.116406        7.82839

EL=   35  NODES=   41   48   47   40      MAT=  2   VOL= 0.9748E-06                                                    2-D SOLID
XC,YC=  1.300     0.2250E-02  TEMP= 482.6  SX,SY,SXY,SZ=  -123.96        -22558.     -0.91239E-03  -22399.
 SIG1,SIG2,SIG3=     -123.96        -22399.        -22558.     S.I.=      22434.     SIGE=      22355.
 STATIC FORCES ON NODE      41 -0.116407        7.82839
 STATIC FORCES ON NODE      48  0.124806        6.83127
 STATIC FORCES ON NODE      47  0.124806        6.83127
 STATIC FORCES ON NODE      40 -0.116406        7.82839

EL=   36  NODES=   42   49   48   41      MAT=  2   VOL= 0.9748E-06                                                    2-D SOLID
XC,YC=  1.300     0.7500E-03  TEMP= 482.6  SX,SY,SXY,SZ=  -123.96        -22558.     -0.48360E-03  -22399.
 SIG1,SIG2,SIG3=     -123.96        -22399.        -22558.     S.I.=      22434.     SIGE=      22355.
 STATIC FORCES ON NODE      42 -0.116407        7.82839
 STATIC FORCES ON NODE      49  0.124806        6.83127
 STATIC FORCES ON NODE      48  0.124806        6.83127
 STATIC FORCES ON NODE      41 -0.116406        7.82839

EL=   37  NODES=   44   51   50   43      MAT=  3   VOL= 0.7595E-05                                                    2-D SOLID
XC,YC=  1.302     0.3250E-02  TEMP= 462.0  SX,SY,SXY,SZ=  -132.16        -2923.5      0.73541E-04  -2785.1
 SIG1,SIG2,SIG3=     -132.16        -2785.1        -2923.5     S.I.=      2791.4     SIGE=      2724.8
 STATIC FORCES ON NODE      44 -0.124806        8.20214
 STATIC FORCES ON NODE      51  0.132931        6.59945
 STATIC FORCES ON NODE      50  0.132931        6.59945
 STATIC FORCES ON NODE      43 -0.124806        8.20214

EL=   38  NODES=   45   52   51   44      MAT=  3   VOL= 0.7595E-05                                                    2-D SOLID
XC,YC=  1.302     0.6750E-02  TEMP= 462.0  SX,SY,SXY,SZ=  -132.16        -2923.5      0.13731E-03  -2785.1
 SIG1,SIG2,SIG3=     -132.16        -2785.1        -2923.5     S.I.=      2791.4     SIGE=      2724.8
 STATIC FORCES ON NODE      45 -0.124805        8.20214
 STATIC FORCES ON NODE      52  0.132931        6.59945
 STATIC FORCES ON NODE      51  0.132931        6.59945
 STATIC FORCES ON NODE      44 -0.124806        8.20214

EL=   39  NODES=   46   53   52   45      MAT=  3   VOL= 0.7595E-05                                                    2-D SOLID
XC,YC=  1.302     0.5250E-02  TEMP= 462.0  SX,SY,SXY,SZ=  -132.16        -2923.5      0.64463E-04  -2785.1
 SIG1,SIG2,SIG3=     -132.16        -2785.1        -2923.5     S.I.=      2791.4     SIGE=      2724.8
 STATIC FORCES ON NODE      46 -0.124806        8.20214
 STATIC FORCES ON NODE      53  0.132931        6.59945
 STATIC FORCES ON NODE      52  0.132931        6.59945
 STATIC FORCES ON NODE      45 -0.124806        8.20214

EL=   40  NODES=   47   54   53   46      MAT=  3   VOL= 0.7595E-05                                                    2-D SOLID
XC,YC=  1.302     0.3750E-02  TEMP= 462.0  SX,SY,SXY,SZ=  -132.16        -2923.5     -0.64437E-04  -2785.1
 SIG1,SIG2,SIG3=     -132.16        -2785.1        -2923.5     S.I.=      2791.4     SIGE=      2724.8
 STATIC FORCES ON NODE      47 -0.124806        8.20214
 STATIC FORCES ON NODE      54  0.132931        6.59945
 STATIC FORCES ON NODE      53  0.132931        6.59945
 STATIC FORCES ON NODE      46 -0.124806        8.20214

EL=   41  NODES=   48   55   54   47      MAT=  3   VOL= 0.7595E-05                                                    2-D SOLID
XC,YC=  1.302     0.2250E-02  TEMP= 462.0  SX,SY,SXY,SZ=  -132.16        -2923.5     -0.13731E-03  -2785.1
 SIG1,SIG2,SIG3=     -132.16        -2785.1        -2923.5     S.I.=      2791.4     SIGE=      2724.8
 STATIC FORCES ON NODE      48 -0.124806        8.20214
 STATIC FORCES ON NODE      55  0.132931        6.59945
 STATIC FORCES ON NODE      54  0.132931        6.59945
 STATIC FORCES ON NODE      47 -0.124805        8.20214

EL=   42  NODES=   49   56   55   48      MAT=  3   VOL= 0.7595E-05                                                    2-D SOLID
XC=  1.302     0.7500E-03  TEMP= 462.0  SX,SY,SXY,SZ=  -132.16        -2923.5     -0.73542E-04  -2785.1
G1,SIG2,SIG3=     -132.16        -2785.1        -2923.5     S.I.=      2791.4     SIGE=      2724.8
ATIC FORCES ON NODE      49 -0.124806        8.20214
ATIC FORCES ON NODE      56  0.132931        6.59945
ATIC FORCES ON NODE      55  0.132931        6.59945
ATIC FORCES ON NODE      48 -0.124806        8.20214

   43  NODES=   51   58   57   50      MAT=  3   VOL= 0.9144E-05                                                    2-D SOLID  4
YC=  1.306     0.8250E-02  TEMP= 453.9  SX,SY,SXY,SZ=  -137.17        -827.00     -0.19744E-04  -683.40
G1,SIG2,SIG3=     -137.17        -683.40        -827.00     S.I.=      689.82     SIGE=      630.41
ATIC FORCES ON NODE      51 -0.132931        3.67842
ATIC FORCES ON NODE      58  0.135326        1.36148
ATIC FORCES ON NODE      57  0.135326        1.36148
ATIC FORCES ON NODE      50 -0.132931        3.67842

   44  NODES=   52   59   58   51      MAT=  3   VOL= 0.9144E-05                                                    2-D SOLID  4
YC=  1.306     0.6750E-02  TEMP= 453.9  SX,SY,SXY,SZ=  -137.17        -827.00     -0.36647E-04  -683.40
G1,SIG2,SIG3=     -137.17        -683.40        -827.00     S.I.=      689.82     SIGE=      630.41
ATIC FORCES ON NODE      52 -0.132931        3.67842
ATIC FORCES ON NODE      59  0.135326        1.36148
ATIC FORCES ON NODE      58  0.135326        1.36148
ATIC FORCES ON NODE      51 -0.132931        3.67842

   45  NODES=   53   60   59   52      MAT=  3   VOL= 0.9144E-05                                                    2-D SOLID  4
YC=  1.306     0.5250E-02  TEMP= 453.9  SX,SY,SXY,SZ=  -137.17        -827.00     -0.17158E-04  -683.40
G1,SIG2,SIG3=     -137.17        -683.40        -827.00     S.I.=      689.82     SIGE=      630.41
ATIC FORCES ON NODE      53 -0.132931        3.67842
ATIC FORCES ON NODE      60  0.135326        1.36148
ATIC FORCES ON NODE      59  0.135326        1.36148
ATIC FORCES ON NODE      52 -0.132931        3.67842

   46  NODES=   54   61   60   53      MAT=  3   VOL= 0.9144E-05                                                    2-D SOLID  4
YC=  1.306     0.3750E-02  TEMP= 453.9  SX,SY,SXY,SZ=  -137.17        -827.00      0.17155E-04  -683.40
G1,SIG2,SIG3=     -137.17        -683.40        -827.00     S.I.=      689.82     SIGE=      630.41
ATIC FORCES ON NODE      54 -0.132931        3.67842
ATIC FORCES ON NODE      61  0.135326        1.36148
ATIC FORCES ON NODE      60  0.135326        1.36148
ATIC FORCES ON NODE      53 -0.132931        3.67842
```

```
XC,YC=  1.306      --  --  --  --   MAT=  3   VOL= 0.9144E-05
        0.2250E-02  TEMP= 453.9     SX,SY,SXY,SZ=  -137.17          -827.00      0.36646E-04  -683.40   2-D SOLID
SIG1,SIG2,SIG3=     -137.17          -683.40          -827.00   S.I.=  689.82   SIGE=     630.41
STATIC FORCES ON NODE     55 -0.132931      -3.67842
STATIC FORCES ON NODE     62  0.135326      -1.36148
STATIC FORCES ON NODE     61  0.135326       1.36148
STATIC FORCES ON NODE     54 -0.132931       3.67842

EL=  48  NODES=  56  63  62  55   ,   MAT=  3   VOL= 0.9144E-05
XC,YC=  1.306      --  --  --  --
        0.7500E-03  TEMP= 453.9     SX,SY,SXY,SZ=  -137.17          -827.00      0.19743E-04  -683.40   2-D SOLID
SIG1,SIG2,SIG3=     -137.17          -683.40          -827.00   S.I.=  689.82   SIGE=     630.41
STATIC FORCES ON NODE     56 -0.132931      -3.67842
STATIC FORCES ON NODE     63  0.135326      -1.36148
STATIC FORCES ON NODE     62  0.135326       1.36148
STATIC FORCES ON NODE     55 -0.132931       3.67842

EL=  49  NODES=  58  65  64  57   ,   MAT=  3   VOL= 0.1071E-04
XC,YC=  1.311      --  --  --  --
        0.8250E-02  TEMP= 444.4     SX,SY,SXY,SZ=  -134.26          1641.7       0.16884E-05   1782.7   2-D SOLID
SIG1,SIG2,SIG3=      1782.7           1641.7          -134.26   S.I.=  1916.9   SIGE=     1850.5
STATIC FORCES ON NODE     58 -0.135326       4.27810
STATIC FORCES ON NODE     65  0.128051       7.44396
STATIC FORCES ON NODE     64  0.128051      -7.44396
STATIC FORCES ON NODE     57 -0.135326      -4.27810

EL=  50  NODES=  59  66  65  58   ,   MAT=  3   VOL= 0.1071E-04
XC,YC=  1.311      --  --  --  --
        0.6750E-02  TEMP= 444.4     SX,SY,SXY,SZ=  -134.26          1641.7       0.24781E-05   1782.7   2-D SOLID
SIG1,SIG2,SIG3=      1782.7           1641.7          -134.26   S.I.=  1916.9   SIGE=     1850.5
STATIC FORCES ON NODE     59 -0.135326       4.27810
STATIC FORCES ON NODE     66  0.128051       7.44396
STATIC FORCES ON NODE     65  0.128051      -7.44396
STATIC FORCES ON NODE     58 -0.135326      -4.27810

EL=  51  NODES=  60  67  66  59   ,   MAT=  3   VOL= 0.1071E-04
XC,YC=  1.311      --  --  --  --
        0.5250E-02  TEMP= 444.4     SX,SY,SXY,SZ=  -134.26          1641.7       0.90019E-06   1782.7   2-D SOLID
SIG1,SIG2,SIG3=      1782.7           1641.7          -134.26   S.I.=  1916.9   SIGE=     1850.5
STATIC FORCES ON NODE     60 -0.135326       4.27810
STATIC FORCES ON NODE     67  0.128051       7.44396
STATIC FORCES ON NODE     66  0.128051      -7.44396
STATIC FORCES ON NODE     59 -0.135326      -4.27810

EL=  52  NODES=  61  68  67  60   ,   MAT=  3   VOL= 0.1071E-04
XC,YC=  1.311      --  --  --  --
        0.3750E-02  TEMP= 444.4     SX,SY,SXY,SZ=  -134.26          1641.7      -0.90098E-06   1782.7   2-D SOLID
SIG1,SIG2,SIG3=      1782.7           1641.7          -134.26   S.I.=  1916.9   SIGE=     1850.5
STATIC FORCES ON NODE     61 -0.135326       4.27810
STATIC FORCES ON NODE     68  0.128051       7.44396

STATIC FORCES ON NODE     67  0.128051      -7.44396
STATIC FORCES ON NODE     60 -0.135326      -4.27810

EL=  53  NODES=  62  69  68  61   ,   MAT=  3   VOL= 0.1071E-04
XC,YC=  1.311      --  --  --  --
        0.2250E-02  TEMP= 444.4     SX,SY,SXY,SZ=  -134.26          1641.7      -0.24787E-05   1782.7   2-D SOLID
SIG1,SIG2,SIG3=      1782.7           1641.7          -134.26   S.I.=  1916.9   SIGE=     1850.5
STATIC FORCES ON NODE     62 -0.135326       4.27810
STATIC FORCES ON NODE     69  0.128051       7.44396
STATIC FORCES ON NODE     68  0.128051      -7.44396
STATIC FORCES ON NODE     61 -0.135326      -4.27810

EL=  54  NODES=  63  70  69  62   ,   MAT=  3   VOL= 0.1071E-04
XC,YC=  1.311      --  --  --  --
        0.7500E-03  TEMP= 444.4     SX,SY,SXY,SZ=  -134.26          1641.7      -0.16888E-05   1782.7   2-D SOLID
SIG1,SIG2,SIG3=      1782.7           1641.7          -134.26   S.I.=  1916.9   SIGE=     1850.5
STATIC FORCES ON NODE     63 -0.135326       4.27810
STATIC FORCES ON NODE     70  0.128051       7.44396
STATIC FORCES ON NODE     69  0.128051      -7.44396
STATIC FORCES ON NODE     62 -0.135326      -4.27810

EL=  55  NODES=  65  72  71  64   ,   MAT=  3   VOL= 0.1229E-04
XC,YC=  1.317      --  --  --  --
        0.8250E-02  TEMP= 433.4     SX,SY,SXY,SZ=  -119.23          4478.3       0.20343E-06   4604.5   2-D SOLID
SIG1,SIG2,SIG3=      4604.5           4478.3          -119.23   S.I.=  4723.7   SIGE=     4661.9
STATIC FORCES ON NODE     65 -0.128051      16.2746
STATIC FORCES ON NODE     72  0.106570      20.4291
STATIC FORCES ON NODE     71  0.106570     -20.4291
STATIC FORCES ON NODE     64 -0.128051     -16.2746

EL=  56  NODES=  66  73  72  65   ,   MAT=  3   VOL= 0.1229E-04
XC,YC=  1.317      --  --  --  --
        0.6750E-02  TEMP= 433.4     SX,SY,SXY,SZ=  -119.23          4478.3       0.70842E-06   4604.5   2-D SOLID
SIG1,SIG2,SIG3=      4604.5           4478.3          -119.23   S.I.=  4723.7   SIGE=     4661.9
STATIC FORCES ON NODE     66 -0.128051      16.2746
STATIC FORCES ON NODE     73  0.106570      20.4291
STATIC FORCES ON NODE     72  0.106570     -20.4291
STATIC FORCES ON NODE     65 -0.128051     -16.2746

EL=  57  NODES=  67  74  73  66   ,   MAT=  3   VOL= 0.1229E-04
XC,YC=  1.317      --  --  --  --
        0.5250E-02  TEMP= 433.4     SX,SY,SXY,SZ=  -119.23          4478.3       0.45326E-06   4604.5   2-D SOLID
SIG1,SIG2,SIG3=      4604.5           4478.3          -119.23   S.I.=  4723.7   SIGE=     4661.9
STATIC FORCES ON NODE     67 -0.128051      16.2746
STATIC FORCES ON NODE     74  0.106570      20.4291
STATIC FORCES ON NODE     73  0.106570     -20.4291
STATIC FORCES ON NODE     66 -0.128051     -16.2746

EL=  58  NODES=  68  75  74  67   ,   MAT=  3   VOL= 0.1229E-04
XC,YC=  1.317      --  --  --  --
        0.3750E-02  TEMP= 433.4     SX,SY,SXY,SZ=  -119.23          4478.3      -0.45282E-06   4604.5   2-D SOLID
SIG1,SIG2,SIG3=      4604.5           4478.3          -119.23   S.I.=  4723.7   SIGE=     4661.9
STATIC FORCES ON NODE     68 -0.128051      16.2746
STATIC FORCES ON NODE     75  0.106570      20.4291
STATIC FORCES ON NODE     74  0.106570     -20.4291
STATIC FORCES ON NODE     67 -0.128051     -16.2746

EL=  59  NODES=  69  76  75  68   ,   MAT=  3   VOL= 0.1229E-04
XC,YC=  1.317      --  --  --  --
        0.2250E-02  TEMP= 433.4     SX,SY,SXY,SZ=  -119.23          4478.3      -0.70807E-06   4604.5   2-D SOLID
SIG1,SIG2,SIG3=      4604.5           4478.3          -119.23   S.I.=  4723.7   SIGE=     4661.9
STATIC FORCES ON NODE     69 -0.128051      16.2746
STATIC FORCES ON NODE     76  0.106570      20.4291
STATIC FORCES ON NODE     75  0.106570     -20.4291
STATIC FORCES ON NODE     68 -0.128051     -16.2746

EL=  60  NODES=  70  77  76  69   ,   MAT=  3   VOL= 0.1229E-04
XC,YC=  1.317      --  --  --  --
        0.7500E-03  TEMP= 433.4     SX,SY,SXY,SZ=  -119.23          4478.3      -0.20420E-06   4604.5   2-D SOLID
SIG1,SIG2,SIG3=      4604.5           4478.3          -119.23   S.I.=  4723.7   SIGE=     4661.9
STATIC FORCES ON NODE     70 -0.128051      16.2746
STATIC FORCES ON NODE     77  0.106570      20.4291
STATIC FORCES ON NODE     76  0.106570     -20.4291
STATIC FORCES ON NODE     69 -0.128051     -16.2746

EL=  61  NODES=  72  79  78  71   ,   MAT=  3   VOL= 0.1390E-04
XC,YC=  1.324      --  --  --  --
        0.8250E-02  TEMP= 421.0     SX,SY,SXY,SZ=  -87.409          7678.0      -0.12606E-06   7772.7   2-D SOLID
SIG1,SIG2,SIG3=      7772.7           7678.0          -87.409   S.I.=  7860.1   SIGE=     7813.2
STATIC FORCES ON NODE     72 -0.106570      32.9328
STATIC FORCES ON NODE     79  0.657720E-01    38.2181
STATIC FORCES ON NODE     78  0.657720E-01   -38.2181
STATIC FORCES ON NODE     71 -0.106570     -32.9328

EL=  62  NODES=  73  80  79  72   ,   MAT=  3   VOL= 0.1390E-04
XC,YC=  1.324      --  --  --  --
        0.6750E-02  TEMP= 421.0     SX,SY,SXY,SZ=  -87.409          7678.0      -0.35137E-06   7772.7   2-D SOLID
SIG1,SIG2,SIG3=      7772.7           7678.0          -87.409   S.I.=  7860.1   SIGE=     7813.2
STATIC FORCES ON NODE     73 -0.106570      32.9328
STATIC FORCES ON NODE     80  0.657720E-01    38.2181
STATIC FORCES ON NODE     79  0.657720E-01   -38.2181
STATIC FORCES ON NODE     72 -0.106570     -32.9328

EL=  63  NODES=  74  81  80  73       MAT=  3   VOL= 0.1390E-04                                          2-D SOLID
```

```
 STATIC FORCES ON NODE      86  0.657720E-01   -38.2181
 STATIC FORCES ON NODE      73 -0.106570      -32.9328

ELT=   64  NODES=   75   82   81   74      MAT=  3.  VOL= 0.1390E-04                                          2-D SOLID
XC,YC=  1.324     0.3750E-02  TEMP= 421.0  SX,SY,SXY,S7=  -87.409        7678.0      0.20249E-06   7772.7
 SIG1,SIG2,SIG3=     7772.7        7678.0        -87.409      S.I.=       7860.1      SIGE=       7813.2
 STATIC FORCES ON NODE      75 -0.106570      -32.9328
 STATIC FORCES ON NODE      82  0.657720E-01   -38.2181
 STATIC FORCES ON NODE      81  0.657720E-01   -38.2181
 STATIC FORCES ON NODE      74 -0.106570      -32.9328

ELT=   65  NODES=   76   83   82   75      MAT=  3   VOL= 0.1390E-04                                          2-D SOLID
XC,YC=  1.324     0.2250E-02  TEMP= 421.0  SX,SY,SXY,S7=  -87.409        7678.0      0.35126E-06   7772.7
 SIG1,SIG2,SIG3=     7772.7        7678.0        -87.409      S.I.=       7860.1      SIGE=       7813.2
 STATIC FORCES ON NODE      76 -0.106570      -32.9328
 STATIC FORCES ON NODE      83  0.657720E-01   -38.2181
 STATIC FORCES ON NODE      82  0.657720E-01   -38.2181
 STATIC FORCES ON NODE      75 -0.106570      -32.9328

ELT=   66  NODES=   77   84   83   76      MAT=  3   VOL= 0.1390E-04                                          2-D SOLID
XC,YC=  1.324     0.7500E-03  TEMP= 421.0  SX,SY,SXY,S7=  -87.409        7678.0      0.12589E-06   7772.7
 SIG1,SIG2,SIG3=     7772.7        7678.0        -87.409      S.I.=       7860.1      SIGE=       7813.2
 STATIC FORCES ON NODE      77 -0.106570      -32.9328
 STATIC FORCES ON NODE      84  0.657720E-01   -38.2181
 STATIC FORCES ON NODE      83  0.657720E-01   -38.2181
 STATIC FORCES ON NODE      76 -0.106570      -32.9328

ELT=   67  NODES=   79   86   85   78      MAT=  3   VOL= 0.1553E-04                                          2-D SOLID
XC,YC=  1.331     0.8250E-02  TEMP= 407.2  SX,SY,SXY,S7=  -33.707        11236.      0.25803E-07   11277.
 SIG1,SIG2,SIG3=     11277.        11236.        -33.707      S.I.=       11311.      SIGE=       11290.
 STATIC FORCES ON NODE      79 -0.657720E-01    54.8857
 STATIC FORCES ON NODE      86  0.286175E-09   -61.4477
 STATIC FORCES ON NODE      85  0.281553E-11   -61.4477
 STATIC FORCES ON NODE      78 -0.657720E-01    54.8857

ELT=   68  NODES=   80   87   86   79      MAT=  3   VOL= 0.1553E-04                                          2-D SOLID
XC,YC=  1.331     0.6750E-02  TEMP= 407.2  SX,SY,SXY,S7=  -33.707        11236.      0.73915E-07   11277.
 SIG1,SIG2,SIG3=     11277.        11236.        -33.707      S.I.=       11311.      SIGE=       11290.
 STATIC FORCES ON NODE      80 -0.657720E-01    54.8857
 STATIC FORCES ON NODE      87  0.385501E-09   -61.4477
 STATIC FORCES ON NODE      86 -0.285722E-09   -61.4477
 STATIC FORCES ON NODE      79 -0.657720E-01    54.8857

ELT=   69  NODES=   81   88   87   80      MAT=  3   VOL= 0.1553E-04                                          2-D SOLID
XC,YC=  1.331     0.5250E-02  TEMP= 407.2  SX,SY,SXY,S7=  -33.707        11236.      0.41783E-07   11277.
 SIG1,SIG2,SIG3=     11277.        11236.        -33.707      S.I.=       11311.      SIGE=       11290.
 STATIC FORCES ON NODE      81 -0.657720E-01    54.8857
 STATIC FORCES ON NODE      88  0.962785E-12   -61.4477
 STATIC FORCES ON NODE      87 -0.388692E-09   -61.4477
 STATIC FORCES ON NODE      80 -0.657720E-01    54.8857

ELT=   70  NODES=   82   89   88   81      MAT=  3   VOL= 0.1553E-04                                          2-D SOLID
XC,YC=  1.331     0.3750E-02  TEMP= 407.2  SX,SY,SXY,S7=  -33.707        11236.     -0.41765E-07   11277.
 SIG1,SIG2,SIG3=     11277.        11236.        -33.707      S.I.=       11311.      SIGE=       11290.
 STATIC FORCES ON NODE      82 -0.657720E-01    54.8857
 STATIC FORCES ON NODE      89 -0.387521E-09   -61.4477
 STATIC FORCES ON NODE      88  0.280576E-11   -61.4477
 STATIC FORCES ON NODE      81 -0.657720E-01    54.8857

ELT=   71  NODES=   83   90   89   82      MAT=  3   VOL= 0.1553E-04                                          2-D SOLID
XC,YC=  1.331     0.2250E-02  TEMP= 407.2  SX,SY,SXY,S7=  -33.707        11236.     -0.74291E-07   11277.
 SIG1,SIG2,SIG3=     11277.        11236.        -33.707      S.I.=       11311.      SIGE=       11290.
 STATIC FORCES ON NODE      83 -0.657720E-01    54.8857
 STATIC FORCES ON NODE      90 -0.284750E-09   -61.4477
 STATIC FORCES ON NODE      89  0.387083E-09   -61.4477
 STATIC FORCES ON NODE      82 -0.657720E-01    54.8857

ELT=   72  NODES=   84   91   90   83      MAT=  3   VOL= 0.1553E-04                                          2-D SOLID
XC,YC=  1.331     0.7500E-03  TEMP= 407.2  SX,SY,SXY,S7=  -33.707        11236.     -0.26170E-07   11277.
 SIG1,SIG2,SIG3=     11277.        11236.        -33.707      S.I.=       11311.      SIGE=       11290.
 STATIC FORCES ON NODE      84 -0.657720E-01    54.8857
 STATIC FORCES ON NODE      91  0.784262E-12   -61.4477
 STATIC FORCES ON NODE      90  0.287654E-09   -61.4477
 STATIC FORCES ON NODE      83 -0.657720E-01    54.8857

      ***** REACTION FORCES *****   TIME =  0.00000E+00  LOAD STEP=   1  ITERATION= 10  CUM. ITER.=

  NOTE - REACTION FORCES ARE IN THE NODAL COORDINATE SYSTEM

    NODE          FX              FY

       7                      41.9627
      14                      65.1837
      21                      35.6729
      28                      20.1778
      35                      27.3931
      42                      18.8472
      49                      15.0334
      56                      10.2779
      63                     -2.91662
      70                     -23.7185
      77                     -53.3619
      84                     -93.1038
      91                     -61.4477

  TOTAL     0.000000E+00     0.465761E-11

   *** LOAD STEP    1   ITER    10  COMPLETED.  TIME=  0.000000E+00  KUSE= 0  CUM. ITER.=    2
 END OF INPUT ENCOUNTERED ON FILE27

 ***** INPUT FILE SWITCHED FROM FILE27 TO FILE18

 PRINTOUT RESUMED BY /GOP


 ***** ROUTINE COMPLETED *****  CP =        69.440
 /EOF ENCOUNTERED ON FILE18


 ***** RUN COMPLETED *****  CP=        69.4900   TIME=   10.1689
```

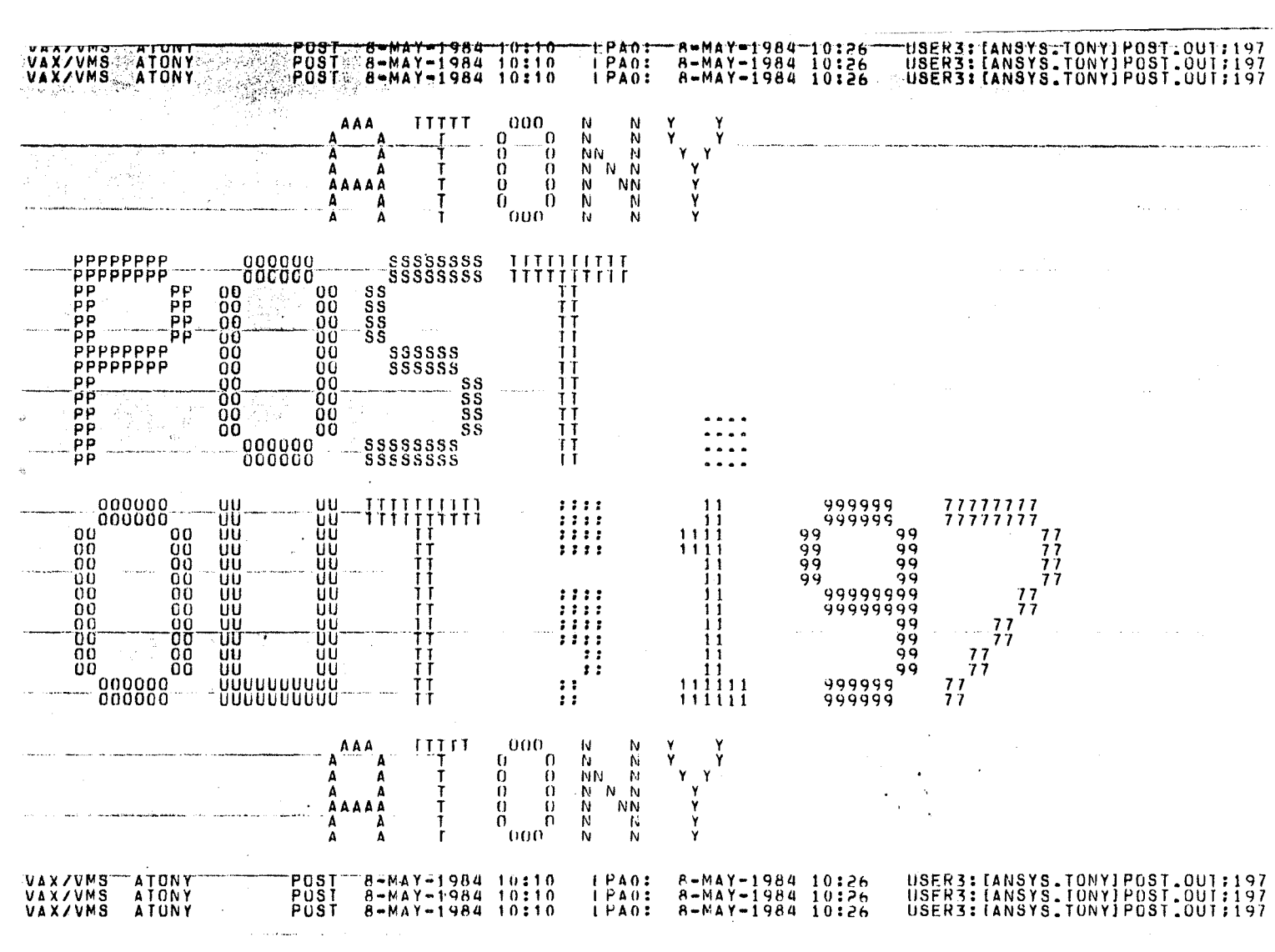

VAX/VMS ATONY POST 8-MAY-1984 10:10 [PA0: 8-MAY-1984 10:26 USER3:[ANSYS.TONY]POST.OUT;197

********** ANSYS INPUT DATA LISTING (FILE18) **********

```
          6     12     18     24     30     36     42     48     54     60     66     72     78
          V      V      V      V      V      V      V      V      V      V      V      V      V
1   /POST21
2   SET,1,10
3   STRESS,1,1,1,1,1,1,1,1,1,1
4   PRINT
5   STRESS,1,200,1
6   FINISH
7   /EOF
```

***** 2-D SOLID ELEMENT POSTPROCESSOR (POST21) *****

LOAD STEP= 1 ITERATION= 10

STRESS COMPONENTS STORED= 1 1 1 1 1 1 1 1 1

LOAD STEP= 1 ITERATION= 10 TIME= 0.00000E+00

NUMBER OF ELEMENTS IN REGION= 72 MAX. NODE NUMBER OF MODEL= 91

GEOMETRY RANGE= 1.295 1.335 0.000 0.009

REGION MAXIMUMS

	NODE	STRESS
SX	60	-139.074
SY	5	-54841.4
SXY	1	-26.3869
SZ	7	-54905.6
SIG1	88	13107.7
SIG2	5	-54841.4
SIG3	7	-54905.6
SIGE	7	54871.6
S.I.	7	54903.7

PRINT NEXT TABLE FROM NODE 1 TO NODE 200 IN STEPS OF 1

THRUST CHAMBER MODEL 10.1721 5/ 8/84 CP= 4.770

ANSYS POST21 NODAL POINT STRESSES

LOAD STEP= 1 ITERATION= 10 TIME= 0.00000E+00

NODE	SX	SY	SXY	SZ	SIG1	SIG2	SIG3	SIGE	S.I.
1	-1.8897	-54841.	-26.387	-54906.	-1.8770	-54841.	-54906.	54872.	54904.
2	-1.8852	-54841.	-0.18282E-03	-54906.	-1.8725	-54841.	-54906.	54872.	54904.
3	-1.8880	-54841.	0.56382E-03	-54905.	-1.8753	-54841.	-54905.	54872.	54904.
4	-1.8876	-54841.	-0.14688E-09	-54905.	-1.8749	-54841.	-54905.	54872.	54904.
5	-1.8880	-54841.	-0.56382E-03	-54905.	-1.8753	-54841.	-54905.	54872.	54904.
6	-1.8852	-54841.	0.18282E-03	-54906.	-1.8725	-54841.	-54906.	54872.	54904.
7	-1.8897	-54841.	26.387	-54906.	-1.8770	-54841.	-54906.	54872.	54904.
8	-48.860	-38066.	-21.751	-38084.	-48.847	-38066.	-38084.	38026.	38036.
9	-48.856	-38066.	-0.31475E-03	-38084.	-48.842	-38066.	-38084.	38026.	38036.
10	-48.859	-38066.	-0.14082E-03	-38084.	-48.845	-38066.	-38084.	38026.	38036.
11	-48.859	-38066.	-0.12460E-09	-38084.	-48.845	-38066.	-38084.	38026.	38036.
12	-48.859	-38066.	0.14082E-03	-38084.	-48.845	-38066.	-38084.	38026.	38036.
13	-48.856	-38066.	0.31475E-03	-38084.	-48.842	-38066.	-38084.	38026.	38036.
14	-48.860	-38066.	21.751	-38084.	-48.847	-38066.	-38084.	38026.	38036.
15	-79.909	-22538.	-11.366	-22523.	-79.901	-22523.	-22538.	22451.	22459.
16	-79.906	-22538.	-0.37923E-03	-22523.	-79.898	-22523.	-22538.	22451.	22459.
17	-79.908	-22538.	-0.72110E-03	-22523.	-79.899	-22523.	-22538.	22451.	22459.
18	-79.908	-22538.	-0.54075E-09	-22523.	-79.900	-22523.	-22538.	22451.	22459.
19	-79.908	-22538.	0.72110E-03	-22523.	-79.899	-22523.	-22538.	22451.	22459.
20	-79.906	-22538.	0.37923E-03	-22523.	-79.898	-22523.	-22538.	22451.	22459.
21	-79.909	-22538.	11.366	-22523.	-79.901	-22523.	-22538.	22451.	22459.
22	-88.945	-23683.	-16.887	-23606.	3142.1	-23621.	-26899.	30003.	30041.
23	-88.943	-23683.	0.12617E-03	-23606.	3142.1	-23621.	-26899.	30003.	30041.
24	-88.943	-23683.	-0.60737E-04	-23606.	3142.1	-23621.	-26899.	30003.	30041.
25	-88.943	-23683.	-0.14652E-08	-23606.	3142.1	-23621.	-26899.	30003.	30041.
26	-88.943	-23683.	0.60737E-04	-23606.	3142.1	-23621.	-26899.	30003.	30041.
27	-88.943	-23683.	-0.12617E-03	-23606.	3142.1	-23621.	-26899.	30003.	30041.
28	-88.945	-23683.	16.887	-23606.	3142.1	-23621.	-26899.	30003.	30041.
29	-106.25	-42145.	-24.276	-42003.	-106.23	-42003.	-42145.	41966.	42039.
30	-106.25	-42145.	0.65065E-03	-42003.	-106.23	-42003.	-42145.	41966.	42039.
31	-106.25	-42145.	0.58462E-03	-42003.	-106.23	-42003.	-42145.	41966.	42039.
32	-106.25	-42145.	-0.20932E-08	-42003.	-106.23	-42003.	-42145.	41966.	42039.
33	-106.25	-42145.	-0.58462E-03	-42003.	-106.23	-42003.	-42145.	41966.	42039.
34	-106.25	-42145.	-0.65065E-03	-42003.	-106.23	-42003.	-42145.	41966.	42039.
35	-106.25	-42145.	24.276	-42003.	-106.23	-42003.	-42145.	41966.	42039.
36	-119.79	-28976.	-16.659	-28822.	-119.78	-28822.	-28976.	28780.	28857.
37	-119.79	-28976.	0.71777E-03	-28822.	-119.78	-28822.	-28976.	28780.	28857.
38	-119.79	-28976.	0.68305E-03	-28822.	-119.78	-28822.	-28976.	28780.	28857.
39	-119.79	-28976.	-0.20128E-08	-28822.	-119.78	-28822.	-28976.	28780.	28857.
40	-119.79	-28976.	-0.68305E-03	-28822.	-119.78	-28822.	-28976.	28780.	28857.
41	-119.79	-28976.	-0.71777E-03	-28822.	-119.78	-28822.	-28976.	28780.	28857.
42	-119.79	-28976.	16.659	-28822.	-119.78	-28822.	-28976.	28780.	28857.
43	-128.54	-10895.	-7.2645	-10747.	-128.54	-10747.	-10895.	10694.	10767.
44	-128.54	-10895.	0.40183E-03	-10747.	-128.54	-10747.	-10895.	10694.	10767.
45	-128.54	-10895.	0.38690E-03	-10747.	-128.54	-10747.	-10895.	10694.	10767.
46	-128.54	-10895.	-0.16861E-08	-10747.	-128.53	-10747.	-10895.	10694.	10767.
47	-128.54	-10895.	-0.38690E-03	-10747.	-128.54	-10747.	-10895.	10694.	10767.
48	-128.54	-10895.	-0.40183E-03	-10747.	-128.54	-10747.	-10895.	10694.	10767.
49	-128.54	-10895.	7.2645	-10747.	-128.54	-10747.	-10895.	10694.	10767.
50	-136.80	-1969.5	-0.99875	-1827.6	-136.80	-1827.6	-1969.5	1766.0	1836.7
51	-136.80	-1969.5	0.38500E-04	-1827.6	-136.80	-1827.6	-1969.5	1766.0	1832.7
52	-136.80	-1969.5	0.36874E-04	-1827.6	-136.80	-1827.6	-1969.5	1766.0	1832.7
53	-136.80	-1969.5	-0.19126E-08	-1827.6	-136.80	-1827.6	-1969.5	1766.0	1832.7
54	-136.80	-1969.5	-0.36877E-04	-1827.6	-136.80	-1827.6	-1969.5	1766.0	1832.7
55	-136.80	-1969.5	-0.38501E-04	-1827.6	-136.80	-1827.6	-1969.5	1766.0	1832.7
56	-136.80	-1969.5	0.99875	-1827.6	-136.80	-1827.6	-1969.5	1766.0	1832.7
57	-139.07	314.00	0.31309	458.03	458.03	314.00	-139.08	539.70	597.11
58	-139.07	314.00	-0.13029E-04	458.03	458.03	314.00	-139.08	539.70	597.11
59	-139.07	314.00	-0.12581E-04	458.03	458.03	314.00	-139.08	539.70	597.11
60	-139.07	314.00	-0.86768E-09	458.03	458.03	314.00	-139.08	539.70	597.11
61	-139.07	314.00	0.12580E-04	458.03	458.03	314.00	-139.08	539.70	597.11
62	-139.07	314.00	0.13029E-04	458.03	458.03	314.00	-139.08	539.70	597.11
63	-139.07	314.00	-0.31309	458.03	458.03	314.00	-139.08	539.70	597.11
64	-131.48	2967.4	1.8201	3103.6	3103.6	2967.4	-131.48	3169.2	3235.1
65	-131.48	2967.4	0.12681E-05	3103.6	3103.6	2967.4	-131.48	3169.2	3235.1
66	-131.48	2967.4	0.11343E-05	3103.6	3103.6	2967.4	-131.48	3169.2	3235.1
67	-131.48	2967.4	-0.16113E-09	3103.6	3103.6	2967.4	-131.48	3169.2	3235.1
68	-131.48	2967.4	-0.11342E-05	3103.6	3103.6	2967.4	-131.48	3169.2	3235.1
69	-131.48	2967.4	-0.12690E-05	3103.6	3103.6	2967.4	-131.48	3169.2	3235.1
70	-131.48	2967.4	-1.8201	3103.6	3103.6	2967.4	-131.48	3169.2	3235.1
71	-109.56	5986.6	3.5121	6100.7	6100.7	5986.6	-109.57	6154.0	6210.2
72	-109.56	5986.6	0.10691E-06	6100.7	6100.7	5986.6	-109.57	6154.0	6210.2
73	-109.56	5986.6	0.15052E-06	6100.7	6100.7	5986.6	-109.57	6154.0	6210.2
74	-109.56	5986.6	-0.86180E-10	6100.7	6100.7	5986.6	-109.57	6154.0	6210.2
75	-109.56	5986.6	-0.15100E-06	6100.7	6100.7	5986.6	-109.57	6154.0	6210.2
76	-109.56	5986.6	-0.10815E-06	6100.7	6100.7	5986.6	-109.57	6154.0	6210.2
77	-109.56	5986.6	-3.5121	6100.7	6100.7	5986.6	-109.57	6154.0	6210.2
78	-68.426	9366.3	5.3779	9439.0	9439.0	9366.3	-68.429	9471.3	9507.5
79	-68.426	9366.3	-0.93660E-07	9439.0	9439.0	9366.3	-68.429	9471.3	9507.5
80	-68.426	9366.3	-0.10904E-06	9439.0	9439.0	9366.3	-68.429	9471.3	9507.5
81	-68.426	9366.3	0.95523E-10	9439.0	9439.0	9366.3	-68.429	9471.3	9507.5
82	-68.426	9366.3	0.10890E-06	9439.0	9439.0	9366.3	-68.429	9471.3	9507.5
83	-68.426	9366.3	0.93608E-07	9439.0	9439.0	9366.3	-68.429	9471.3	9507.5
84	-68.426	9366.3	-5.3779	9439.0	9439.0	9366.3	-68.429	9471.3	9507.5
85	-2.5543	13101.	6.3527	13108.	13108.	13101.	-2.5574	13107.	13110.
86	-2.5543	13101.	0.49837E-07	13108.	13108.	13101.	-2.5574	13107.	13110.
87	-2.5543	13101.	0.57861E-07	13108.	13108.	13101.	-2.5574	13107.	13110.
88	-2.5543	13101.	-0.18997E-09	13108.	13108.	13101.	-2.5574	13107.	13110.
89	-2.5543	13101.	-0.58096E-07	13108.	13108.	13101.	-2.5574	13107.	13110.
90	-2.5543	13101.	-0.49793E-07	13108.	13108.	13101.	-2.5574	13107.	13110.
91	-2.5543	13101.	-6.3527	13108.	13108.	13101.	-2.5574	13107.	13110.
MAXIMUM VALUE									
NODES	60	5	1	7	88	5	7	7	7
STRESS	-139.07	-54841.	-26.387	-54906.	13108.	-54841.	-54906.	54872.	54904.

PLOT DATA (IF ANY) WRITTEN ON FILE21

***** ROUTINE COMPLETED ***** CP = 5.630

/EOF ENCOUNTERED ON FILE18

***** RUN COMPLETED ***** CP= 5.6800 TIME= 10.1725

```
VAX/VMS  ATONY        Q  8-MAY-1984 10:10    LPA0:   8-MAY-1984 10:27    USER3:[ANSYS.TONY]Q.LOG;1
VAX/VMS  ATONY        G  8-MAY-1984 10:10    LPA0:   8-MAY-1984 10:27    USER3:[ANSYS.TONY]G.LOG;1
VAX/VMS  ATONY        Q  8-MAY-1984 10:10    LPA0:   8-MAY-1984 10:27    USER3:[ANSYS.TONY]Q.LOG;1

                        AAA    TTTTT   000   N   N  Y   Y
                       A   A     T    0   0  N   N  Y   Y
                       A   A     T    0   0  NN  N   Y Y
                       A   A     T    0   0  N N N    Y
                       AAAAA     T    0   0  N  NN    Y
                       A   A     T    0   0  N   N    Y
                       A   A     T     000   N   N    Y


      QQQQQQ
     QQQQQQQ
    QQ      QQ
    QQ      QQ
    QQ      QQ
    QQ      QQ
    QQ      QQ
    QQ      QQ
    QQ   QQ QQ
    QQ   QQ QQ
    QQ     QQ        ....
    QQ     QQ        ....
     QQQQ  QQ        ....
     QQQQ  QQ        ....

    LL          000000      GGGGGGGG       ::::         11
    LL          OOOOOO      GGGGGGGG       ::::         11
    LL        00      00  GG               ::::       1111
    LL        00      00  GG               ::::       1111
    LL        00      00  GG                            11
    LL        00      00  GG                            11
    LL        00      00  GG               ::::         11
    LL        00      00  GG               ::::         11
    LL        00      00  GG  GGGGGG       ::::         11
    LL        00      00  GG  GGGGGG       ::::         11
    LL        00      00  GG      GG         ::         11
    LL        00      00  GG      GG         ::         11
    LLLLLLLLLL    000000      GGGGGG         ::       111111
    LLLLLLLLLL    OOOOOO      GGGGGG         ::       111111

                        AAA    TTTTT   000   N   N  Y   Y
                       A   A     T    0   0  N   N  Y   Y
                       A   A     T    0   0  NN  N   Y Y
                       A   A     T    0   0  N N N    Y
                       AAAAA     T    0   0  N  NN    Y
                       A   A     T    0   0  N   N    Y
                       A   A     T     000   N   N    Y

VAX/VMS  ATONY        Q  8-MAY-1984 10:10    LPA0:   8-MAY-1984 10:27    USER3:[ANSYS.TONY]Q.LOG;1
VAX/VMS  ATONY        Q  8-MAY-1984 10:10    LPA0:   8-MAY-1984 10:27    USER3:[ANSYS.TONY]Q.LOG;1
VAX/VMS  ATONY        Q  8-MAY-1984 10:10    LPA0:   8-MAY-1984 10:27    USER3:[ANSYS.TONY]Q.LOG;1
```

```
G:LOG;1                    8-MAY-1984 10:27                PAGE 1

$ CURVER = 1
$ SET NOVERIFY
HAVE A HAPPY DAY!!
$ DUMMY = 0
$ EXIT
$ SET DEF [ANSYS.TONY]
$ ASS SNEW2.CER FOR005
$ ASS SNEW2.OUT FOR006
$ RUN [ANSYS.ANSYS]ANSYS
$ PRINT SNEW2.OUT
  JOB 1778 ENTERED ON QUEUE SYS$PRINT
$ ASS SNEWK.STR FOR005
PREVIOUS LOGICAL NAME ASSIGNMENT REPLACED
$ ASS SNSTAL.OUT FOR006
PREVIOUS LOGICAL NAME ASSIGNMENT REPLACED
$ RUN [ANSYS.ANSYS]ANSYS
$ PRINT SNSTAL.OUT
  JOB 1779 ENTERED ON QUEUE SYS$PRINT
$ ASS POST.ANS FOR005
PREVIOUS LOGICAL NAME ASSIGNMENT REPLACED
$ ASS POST.OUT FOR006
PREVIOUS LOGICAL NAME ASSIGNMENT REPLACED
$ RUN [ANSYS.ANSYS]ANSYS
$ PRINT POST.OUT
  JOB 1780 ENTERED ON QUEUE SYS$PRINT
  ATONY       JOB TERMINATED AT  8-MAY-1984 10:10:23.14

  ACCOUNTING INFORMATION:
  BUFFERED I/O COUNT:              297      PEAK WORKING SET SIZE:    500
  DIRECT I/O COUNT:                574      PEAK PAGE FILE SIZE:     4938
  PAGE FAULTS:                   11289      MOUNTED VOLUMES:            0
  ELAPSED CPU TIME:      0 00:02:31.30      ELAPSED TIME:      0 00:04:37.22
```

APPENDIX 3

PHOTOGRAPHS OF TEST SPECIMENS

This appendix is supplied to document the coating test specimens used for this program through photographs.

Figure 90 shows two flat and one ring specimen before testing.

Figure 91 shows two flat bend specimens after testing. The top specimen was bent with the coating in tensions; the bottom specimen with the coating in compression. The flake shown with the bottom specimen is a piece of coating which spalled from the middle span.

Figures 92 and 93 show close-ups of two bend specimens after test. Figure 92 shows a coating failure due to compressive stress and Figure 93 shows a coating which has been subjected to substantial tensile bending stress.

Figure 94 shows four bend specimens after test, and Figure 95 shows a close-up of one of these.

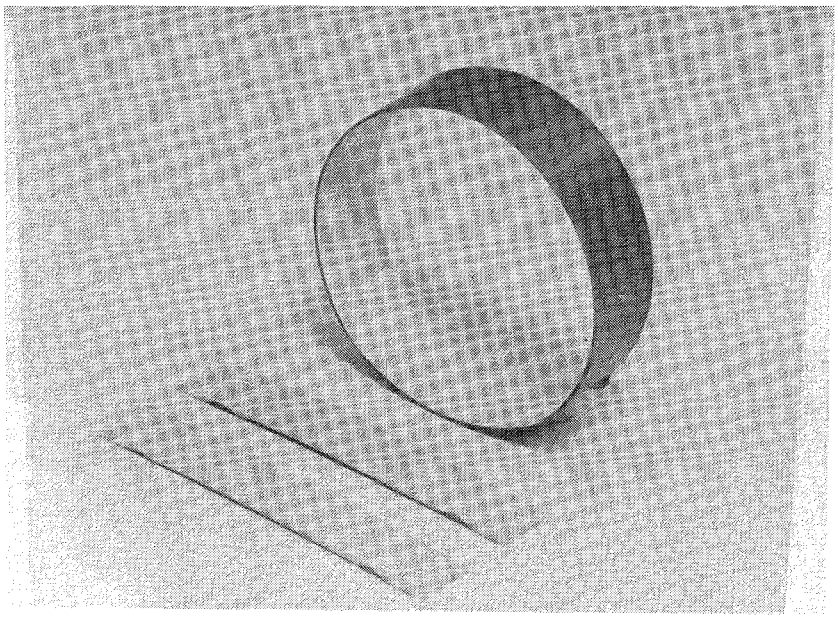

Figure 90. Specimens Prior to Testing

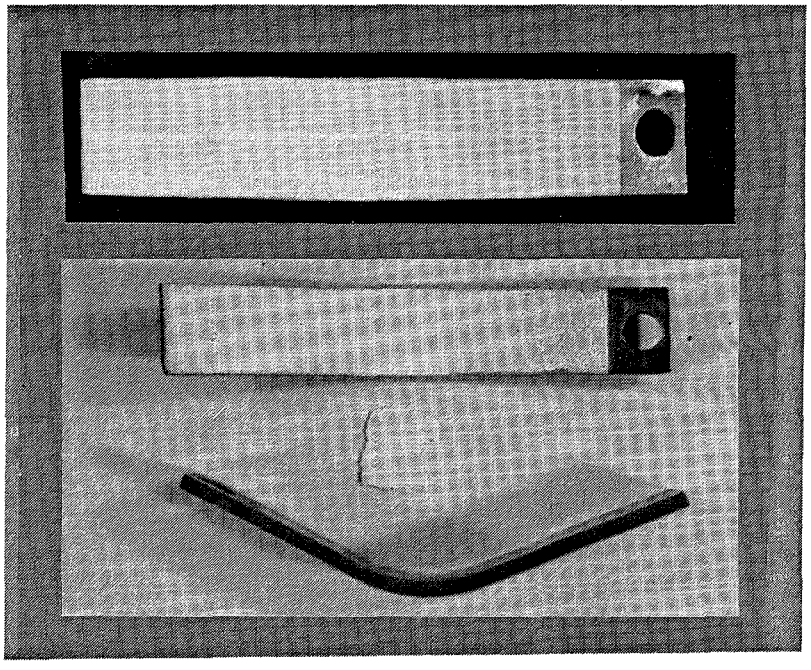

Figure 91. Two Bend Specimens Ater Test
Upper: Coating in Tension
Lower: Coating in Compression

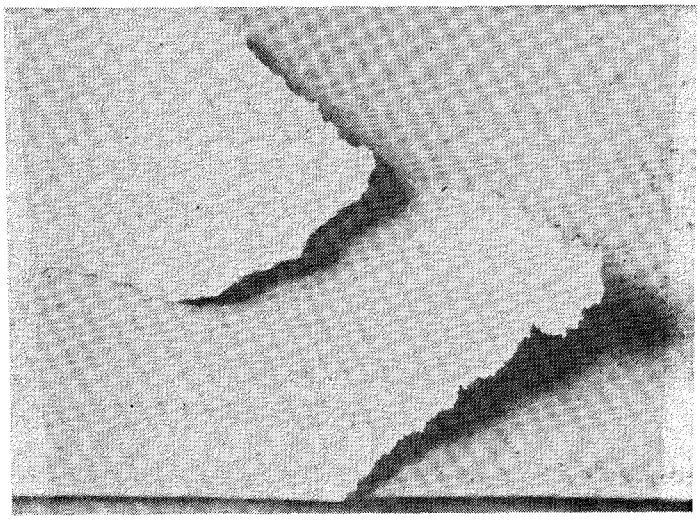

Figure 92. Compressive Coating Failure

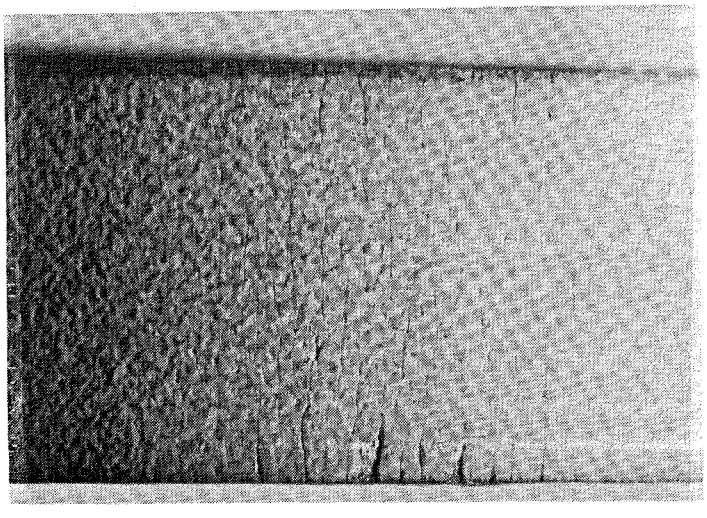

Figure 93. Tensile Coating Cracks

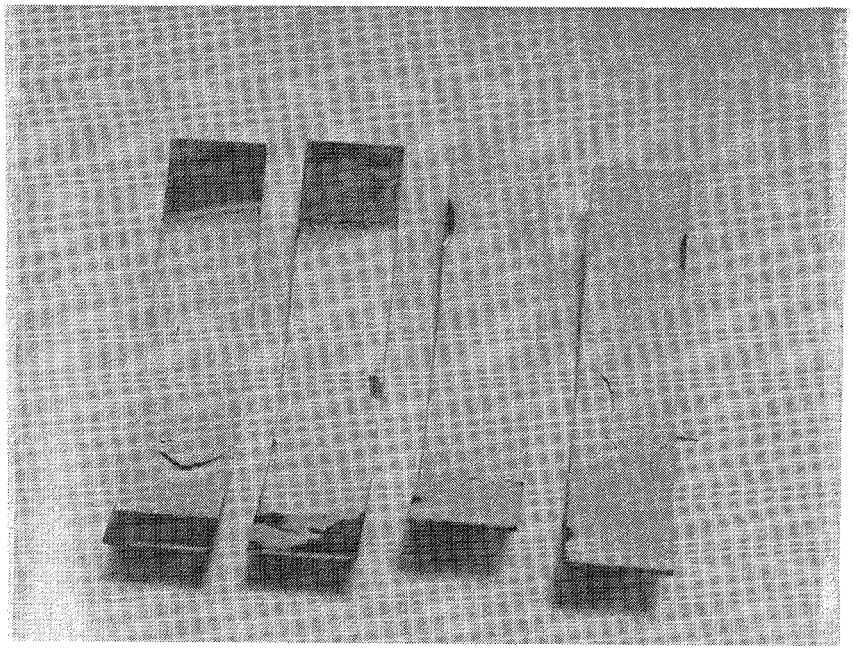

Figure 94. Specimens After Test

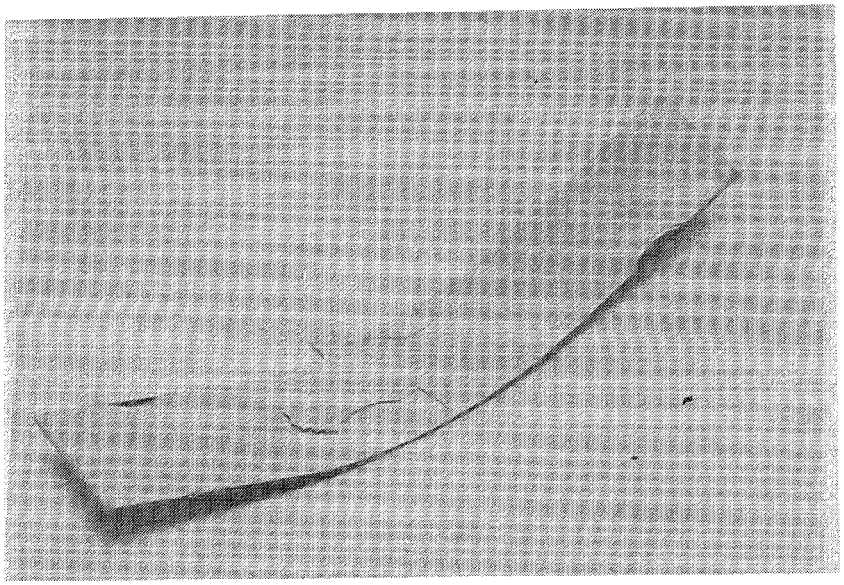

Figure 95. Bend Specimen After Test

End of Document